Antenna designs using matching circuits for 4G communicating devices

Aykut Cihangir

UNIVERSITE DE NICE-SOPHIA ANTIPOLIS

ECOLE DOCTORALE STIC

SCIENCES ET TECHNOLOGIES DE L'INFORMATION ET DE LA COMMUNICATION

ANTENNA DESIGNS USING MATCHING CIRCUITS FOR 4G COMMUNICATING DEVICES

THESE

POUR L'OBTENTION DU GRADE DE

DOCTEUR EN SCIENCES DE L'UNIVERSITE DE NICE-SOPHIA ANTIPOLIS

PAR

AYKUT CIHANGIR

DIRECTEUR DE THESE: CYRIL LUXEY

SOUTENANCE PREVUE LE 6 MARS 2014

Jury:

M. Ala SHARAIHA, Professeur à l' Université de Rennes (Rapporteur)
M. Laurent DUSSOPT, CEA-LETI (Rapporteur)
M. Christian PERSON, Professeur au Lab-STICC (Examinateur)
M. Frédéric Gianesello, STMicroelectronics (Examinateur)
M. Cyril LUXEY, Professeur à l'Université de Nice-Sophia-Antipolis (Directeur de thèse)
M. Fabien FERRERO, Maitre de conférences, LEAT (Co-Encadrant)
M. Olivier Pajona, Ethertronics (Invité)

TABLE OF CONTENTS

TABLE OF ACRONYMS

CA	Carrier Aggregation	**LTE**	Long Term Evolution
CE	Coupling Element	**MEMS**	Micro Electro-Mechanical Systems
EM	Electromagnetics	**MIMO**	Multiple Input Multiple Output
GSM	Global System for Mobile Telecommunications	**MN**	Matching Network
HB	High-Band	**PCB**	Printed Circuit Board
IFA	Inverted F Antenna	**PIFA**	Planar Inverted F Antenna
LB	Low-Band	**SMD**	Surface Mount Device
LDS	Laser Direct Structuring	**UMTS**	Universal Mobile Telecommunications System

ABSTRACT

With the introduction of the fourth generation (4G) of cellular mobile communications, there has been an increase in the frequency bands that a generic mobile phone should be able to operate. This requirement poses some challenges in the design of the transceiver modules of the device as well as the RF front-end and the antenna.

From the antenna design point of view, the newly added frequency bands especially LTE bands 12-13-17 which goes down to 700MHz creates the main design challenge: covering 700-960MHz (30% bandwidth) in the low-band, considering also backward compatibility with the former technologies like GSM850/900. Since the space reserved for the antenna is electrically small in this frequency range, special design techniques are necessary to obtain the required bandwidth for a generic mobile terminal antenna.

It should also be taken into account in the design phase, that the antenna needs to be appropriate for operation in the data-rate enhancement techniques like MIMO (multiple input multiple output) and carrier aggregation in LTE-Advanced. Furthermore, considering the real use cases of the mobile terminal, the effect of the user (hand, head and both) on the antenna performance should also be investigated.

In this thesis, several antenna designs for 4G coverage in mobile terminals are proposed. Different antenna topologies are evaluated consisting of tunable/passive antennas as well as single/multi-feed structures.

The "Introduction" chapter starts with a summary about the evolution of cellular communications starting from the first analog systems evolving to the fourth generation. General information about mobile phone antennas from the past decades is then presented ending with some examples of today's smartphone antennas. Electrically-small antennas are then presented briefly with their basic specifications and some state-of-the-art antennas for mobile terminals proposed in literature. The chapter concludes with a comparison between single-feed and multi-feed solutions with their advantages/disadvantages in LTE-Advanced technology.

Some tunable antennas, designed within the scope of the Artemos Project are presented in Chapter II. Firstly, two antenna designs using MEMS switches for band-switching between low-band (700-960MHz) and high-band (1.7-2.7GHz) are proposed, using antenna-parasitic strips for bandwidth enlargement. A circuit model is also proposed, modeling an antenna in combination with a grounded parasitic strip. A problem seen as radiation efficiency drop in these structures is also addressed with some solutions. Finally, a tunable antenna using tunable BST capacitors at the antenna feed is presented in this chapter.

A novel coupling element (CE) type antenna is proposed in Chapter III, which enables a more space-efficient design in comparison to plain CEs. First, the characteristics of the novel "hollow CE" is compared with a plain CE and two dual-feed antenna solutions are presented, using hollow CEs. As an application example, a MIMO structure using two hollow CEs is then given, using the neutralization line technique for higher isolation and lower correlation.

In Chapter IV, two single-feed antenna designs are proposed, manufactured using Laser Direct Structuring (LDS) technology. The first antenna can cover low-LTE/GSM/UMTS bands (700-960MHz and 1.7-2.2GHz) and the coverage of higher LTE and Wi-Fi bands (2.4-2.7GHz) is added in the second antenna. The effect of the user (hand and head) is investigated through measurements. An antenna resistant to detuning (due to the user) is then evaluated from these results as a future perspective.

A new use case of CE antennas is introduced in Chapter V, exploited to cover the 4G cellular communication bands in electronic eyewear devices, which are gaining popularity nowadays. First, a feasibility study is presented introducing the devices under design by several different companies. The bandwidth potential and SAR levels are evaluated according to different positioning of the CE in the eyewear device. Afterwards, three different antennas are proposed considering realistic casing and spectacles for the device.

Finally, a conclusion is done in Chapter VI, summarizing the general results from this thesis with some low-term and mid-term future perspectives.

CHAPTER I
INTRODUCTION

1. EVOLUTION OF CELLULAR COMMUNICATIONS

For more than thirty years, cellular communication has been under a substantial growth, according to the user demand. The first mobile communication systems were launched approximately around 1980s, giving the telephone users the freedom to make or accept calls, without the need for a fixed landline.

A cellular communication system is basically composed of three layers which are the core, the edge and the access subsystems [1]. Among these, the core is the nucleus of the network, that performs the handling of the voice calls, traffic control, user authentication and user profile (like charging the customer for the used services). The edge subsystem is an interface between the core and the access subsystems. The access subsystem (also called NodeB or Base Transceiver Station) is then responsible for establishing the air link with the mobile user equipment (UE). Different multiplexing schemes are used to serve a number of mobile users and duplexing techniques like FDD (Frequency Division Duplexing) and TDD (Time Division Duplexing) are used to establish a two-way communication (uplink and downlink) between the base station and mobile terminal. The land to be serviced is divided into some cells where these cells are served by base stations. The user can move between different cells and the handover is done automatically, transparent to the user.

The first mobile communications services (first generation or 1G) were launched in different parts of the world after 1979 [2]. These networks were based on analog systems for voice communications. The system used frequency modulation for modulating the voice signal and each user was assigned a specific frequency by Frequency Division Multiple Access (FDMA).

Approximately ten years later, the second generation of mobile communications (2G) was announced and the modulation scheme was changed from analog to digital, allowing also data transfer for services like Short Message Service (SMS). Multiple number of users were handled by using either TDMA (Time Division Multiple Access) or CDMA (Code Division Multiple Access). The most popular of the 2G standards is the GSM (Global System for Mobile Communications), which uses TDMA for multiplexing and FDD for duplex communication as uplink and downlink. GMSK (Gaussian Minimum Shift Keying) was chosen as the modulation scheme to provide better spectral efficiency. A main advantage of the GSM standard for the users was also the Subscriber Identity Module (SIM card), a card that carries the subscriber information and mobile number so that a user can change between different handset hardware by simply changing the SIM cards.

GPRS is a service launched on 2G systems, providing the user data services like MMS (Multimedia Messaging Service) and Wireless Application Protocol (WAP), making it being accepted as the 2.5G. GPRS was able to provide data rates up to 80kbit/s, which was increased later up to around 200kbit/s with the evolution to EDGE, called as the 2.75G.

With the release of the IMT-2000 standard by International Telecommunication Union, the downlink data rates of several Mbit/s started to be achieved. Systems like UMTS (W-CDMA), WiMax and CDMA2000 are examples of so-called 3G mobile communications, which introduced high-speed internet access, higher quality video and audio streaming. The most widespread radio interface is the W-CDMA using 2100MHz frequency for transmission over 5MHz bandwidth and FDD for duplexing. The downlink data rate was increased to 14Mbit/s and 28Mbit/s with the improvements called HSPA and HSPA+ (in the year 2008) respectively. A further improvement on the 3G systems towards 4G was the LTE (Long Term Evolution, 3.9G), targeting downlink data rates up to 100Mbit/s. LTE specification allows the usage of QPSK, 16QAM and 64QAM modulation types and channel bandwidth of up to 20MHz, with FDD and TDD for duplexing schemes. Additional usage of MIMO

(Multiple Input Multiple Output) can increase the maximum data rate from 100Mbit/s to 326Mbit/s. The access scheme used for the downlink is OFDMA (Orthogonal Frequency Division Multiple Access) for downlink and SC-FDMA (Single Carrier Frequency Division Multiple Access) for uplink.

2. GENERAL INFORMATION ON 4G TECHNOLOGIES

The successor of the 3G communication systems is the LTE-Advanced (LTE-A) which is accepted to be the fourth generation (4G) of the cellular communication systems. With this technology, the modulation schemes of QPSK, 16QAM and 64QAM are used to obtain peak data rates of up to 1Gbit/s for a low-mobility user in downlink (100Mbit/s for high mobility) and 500Mbit/s for uplink. OFDMA is used for multiple access in the downlink whereas SC-FDMA is used for uplink. The exploitation of multi-antenna systems (both for receive diversity or MIMO) is also available to reach the peak data rates. The available frequency bands for the 4G systems are shown in Figure 1, including also the 3G bands. A 4G mobile terminal should also be able to operate in the former 3G bands for backward compatibility since there is a risk of the lack a 4G base station everywhere the user may be located.

Figure 1 Frequency Allocation for 4G Systems

The LTE/4G frequency bands are presented in Table 1 and Table 2 for FDD LTE and TDD LTE respectively. It can be seen that the channel bandwidths allocated to each band is variable between 1.4MHz and 20MHz. Generally for the lower frequency bands (like bands 12 and 13) the maximum allowable channel bandwidth is up to 10MHz whereas for higher frequency bands (like band 3 or 10), bandwidths up to 20MHz is possible per channel. The multiple access scheme used in the 4G systems is OFDMA (Orthogonal Frequency Division Multiple Access), making the system more robust to fading, allowing higher data rates.

Another novelty introduced with LTE-A is the carrier aggregation, which is basically the utilization of more than one available channel for a single user. This way, the maximum achievable data rate offered to the customer can be increased. Three types of carrier aggregation are available for LTE-A as shown in Figure 2. The first type marked as (a) uses two adjacent frequency channels for a user which is called contiguous intra-band carrier aggregation. In the second type, two channels in the same band are aggregated, which are separated by other channels, making it non-contiguous intra-band carrier aggregation. Finally in the final case, two channels from two different bands are used together, which is called inter-band carrier aggregation. For example for a service provider with a license for transmitting in LTE Band 2 and Band 13, it is possible to provide data to a user over these two channels (20MHz in Band 2 and 10MHz in Band 13, making a total of 30MHz maximum bandwidth) simultaneously using inter-band carrier aggregation. A maximum bandwidth allocation of 100MHz per user is possible through carrier aggregation in LTE-A.

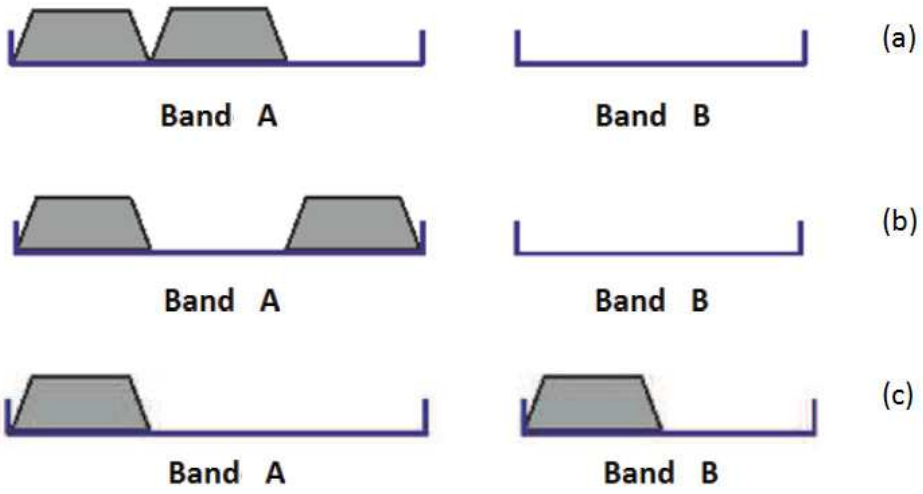

Figure 2 Carrier Aggregation Methods in LTE-A

Table 1 LTE FDD Frequency Bands

LTE Band	Area	DL Frequency	UL Frequency	Bandwidth (MHz)
1	All	2110-2170MHz	1920-1980MHz	5,10,15,20
2	NAR	1930-1990MHz	1850-1910MHz	1.4,3,5,10,15,20
3	All	1805-1880MHz	1710-1785MHz	1.4,3,5,10,15,20
4	NAR	2110-2155MHz	1710-1755MHz	1.4,3,5,10,15,20
5	NAR	869-894MHz	824-849MHz	1.4,3,5,10,15,20
6	APAC	875-885MHz	830-840MHz	5,10
7	EMEA	2620-2690MHz	2500-2570MHz	5,10,15,20
8	All	925-960MHz	880-915MHz	1.4,3,5,10
9	APAC	1845-1880MHz	1750-1785MHz	5,10,15,20
10	NAR	2110-2170MHz	1710-1770MHz	5,10,15,20
11	Japan	1476-1496MHz	1428-1448MHz	5,10
12	NAR	729-746MHz	699-716MHz	1.4,3,5,10
13	NAR	746-756MHz	777-787MHz	5,10
14	NAR	758-768MHz	788-798MHz	5,10
17	NAR	734-746MHz	704-716MHz	5,10
18	Japan	860-875MHz	815-830MHz	5,10,15
19	Japan	875-890MHz	830-845MHz	5,10,15
20	EMEA	791-821MHz	832-862MHz	5,10,15,20
21	Japan	1496-1511MHz	1448-1463MHz	5,10,15
22		3510-3590MHz	3410-3490MHz	5,10,15,20
23	NAR	2180-2200MHz	2000-2020MHz	1.4,3,5,10,15,20
24	NAR	1525-1559MHz	1626.5-1660.5MHz	5,10
25	NAR	1930-1995MHz	1850-1915MHz	1.4,3,5,10,15,20
26	NAR	859-894MHz	814-849MHz	1.4,3,5,10,15
27	NAR	852-869MHz	807-824MHz	1.4,3,5,10
28	APAC	758-803MHz	703-748MHz	3,5,10,15,20
29	NAR	717-728MHz	-	3,5,10
30	NAR	2350-2360MHz	2305-2315MHz	5,10
31	CALA	462.5-467.5MHz	452.5-457.5MHz	1.4,3,5

Table 2 LTE TDD Frequency Bands

LTE Band	Area	Frequency	Bandwidth (MHz)
33		1900-1920MHz	5,10,15,20
34	EMEA	2010-2025MHz	5,10,15
35	NAR	1850-1910MHz	1.4,3,5,10,15,20
36	NAR	1930-1990MHz	1.4,3,5,10,15,20
37	NAR	1910-1930MHz	5,10,15,20
38	China	2570-2620MHz	5,10,15,20
39	China	1880-1920MHz	5,10,15,20
40	China	2300-2400MHz	5,10,15,20
41	All	2496-2690MHz	5,10,15,20
42		3400-3600MHz	5,10,15,20
43		3600-3800MHz	5,10,15,20
44	APAC	703-803MHz	3,5,10,15,20

3. EVOLUTION OF MOBILE PHONE ANTENNAS

The evolution of the cellular mobile communications systems have also changed the characteristics of mobile phone antennas. This evolution was sometimes driven by technical requirements like newly added frequency bands as well as user demand about aesthetical properties. Detailed analysis about the evolution of mobile terminal antennas and possible techniques are presented in [3] and [4].

Older mobile phones had an external antenna on the top of the chassis through the end of 1990s. These antennas were generally either helix type, monopole (whip) type or a combination of both for dual-band operation. The length of the whip antenna was arranged as a quarter of the operating wavelength, forming an even better configuration if the metallic chassis of the phone or the PCB was also a quarter wavelength long, therefore having a full structure like a dipole. To reduce the length of the whip antenna, a good alternative was the helical (or helix) antenna, which can be thought of the convoluted version of the whip antenna (Figure 3). To obtain a multiband structure, it was possible to use a helix antenna with a whip passing through the center axis (Figure 4), two helix antennas with different radii sharing a common axis or two helical antennas with different pitches. Despite having very good efficiency performance, the external antennas had a drawback of having high Specific Absorption Rate (SAR).

Figure 3 Examples of External Antenna for Mobile Phones

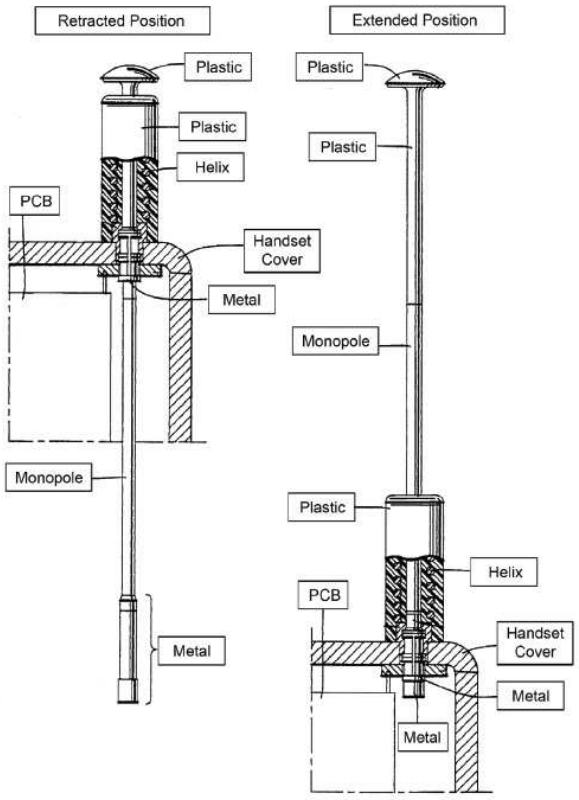

Figure 4 A Monopole & Helix Antenna for Mobile Phones, [3]

Through the end of 1990s, mobile phones having internal antennas started to be released on the market. Nokia released two models in 1998 and 1999 (8810 and 3210), which had internal antennas (Figure 5). One of the major internal antenna type, which was extensively used in mobile phones is the Planar Inverted F Antenna (PIFA), which can be thought of a patch antenna with a connection to the ground plane from some physical point of the antenna[5-6]. Multiband behavior was obtained easily by creating some slots in the rectangular plate to alter the current paths (Figure 6). Using some

parasitic elements either connected to ground plane on one end or left floating in both ends was also an alternative for multiband operation.

Figure 5 Mobile Phone Models Switching From External to Internal Antennas

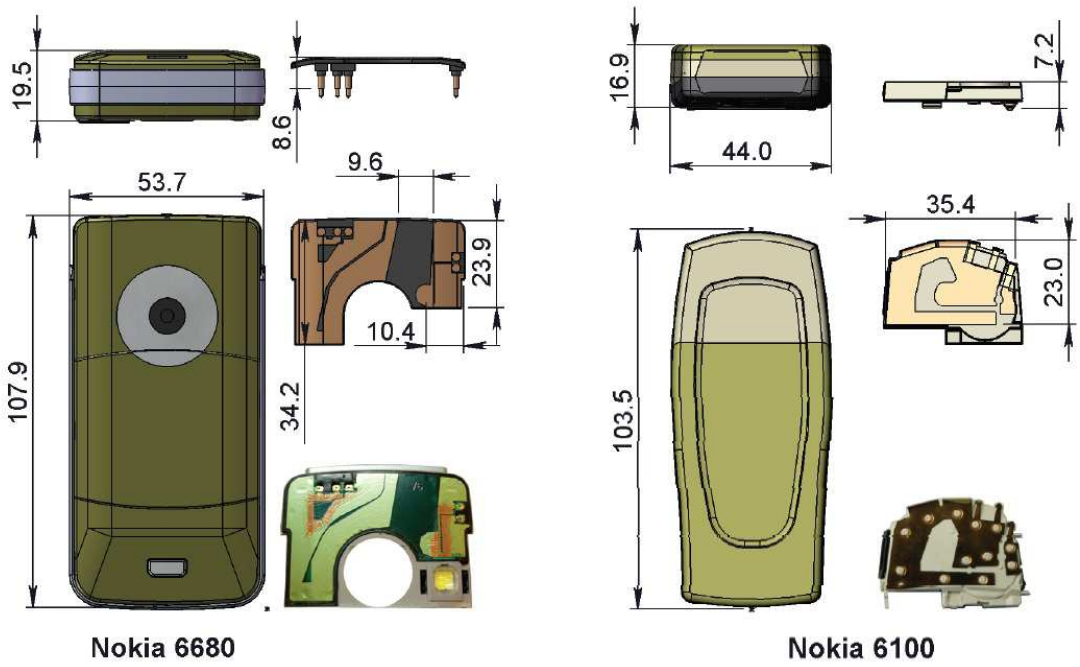

Figure 6 Examples of PIFA Antennas Used in Mobile Phones [3]

Another major internal antenna type used in mobile phones was the planar monopole antennas, which do not have a direct connection to the system ground plane. This type of antennas may require a ground clearance region in the vicinity (generally on one edge of the PCB) for acceptable performance. Techniques like adding parasitic elements or adding parallel branches to the radiating element can be used for multiband operation. This type of antenna was not used in the mobile terminals until recently due to the high SAR values exceeding the limits. The opportunity to place the antenna at the bottom of the mobile phone enabled their usage, since the SAR values were now suitable due to longer distance between the antenna and head when the antenna is on the bottom of the mobile terminal.

Throughout the evolution of the mobile phone antennas, it was generally needed to minimize the volume/area occupied by the antenna. Techniques like etching slots or meandering were used to alter the currents on the antenna element and/or the PCB, called inductive loading. Similarly, capacitive loading was also used for this purpose, this time to manipulate the electrical near fields (like bending the antenna closer to the ground plane). Dielectric loading was also a common method by covering the vicinity of the radiating structure with a relatively high permittivity material to decrease the resonance frequency.

As new standards and new frequency bands were introduced to the mobile communication systems, antennas with wider operating frequency bandwidth in approximately the same volume were needed. Parasitic elements (either grounded or floating) which are excited capacitively by the main antenna, creating additional resonances or changing the frequencies of existing resonances could be used for bandwidth enhancement. Another common technique is also the usage of matching networks, which can either be distributed along the antenna element (for example an inductor on the grounding point of a PIFA) or introduced directly at the feed for arranging the antenna input impedance in a desired way. The matching network can be either composed of completely passive elements (like SMD capacitors and inductors), completely active elements (like a tunable varactor at the antenna feed to tune the impedance) or a combination of both.

4. EXAMPLES OF ANTENNAS IN MODERN SMARTPHONES

This section aims to presents some examples of antennas and their placement in modern smartphones. The first example is the iPhone 4GS, which uses "coupling element" type antennas, whose general properties will be detailed later in this chapter. In iPhone 4GS, the metallic portions of the phone casing (referred to as bezel) are used as radiating structures. For this purpose the bezel is split into two, longer one forming the GSM/UMTS antenna and the shorter other forming the Bluetooth/Wi-Fi/GPS antenna. However, this structure had the problem of being very sensitive to user's hand, especially when the finger is placed between the gap separating the two metallic structures.

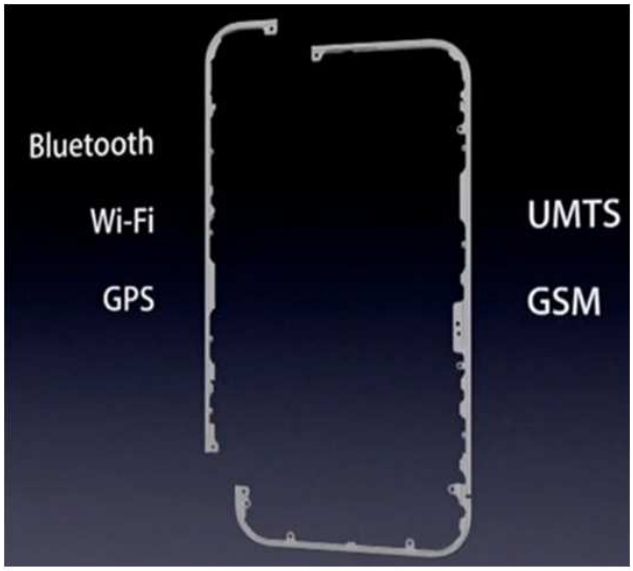

Figure 7 Antenna Placement of iPhone 4GS

In iPhone 5, the cellular antenna seen in Figure 8 was placed at the bottom of the phone and another antenna responsible for Wi-Fi operation was used at the top.

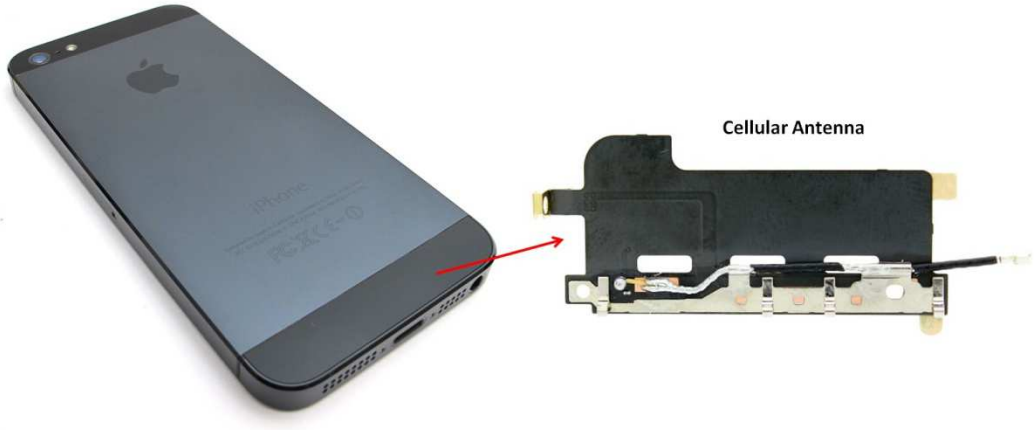

Figure 8 Antenna Placement of iPhone 5

A patent from Apple. Inc about a mobile phone antenna using again the metallic portions (bezel) of the phone casing as the radiating element can be seen in [7]. The antenna proposed in the patent is a loop antenna structure which is fed directly from the gap (shown as 18 in Figure 9), to minimize the fields across it and thus minimize any user effects due to the finger touching the gap (like the problem in iPhone 4GS). For impedance matching, a shunt inductance (formed by a metallic strip shown as 70 in the figure) and a series capacitance (shown as 100) is used at the antenna feed.

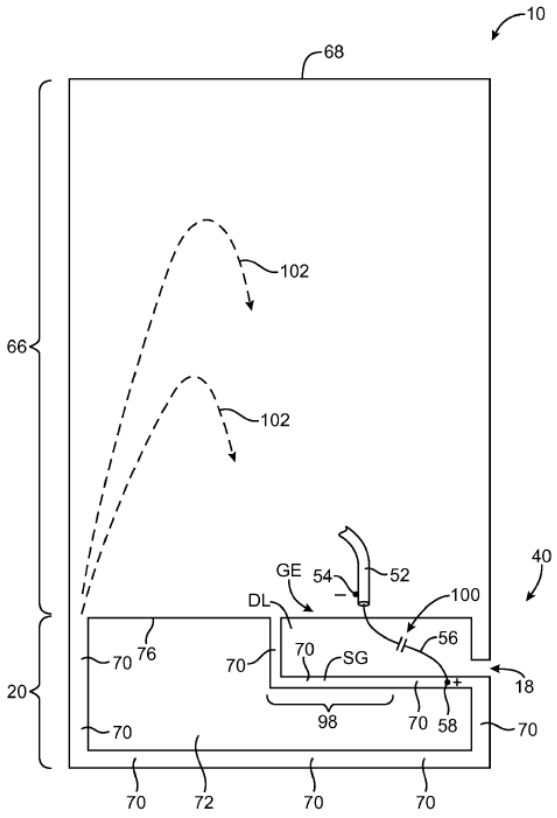

Figure 9 Antenna Structure Proposed in [7]

Another example is HTC Desire S as seen in Figure 10. This phone has three antennas realized using MID technology on plastic. The Bluetooth/Wi-Fi and GPS antennas are situated at the top of the phone whereas the IFA type pentaband antenna for GSM/UMTS is at the bottom.

Figure 10 Antenna Placement of HTC Desire S

The final example is Samsung Galaxy SII, which houses three antenna structures manufactured using MID technology, similarly as in HTC Desire S. In this phone, the GSM and Bluetooth/Wi-Fi antennas are located at the bottom and the GPS antenna is located at the top, just over the camera.

Figure 11 Antenna Placement of Samsung Galaxy SII

5. THEORY OF SMALL ANTENNAS

The popularity of internal antennas for mobile phones has gained a great popularity by the users after their introduction. This is why, the external antenna structures have quickly disappeared from the mobile terminal market. Since the frequency bands used for both GSM850/900, as well as the newly added frequency bands for LTE (like bands 12-13) go down to 700MHz, the free space wavelength rise up to 43cm for cellular communication bands. Considering the space that is available for the antenna in a mobile phone (generally lower than 20mm X 50mm X 7mm), it is evident that the antenna will be electrically small in the target frequency bands. It is also worthwhile to note that the space reserved for the antenna is subject to further decrease in smart phones having larger and larger touch screens and more and more electronic components to be placed like USB connector, camera, battery etc. The main drawback of an electrically small antenna is the low real part and high imaginary part of impedance, which makes it naturally narrowband. Electrically small antennas have been largely investigated in the literature [8-13].

A fundamental and intrinsic parameter of an electrically small antenna is its Quality Factor (Q), which is defined as the ratio of 2π times the energy stored in the near fields excited by the antenna to the energy radiated plus dissipated per cycle. The potential bandwidth of an antenna is inversely proportional to its quality factor, which results in low bandwidth potential for a high-Q antenna. The lowest obtainable radiation quality factor can be calculated from Equation-1 which is known as the Chu limit for electrically small antennas.

$$Q_r = \frac{1}{(ka)^3} + \frac{1}{(ka)} \qquad \text{(Equation-1)}$$

where k is the wavenumber (2π/λ) and a is the radius of the smallest sphere that can enclose the antenna. It is necessary to note that this value is an optimistic theoretical value considering a linearly polarized antenna radiating only in one (TE or TM) mode.

$$FBW = \frac{1}{Q}\sqrt{\frac{(TS-1)(S-T)}{S}} \qquad \text{(Equation-2)}$$

The obtainable frequency bandwidth can be calculated from Equation-2 as also presented in [14], where S is the maximum target VSWR and T is the coupling coefficient as given in [15]. For a value of T=1, Equation 2 reduces to:

$$BW_{cc} = \frac{1}{Q}\frac{(S-1)}{\sqrt{S}} \qquad \text{(Equation-3)}$$

This situation is called the "critically coupled" case, where the input impedance of the antenna is matched exactly to Z_0 (generally 50Ω) at a single frequency point (red curve in Figure 12). An alternative to get higher impedance bandwidth is to get optimal overcoupling, where the antenna is not matched exactly to Z_0, but matched in a wider bandwidth with a higher $|s_{11}|$ (for example with -7dB instead of -15dB), still under a predetermined target reflection coefficient level (blue curve in Figure 12). Some examples of using a matching network to obtain optimally overcoupled antennas are presented in [16-17].

For the calculation of the Q-factor of an antenna from its input impedance, Equation-4 was proposed in [13], which proposes a fast and reliable calculation method.

$$Q(\omega) = \frac{\omega}{2R(\omega)} \sqrt{[R'(\omega)]^2 + \left[X'(\omega) + \frac{|X(\omega)|}{\omega}\right]^2} \qquad \text{(Equation-4)}$$

where ω represents the angular frequency point, R(ω) and X(ω) stands for the real and imaginary parts of the impedance at angular frequency ω, and R'(ω) and X'(ω) are the first derivates of R(ω) and X(ω) according to the frequency. This formula is valid for a single resonant antenna close to its resonance frequency but it has proven reliable performance so far.

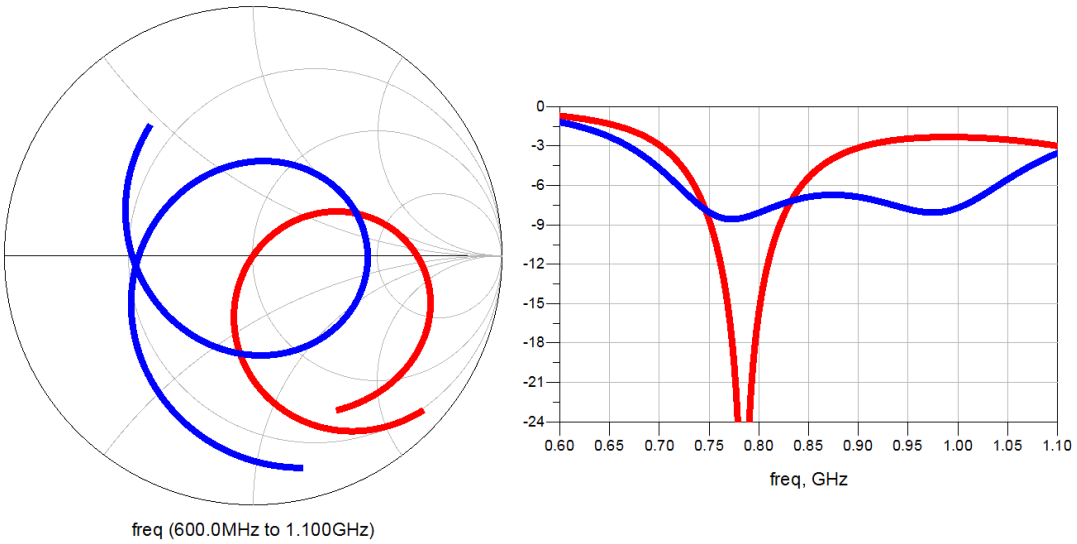

Figure 12 Critical Coupling vs Optimal Overcoupling

6. COUPLING ELEMENT ANTENNAS

As stated also in [18-21], the ground plane of the printed circuit board (PCB) in a mobile terminal plays the major role for radiation especially in the lower-frequency bands, where 90% of the total radiation comes from the PCB at 900MHz for instance[21]. The role of the ground plane in the lower frequency bands occurs regardless of the type of the antenna used, which is evident from the dipole-type vertically-polarized radiation pattern observed at low frequencies. The ground plane is also effective on the radiation in the higher bands being responsible for up to approximately 50% of the total radiation at 1800MHz.

Considering this fact, coupling element (CE) antennas were widely proposed mostly in the literature, to cover the cellular communication frequency bands in a mobile phone. Coupling element antennas are inherently non-resonant antennas, designed with the purpose of exciting the proper currents (chassis wavemodes) on the system ground plane [20-22]. In this antenna-scheme, the currents are induced on the PCB by capacitive excitation and the excitation is stronger close to the resonance frequencies of the PCB (which depends on its dimensions). For a 100mm ground plane length, the first chassis wavemode (longitudinal mode) occurs around 1.1GHz if a 10mm distance is set between the CE and this PCB. The feeding mechanism of the CE is similar to the one of a monopole, with no inductive contact to the PCB ground plane. In this way, the antenna-structure exhibits a low quality-factor and thus high bandwidth potential (BP) is obtained. Figure 13, which is taken from [14] explains the general behavior of a CE placed on a 100mm X 40mm ground plane without any ground clearance (CE placed directly on the ground plane). The major axis wavemodes

(first and second) are shown in the figure, occurring at 1.17GHz and 2.61GHz respectively. These wavemode resonances affect the input impedance of the antenna by slowing down the change of the impedance around these frequency points due to the low-Q property of the relatively wide ground plane, as presented in the smith chart. This effect can be best observed in the plotted quality factor, having some minima in these frequencies, corresponding to high bandwidth potentials. The antenna shall then be matched to the desired target frequency band using an appropriate matching network at the feed.

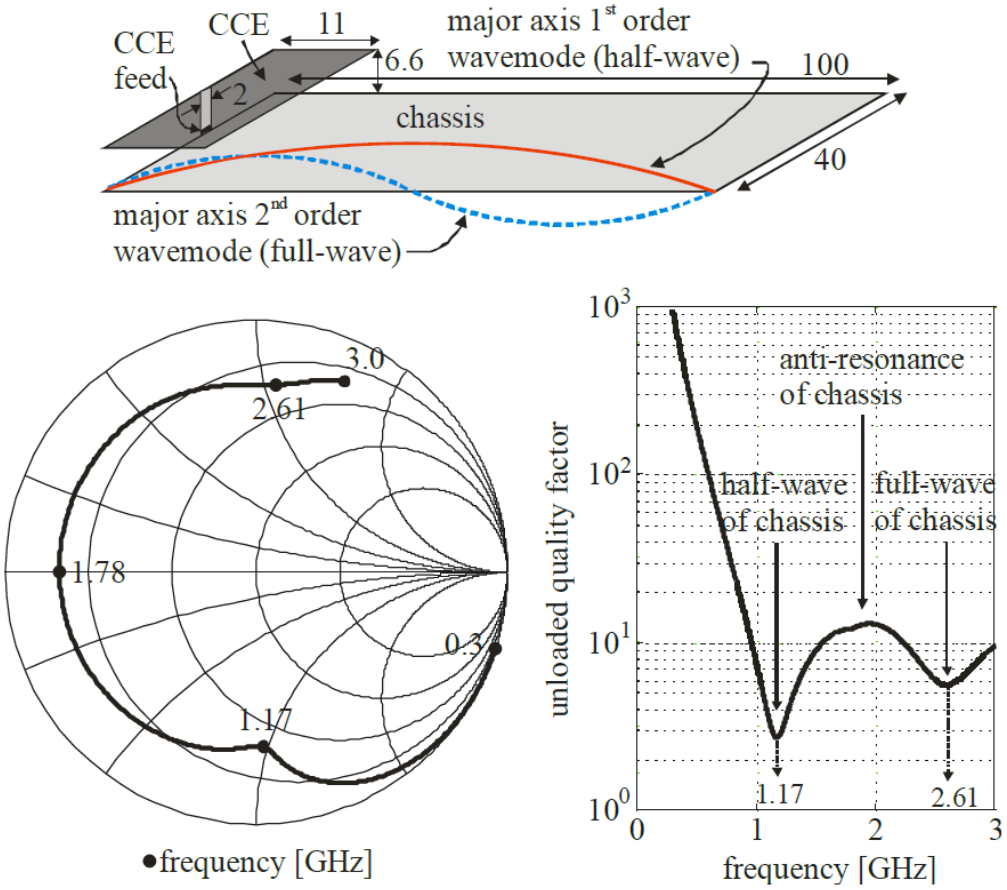

Figure 13 Summary of the Coupling Element Antenna Behavior

Despite the high obtainable bandwidth potential, the main drawback of this approach is the need for a tunable or a complex MN (complex in terms of design or large number of SMD components) if dual-band coverage is needed which increase the losses due to internal resistances of those SMD components. Another disadvantage is the necessity to keep the region between the CE and the ground plane clear from any metal components (ground clearance) that can distort the E-field distribution in this area and thus degrade the BP. Some CE designs targeting only the GSM/DCS/PCS/UMTS bands have been already presented in [23-24]. In [23], two CEs were placed on one of the short edges of the PCB, one responsible for the coverage of GSM frequency band (824-960MHz) and the other for DCS/PCS band (1.71-1.99GHz), with their associated MNs at each feed (Figure 14). To obtain a single feed topology in the final design, special attention was paid on the MNs, to get a high impedance behavior for the low-band MN at high-band frequency and vice versa. The two MN branches were then combined together. In [24], again a two CE configuration (called ground plane boosters) was proposed and this time, the two MN branches were connected together

after using notch-filters at each branch (Figure 15). In [25], two CEs which are separately fed have been used for dual-band operation for covering only GSM/DCS/PCS bands. A tunable MN topology for a CE has been proposed in [26] to cover DVB-H, GSM and UMTS frequency bands. In [27-28], two designs have been proposed to additionally cover the low LTE frequency band starting from 700MHz. Antenna proposed in [27] can cover low LTE and UMTS bands (700-960MHz and 1.7-2.2GHz) using a single CE. The matching network at the feed consists of a two-branched MN for dual-band operation, having 9 SMD components. In [28], the coverage band is increased as 700-960MHz and 1.7-2.7GHz, covering whole 4G communication band. The antenna is like a dual-feed structure, where the low-band (LB) feed uses the radiating element as a CE, whereas the high-band (HB) feed has an offset in the excitation region, using also the resonant properties of the radiating element (Figure 16). These two feeds are combined together to obtain a single feed, after introducing a two branch MN (of 8 lumped components) where each branch behaves as an open circuit to the other.

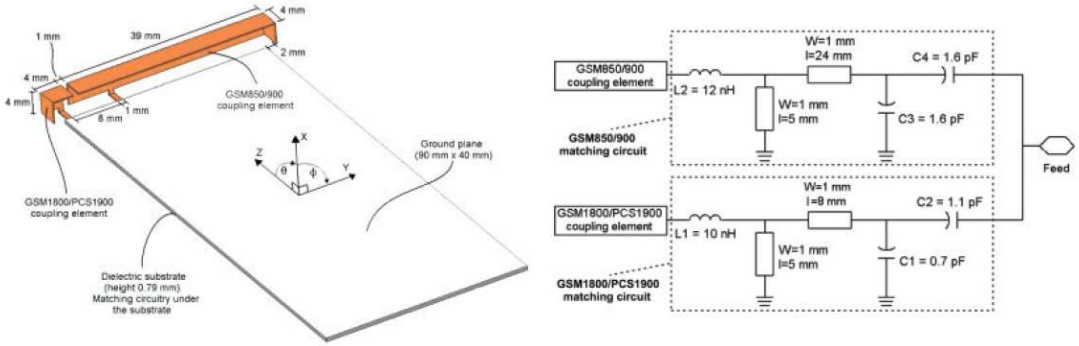

Figure 14 Quad-Band Coupling Element Antenna Structure in [23]

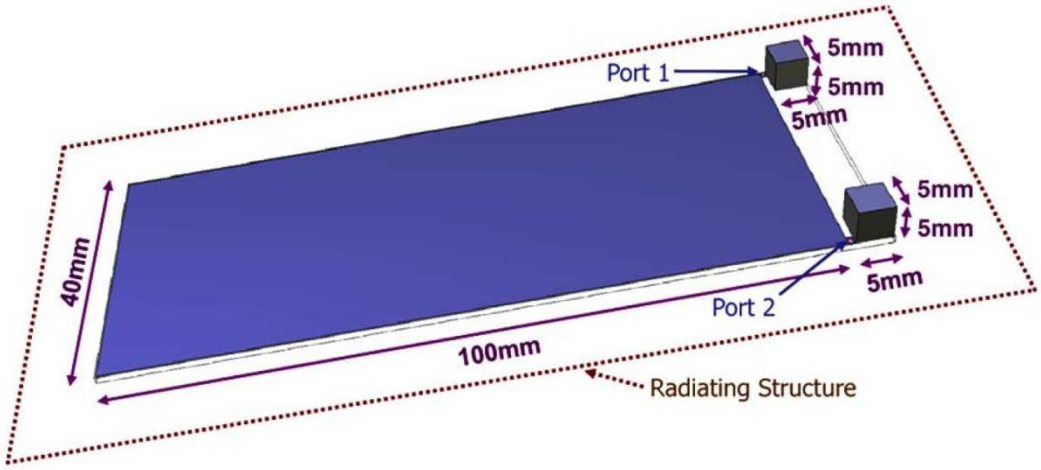

Figure 15 Ground Plane Booster Antenna in [24]

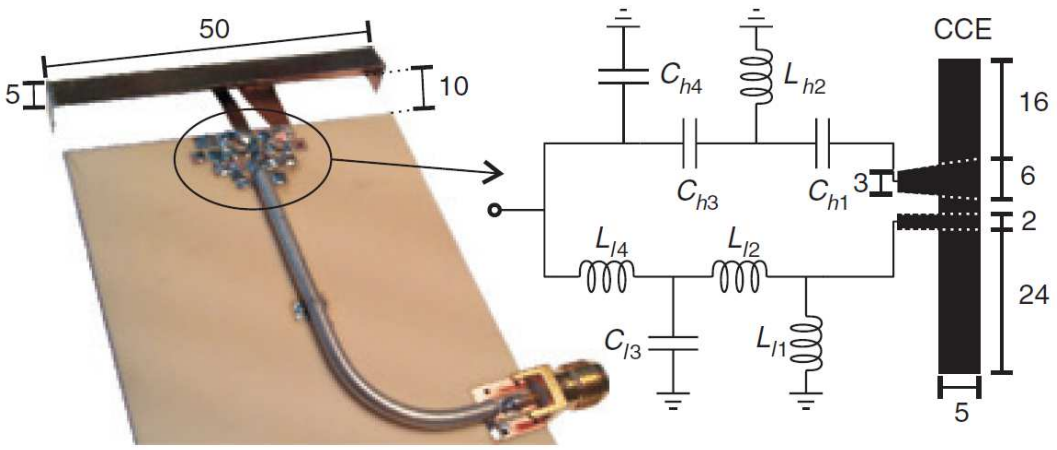

Figure 16 Multi-Band Mobile Terminal Antenna in [28]

7. ANTENNAS USING PARASITIC ELEMENTS FOR BANDWIDTH ENLARGEMENT

For operation in the main 4G frequency bands, wideband antenna behavior is needed covering 30% bandwidth in the low-band (700-960MHz) and 45% bandwidth in the high-band (1.7-2.7GHz). The coverage of the low-band (LB) is more challenging since the antenna is electrically small and thus the bandwidth potential is limited. For bandwidth enhancement, antennas using different kinds of parasitic elements have also been proposed in literature [29-38]. In these antennas, the main methodology is to capacitively excite a longer metal strip connected to the ground plane through a shorter driven strip. In [29-30], a monopole driven strip is used to excite a longer parasitic element connected to the ground plane on one edge. The LB coverage is mainly achieved by the capacitive excitation of the parasitic element and the HB is covered using the driven monopole and the higher order resonances of the parasitic strip. In [31-32], the parasitic element was connected to the ground plane on both edges forming a loop, again excited by a driven strip on the other side of the PCB (Figure 17). To increase the length of the loop parasitic, meandering was used making the design more complex and sensitive to manufacturing tolerances. In the antennas proposed in [33-36], casings for the PCB were also taken into consideration, whose loss tangent vary between 0.01-0.02 (Figure 18). In this way the advantage of dielectric loading was used to be able to achieve LB coverage more comfortably. Dielectric casings were also used in the antennas proposed in [37-38], with loss tangents between 0.02 and 0.06. Although they are called as PIFAs with coupled feeds, the main idea is the same as using a monopole like exciter (without ground connection), to excite capacitively a metal strip connected to ground in one end. The possible drawback of these antennas is the relatively complicated design and complicated antenna layout, which may be a problem when the manufacturing errors are concerned.

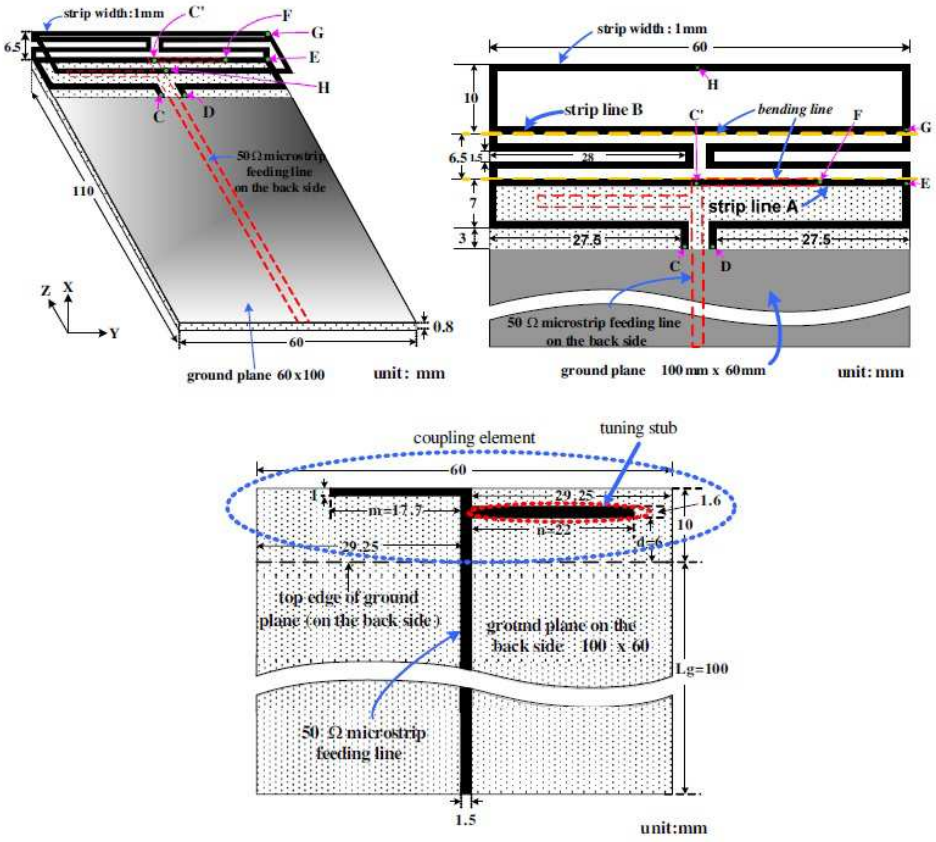

Figure 17 Meandered Loop Antenna in [32]

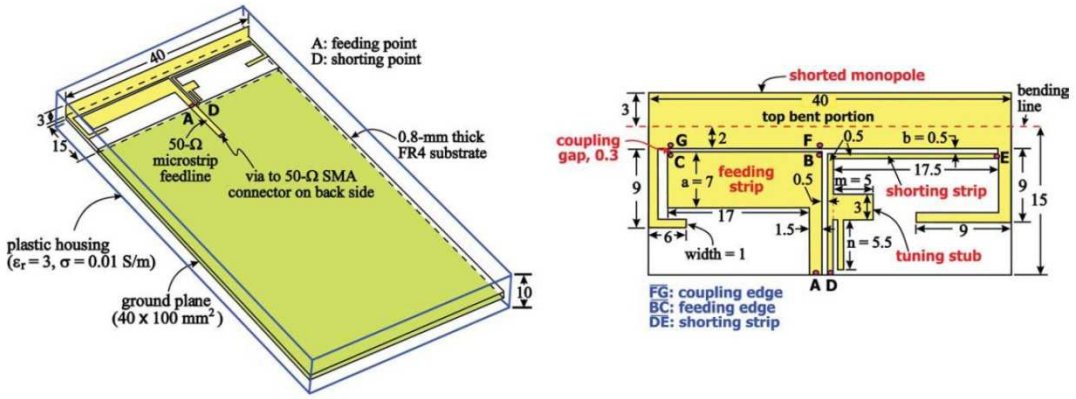

Figure 18 Small Size 11 Band Antenna in [34]

8. SINGLE-FEED AND MULTI-FEED ANTENNA STRUCTURES

The majority of the commercial mobile phones in the market use a single feed antenna design. A study about the advantages and disadvantages of using multi-feed antenna designs compared to single feed antennas was done in [39]. In the current single feed designs, an antenna which is able to cover the required standard frequency ranges (for example GSM850/900, DCS/PCS) is connected to a "Single Pole Multi Throw" antenna switch in the RF front end. According to the communication standard used at the instant, the output of the switch (considering the receive scenario) is changed to connect the signal from the antenna to the appropriate duplexer.

With the introduction of LTE-A, it is possible to receive cellular communication data over two different frequency bands (carrier aggregation), meaning there can be more than one receive chain in the front-end simultaneously. For the inter-band carrier aggregation, the signals picked up by a single feed antenna (for example one at 940MHz and one at 2150MHz) should be transmitted to the front end at the same time, which is not possible with a "Single Throw" switch. The switch should have a logic to have two active throws at the same time, which may results in worse linearity performance and higher insertion loss. In addition to these, special care should be given to prevent the two different front-ends (duplexers) from loading each other since they will be connected together at the switch.

Another solution different from having more than one active throws at the antenna switch, is to add a diplexer just after the antenna in the receive path, that will direct the different frequency signals to the appropriate duplexers, for inter-band carrier aggregation. However this will also result in increased insertion loss in the front-end.

Al alternative solution to overcome these complexities using single-feed antennas for inter-band carrier aggregation is to use multi-feed antennas, for example one covering the lower frequency band (700-960MHz) and other for higher frequency band (1.7-2.7GHz). In this way, the necessity of using a complex antenna switch or a diplexer is overcome for inter-band carrier aggregation. The drawback of this approach is the isolation between the antenna feeds. Isolation should be as high as possible (targeted better than 10dB as a rule of thumb), since it can otherwise cause efficiency losses due to unwanted coupling from one antenna to the other. Obtaining good isolation is also challenging, since the space reserved for the antenna is small in terms of wavelength (especially in lower frequencies) and the separate antennas have to be placed physically close to each other.

9. MOTIVATION OF THE THESIS

This study was done within the scope of the ARTEMOS project, a European Union project with a duration of 36 months. The main aim of the project is to obtain frequency agile, multimode, multi standard RF architectures for mobile communication devices, to decrease the bill of materials and cost of the systems. This target is represented in Figure 19, where the number of RF front-ends for several different communication standards in a typical system nowadays is reduced by proposing tunable front-end modules. Another aim of the project is to design and manufacture tunable components, which are BST capacitors, MEMS switches and MEMS varactors, to be delivered to the partners working on the RF front end and the antenna element.

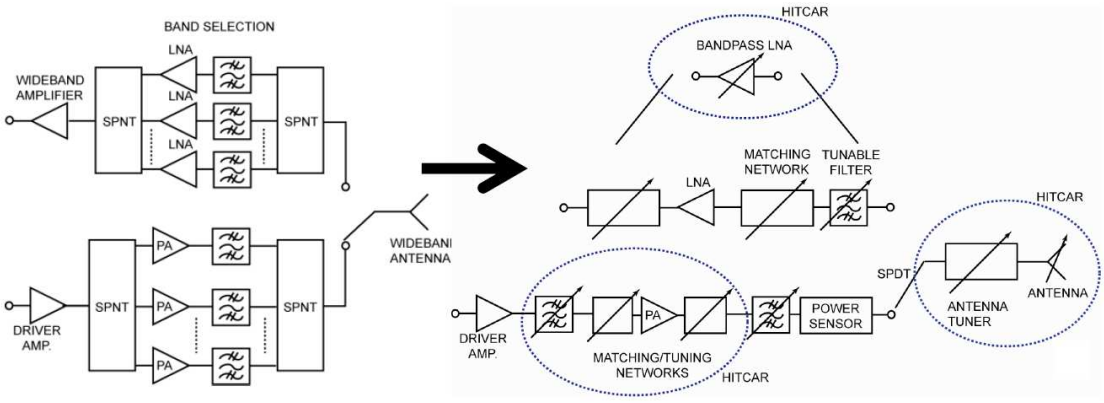

Figure 19 Tunable RF Front End Targeted in ARTEMOS Project

Keeping this in mind, the aim of this study is to design, manufacture and test some novel antenna topologies for handheld mobile terminals. Particular effort is to be focused on either covering the target bands with very simple antenna layouts or achieving lower reflection coefficient in the target band compared to the antennas in the literature mentioned before. Another aim is to investigate the effect of the user (hand and head) on the antenna performances and propose a novel antenna topology which minimizes these effects. Both passive and active antenna topologies are to be evaluated for the coverage of 4G frequency bands, decided as:

-Low-Band (LB): 700-960MHz
-High-Band (HB):1700-2700MHz.

With this target, the frequency bands of the communication standards low-LTE, GSM850/900, DCS/PCS, WLAN2400 and high-LTE will be covered. As a rule of thumb, -6dB in free space is accepted as the target reflection coefficient for the antennas. For the maximum limit of the antenna height, 5mm is taken, to be in compliance with the trends of current smart phone designs. For the same reason, maximum dimensions around 120mm X 60mm (for length and width respectively) was accepted for the PCB that will support the antenna. For the feeding scheme, both single-feed and multi-feed antennas were evaluated.

REFERENCES OF THIS CHAPTER

[1] CK Toh, "4G LTE Technologies: System Concepts," Technology White Paper, Available: http://www.alicosystems.com/4G%20LTE%20Technologies%20System%20Concepts.pdf.

[2] T.S. Rappaport, S. Sun, R. Mayzus, H. Zhao, Y. Azar, K. Wang, G.N. Wong, J.K. Schulz, M. Samimi, F. Gutierrez, "Millimeter Wave Mobile Communications for 5G Cellular: It Will Work!," Access, IEEE , vol. 1, pp.335-349, 2013

[3] C. Rowell, E.Y. Lam, "Mobile-Phone Antenna Design," IEEE Antennas and Propagation Magazine, Vol. 54, No. 4, August 2012, pp 14-34.

[4] M. Secmen, "Multiband and Wideband Antennas for Mobile Communication Systems, Recent Developments in Mobile Communications - A Multidisciplinary Approach," Dr Juan P. Maícas (Ed.), ISBN: 978-953-307-910-3, InTech, DOI: 10.5772/25921.

[5] P. Ciais, C. Luxey, A. Diallo, R. Staraj, G. Kossiavas, "Pentaband internal antenna for handset communication devices," Microw. Opt. Technol. Lett., vol. 48, pp. 1509–1512.

[6] P. Ciais, R. Staraj, G. Kossiavas, C. Luxey, "Design of an internal quad-band antenna for mobile phones," Microwave and Wireless Components Letters, IEEE , vol.14, no.4, pp.148,150, April 2004

[7] M. Pascolini et al., "Bezel Gap Antennas," U.S. Patent 8 270 914, September 18, 2012.

[8] L.J. Chu, "Physical Limitations of Omnidirectional Antennas," Journal of Applied Physics, 1948, pp. 1163–1175

[9] Wheeler, H.A., "Fundamental Limitations of Small Antennas," Proceedings of the IRE , vol.35, no.12, pp.1479,1484, Dec. 1947

[10] Collin, R.E.; Rothschild, S., "Evaluation of antenna Q, " Antennas and Propagation, IEEE Transactions on , vol.12, no.1, pp.23,27, Jan 1964

[11] Hansen, R.C., "Fundamental limitations in antennas, " Proceedings of the IEEE , vol.69, no.2, pp.170,182, Feb. 1981

[12] McLean, J.S., "A re-examination of the fundamental limits on the radiation Q of electrically small antennas," Antennas and Propagation, IEEE Transactions on , vol.44, no.5, pp.672, May 1996

[13] Yaghjian, A.D.; Best, S.R., "Impedance, bandwidth, and Q of antennas", Antennas and Propagation, IEEE Transactions on , vol.53, no.4, pp.1298,1324, April 2005

[14] J. Holopainen, "Compact UHF-band antennas for mobile terminals:focus on modelling, implementation, and user interaction," Ph.D. dissertation, Department of Radio Science and Engineering, AALTO University, Helsinki, 2011.

[15] H.F. Pues, A.R. van de Capelle, "An impedance-matching technique for increasing the bandwidth of microstrip antennas," IEEE Transactions on Antennas and Propagation, Vol. 37, No. 11, November 1989, pp 1345-1354.

[16] Antoniades, M.A.; Eleftheriades, G.V., "A multiband monopole antenna using a double-tuned wheeler matching network," Antennas and Propagation (EuCAP), 2010 Proceedings of the Fourth European Conference on , vol., no., pp.1,4, 12-16 April 2010

[17] Selvanayagam, M.; Eleftheriades, G.V., "A Compact Printed Antenna With an Embedded Double-Tuned Metamaterial Matching Network," Antennas and Propagation, IEEE Transactions on , vol.58, no.7, pp.2354,2361, July 2010

[18] P. Vainikainen, J. Ollikainen, O. Kivekäs, and I. Kelander, Patent FI114260, Modular coupling structure for a radio device and a portable radio device, Finland, Appl. 20002529, 17.11.2000, (15.09.2004), 22 p.

[19]P. Vainikainen, J. Ollikainen, O. Kivekas, I. Kelander, "Performance Analysis of Small Antennas Mounted on Mobile Handsets," Proceedings of the COST 259 Final Workshop-Mobile and Human Body Interaction, 2000, p. 8.

[20]P. Vainikainen, J. Ollikainen, O. Kivekas, I. Kelander, "Resonator-based analysis of the combination of mobile handset antenna and chassis," IEEE Transactions on Antennas and Propagation, vol.50, no. 10, pp.1433-1444, October 2002.

[21]J. Villanen, J. Ollikainen, O. Kivekas, P. Vainikainen, "Coupling element based mobile terminal antenna structures," IEEE Transactions on Antennas and Propagation, vol.54, no.7, pp. 2142,2153, July 2006.

[22]J. Holopainen, R. Valkonen, O. Kivekas, J. Ilvonen, P. Vainikainen, "Broadband Equivalent Circuit Model for Capacitive Coupling Element–Based Mobile Terminal Antenna," IEEE Antennas and Wireless Propagation Letters, vol. 9, pp. 716-719, 2010.

[23]J. Villanen, C. Icheln, P. Vainikainen, "A coupling element-based quad-band antenna structure for mobile terminals," Microwave and Optical Technology Letters, vol. 49, no. 6, June 2007, pp. 1277–1282.

[24]A. Andujar, J. Anguera, C. Puente, "Ground Plane Boosters as a Compact Antenna Technology for Wireless Handheld Devices," IEEE Transactions on Antennas and Propagation, vol. 59, no. 5, pp. 1668-1677, May 2011.

[25]W.L. Schroeder, P. Schmitz, C. Thome, "Miniaturization of mobile phone antennas by utilization of chassis mode resonances", German Microwave Conference, 2006.

[26]D. Manteuffel, M. Arnold, "Considerations on configurable multi-standard antennas for mobile terminals realized in LTCC technology," 3rd European Conference on Antennas and Propagation 2009 (EuCAP 2009), pp. 2541-2545, 23-27th March 2009.

[27]R. Valkonen, J. Ilvonen, P. Vainikainen, "Naturally non-selective handset antennas with good robustness against impedance mistuning," 6th European Conference on Antennas and Propagation 2012 (EUCAP 2012), pp.796-800, 26-30th March 2012.

[28]R. Valkonen, J. Ilvonen, C. Icheln, P. Vainikainen, "Inherently non-resonant multi-band mobile terminal antenna," IET Electronics Letters, vol. 49, no. 1, pp. 11-13, 3rd January 2013.

[29]F.-H. Chu, K.-L. Wong, "Internal coupled-fed loop antenna integrated with notched ground plane for wireless wide area network operation in the mobile handset," Microwave and Optical Technology Letters, vol. 54, no. 3, pp. 599–605, March 2012.

[30]C.-W. Yang, Y.-B. Jung, C.-W. Jung, "Octaband Internal Antenna for 4G Mobile Handset," IEEE Antennas and Wireless Propagation Letters, vol.10, pp.817-819, 2011.

[31]W-S. Chen, B-Y. Lee, Y-T. Liu, "A printed coupled-fed loop antenna with two chip inductors for the 4G mobile applications," Microwave and Optical Technology Letters, vol. 54, no. 9, pp. 2157–2163, September 2012.

[32]C.-W. Chiu, C.-H. Chang, Y.-J. Chi, "A meandered loop antenna for LTE/WWAN operations in a smart phone," Progress In Electromagnetics Research C, vol. 16, pp. 147-160, 2010.

[33]S-C. Chen, K-L. Wong, "Wideband monopole antenna coupled with a chip-inductor-loaded shorted strip for LTE/WWAN mobile handset," Microwave and Optical Technology Letters, vol. 53, no. 6, pp. 1293–1298, June 2011.

[34]S-C. Chen, K-L. Wong, "Small-size 11-band LTE/WWAN/WLAN internal mobile phone antenna," Microwave and Optical Technology Letters, vol. 52, no. 11, pp. 2603–2608, November 2010.

[35]F-H. Chu, K-L. Wong, “On-board small-size printed LTE/WWAN mobile handset antenna closely integrated with system ground plane,” Microwave and Optical Technology Letters, vol. 53, no. 6, pp. 1336–1343, June 2011.

[36]C-T. Lee, K-L. Wong, “Planar Monopole With a Coupling Feed and an Inductive Shorting Strip for LTE/GSM/UMTS Operation in the Mobile Phone,” IEEE Transactions on Antennas and Propagation, vol. 58, no. 7, pp. 2479-2483, July 2010.

[37]K-L. Wong, M-F. Tu, T-Y. Wu, W-Y. Li, “Small-size coupled-fed printed PIFA for internal eight-band LTE/GSM/UMTS mobile phone antenna,” Microwave and Optical Technology Letters, vol. 52, no. 9, pp. 2123–2128, September 2010.

[38]K-L. Wong, W-Y. Chen, C-Y. Wu, W-Y. Li, “Small-size internal eight-band LTE/WWAN mobile phone antenna with internal distributed LC matching circuit,” Microwave and Optical Technology Letters, vol. 52, no. 10, pp. 2244–2250, October 2010.

[39]P. Ikonen, J. Ella, E. Schmidhammer, P. Tikka, P. Ramachadran, P. Annamaa, “Multi-feed RF front-ends and cellular antennas for next generation smartphones,” Available at: http://www.epcos.com/blob/531106/download/2/pdf-techarticle.pdf

CHAPTER II
TUNABLE ANTENNAS

This section presents several tunable antenna topologies, designed for operation in the 4G-LTE frequency bands (i.e 700-960MHz, 1.7-2.7GHz). The antennas are designed and manufactured using tunable components provided by the ARTEMOS partners. To obtain tunability in the matching response, MEMS switches and BST capacitors have been considered.

1. ANTENNA DESIGNS USING MEMS SWITCHES

The utilization of MEMS switches in reconfigurable antenna design has been a popular topic in recent years, especially due to their low loss in the microwave frequency bands. The reconfigured antenna properties of the these antennas have a diversity, like pattern reconfiguration (both in single and array antennas), switching between two operating frequency bands, tuning the matching level by MEMS capacitors (varactors) and changing the properties of antenna feeding networks [1]. For example in [2], MEMS switches were used to change the ground connection point of a PIFA to achieve polarization reconfigurability. In [3-4], the switches were used to obtain reconfigurability in the operating band. Figure 20 shows the proposed reconfigurable MN topology in [3], together with the manufactured prototype in the same study.

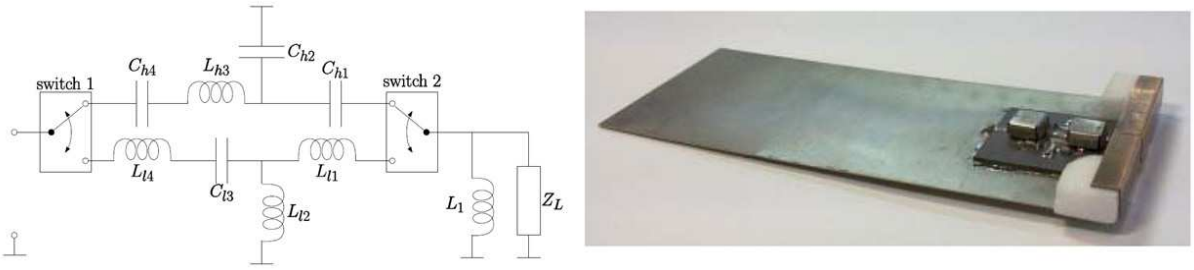

Figure 20 MN Topology and Manufactured Prototype in [3]

There are a number of COTS products available on the market, some of which are given in [5-6] and whose RF performance specifications are mentioned in Table 3.

Table 3 Specifications of Some Available MEMS Products

	MEMS-1	MEMS-2
Frequency Bandwidth	DC-40GHz	DC-10GHz
Insertion Loss at 2GHz	-0.29dB	-0.25dB
Isolation at 2GHz	-34dB	-45dB
Maximum RF Input Power	40dBm (cold sw.)	36dBm
Input IP3	>65dBm	
Switching ON Time	<10 µs	<100 µs
Control Voltage	90V	35V

In this study, the MEMS switches have been evaluated to achieve band-switching between the Low-Band (700-960MHz) and High-Band (1.7-2.7GHz) of 4G communication standards. Two antenna topologies are proposed, each using a parasitic strip connected to ground for the enlargement of matching bandwidth. The two topologies are different in the way the MEMS switches are exploited. In the first design, two MEMS switches are used to select between one of the two matching network

(MN) branches, like in [3] and [4]. The second design uses only one MEMS switch, to select between one of the driven strips.

The MEMS switches used in this study are designed and manufactured by DELFMEMS [7], who is also a partner in the Artemos project. DelfMEMS technology is different from the other RF MEMS switches on the market, i.e. classical cantilevers (clamped-free membrane) or bridges (clamped-clamped membrane). Indeed, based on a state-of-the-art IP, DelfMEMS switches enable high performances with their specific mechanical structures featuring two main innovations: a movable membrane without anchors in the substrate and two forced on/off states to obtain a push-pull behavior. The membrane used for the electromechanical function is simply supported by two pillars, and two sets of electrodes placed either side of the pillars allow the actuation of the device. As illustrated in Figure 21(on left), the two forced states are obtained when the electrostatic forces are generated with the different electrodes, respectively internal/external electrodes for a ON/OFF state. Such operation ensures good contact forces in the ON state thus reducing the contact resistance, and provides high restoring forces for the OFF state to counter potential stiction or self actuation phenomena while ensuring important isolation.

In addition to good RF characteristics, this new mechanical structure demonstrates high reliability performances mainly because of its anti-stiction capabilities and the limitation of bounces thanks to a smart use of the different internal/external electrodes.

The insertion loss of the devices is measured to be between -0.2 and -0.25dB at 2GHz (Figure 21, on right). A high level of isolation is observed in OFF state, better than 45dB below 3GHz thanks to isolated RF and DC paths and because a gap larger than the thickness of the sacrificial layer is obtained between the contacts placed on the membrane and those on the transmission line

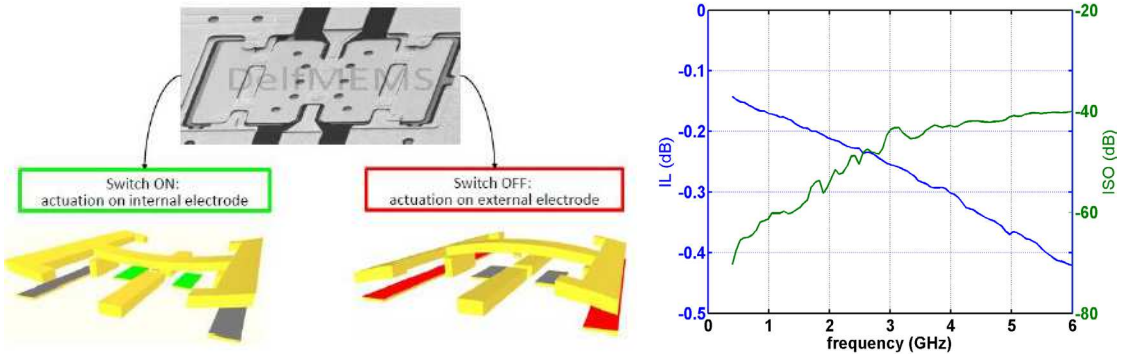

Figure 21 ON/OFF Switching Topology and Performance of MEMS

Table 4 Performance Summary of MEMS switches from DELFMEMS

Parameters	Value
Frequency bandwidth	0.3-5 GHz
Insertion loss	0.2-0.25 dB @2GHz
Reflection coeff.	< -15 dB @2GHz
Isolation	> 50 dB @2GHz
RF power	+33 dBm for cold switching +20 dBm for hot switching
Input IP3	> 70 dBm
Switching time	<10 µs for actuation voltage greater than 50V
Control signal level	50-70 V
Switching frequency	up to 10 kHz
Electrostatic self-actuation (OFF state)	< 50 V peak peak
Size	3,6 mm²
Packaging type	silicon cap

1.1. ANTENNA DESIGN-I

The proposed antenna layout can be observed in Figure 22. The antenna is directly printed on FR4 substrate, with the PCB dimensions of 120mm X 60mm X 0.8mm. There is a ground plane of length 107mm under the substrate on one side of the PCB, leaving a ground clearance of 13mm for the antenna. The antenna is basically composed of a driven strip, which capacitively excites a parasitic strip connected to the ground plane. The parasitic strip is connected to the ground plane over an inductor (12nH), which increases the electrical length of the parasitic strip. A MN, consisting of two branches is introduced at the antenna feed (Figure 23), to tune the antenna either in the LB or in the HB. According to the states of the two SPDT (Single Pole Double Throw) switches, one of the branches is connected to the antenna feed, which matches the impedance in different frequency bands. The LB MN branch consists of two inductors, whereas the HB MN is a single capacitor.

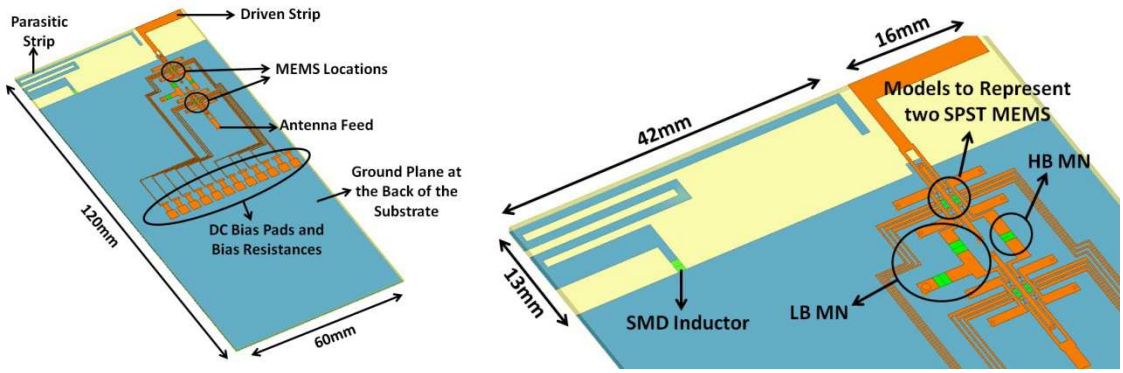

Figure 22 Layout for Antenna Design-I Using MEMS

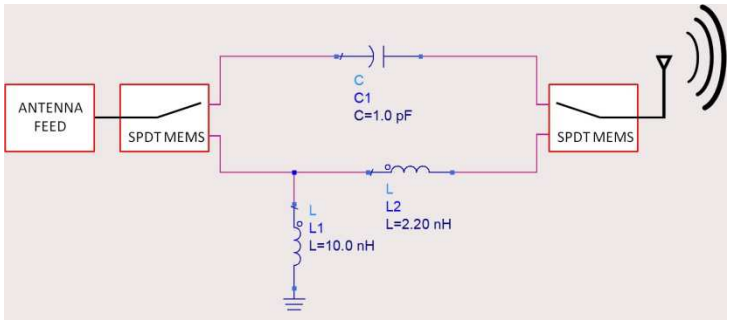

Figure 23 Switchable Matching Network Topology

1.1.1. Effect of the Parasitic Strip over the Bandwidth Potential

The effect of the parasitic strip has been studied in the absence of any matching network at the antenna feed. The simulated antenna input impedance with and without the parasitic strip can be observed in Figure 24, plotted between 700-960MHz. A significant increase can be noticed in the real part of the impedance, with the resonance appearing around 730MHz. Here, the term "resonance" is used to indicate a significant increase in the real part of the antenna (the loop forming in the smith chart), since under normal conditions the real part of the impedance of an electrically small antenna is low. The increase in the real part of the input impedance can be seen in Figure 25, for "with Parasitic" case.

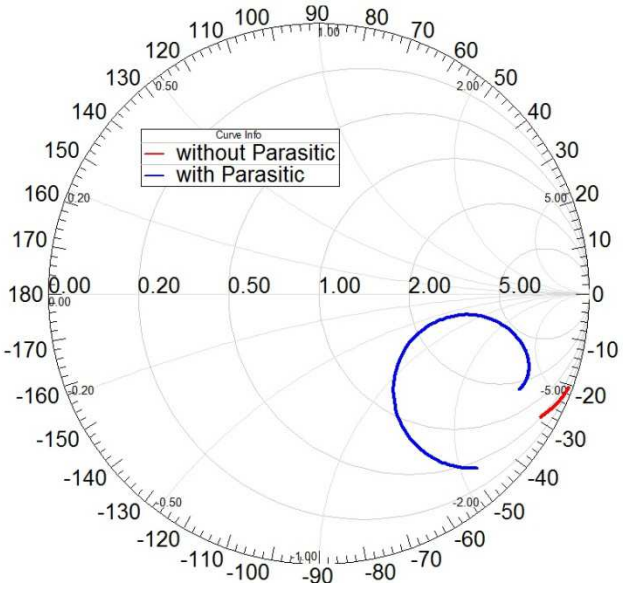

Figure 24 Input Impedance of the Antenna With/Without Parasitic Strip from 700 960 MHz

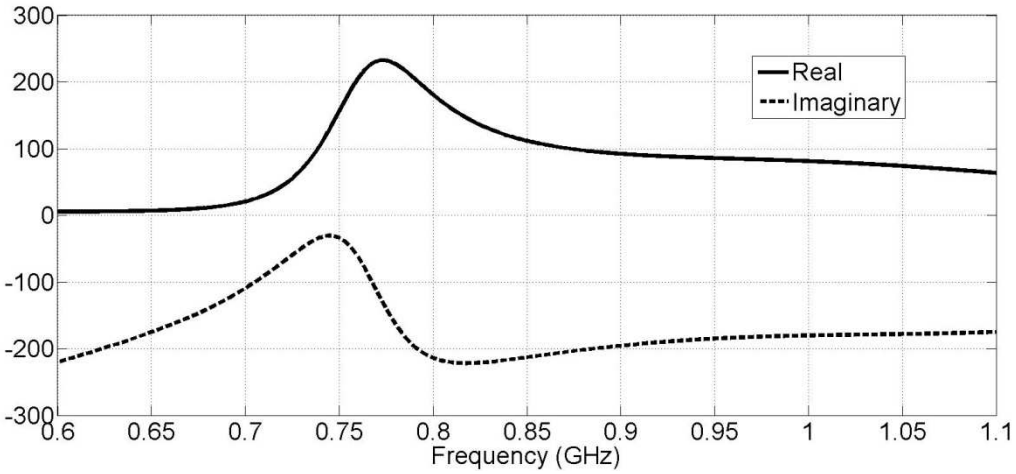

Figure 25 Input Impedance (Real/Imaginary) of the Antenna With Parasitic Strip

The surface current density of the antenna presented in Figure 26 also verifies this statement. At 700MHz, the currents induced on the parasitic strip are strong, creating a current path from the driven strip to the parasitic strip and returning to the feed through ground connection. At 950MHz, the currents are significantly weaker on the parasitic element. As previously discussed, the excitation of the ground plane plays a major role in the whole radiation mechanism of the structure and therefore the radiation efficiency and also the matching coverage of the LB. When the current distribution on the ground plane is investigated, it may be concluded that the first chassis wavemode of the ground plane is excited uniformly at 950MHz.

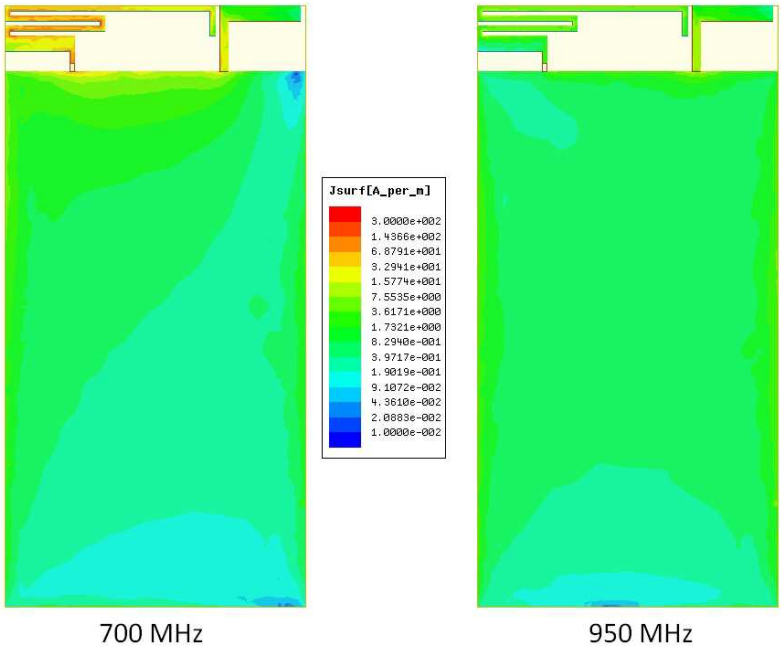

Figure 26 Surface Currents of the Antenna and The Chassis in LB

The bandwidth potential of the two cases (with/without parasitic element) has been investigated using the software Optenni Lab [8]. For this computation, the software optimizes a matching network (composed of two elements) for each frequency point and determines the frequency interval that rests under a pre-defined reflection coefficient value (-6dB chosen here). In this way, a realistic

bandwidth potential value is given instead of well-known, too optimistic theoretical maximum value. It can be seen in Figure 27 that introducing the parasitic strip increases the bandwidth potential considerably in the LB. The computed bandwidth potential gets closer to the target curve (in red), which states the bandwidth potential needed at each frequency point to cover 700-960MHz.The parasitic strip enables a bandwidth potential of approximately 250MHz at the center frequency (830MHz), with a two element MN.

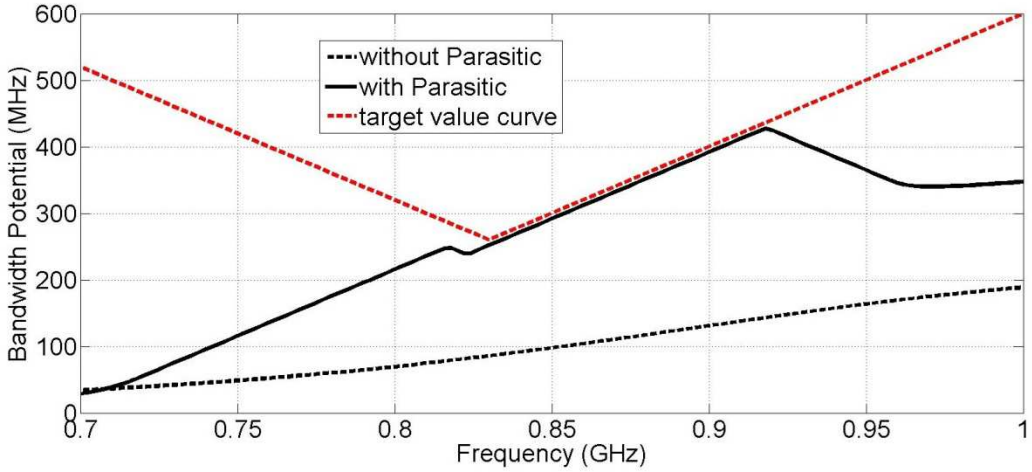

Figure 27 Comparison of BW Potential of the antenna With/Without Parasitic Element

The effect of the parasitic strip for creating an additional resonance in the LB was also investigated through circuit models. Circuit models were proposed for the driven strip in the absence of parasitic strip (Figure 28 on left) and for the parasitic strip alone when it is directly fed (Figure 28 on right). The circuit models for these two configurations are modeled as a series RLC circuit with a shunt capacitor in front which represents the capacitive coupling to the ground plane. A good correspondence between the simulated EM model and the circuit models can be observed (all smith chart curves are plotted between 700-960MHz).

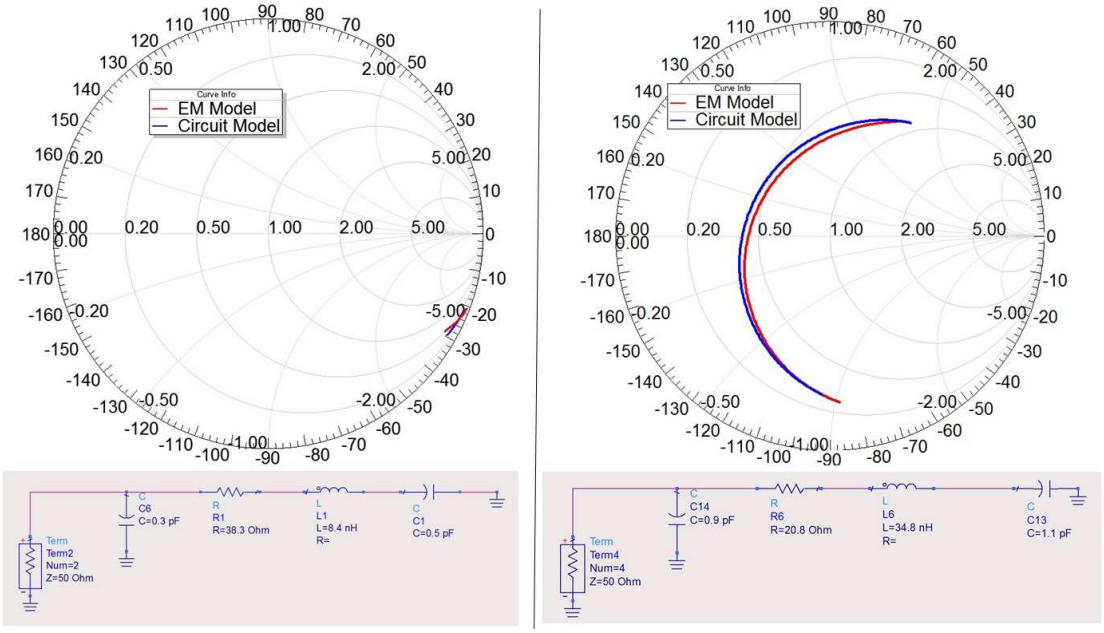

Figure 28 Circuit Model of the Driven (on left) and Parasitic Strips (on right)

Using these two circuit models as building blocks, the circuit model in Figure 29 is obtained. The circuits for the driven strip and parasitic strip are marked with the black and red circles respectively. A transformer model is used to stand for the capacitive coupling between the strips. The creation of the resonance in the LB can be observed for the circuit model, making a good compliance with the EM simulations.

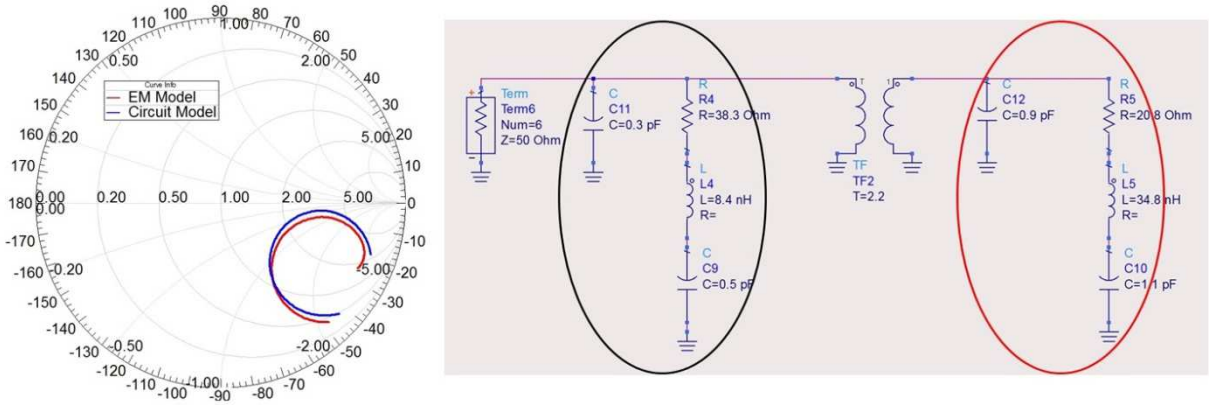

Figure 29 Circuit Model of the Combination of Driven and Parasitic Strips

The effect of the parasitic element in the HB (1.7-2.7GHz) can be observed in Figure 30. With the introduction of the parasitic element into the "driven strip only" case (red curve) two additional resonances are created around 1.85GHz and 2.4GHz. If the current distributions are observed at these two frequencies, it can be seen that the parasitic element is excited strongly in two different operating modes. Considering this fact, it can be concluded that the role of the parasitic strip is not only in the LB. It also contributes to the current distribution in the HB frequencies.

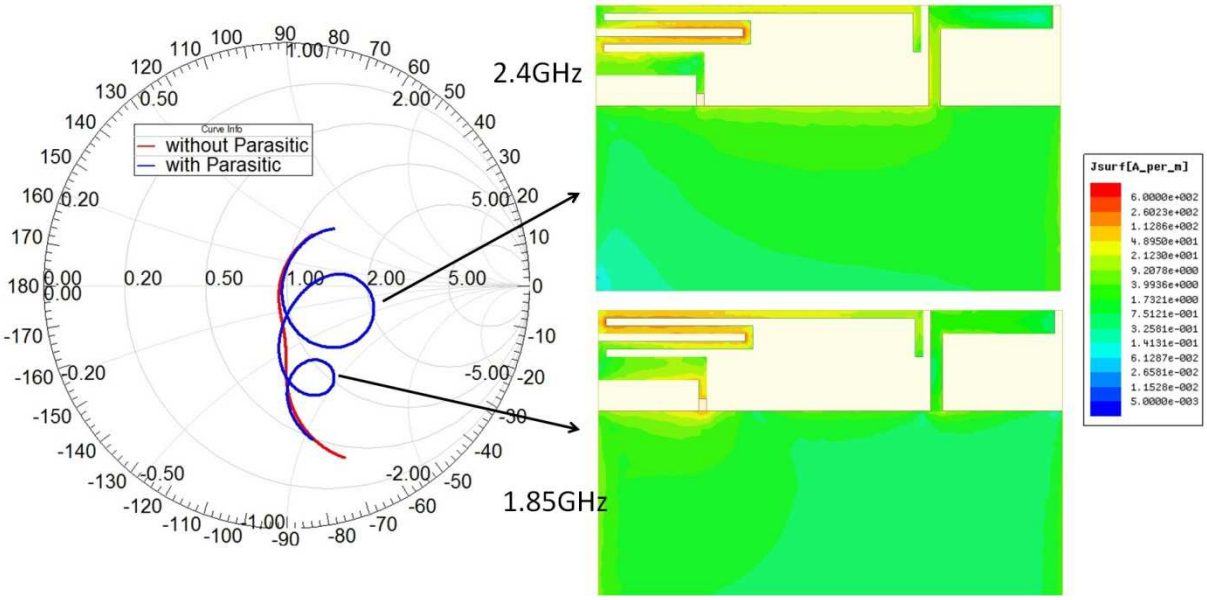

Figure 30 The Effect of the Parasitic Strip in the HB

1.1.2. Antenna Simulations With MEMS Switches and Matching Network

The antenna whose layout has been given in Figure 22 was simulated using Ansoft HFSS [9]. In the full EM simulations, the MEMS switches and SMD components were replaced by simulation ports and measured S-parameters from the manufacturers were used at those ports with a circuit post-processing simulation done in Agilent ADS [10], to obtain more realistic results. The DC bias pads for the MEMS switches and the wirebondings (to connect the MEMS die to the traces on the PCB) were also taken into account in the full EM simulation(Figure 31).

The main criteria when optimizing the antenna was to first obtain enough bandwidth potential for the LB coverage. The main antenna parameters that were tuned for this, were the coupling gap between the driven strip and the parasitic strip, the length of the parasitic strip (that changes the frequency of the resonance) and the inductance value on the ground connection of the parasitic strip (tuning the electrical length and thus resonance frequency). Since the antenna is longer in terms of wavelength, the coverage is simpler for the HB.

The simulated input impedances of the final optimized layout, with and without MN can be seen in Figure 32, plotted for LB (700-960MHz) on left and plotted for HB (1.7-2.7GHz) on right. It is worthwhile to note that the SMD component values in the MN were tuned taking into account also the transmission lines between SMDs and also the wirebondings. To show the effect of the transmission lines between MN elements, simulation were also done by connecting the lumped elements directly in the circuit simulator (dashed curves in Figure 31) and neglecting the wirebondings. It is seen that the transmission lines might have a strong effect depending on the input impedance of the antenna before the MN.

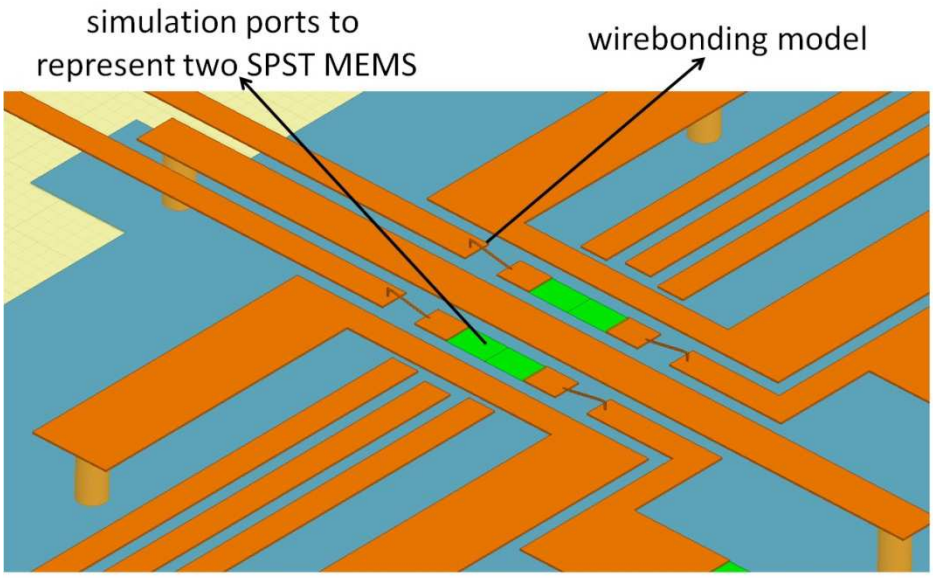

Figure 31 Simulation Model Showing Wirebondings and MEMS Modelling

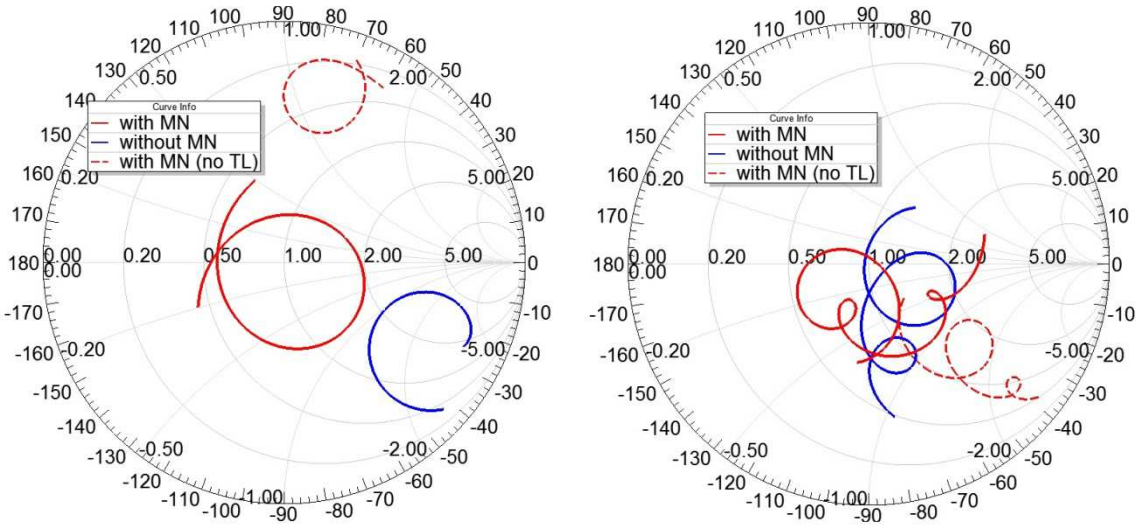

Figure 32 Simulated Antenna Impedance With/Without MN (LB on left, HB on right)

The simulated reflection coefficient of the antenna can be seen in Figure 33. Without any MN, the antenna is far from being matched in the LB (red dotted curve). With proper switching of the MEMS switches to select the LB MN (black curve), the antenna can be matched in the LB with a reflection coefficient below -6dB . Likewise, by choosing the HB MN branch, the antenna has a reflection coefficient below -6dB in the HB.

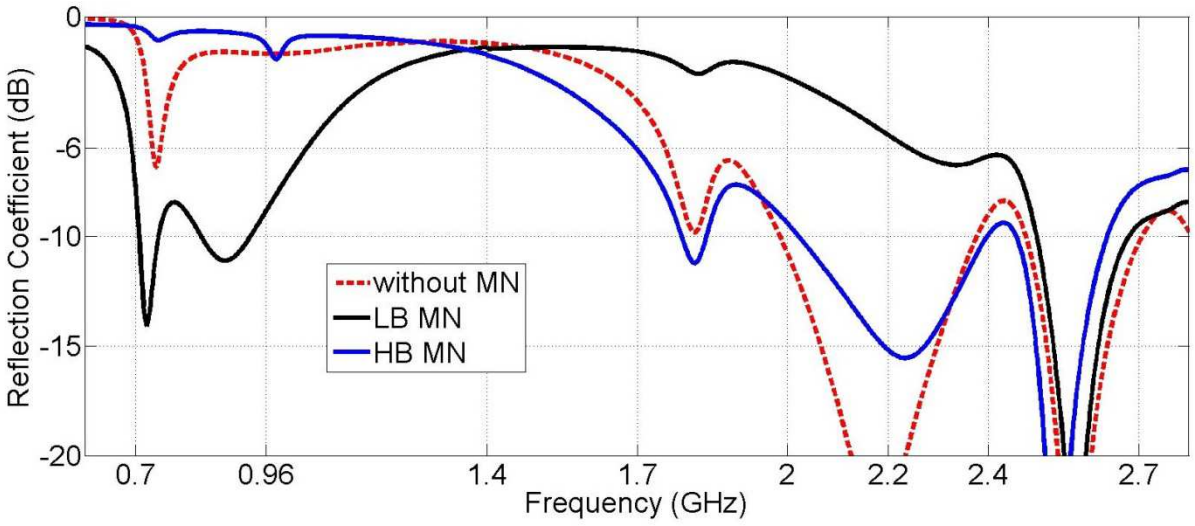

Figure 33 Simulated Reflection Coefficient of the Antenna With/Without MN

1.1.3. Measurement Results for Antenna Design I

The proposed antenna has been manufactured on FR4 substrate and the integration of the MEMS switches to the PCB was done using wirebonding (Figure 34).

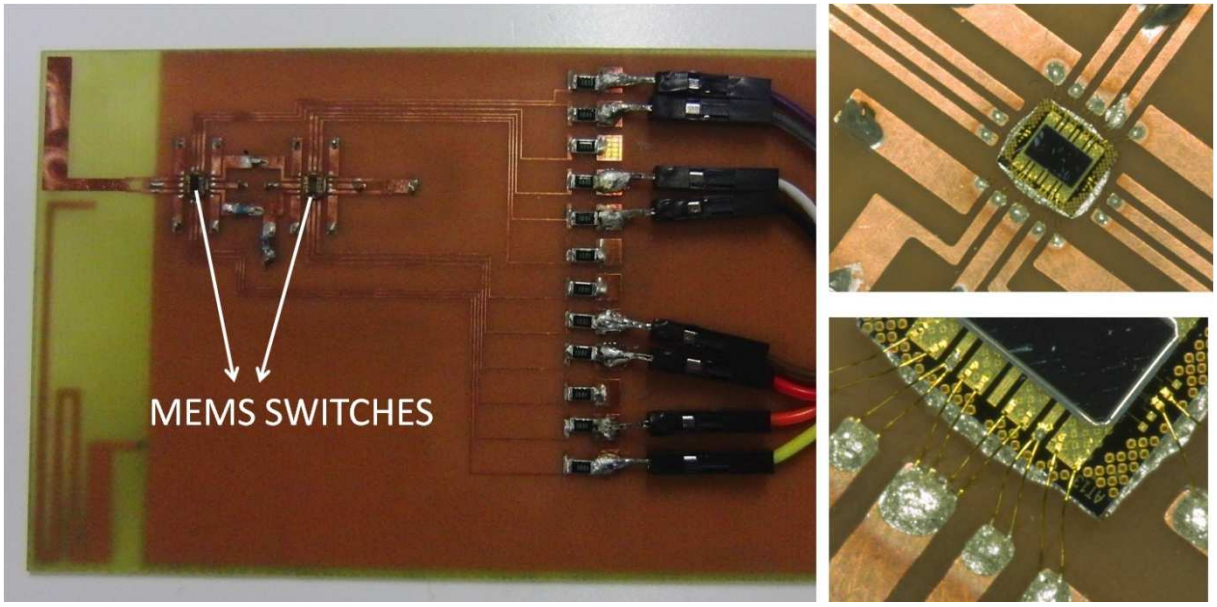

Figure 34 Pictures of the Manufactured Prototype for Antenna Design I

Due to the lack of encapsulation of the MEMS dies, problems were faced during the measurements mainly about the MEMS reliability and repeatability of the measurements. For this reason, as a backup solution, passive prototypes were manufactured where the MEMS switches are by-passed using soldered wires for ON state and left open for OFF state. The comparison of the measured reflection coefficient (for passive prototypes) and the simulation results can be seen in Figure 35 and Figure 36. A good correspondence is observed between simulations and measurements in terms of matching and input impedance behavior through both LB and HB.

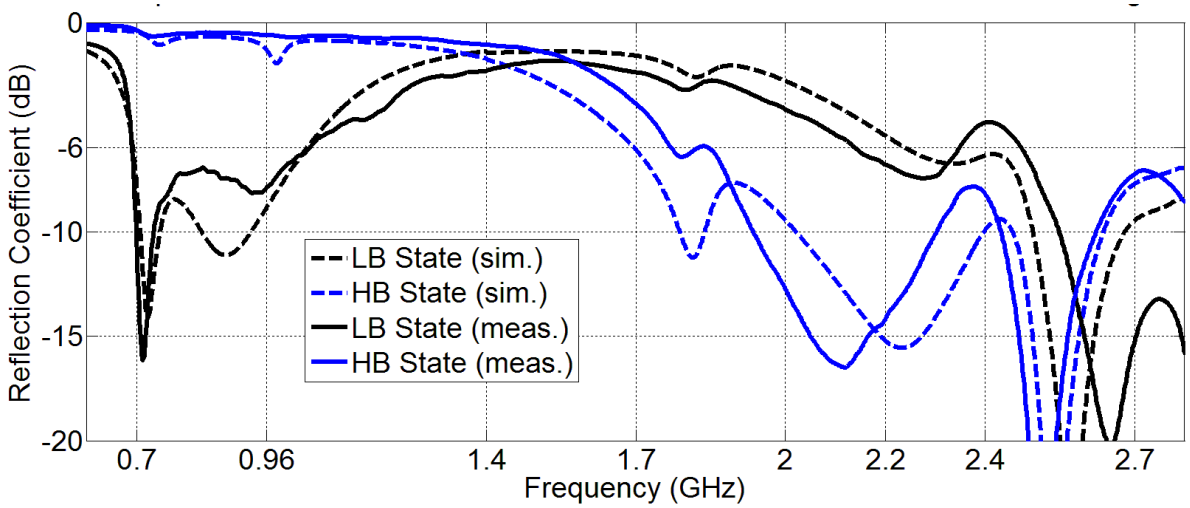

Figure 35 Comparison of Simulated and Measured Reflection Coefficient for Antenna Design I

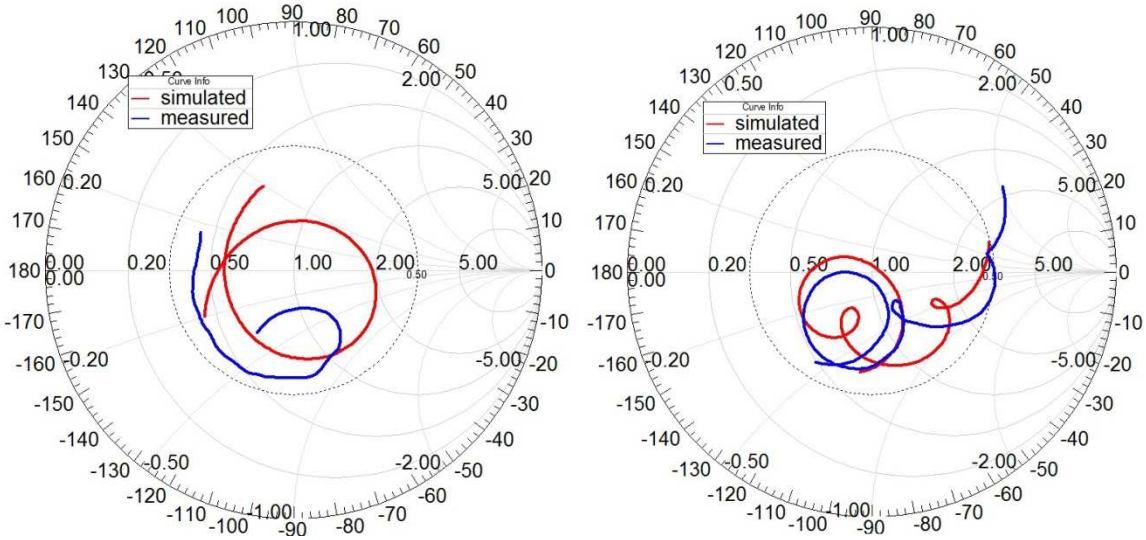

Figure 36 Comparison of Simulated and Measured Input Impedance for Antenna Design I (LB on left, HB on right)

The total efficiency of the passive prototype was measured in a Satimo Starlab station [11], in LB and HB (Figure 37). The measured total efficiency (including mismatch losses) can be seen in Figure 38 to be between -3.5dB and -1.5dB in the LB and between -3.5dB and -1.1dB in the HB.

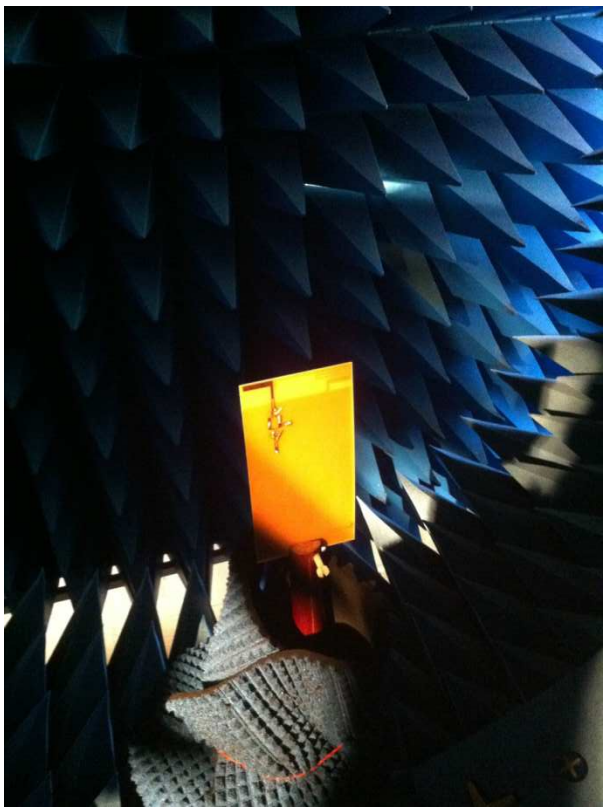

Figure 37 Efficiency Measurement Setup

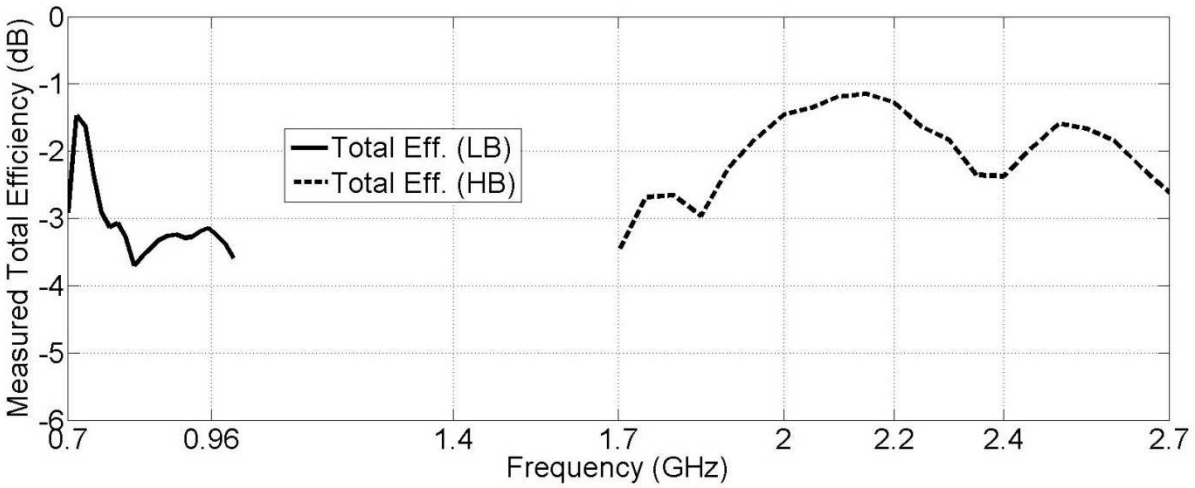

Figure 38 Measured Total Efficiency for Antenna Design I

The comparison of the simulated and measured 3D Gain pattern for the antenna in three different frequencies can be observed in Figure 39. A good compliance is seen between the simulated and measured patterns. In the LB, a dipole type radiation is observed as expected, since the ground plane is the main radiator. The antenna becomes more directive in the HB, as the electrical length of the antenna increases. The vertical polarization (when the PCB is held vertically) is dominant in both bands, where the measured maximum gain differs by more than 10dB in the LB and around 2-4dB in the HB when compared to horizontal polarization.

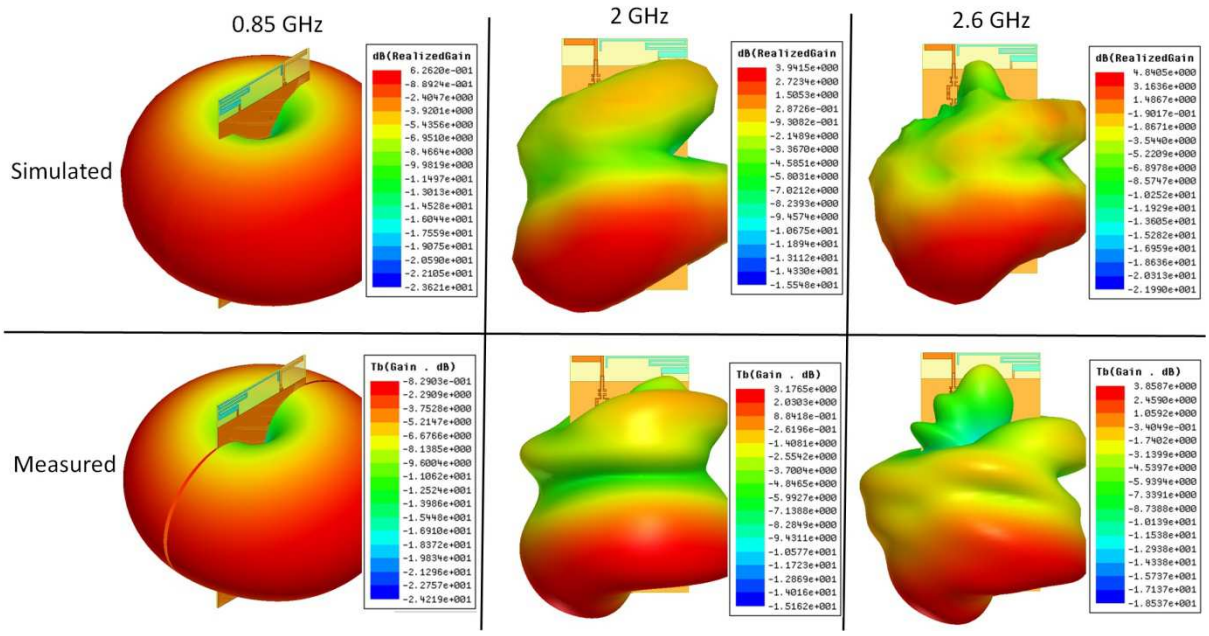

Figure 39 Simulated and Measured 3D Gain Patterns for Antenna Design I

A situation about the radiation efficiency was observed, having a closer look at the HB performance of the antenna. The simulated radiation efficiency is compared with the radiation efficiency calculated from the measured total efficiency (using the measured reflection coefficient) in Figure 40. Firstly, there is a difference of approximately 0.5dB between simulated and measured radiation efficiency, whose possible cause is the accuracy of the measurement set-up given as +/-1dB

in the product datasheet. Besides from that, a slight drop in the radiation efficiency can be seen around 1.85GHz and 2.45GHz both in simulations and measurements. As previously stated in Figure 30, these two frequencies correspond to the strong excitation frequencies of the parasitic strip in the HB. The cause of this radiation efficiency drop was further investigated and will be explained in Section 1.3 of this chapter because it's an important issue in many practical antenna designs for mobile phones.

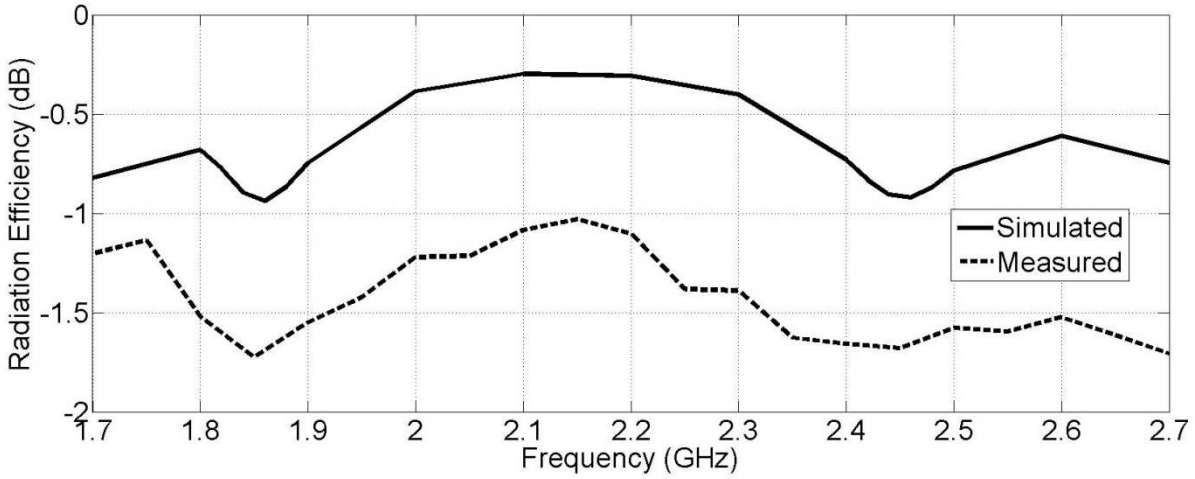

Figure 40 Simulated and Measured Radiation Efficiency in HB for Antenna Design I

1.2. ANTENNA DESIGN-II

A second alternative antenna design was also proposed, using MEMS switches again for band-switching between the LB and HB. The antenna excitation methodology was changed from selecting between two MN branches to selecting between two driven strips. The proposed antenna layout can be seen in Figure 41. The antenna is directly printed on the FR4 substrate having dimensions of 115mm X 60mm X 0.8mm, with a ground clearance of 15mm for the antenna. The antenna consists of two driven strips, one for LB coverage and one for HB coverage. To increase the bandwidth potential in the LB, a parasitic element (printed under the substrate) was again used, which is capacitively excited by the LB driven strip and connected to the ground plane over an SMD inductor (18nH) on the other end. The inductor used in the ground connection helps to increase the electrical length of the parasitic strip, thus decreasing the resonance frequency created by the parasitic strip. The number of SPDT MEMS switches is reduced to one (instead of two in the former case) and the switch is used to direct the excitation current either through the LB path or the HB path as seen in Figure 41. When the LB driven strip is excited, the parasitic strip is also capacitively excited, enabling a higher bandwidth potential in the LB.

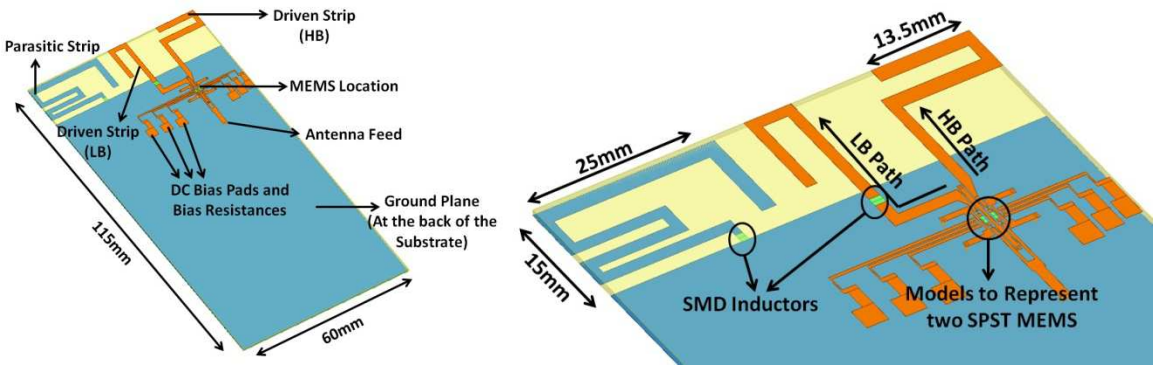

Figure 41 Layout of the Antenna Design-II Using MEMS Switches

1.2.1. Antenna Simulations With MEMS Switches and Matching Network

The simulated input impedance when removing the HB driven strip (considering only the LB driven strip with the parasitic element) can be observed in Figure 42 (Blue curve), on the left smith chart (plotted between 700-960MHz). A resonance is created by the parasitic strip similarly to the one created for Design I, which appears as a new loop in the smith chart. The LB response of the antenna is matched to 50Ω using a series inductor (27nH) on the LB driven strip. The red curve in the same figure presents the input impedance after the HB driven strip and the SMD inductor is introduced to the antenna. If the HB response of the antenna for "HB driven strip only" case is observed on the right smith chart, it can be seen that the parasitic strip creates a resonance in this band also at 1.76GHz.

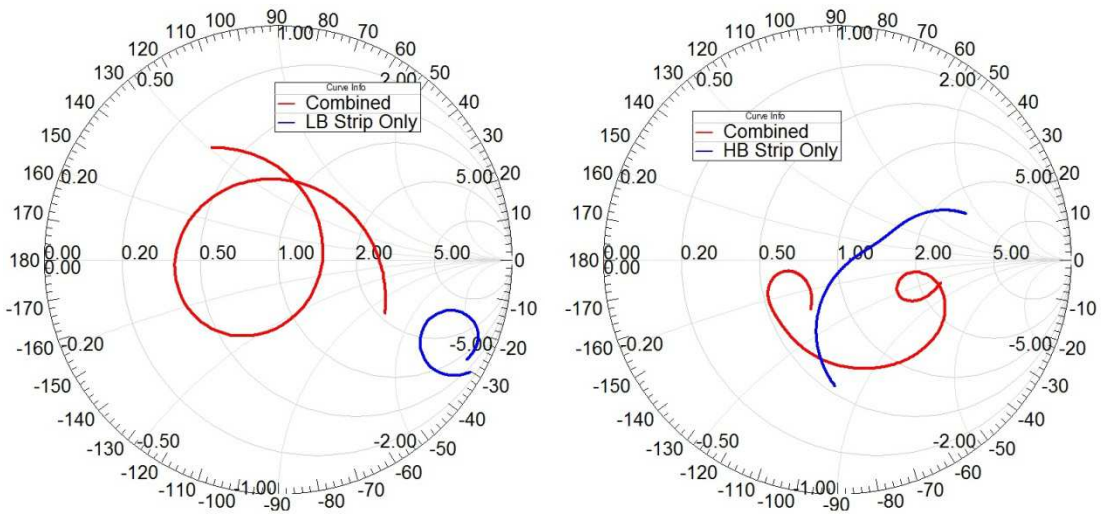

Figure 42 Simulated Input Impedance for Antenna Design II (LB on left, HB on right)

The role of the parasitic strip in the HB can be seen with the surface currents presented in Figure 43. At 1.76GHz, strong currents are excited on the parasitic strip, which appear weaker at any other frequencies (2.2GHz presented here).

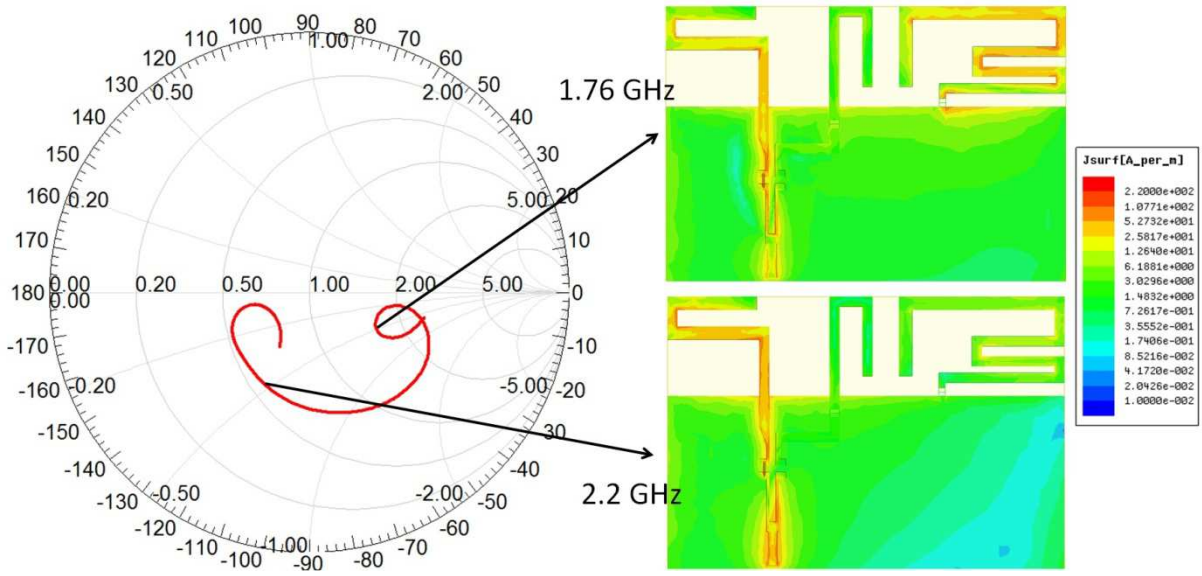

Figure 43 Surface Current Distribution for Antenna Design II in HB

1.2.2. Measurement Results for Antenna Design II

The S-parameter measurements of this prototype have been done both with real MEMS devices and with passive prototypes. In passive measurements, to represent the ON-state of the MEMS, a simple wire was soldered bypassing the MEMS and the connection was left open to represent the OFF-state. The measured reflection coefficient for the antenna in the LB and HB states can be seen in Figure 44. The target bands are covered with a reflection coefficient below -6dB in both passive measurements and real MEMS measurements, using the band-switching topology.

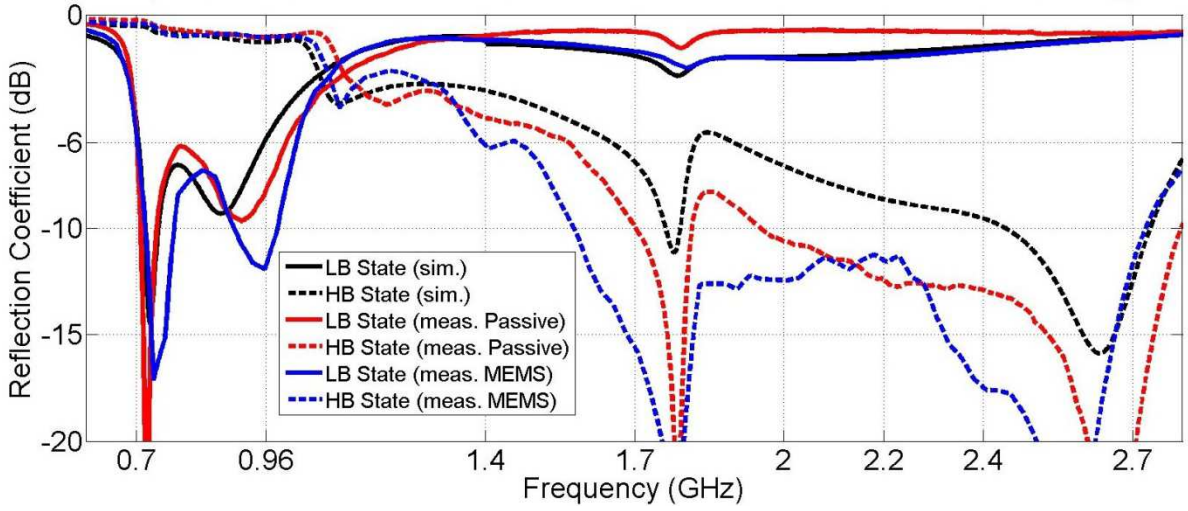

Figure 44 Comparison of Simulated and Measured Reflection Coefficient for Antenna Design II

The simulated and measured (with passive prototypes) input impedance makes a good compliance as seen in Figure 45. Comparing the simulated impedance response with the one measured with MEMS, it can be told that the MEMS switches turned out to be more lossy in the measurements than expected, since the locus in the smith chart is closer to the center (50Ω).

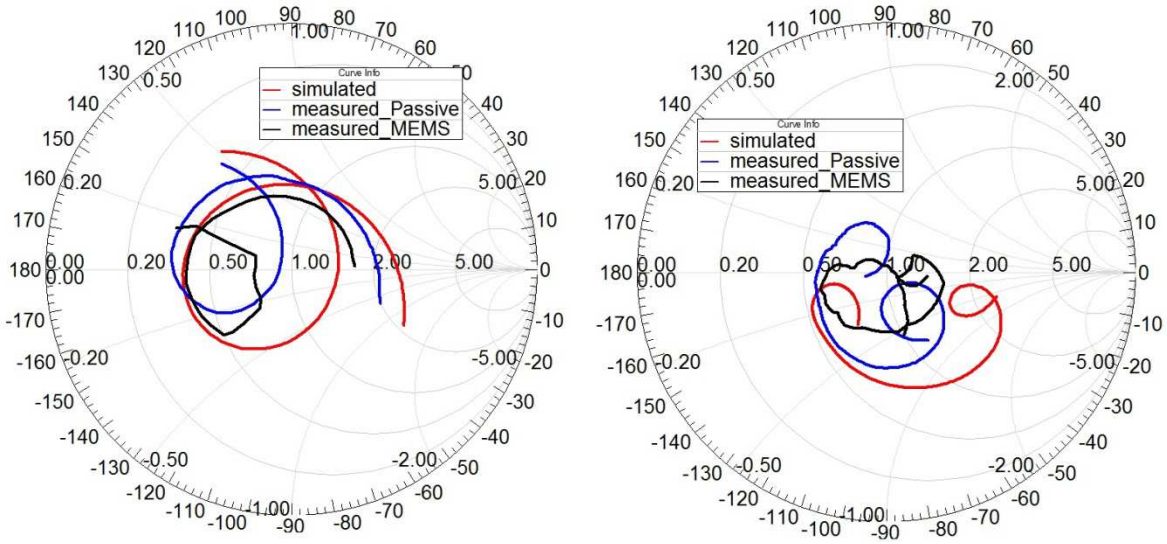

Figure 45 Comparison of Simulated and Measured Impedance for Antenna Design II (LB on left, HB on right)

The total efficiency of the antenna was also measured (for passive prototypes only, due to reliability issues) for LB and HB cases (Figure 47). The manufactured prototype can be observed in Figure 46.There is an efficiency higher than -3dB except around 700MHz in the LB and higher than -2.5dB in the HB.

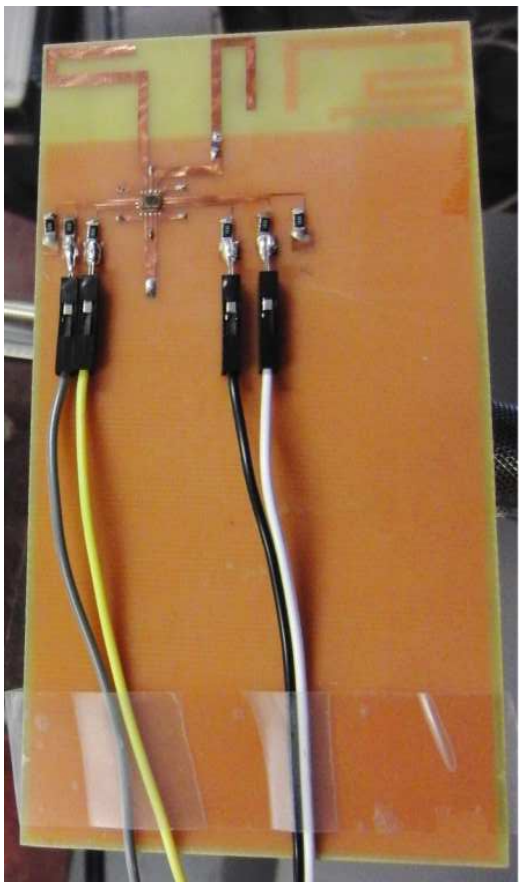

Figure 46 Manufactured Prototype for Antenna Design II

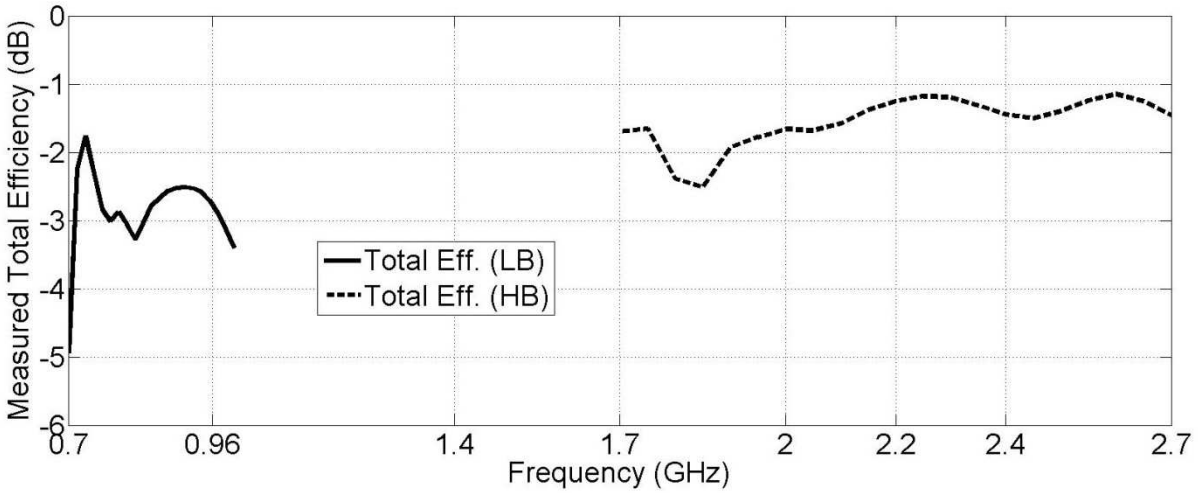

Figure 47 Measured Total Efficiency for Antenna Design II

The measured 3D gain patterns are compared with simulations in Figure 48. A good compliance in terms of pattern shape can be seen between simulations and measurements. As in the previous antenna, the LB pattern is a dipole type pattern and the gain increases in the higher frequency bands. The dominant polarization is again vertical, maximum gain being more than 10dB superior in LB and 1.5-2dB superior in HB when compared to horizontal polarization.

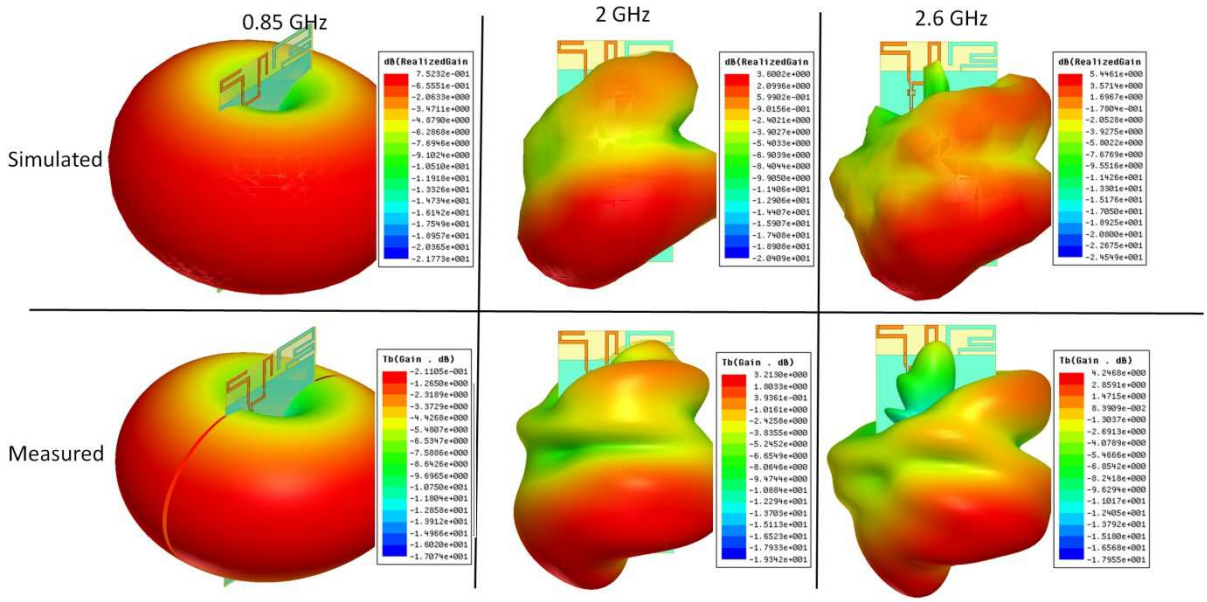

Figure 48 Simulated and Measured 3D Gain Patterns for Antenna Design II

A radiation efficiency drop issue can be also observed also for this prototype around 1.8GHz in Figure 49. It is worthwhile to note that the measured radiation efficiency in this figure is calculated from the measured total efficiency using the measured reflection coefficient. The efficiency drop is observed again at a frequency point, where the parasitic strip is strongly excited. Explanations about this problem will be given with some proposed solutions in next Section 1.3.

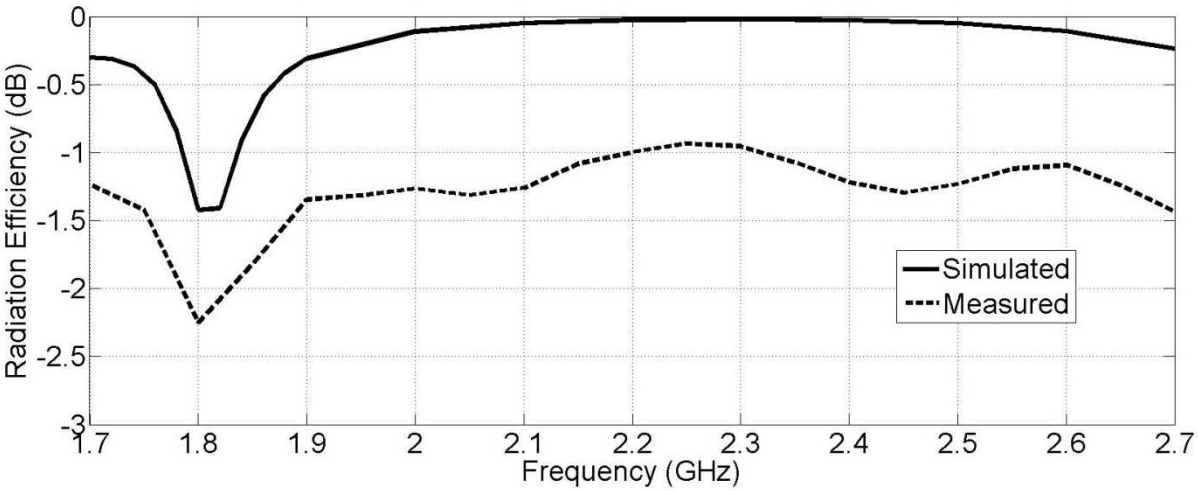

Figure 49 Simulated and Measured Radiation Efficiency in HB for Antenna Design II

1.3. RADIATION EFFICIENCY DROP IN ANTENNA PROTOTYPES

As presented in Figure 40 and Figure 49 of this chapter, a narrowband drop in the radiation efficiency was observed for both prototypes both in simulation and measurement, at the frequency regions corresponding to the excitation of the parasitic element in the HB. For the situation here, the drops observed are not causing a deep null in the radiation efficiency, but instead decreasing it as much as between 0.5-2dB from the general trend in simulations. However it should be noted that depending on the antenna topology, the problem may be more dramatic causing deep efficiency drops.

To investigate the reason of this situation, the surface currents were plotted in Figure 50 for antenna design I, at the frequency points of 1.86GHz and 2.46GHz, where a radiation efficiency drop of approximately 10% (-0.5dB) is observed from the general trend of the neighboring frequencies. Since the parasitic strip contributes to the HB frequency behavior at these two frequencies, strong currents can be observed on it (encircled with black ellipses in Figure 50). The direction of the current flow stays in opposite directions around the meander region, in a physically close manner. The fields created from these currents tend to cancel each other in the far-field region of the antenna, which leads to a radiation efficiency drop.

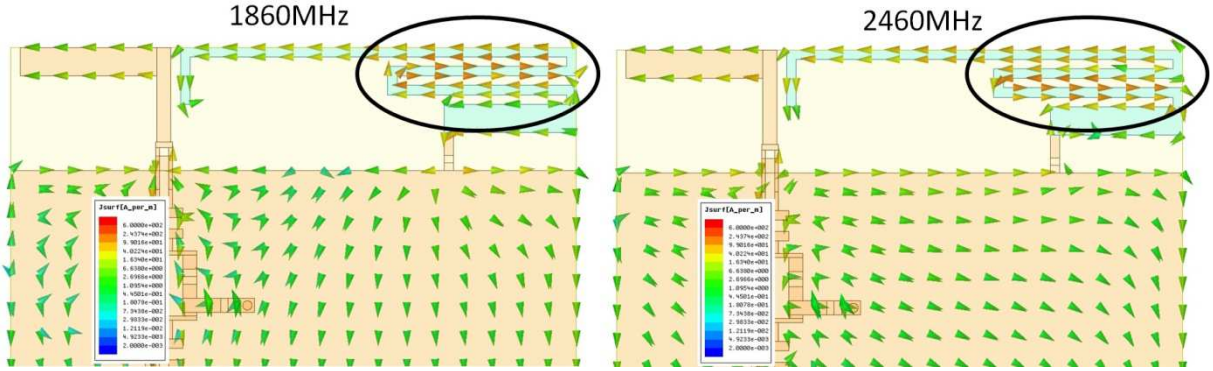

Figure 50 Surface Currents for the Efficiency Drop in Antenna Design I

To mitigate this effect and also for verifying the cause of the drop (suspected as the reverse currents on the meander region), the topology of the parasitic element was modified as seen in Figure 51, removing the meander line. Since the electrical length of the parasitic element is now shorter, the SMD inductor value on the ground connection is increased from 12nH to 16nH. In this way, the role of the parasitic element in the LB is maintained (for creating an additional resonance to increase bandwidth potential). For the simulations to be fair, no other property of the antennas nor the component values were changed. It can be seen in Figure 51 with the simulated reflection coefficient that the target bands can still be covered after this modification, although some tuning might be needed in the HB. The radiation efficiency of the modified structure is compared with the original case in Figure 52. The drops in the radiation efficiency are now satisfactorily solved with the modified structure.

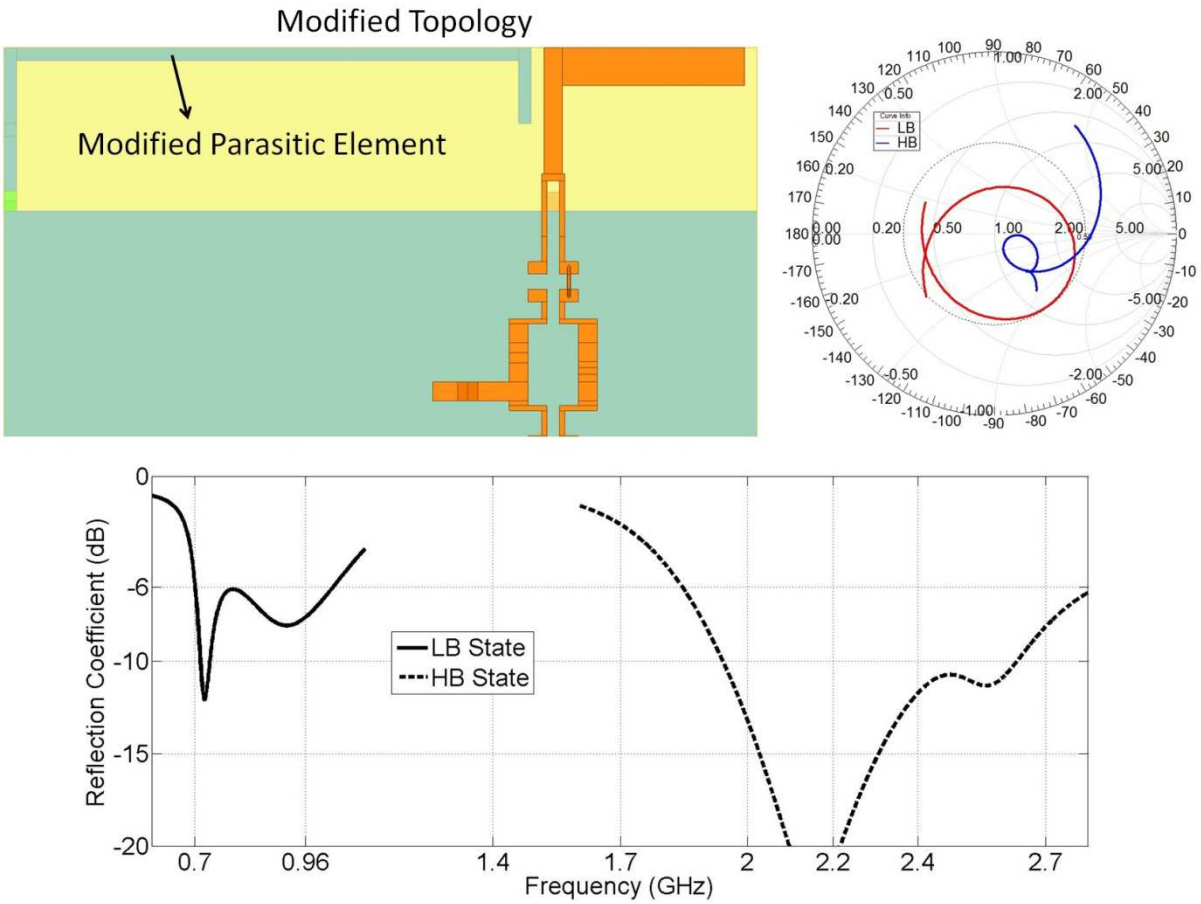

Figure 51 Modified Topology to Mitigate the Efficiency Drop for Antenna Design I and Simulated Input Impedance and Reflection Coefficient

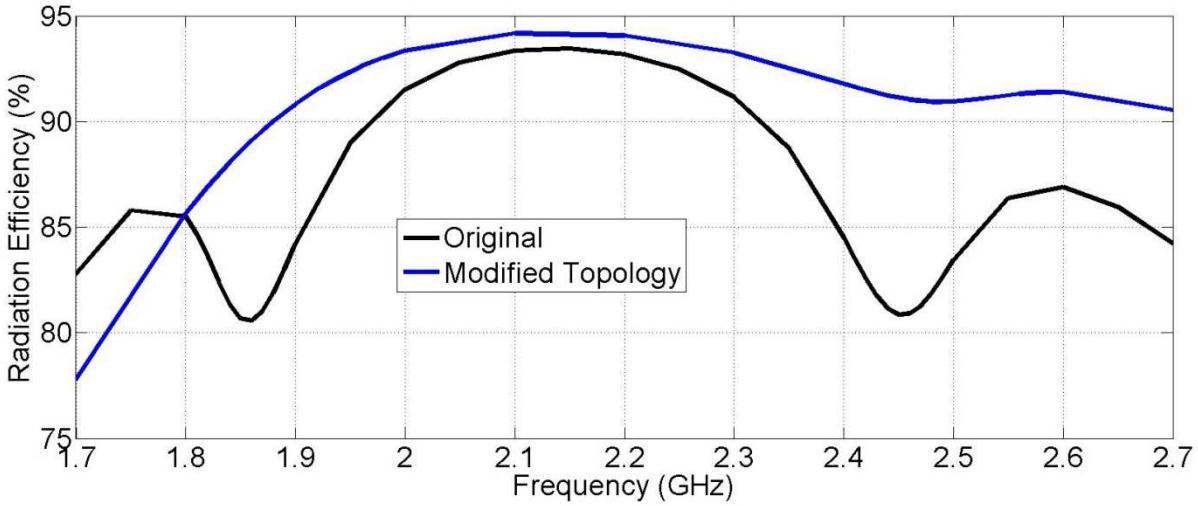

Figure 52 Simulated Radiation Efficiency of the Modified Topology for Antenna Design I

A similar study was done with antenna design II also. The surface currents in opposite directions on the meander line can be observed in Figure 53 at 1800MHz.

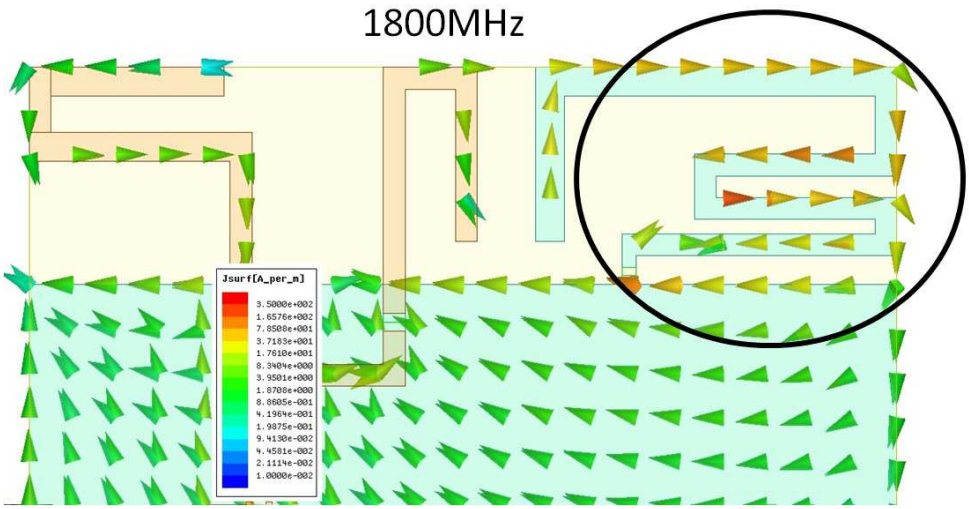

Figure 53 Surface Currents for the Efficiency Drop in Antenna Design II

Two different modified topologies are proposed in Figure 54, avoiding any meander line on the parasitic strip. To compensate the shortening of the electrical length of the parasitic element, the SMD inductor value on the ground connection point was increased to 27nH in modified topology-1 and to 29nH in modified topology-2 (from 18nH). A good matching behavior concerning the target frequency bands can be achieved with the two topologies.

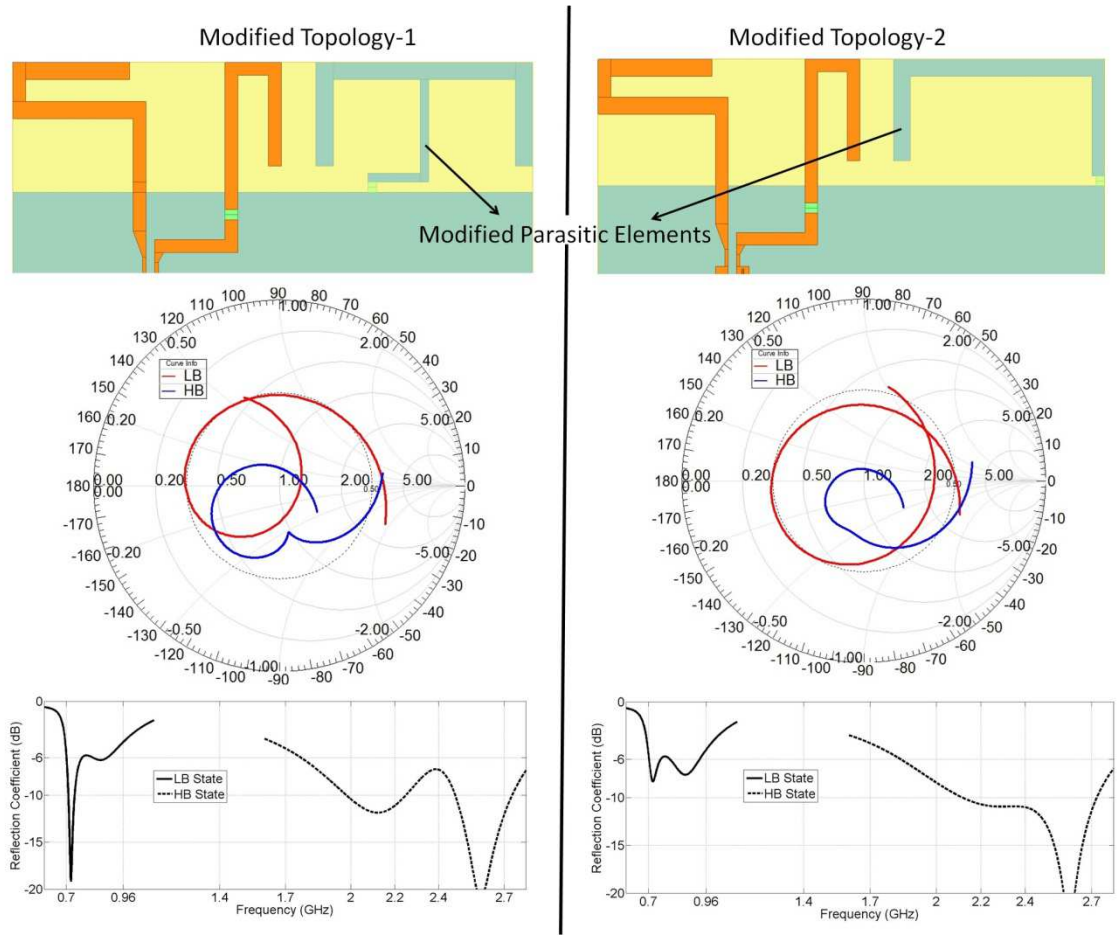

Figure 54 Modified Topology to Mitigate the Efficiency Drop for Antenna Design II

The effect of this modification on the simulated radiation efficiency is presented in Figure 55. Although the 25% efficiency drop at 1.8GHz is prevented, a drop of approximately 10% is again seen in modified topology-1 at the frequency where the parasitic strip is excited. This can further be avoided by modifying the layout as in modified topology-2.

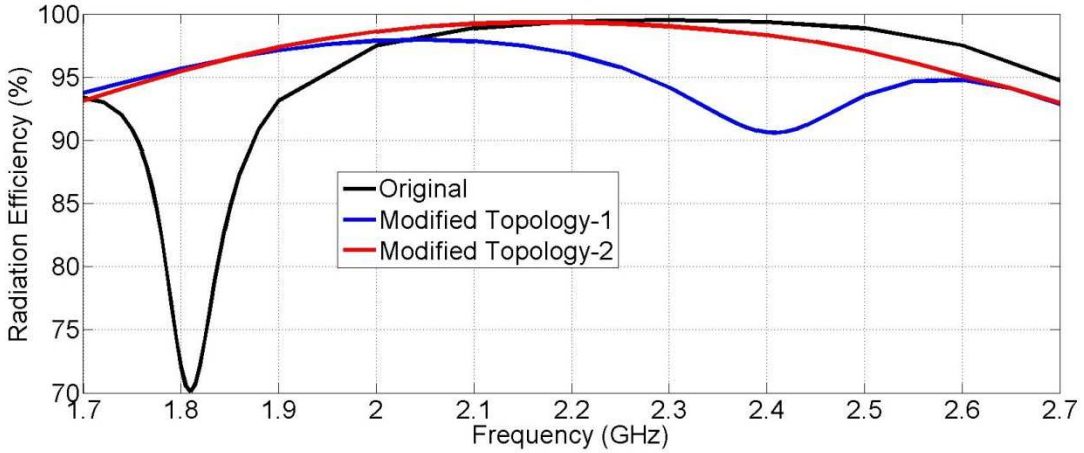

Figure 55 Simulated Radiation Efficiency of the Modified Topology for Antenna Design II

The fabrication of the modified antennas were not possible due to time constraints so the measurement results are not presented here.

2. ANTENNA DESIGN USING BST CAPACITOR

Another tunable component for use in the tunable antennas from the Artemos Project is the tunable BST(**B**arium **S**trontium **T**itanate) capacitors from CEA-LETI[12]. This type of tunable capacitors have been used for matching band reconfigurability in [13-14]. In [13], a tunable capacitor with a tuning range between 1.4-4.2pF was used in a tunable matching network at the feed of a COTS chip antenna to tune the matching bandwidth between 1.55-1.7GHz(Figure 56). A tunable dual-band IFA was proposed in [14], whose matching bands are tuned using a series LC resonator in parallel with a BST capacitor on the IFA. In this way the LB of the antenna is tuned between 822-1050MHz and HB is tuned between 1.42-2.2GHz using the BST capacitor having a tuning range of 3.3:1.

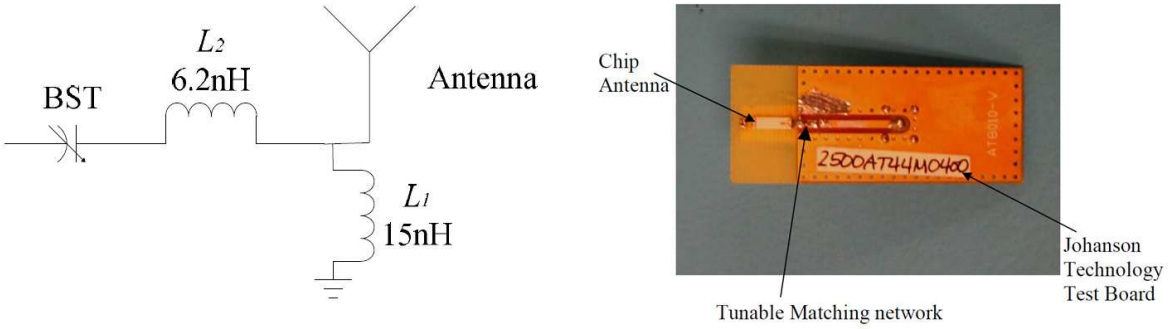

Figure 56 Tunable Matching Network and Test Prototype in [13]

For this study, CEA-LETI has implemented tunable Metal/Insulator/Metal capacitors using $Ba_{0.7}Sr_{0.3}TiO_3$ as the dielectric material. A general layout of the BST tunable capacitor can be seen in Figure 57. Tunability in the capacitance value is achieved by changing the applied bias voltage between the top and bottom metal plates. This voltage difference changes the permittivity of the BST material, which in turn changes the capacitance between the plates.

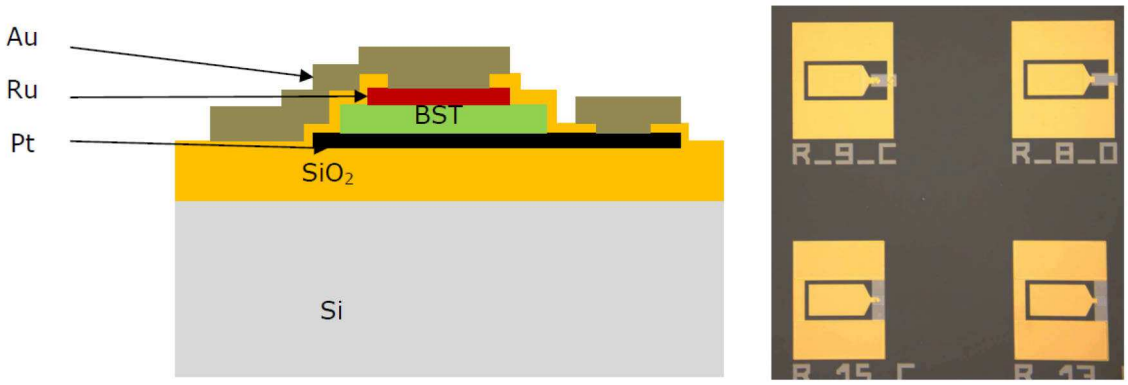

Figure 57 Layout of a BST Capacitor and Photograph of Manufactured Dies

The main challenge of using these tunable capacitors is the relatively low tunability range, which was agreed to be between 2.5-4pF with the manufacturer. The measured capacitance value versus the applied bias voltage for the BST capacitor can be seen in Figure 58. The tunable capacitor is exploited to achieve matching tunability in the LB, with a simple and low-cost antenna geometry. For the coverage of the HB, another antenna which is separately fed is used, obtaining a dual-feed configuration.

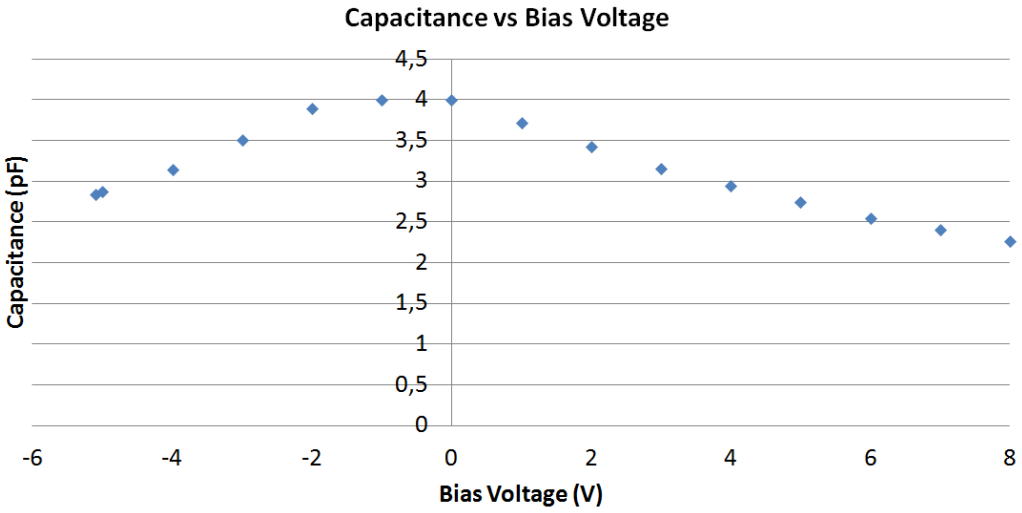

Figure 58 Measured Capacitance vs Bias Voltage for BST Capacitors

2.1. ANTENNA MODEL AND SIMULATION RESULTS

The proposed antenna model can be seen in Figure 59. As already mentioned, the antenna has a dual-feed structure, where one of the feeds is responsible for LB coverage and the other is responsible for HB coverage. All the antenna structure is again printed on FR4 substrate, having total dimensions of 120mm X 59mm X 0.8mm, with a ground clearance of 15mm on one of the short edges. The LB antenna is a simple coupling element (CE), which is tuned to the desired band using a pre-matching network and the tunable BST capacitor. The HB antenna is a simple monopole, fed through the second feed of the antenna.

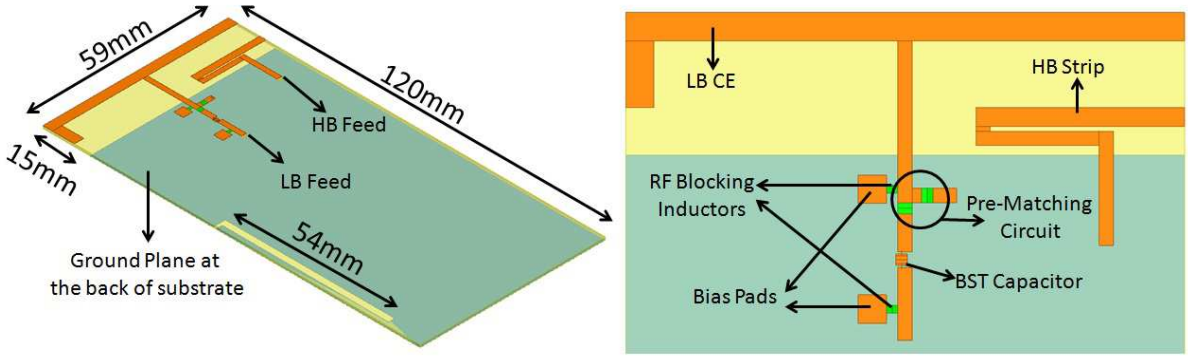

Figure 59 Simulation Model of the BST Antenna

Since the tunable capacitor has a relatively low tuning range (4 : 2.5), a slot of 54mm length was etched on the ground plane, to create an additional resonance around 950MHz, which makes the coverage of the LB easier. The slot basically changes the current distribution on the ground plane and the chassis resonance shifts to lower frequencies since the electrical length of the ground plane increases. The length of the slot is an important parameter in the design phase of the antenna. Changing this length modifies the frequency of resonance, seen in the blue curve in Figure 60. The length was optimized as 54mm after a parametric study. The effect of the slot can be observed in Figure 60, plotted between 700-960MHz.

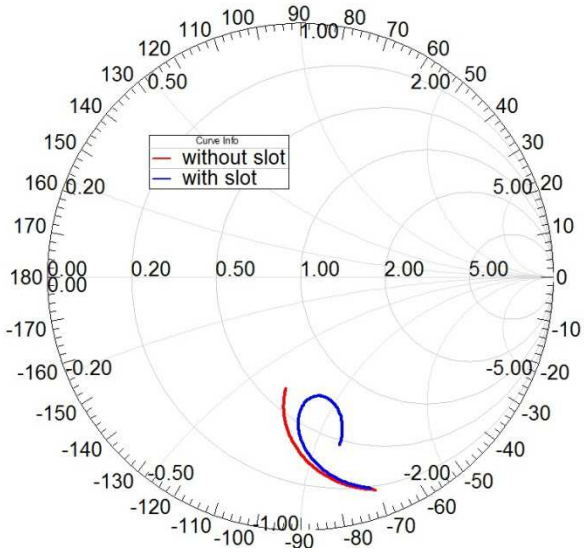

Figure 60 Effect of the Slot in the Ground Plane

The left smith chart in Figure 61 presents the simulated input impedance of the antenna when the LB CE is simulated in the absence of the HB monopole and vice versa. The red curve is plotted for frequency interval 700-960MHz and blue curve plotted between 1.7-2.7GHz. The response of the combined antenna structure, after the pre-matching using a shunt inductor of 30nH and series inductor of 22nH is given on the right in Figure 61. One thing to notice here is the additional resonance created in the HB around 1900MHz. According to the surface currents plotted in Figure 62, this new resonance comes from the currents induced on the LB CE. Afterwards these currents flow to the ground plane over the shunt inductor and also to the LB feed of the antenna, which should be kept under a specific level to achieve enough port-to-port isolation.

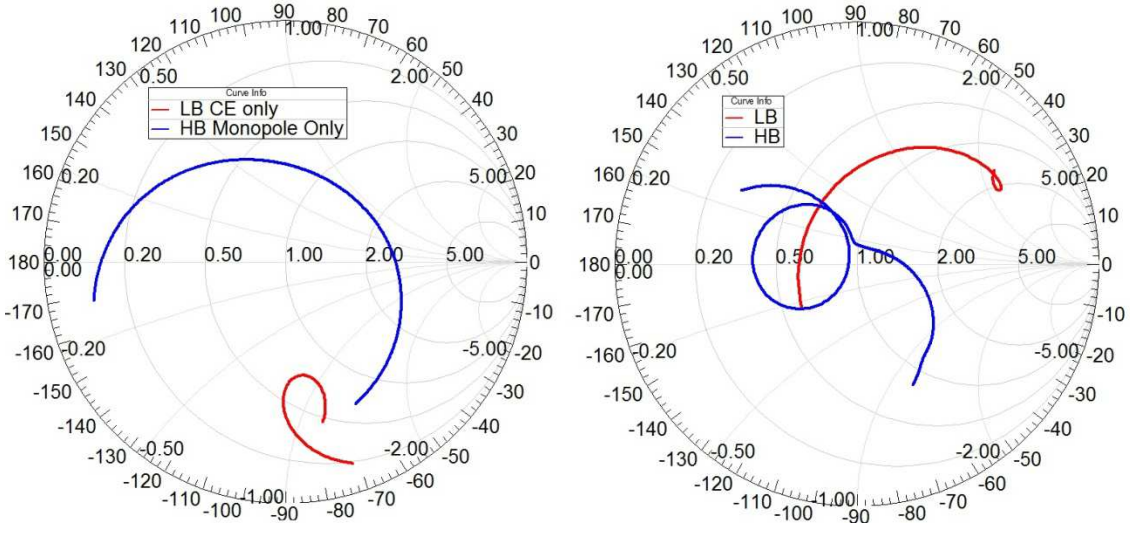

Figure 61 Simulated Input Impedance of the Antenna (LB CE and HB Monopole Simulated Alone on left, After Pre-Matching on right)

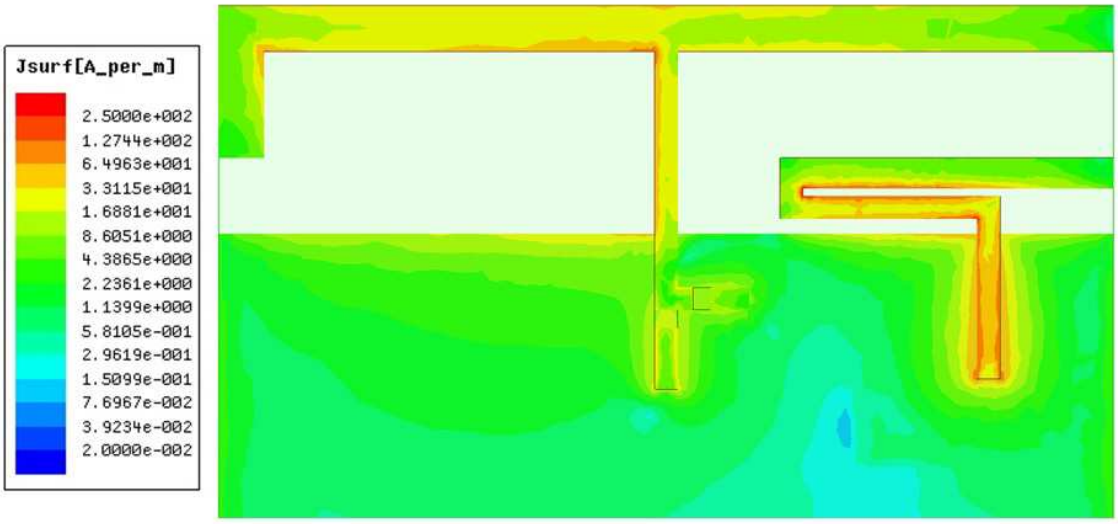

Figure 62 Surface Currents for BST Antenna at 1900MHz After Pre-Matching

Simulations were done for the antenna taking into account the wirebondings and RF Blocking inductors (120nH) for the DC bias pads, that are necessary for the integration of the BST capacitor. For the SMD components, the measurement results from the manufacturers were used. The simulated reflection coefficient in the LB for the BST capacitance changing from 2.5pF to 4pF is given in Figure 63. By increasing the capacitance value, the impedance curve moves in clockwise direction on a constant resistance circle in smith chart, enabling the coverage of lower frequencies. The resonance created by the slot in the ground plane helps considerably for the matching in the high-edge of the band. With this configuration, the frequency interval of 725-960MHz can be covered with a reflection coefficient below -6dB.

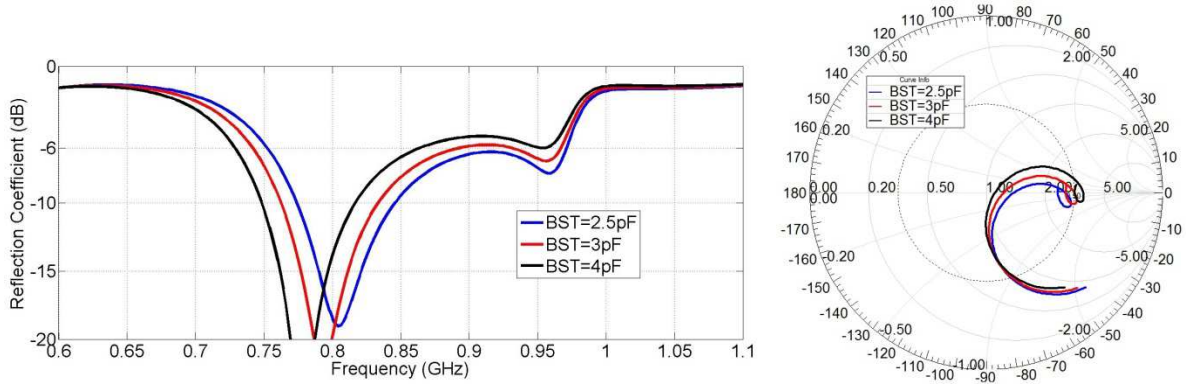

Figure 63 Simulated Reflection Coefficient in the LB for Different BST Capacitance Values

It was seen that the HB performance is not affected by the change in the tunable capacitor. Figure 64 shows the total antenna s-parameters when the BST capacitor is set to 2.5pF. The HB antenna can cover the 1.7-2.7GHz frequency interval with a reflection coefficient below -6dB. The isolation between the two ports is almost always higher than 10dB, making a minimum of 10dB around 2GHz. As shown in Figure 62, this frequency region is where the strong coupling to the LB CE from the HB monopole is observed.

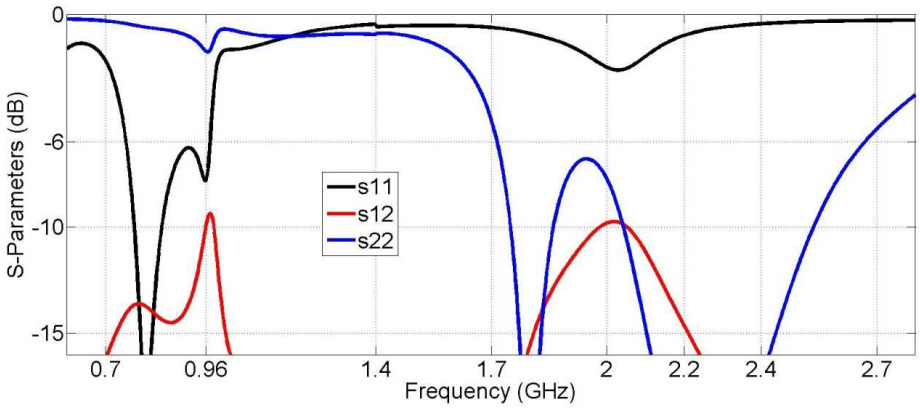

Figure 64 Simulated Reflection Coefficient for BST=2.5pF

The proposed antenna is currently under the manufacturing phase, which will be followed by the integration of the BST capacitor and the measurements to validate the simulation results.

3. CONCLUSIONS

In this chapter, three tunable antenna topologies have been proposed. Two of these antennas use MEMS switches to achieve band-switching between the LB (700-960MHz) and HB (1700-2700MHz), whereas the third antenna uses a BST tunable capacitor to tune the LB reflection coefficient.

The main difference between the two antenna using MEMS switches was the methodology of utilizing the switches. The first antenna uses two MEMS, to select between one of the MN branches and the second antenna uses a single MEMS to select between two driven strips. The simulation results have been validated with the measurements using manufactured passive prototypes for the first design and the antenna was shown to cover the target bands with a reflection coefficient below -6dB. For the second design, measurement results with both passive prototypes and real MEMS switches were presented.

In Section 1.3, a situation observed during the efficiency measurements of the antennas was investigated. A drop in the radiation efficiency was seen in both simulations and measurements, which is narrow-band and corresponds to the frequency regions where the parasitic element is excited capacitively in the HB. It was shown through simulated current distributions that the cause of this situation was the currents flowing in opposite directions on the meander line, which tend to create cancelling field in the far-field region of the antenna. Some modifications on the antenna topologies were successfully proposed to mitigate this effect.

Finally, an antenna design using a BST tunable capacitor was presented, that achieves tunability in the LB reflection coefficient. This antenna was a dual-feed structure where the HB antenna is separately-fed and is not affected by the changing capacitance value. It was shown through simulations that the frequency interval of 725-960MHz and 1.7-2.7GHz can be covered with a tunable capacitance ranging between 2.5-4pF, with an isolation higher than 10dB between the feeds.

REFERENCES FOR THIS CHAPTER

[1] Haridas, N.; Erdogan, A.T.; Arslan, T.; Walton, Anthony J.; Smith, S.; Stevenson, Tom; Dunare, C.; Gundlach, A.; Terry, J.; Argyrakis, Petros; Tierney, K.; Ross, A.; O'Hara, T., "Reconfigurable MEMS Antennas," Adaptive Hardware and Systems, 2008. AHS '08. NASA/ESA Conference on , vol., no., pp.147,154, 22-25 June 2008

[2] Mowler, M.; Lindmark, B., "Reconfigurable mems antenna for wireless applications," Antennas and Propagation, 2006. EuCAP 2006. First European Conference on , vol., no., pp.1,6, 6-10 Nov. 2006

[3] R. Valkonen, C. Luxey, J. Holopainen, C. Icheln and P. Vainikainen, "Frequency-reconfigurable mobile terminal antenna with MEMS switches," Proceedings of the 4th European Conference on Antennas and Propagation (EuCAP 2010), pp.1-5, 12-16th April 2010.

[4] R. Valkonen, J. Holopainen, C. Icheln and P. Vainikainen, "Broadband tuning of mobile terminal antennas," Proc. of the European Conf. on Antennas and Propagation (EuCAP2007), Edinburgh, UK, Nov. 2007.

[5] Radant MEMS Company Website, Available at: http://www.radantmems.com/

[6] OMRON Company Website, Available at: http://www.omron.com/

[7] DELFMEMS Company Website, Available at: http://www.delfmems.com/

[8] Optenni Lab, Information Available at: http://www.optenni.com/optenni-lab/

[9] ANSYS HFSS, Information Available at: http://www.ansys.com/products/hf/hfss/

[10] Agilent ADS, Information Available at: http://www.home.agilent.com/

[11] Satimo Starlab, Information Available at: http://www.satimo.com/content/products/starlab

[12] CEA-LETI Company Website, Available at: http://www-leti.cea.fr

[13] Nan Ni; Cardona, A.H., "Tunable 3.5GHz and 1.5GHz chip antennas based on thin-film BaSrTiO3 capacitors," Radio and Wireless Symposium (RWS), 2011 IEEE , vol., no., pp.58,61, 16-19 Jan. 2011

[14] Nan, Ni., Cardona, A.H. "Tunable Dual-band IFA Antenna using LC Resonators," Available: http://arxiv.org/ftp/arxiv/papers/1109/1109.0762.pdf

CHAPTER III
THE HOLLOW COUPLING ELEMENT APPROACH

As previously mentioned in the Introduction part, coupling elements (CE) have been widely proposed in literature for mobile terminal antennas, to obtain a wide-band matching response using the space available for the antenna, which is typically electrically-small. In this scenario, the CE is used just as an exciter to induce the proper currents on the terminal ground plane, whose dimensions are generally close to a 0.25-0.3 free space wavelength in the frequency band of 700-960MHz. In this way, the quality factor of the antenna is significantly reduced thanks to the low-Q nature of the thick ground plane and a high bandwidth potential is enabled. Since they are inherently non-resonant, CEs need a matching network at the antenna feed, to be tuned to the desired operating frequency. The main drawback of using CEs for 4G/LTE standards is the necessity of MNs with a high number of components to achieve dual-band coverage which increases both the losses and the cost.

This chapter presents a new design, namely a modified version of the traditional plain coupling element approach, by removing the inner metal part of the CE. This way, a hollow structure is obtained and the space available inside the CE can be used to insert another antenna to cover other frequency bands. In terms of input impedance, negligible difference is observed in the LB, by making the CE hollow. Two antenna designs using the new approach are designed, optimized and presented to cover the 700-960MHz and 1.7-2.7GHz bands. Finally, a dual-antenna MIMO structure using the same technique is presented as an application example to operate in the LB frequency range.

1. THE HOLLOW COUPLING ELEMENT APPROACH

The proposed approach combining a non-resonant CE and a resonant antenna is presented in this section. The LB coverage is achieved using a 3D CE. The HB coverage is then achieved by integrating another antenna with a separate feed.

1.1. COMPARISON OF THE HOLLOW CE WITH A PLAIN CE

As previously mentioned, the traditional plain CE has been modified to obtain a more space-efficient structure with negligible performance trade-off. The main issue is to produce the same coupling behavior as the one produced with a plain element or more generally, to understand which section of a plain CE is important to couple to the PCB. This approach was first described for a single band CE with a 7mm height, covering only the LB 700-960MHz frequency range in the previous publications of the authors [1]. In [2], the HB antenna was inserted inside the hollow CE and the dual band coverage with good isolation was presented with simulations. Here, a further optimized CE layout in terms of occupied space (only 3mm height) is used to make a comparison between plain and hollow CEs in terms of impedance and bandwidth potential. For the comparison, the model given in Figure 65 have been used.

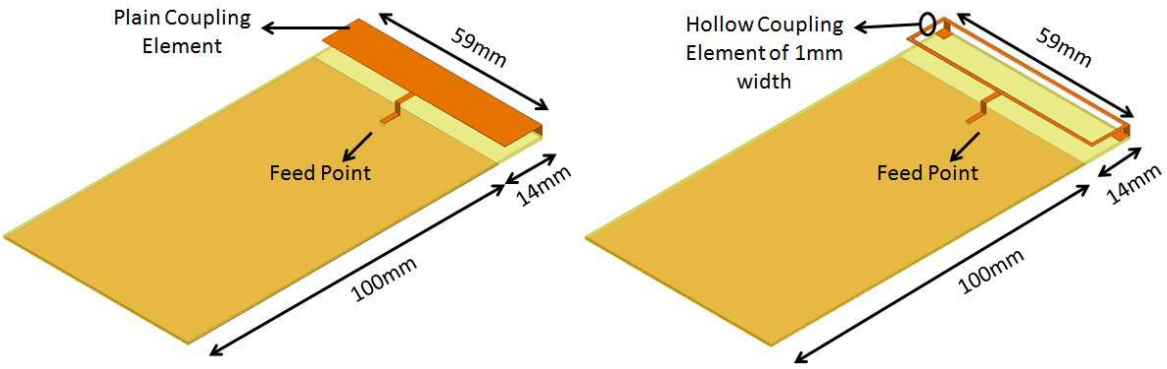

Figure 65 Antenna topologies used for the plain/hollow CE comparison

The plain CE consists of a rectangular metal sheet (59×14mm2) with 3mm height from the FR4 substrate. The feed of the CE is achieved through a vertical metal strip from the center of the PCB. The total PCB dimensions are 114×59×0.8mm^3 with a ground clearance of 14mm under the CE. For a fair comparison, all PCB dimensions and feeding location were kept the same for the hollow. The metal region inside the plain CE was removed to form the so-called hollow CE, leaving only a rectangular ring having a strip width of 1mm. The two CEs were simulated with the full wave electromagnetic simulator Ansoft HFSS. The simulated input impedance of the two CEs can be observed in Figure 66. The input impedance of the hollow CE shows minor deviation from the input impedance of the plain CE.

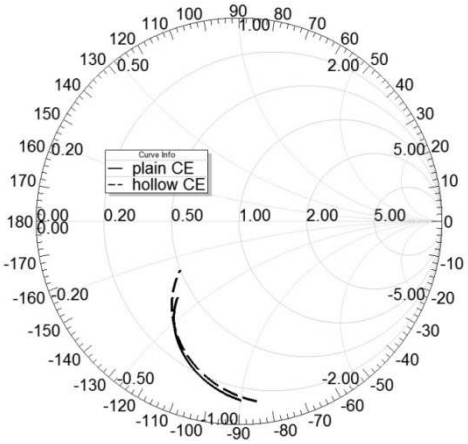

Figure 66 Input impedance of the plain and the hollow CEs (700MHz to 960MHz)

The currents induced on the system ground plane for the plain and hollow CEs can be observed in Figure 67. In both situations, the longitudinal mode (the fundamental) of the currents is induced almost at the same strength.

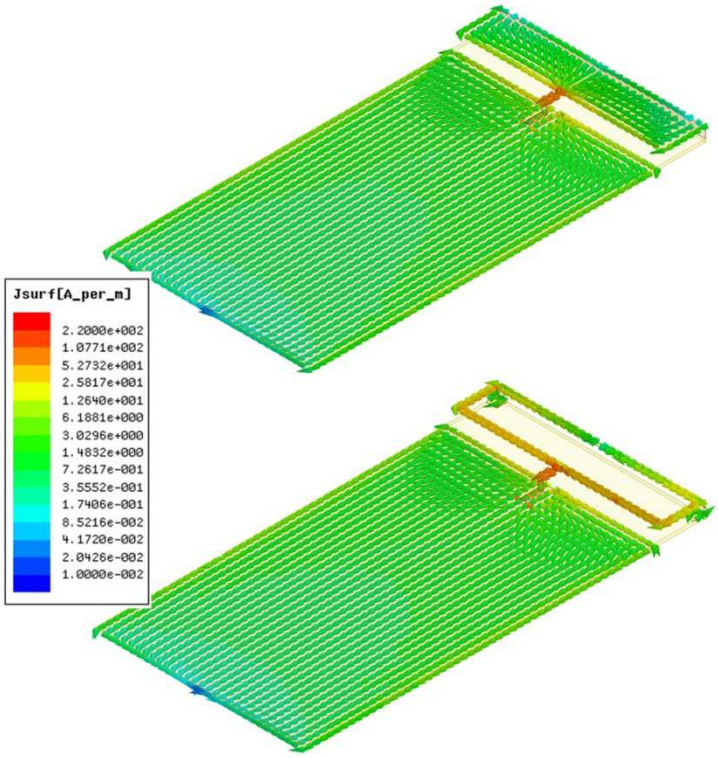

Figure 67 Comparison of the Ground Plane Currents (Plain CE on top, Hollow CE on bottom)

The E-field distribution under both CEs is observed in Figure 68. It can be told that fields under the hollow CE are weaker than the fields under the plain CE especially through the center of the hollow region. Using this fact, the HB antenna is proposed to be placed in this region, to get better port-to-port isolation.

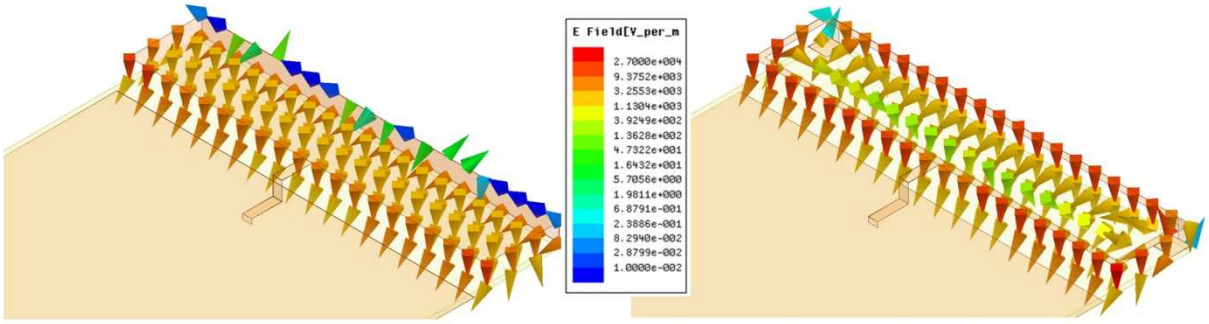

Figure 68 Comparison of the E-field Under the CEs (Plain CE on left, Hollow CE on right)

The bandwidth potential (BP) of the two CEs is compared with the help of the commercial software Optenni Lab. The BP is a realistic value computed from the input impedance of each CE (obtained from the full wave simulation) which is given for a certain number of matching components and a certain threshold for the reflection coefficient. At every frequency point f_0, the software generates a MN to match as much as possible frequency points around f_0 with a reflection coefficient below the threshold, chosen as -6dB here. The frequency interval around f_0 which gives a reflection coefficient below -6dB is given as the optimized BP (symmetrically around f_0). The BP obtained in this way is a realistic value compared to very optimistic theoretical values computed from the quality factor. As can be seen in Figure 69, the BP of the hollow CE is only slightly lower

(30MHz) than the BP of the plain CE in the LB, which proves again the equivalence between the plain and the novel hollow CE in terms of matching behavior. In the center of the 700-960MHz band, the obtainable BP is around 200MHz (for a -6dB reflection coefficient). It should be kept in mind that this BP value is obtained with a MN of two lumped components which is foreseen to be increased above the required 260MHz to cover the full LB by using more matching network components.

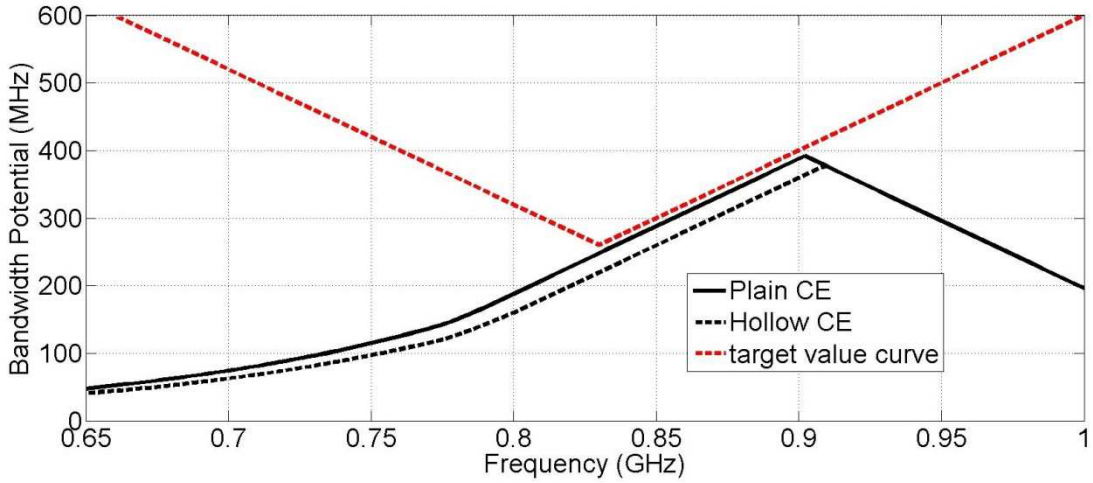

Figure 69 Bandwidth Potential Comparison of the Plain and Hollow CEs

1.2. INTEGRATION OF HIGH BAND ANTENNA WITHIN THE HOLLOW CE

As previously mentioned, the space gained by making the plain CE hollow can now be used to integrate a high-band antenna. For ease of manufacturing, it was decided to focus on a fully printed HB antenna design (directly on the FR4 substrate). Since it was observed that the E-field under the hollow CE was weaker through the center of the hollow region (Figure 68), the HB antenna was planned to be placed in this area to obtain high port-to-port isolation.

The optimized layout of the proposed antenna can be seen in Figure 70. The total PCB dimensions are 114×59×0.8mm^3, with a ground clearance region of 59×14mm^2 on one side of the PCB. A simple monopole is used for the HB coverage, placed 8.5mm away from the edge of the PCB. To tune the hollow CE as to cover 700-960MHz, a MN (seen in Figure 71) consisting of four lumped components was designed with the Optenni Lab software. The main objective of this MN is to get a reflection coefficient below -6dB for the hollow CE between 700-960MHz. There is also another functionality of the MN, which is to act as a band-stop filter in the HB frequency range to help in resisting the possible currents from the HB antenna to reach the LB antenna port. Very high isolation levels were possible using this strategy in the HB, so the matching response of the HB antenna was the primary goal when determining the exact location and orientation of the HB antenna.

After the circuit optimization of the MN, an additional full-wave optimization was performed to take into account the existing transmission lines between the SMD components and the vias connected to the ground plane.

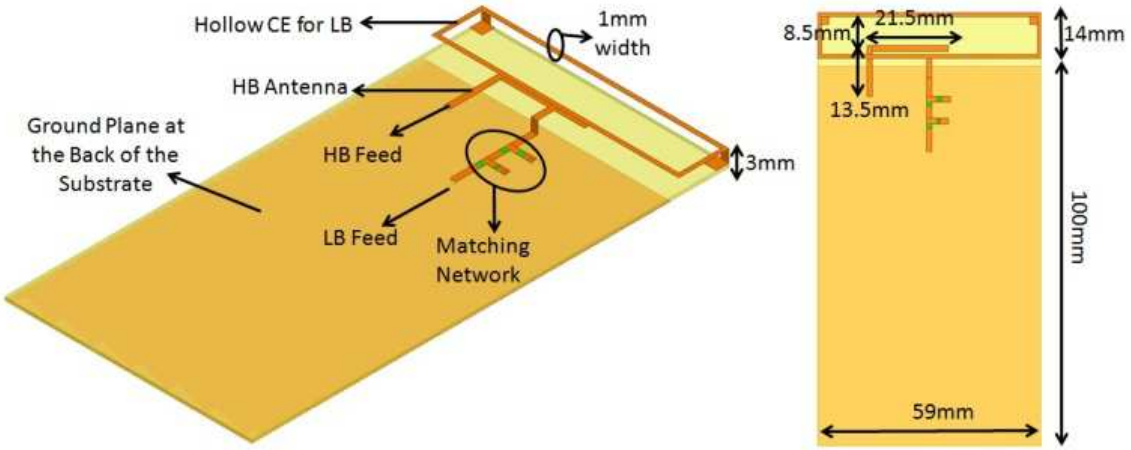

Figure 70 Simulation Model of the Hollow CE Antenna

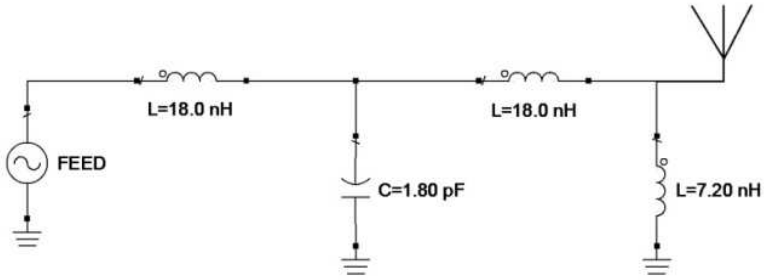

Figure 71 Matching Network used at the LB CE feed

The simulated input impedance of the LB antenna alone (without the HB antenna) with and without the MN can be seen in Figure 72, plotted from 700MHz to 960MHz. When the HB antenna is introduced, the S-parameters seen in Figure 73 are obtained. It can be seen that the target bands can be covered with a reflection coefficient below -6dB, except a small frequency range on the lower edge of the HB (1.7-1.75GHz). The port-to-port isolation is always higher than 9dB in the LB having a minimum value of 9.3dB at 740MHz. The port-to-port isolation is higher than 30dB in the HB.

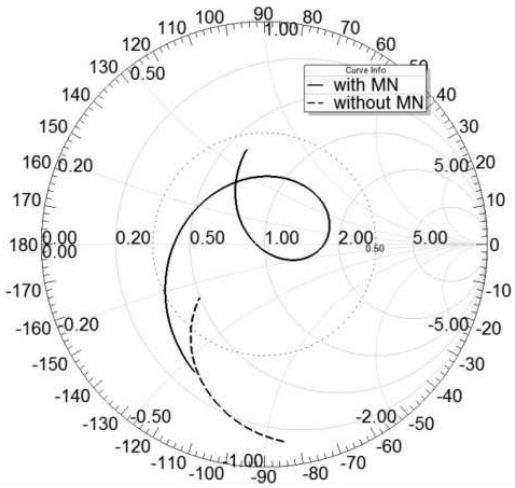

Figure 72 Simulated Input Impedance of the LB CE Alone (with and without MN)

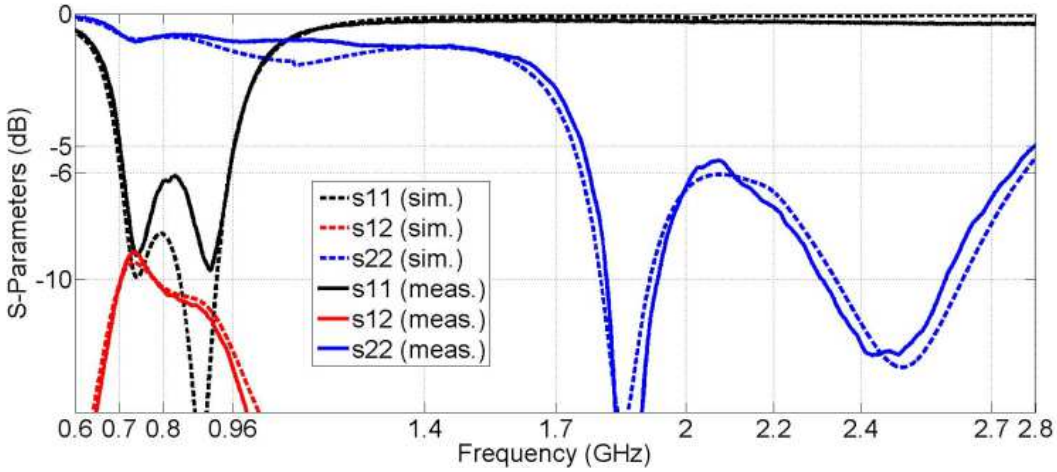

Figure 73 Simulated and Measured S-parameters of the Hollow CE Antenna

To investigate the role of the LB CE for the HB performance, the HB antenna was also simulated alone and with the CE. Figure 74 presents the simulated input impedance of the HB antenna (plotted between 1.7-2.7GHz) in these two cases. It is obvious that the wideband HB response is not due to the HB antenna alone. As can be seen from the input impedance shown in smith chart, an additional resonance in the HB is created by the coupling from the HB antenna to the LB CE. This coupling does not induce an isolation problem since the MN of the LB antenna is designed on purpose to provide a stop-band behavior from 1.7 to 2.7GHz. Proof is given in Figure 75, where the current distribution on the LB CE created by the HB antenna is observed at different frequencies. At 2GHz, it is seen that the currents on the HB antenna are weaker and the currents on the LB CE are stronger which suggests a high level of coupling. However, the current induced on the LB CE are shorted to the ground plane through the first shunt inductor (7.2nH) of the MN. In this way, the port-to-port isolation is kept high. If the currents at 2.3GHz are observed, it is seen that the HB antenna is strongly excited whereas the coupling to the LB CE is weaker.

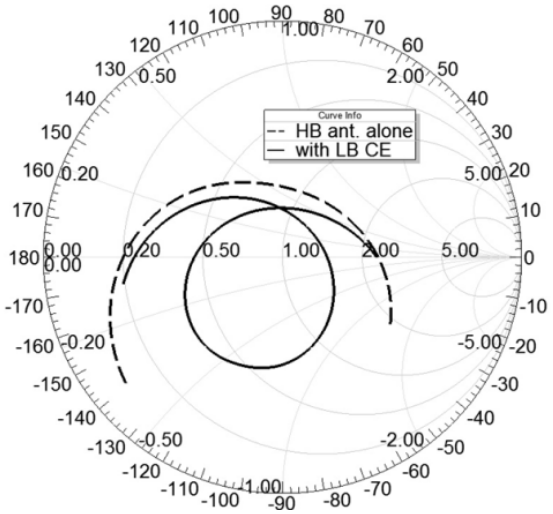

Figure 74 Simulated Input Impedance of the HB antenna alone and with the LB CE

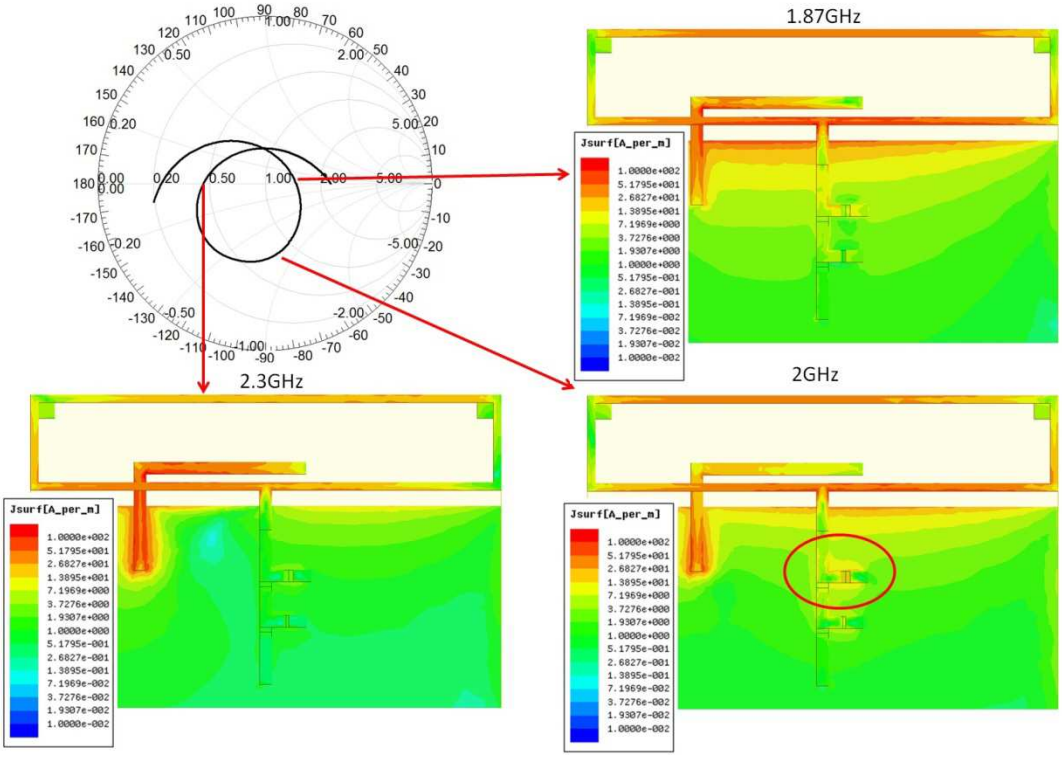

Figure 75 Current Distribution on the LB CE when the HB Port is Excited

1.2.1. Measurement Results

The proposed antenna was manufactured on FR4 substrate (Figure 76). As seen in Figure 73 and Figure 77, there is a fair agreement between simulated and measured S-parameters. The small differences between simulation and measurement are coming from the manufacturing tolerances in the 3D CE section and its orientation. The target bands are covered with a reflection coefficient below -6dB.

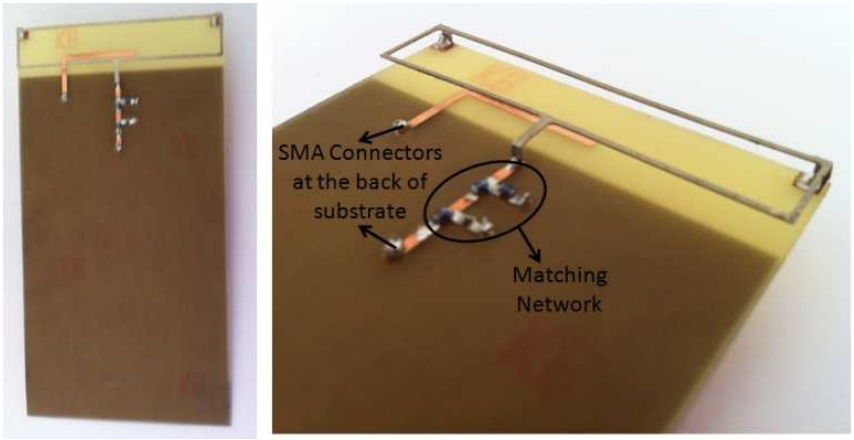

Figure 76 Manufactured Prototype of the Hollow CE Antenna

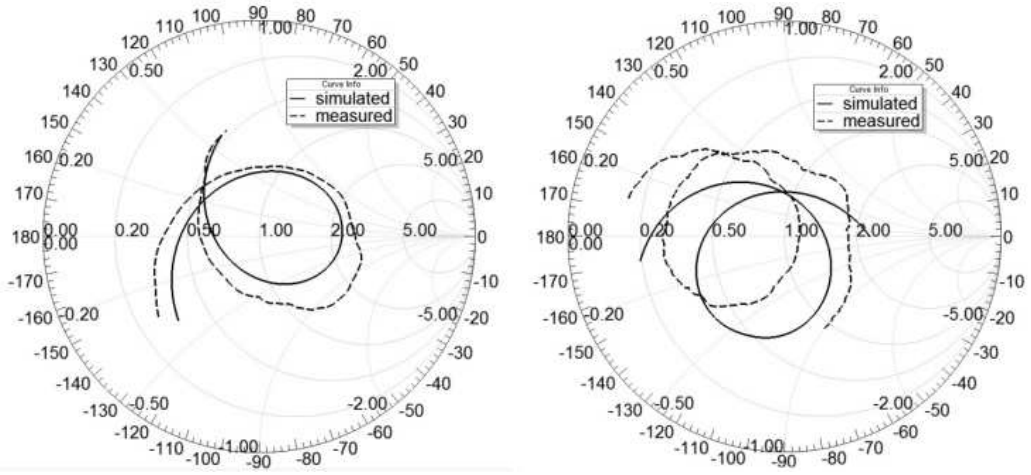

Figure 77 Simulated and Measured Input Impedance of the Hollow CE Antenna (LB on left, HB on right)

The total efficiency and the 3D gain patterns have also been measured in a Satimo Starlab Station. The total efficiency of the proposed antenna in LB and HB are presented in Figure 78 (the HB port is loaded by 50Ω when the LB efficiency is measured and vice versa). The measured total efficiency (including mismatch and component losses) in LB varies between -6dB and -2dB and between -4dB and -1dB in HB. When the simulated and measured 3D gain patterns are compared, a fair agreement is observed (Figure 79). In LB, a dipole-like radiation is observed (as expected) as the main radiator is the currents induced on the ground plane by the CE. Both in LB and HB, no wide-angle deep nulls are seen in the radiation patterns which is an important aspect for mobile phone communications where the base-station orientation is never known in advance.

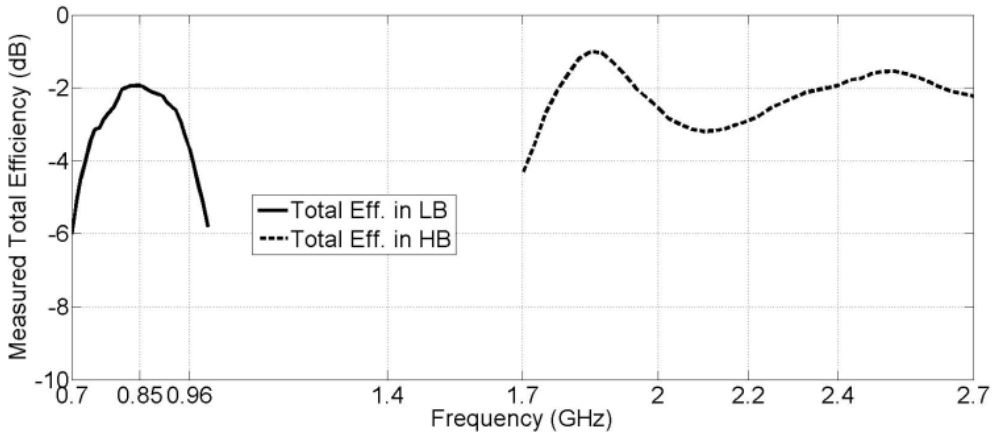

Figure 78 Measured Total Efficiency of the Hollow CE Antenna

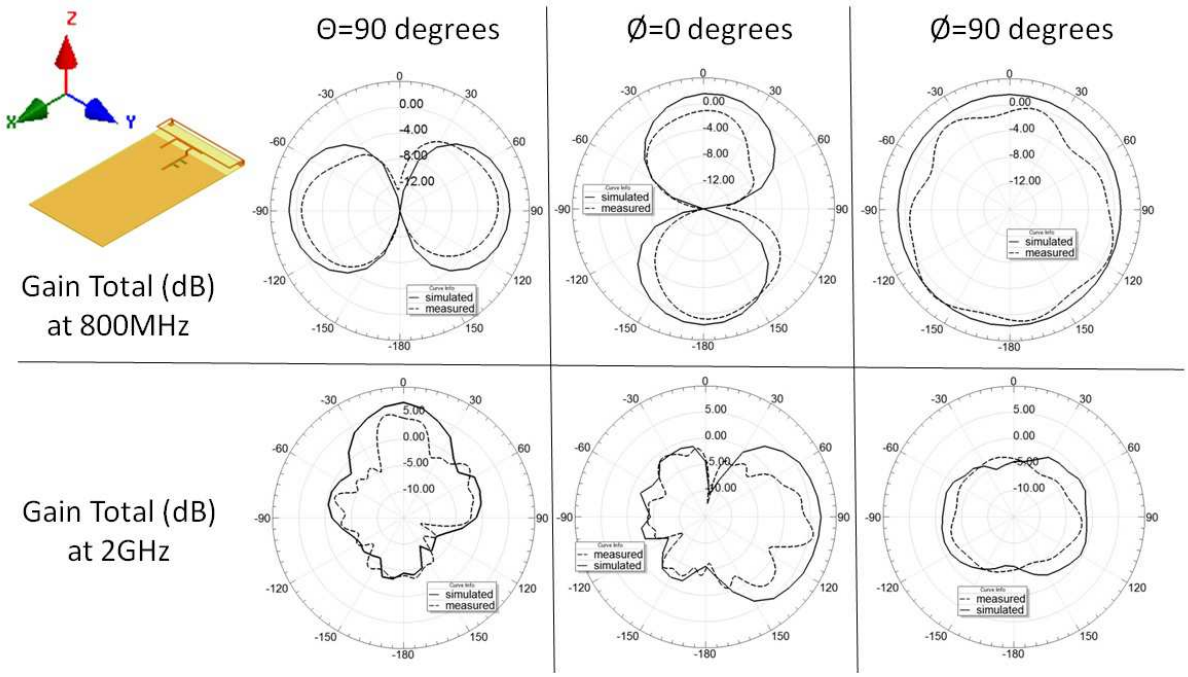

Figure 79 Simulated and Measured Total Gain Patterns for Different Cut Planes

1.3. PRINTED COUPLING ELEMENT ANTENNA

1.3.1. Antenna Design

The dual-feed antenna approach presented in Section 1.1 for a 3mm height 3D hollow CE was then enhanced to design an antenna-structure totally printed on the FR4 substrate for the ease of manufacturing and low cost purpose. The main difference with the previous antenna structure is the location of the printed HB antenna on the FR4 substrate. Since it was not possible to integrate the HB antenna inside the printed CE, it was placed on the left side of the PCB where the E-fields were found to be the weakest in simulations. The PCB and ground plane dimensions were set the same as the previous antenna structure (Figure 80). The dimensions of the hollow CE were set as 59×4mm2 with a strip width of 1mm. Moreover, a two-component MN was found to be necessary at the HB antenna port.

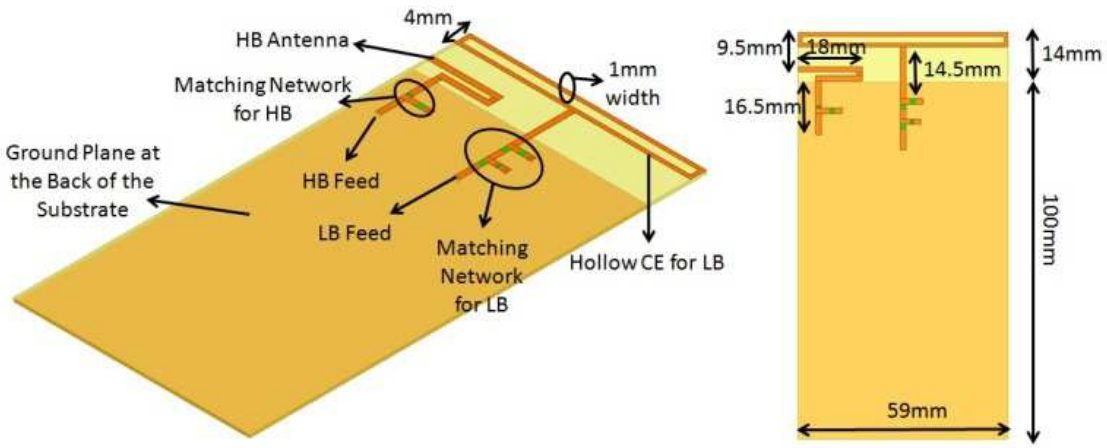

Figure 80 Simulation Model of the Printed CE Antenna

The effect of hollowing the printed CE instead of using a printed plain CE was investigated (Figure 81). Figure 82 shows a comparison of the bandwidth potential for the plain and hollow printed CEs, with the same dimensions. It was seen that making the CE hollow enables to cover an extra 25MHz around the center of the target LB. This is mainly due to the ring shape (loop) of the hollow CE which provides an inductive effect on its input impedance.

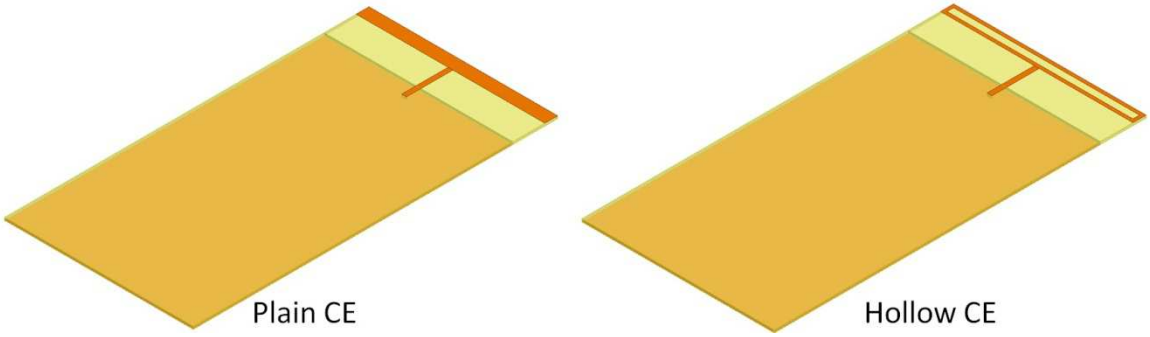

Figure 81 Plain and Hollow CE Geometries Used for Comparison

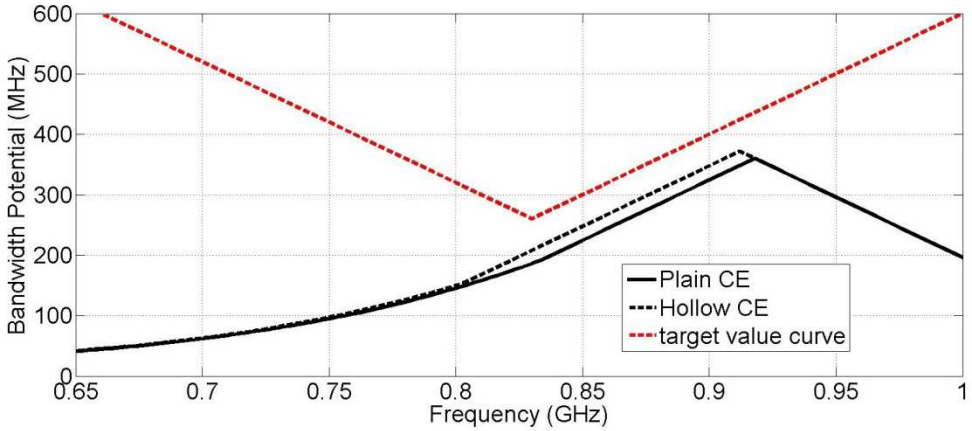

Figure 82 Comparison of Bandwidth Potentials for Plain and Hollow Printed CE

As seen in Figure 83, the real part of the impedance increases and the magnitude of the imaginary part decreases when the CE is made hollow. The e-field distribution between the hollow CE and the ground plane at 750MHz is plotted in Figure 84. The fields are the strongest close to the corners of the hollow CE and decreases as we move away from the CE.

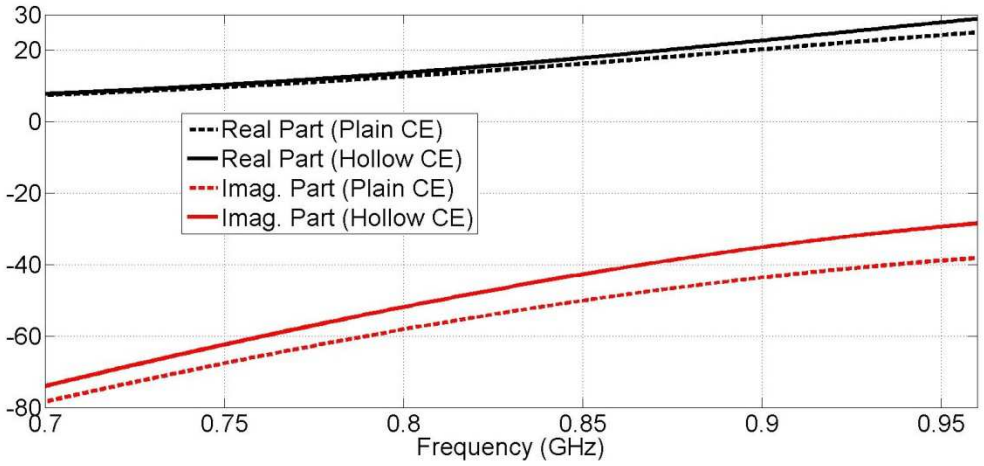

Figure 83 Comparison of Input Impedance for Plain and Hollow Printed CE

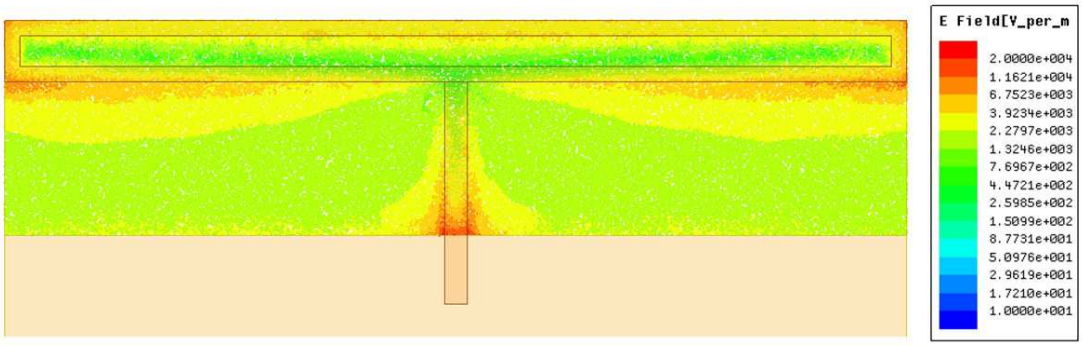

Figure 84 E-Field Distribution at 750MHz for Hollow Printed CE

The MNs for both LB and HB antenna ports were designed with Optenni Lab software (Figure 85). For the optimization of the LB antenna MN, it was intended to have a low reflection coefficient in the LB and a band-stop behavior in the HB. The same goals have been evaluated for the HB, having a stop-band in the LB. The component values were then fine-tuned with the full-wave electromagnetic simulator taking into account the linking transmission lines and vias.

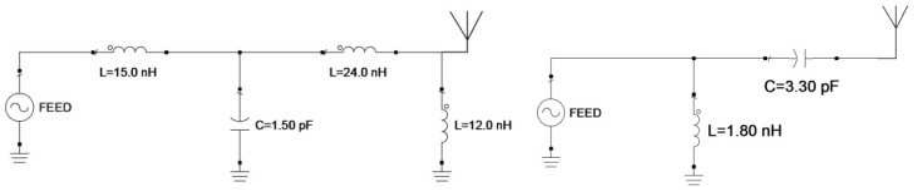

Figure 85 MN Topologies for the Printed CE Antenna (LB on left, HB on right)

The simulated input impedance of the printed CE alone can be seen in Figure 86 with and without the MN. The simulated S-parameters for the whole structure including the HB antenna can be observed in Figure 87. The target frequency bands are covered with a reflection coefficient below -6dB except the frequency interval between 700 and 720MHz. The achieved isolation level is higher than 23dB through both bands which is a consequence of both the antenna placement and the band-stop behavior of the two MN's.

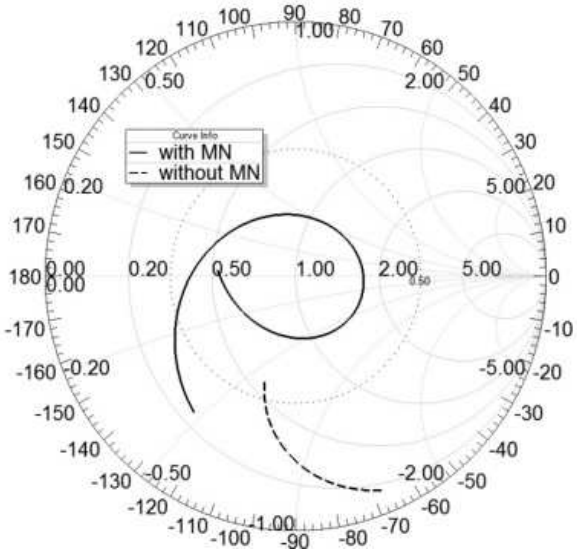

Figure 86 Simulated Input Impedance of the Printed CE Alone (with and without MN)

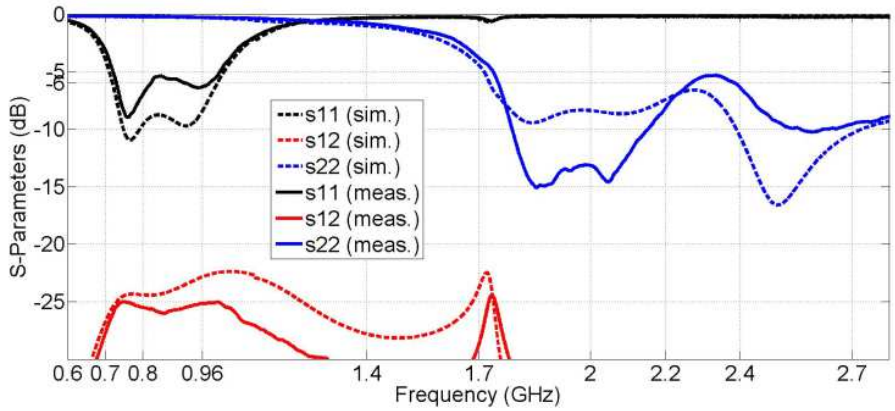

Figure 87 Simulated and Measured S-parameters of the Printed CE Antenna

To explain the wideband behavior of the HB antenna, its input impedance is plotted alone and also when the printed CE is introduced (Figure 88). Additional resonances are created from the coupling between this HB antenna and the LB CE. For instance, the HB antenna is strongly excited at 1.8GHz (Figure 89) whereas at 2.5GHz, the excitation is lower with a stronger coupling with the LB CE. Although there exists some coupling between both antennas at different frequencies, a high isolation is still maintained with the help of the band-stop characteristics of the MNs.

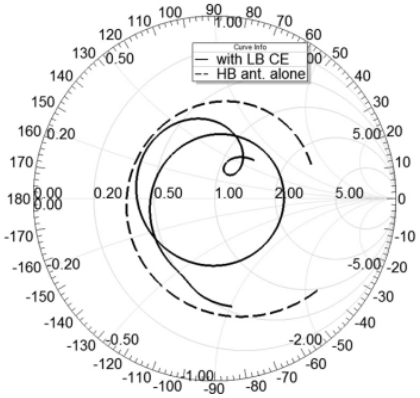

Figure 88 Simulated Input Impedance of the HB antenna alone and with the Printed CE

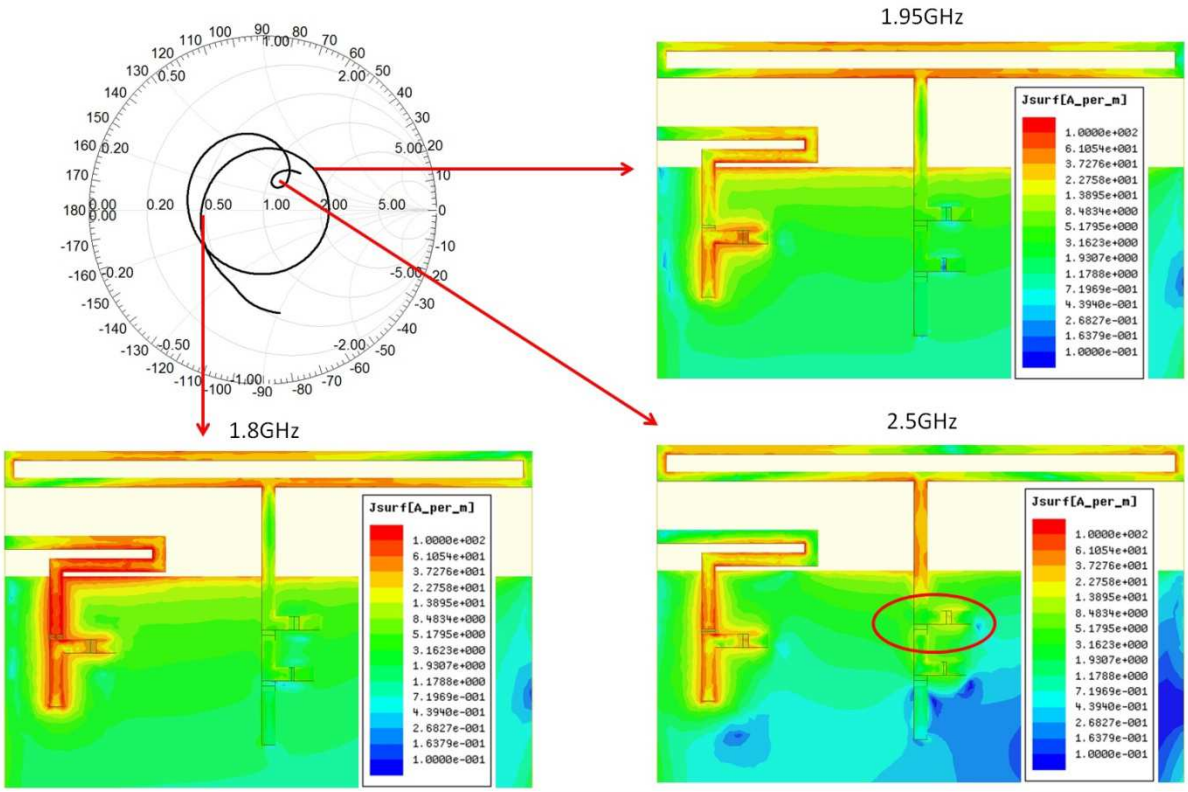

Figure 89 Current Distribution on the Printed CE when the HB Port is Excited

1.3.2. Measurement Results

The printed antenna structure has been manufactured on FR4 substrate as seen in Figure 90. The comparison of the simulated and measured S-parameters can be seen in Figure 87 and on smith chart in Figure 91. There is a fair agreement between the simulated and measured results. The proposed printed antenna can cover the target bands with a measured reflection coefficient below -6dB except the frequency interval of 700-720MHz and also a small overshoot up to -5.5dB around 850MHz.

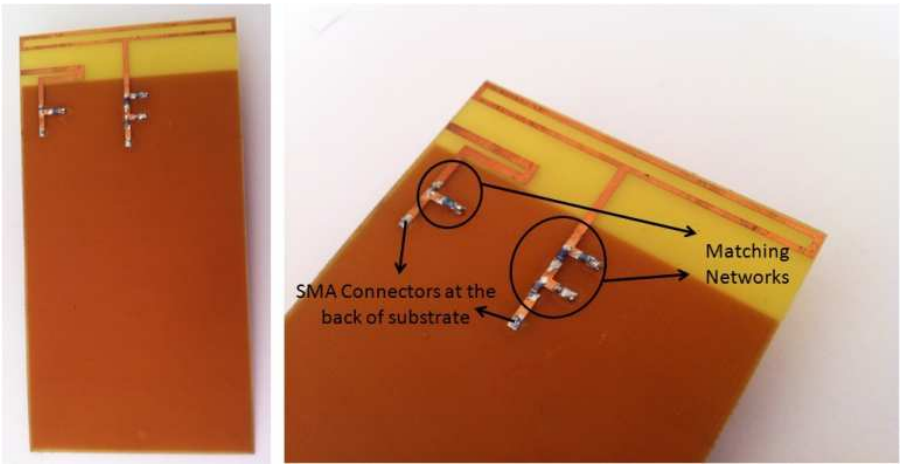

Figure 90 Manufactured Prototype of the Printed CE Antenna

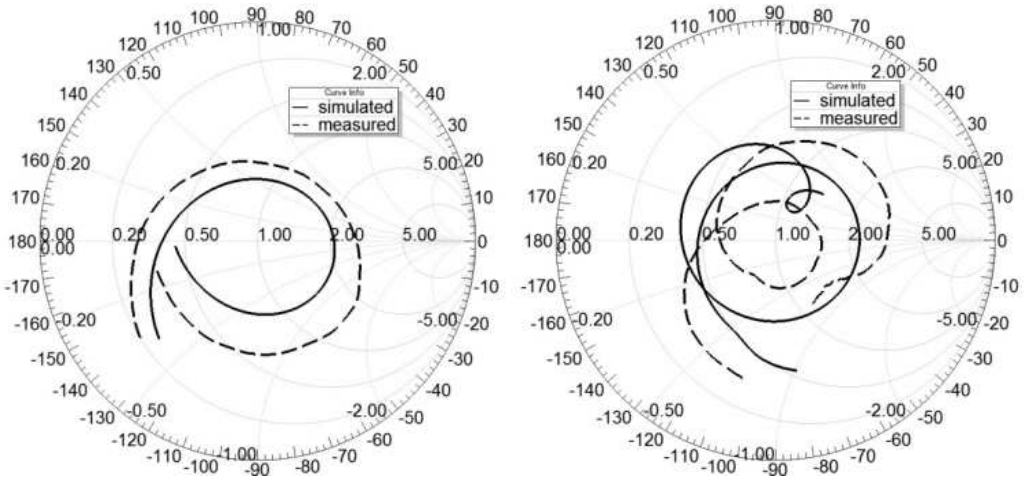

Figure 91 Simulated and Measured Input Impedance of the Printed CE Antenna (LB on left, HB on right)

The total efficiency was measured to vary from -5dB to -1.5dB in the LB and from -4dB to -1.2dB in the HB. The simulated and measured 3D gain radiation patterns are also in good agreement as seen in Figure 93.

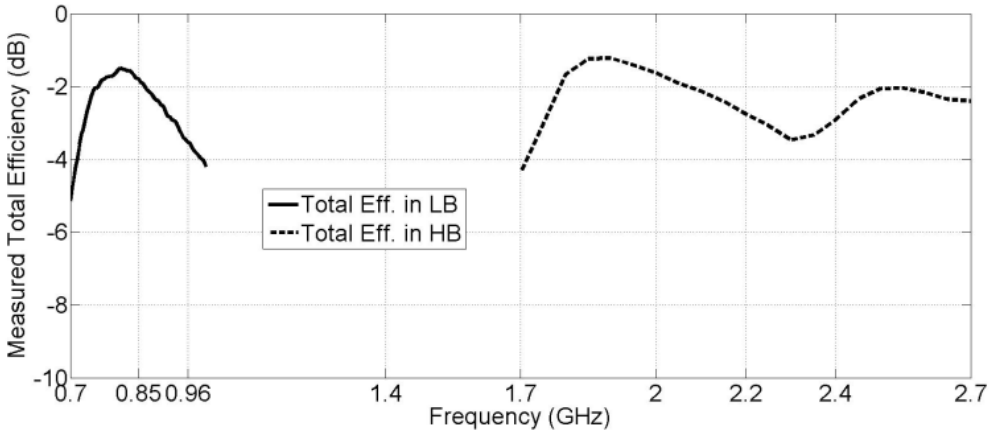

Figure 92 Measured Total Efficiency of the Printed CE Antenna

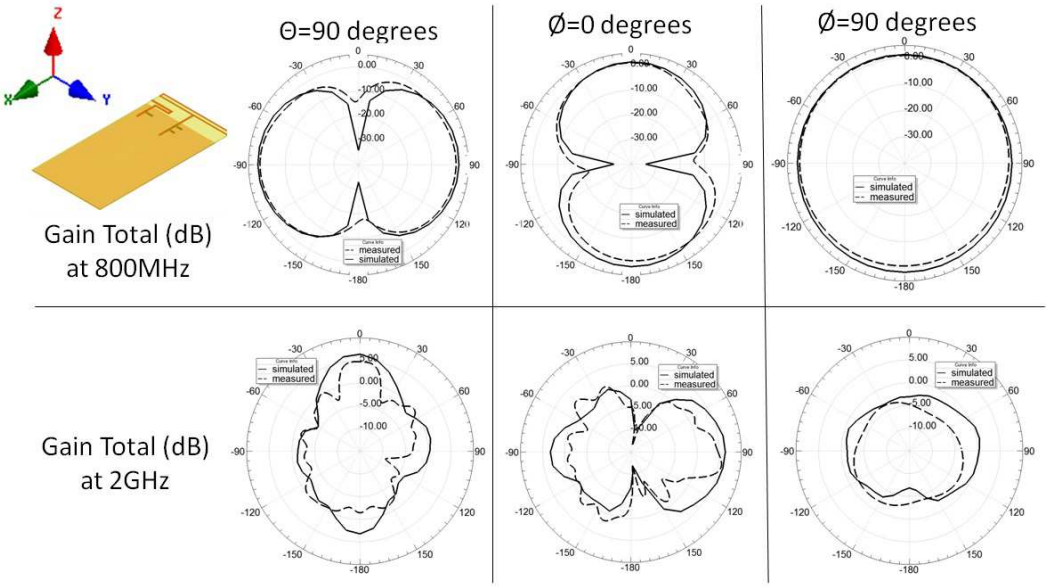

Figure 93 Simulated and Measured Total Gain Patterns for Different Cut Planes

2. TWO-ELEMENT MIMO ANTENNA USING HOLLOW COUPLING ELEMENTS

The newly proposed hollow CE was evaluated in a dual-MIMO antenna scenario as an application example. The target frequency band is 700-960MHz (for a reflection coefficient below -6dB) for both antenna structures. It is aimed to have an isolation better than 10dB between the feeds and an ECC (envelope correlation coefficient) lower than 0.5. Similar studies have been done like in [3-5] to achieve MIMO operation in mobile terminals. In [3], two meandered monopoles were placed on the short edge of a mobile terminal PCB with a hybrid coupler at the feeds to improve isolation. With this antenna, good matching bandwidth and good isolation was achieved only in a very limited bandwidth (between 705-725MHz). A similar structure having two meandered monopoles is also presented in [4], using a suspended line to increase isolation. This antenna is also narrowband, with MIMO operation only in LTE band-13 (746-787MHz). In [5], first an active antenna structure is proposed to cover 700-960MHz with four different states and then the MIMO performance is investigated with combinations of active-passive antennas.

As widely known, it is a challenging problem to obtain a MIMO antenna with low ECC (envelope correlation coefficient) and high isolation for a typical mobile terminal in whole LB (700-960MHz), where the antenna is electrically small and most of the radiation comes from the excitation of the ground plane. Due to this fact, it is hard to obtain a high level of isolation between the two antenna feeds. Although a good isolation in terms of S_{21} is obtained, it is not sufficient to get an acceptable Envelope Correlation Coefficient (ECC) since the radiation patterns should also be different for the two antennas. For this purpose, two identical hollow CEs were placed on the two corners of the short edge of the PCB as in [6]. In this way, a good ECC from the 3D pattern point of view can be expected. To increase the port-to-port isolation between the two CEs, the neutralization technique, which is explained in [7] was used.

2.1. THE LTE MIMO ANTENNA MODEL

The simulation model of the antenna can be observed in Figure 94. An FR4 substrate of 0.8mm thickness was used as the PCB. The height of the antenna is 4.2mm above the substrate. The CEs on each corner are identical, each with a MN of 4 SMD components at the antenna feeds (Figure 95). To increase the inductive effect of the neutralization line, an inductor of 100nH was used in the middle of this line.

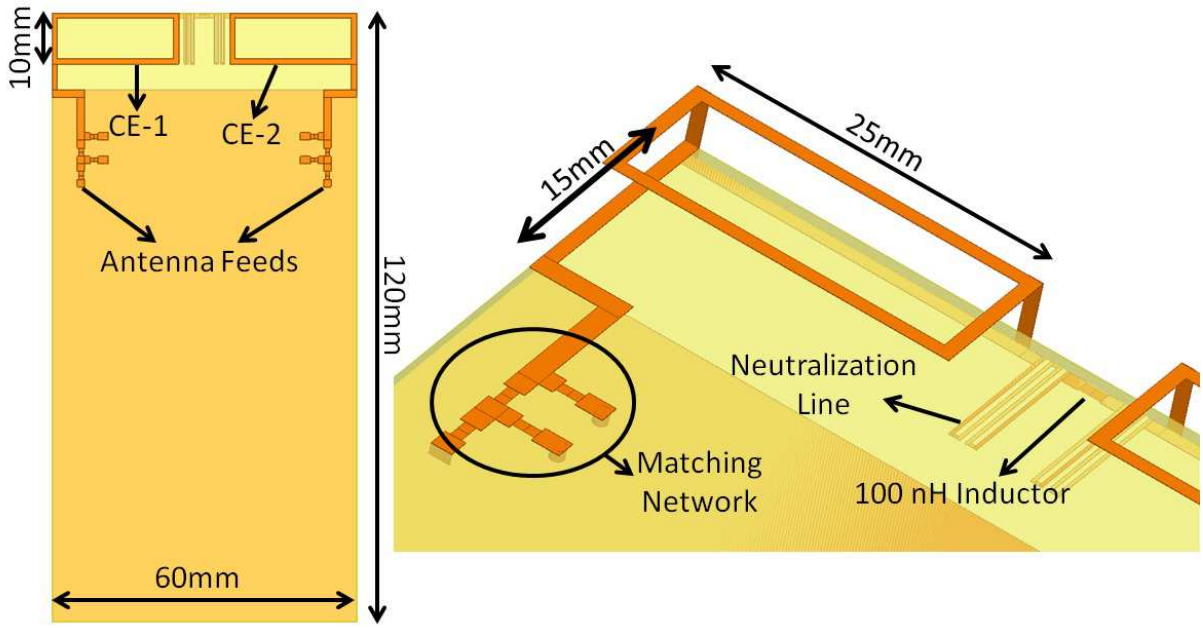

Figure 94 The LTE MIMO Antenna Simulation Model

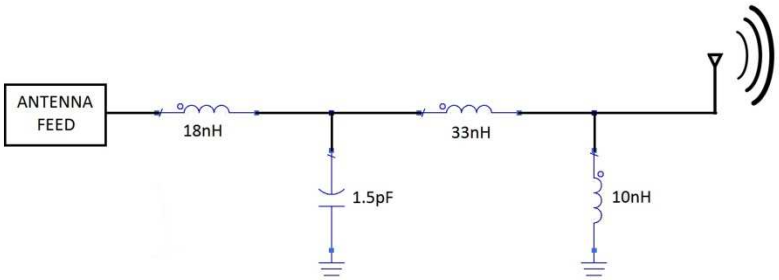

Figure 95 The MN for LTE MIMO CEs

To illustrate the effect of the MN on the input impedance, simulation results have been plotted in Figure 96, between 700-960MHz. As shown with the red curve, the single CE is far from being matched without the MN. The MN (optimized using Optenni Lab software), creates an optimally overcoupled response to obtain the highest possible matching bandwidth.

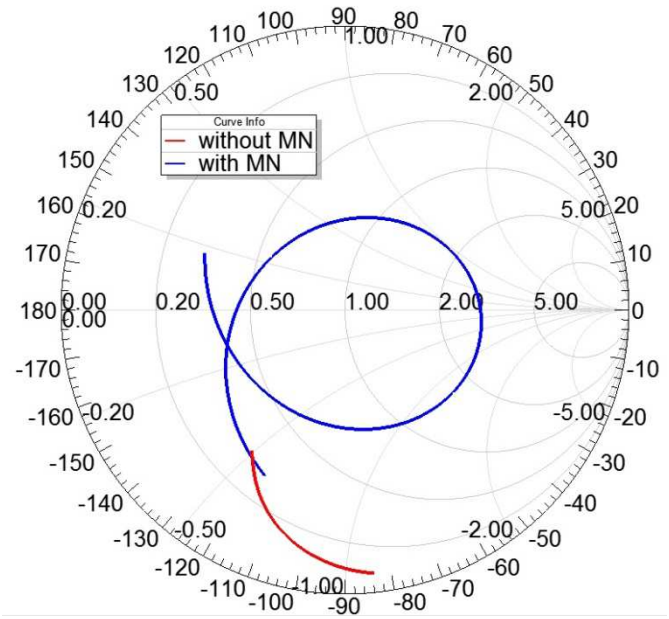

Figure 96 Input Impedance of a Single CE with/without MN

Figure 97 presents the currents on the ground plane when a single CE is placed on top left corner of the PCB. It can be seen that the main direction of current flow on the ground plane is through the long edge of the ground plane, continuing the short edge and having the lowest value close to the corner. The currents flowing on the short edge introduce an offset in the radiation pattern as seen in Figure 98 (at 800MHz). The pattern is different from regular patterns in the sense that it is slightly rotated through the diagonal direction of the PCB, which is an interesting feature to obtain a reasonable ECC value when the second CE is added.

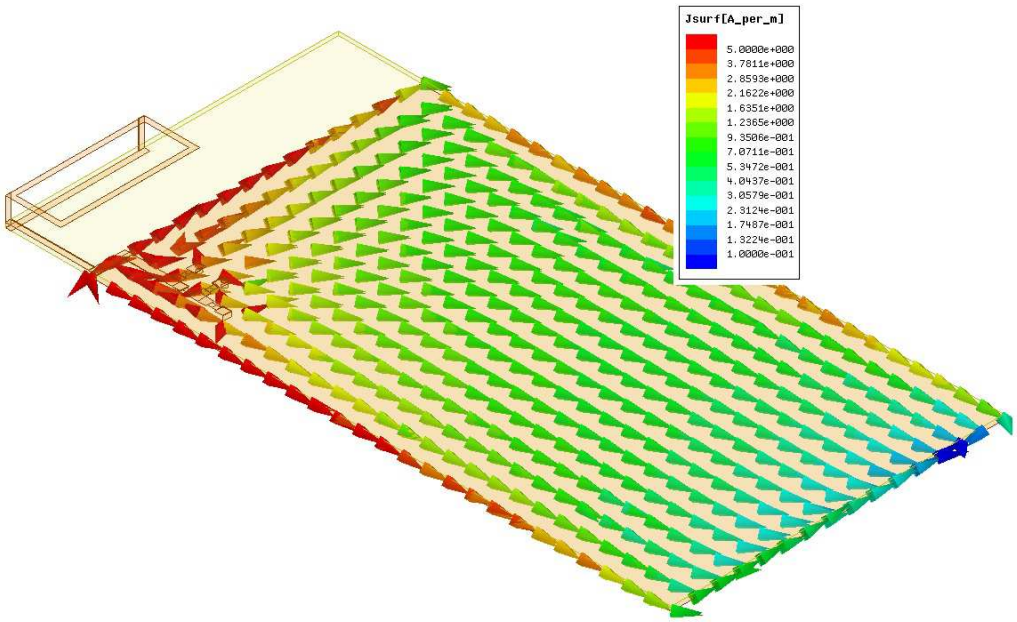

Figure 97 Current Distribution on the Ground Plane of a Single CE with MN

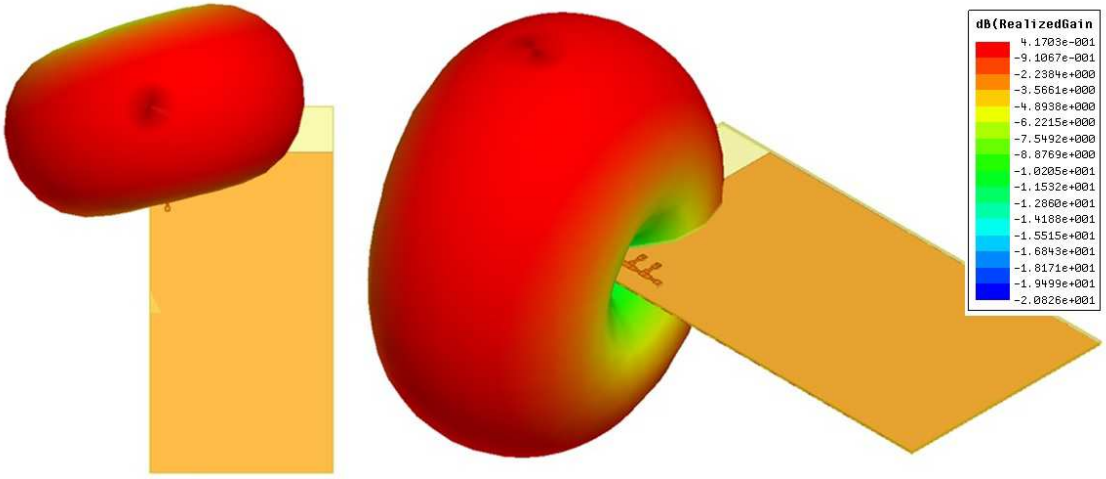

Figure 98 3D Radiation Pattern of a Single CE placed at the Top Left Side of the PCB

Another very important point for this antenna is the neutralization line added between the two CEs, connecting them inductively to increase the isolation between their feeds. The main idea behind this technique is to create an additional inductive path (to the existing capacitive coupling path). In this way, the currents between the two antennas are forced to flow somewhere else than the non-excited feed. Detailed description of the methodology is not given here for the sake of brevity. The antenna (consisting of both CEs on each corner with MNs) was simulated both with and without the neutralization line and the results are presented in Figure 99. The isolation is poor in the absence of the neutralization, falling down to 4.5dB around 720MHz. After the neutralization line is introduced, a significant improvement is seen in the isolation, being better than 10.2dB through the target band (30% bandwidth). The simulated reflection coefficient for the CEs (with MNs) is below -6dB between 740-940MHz.

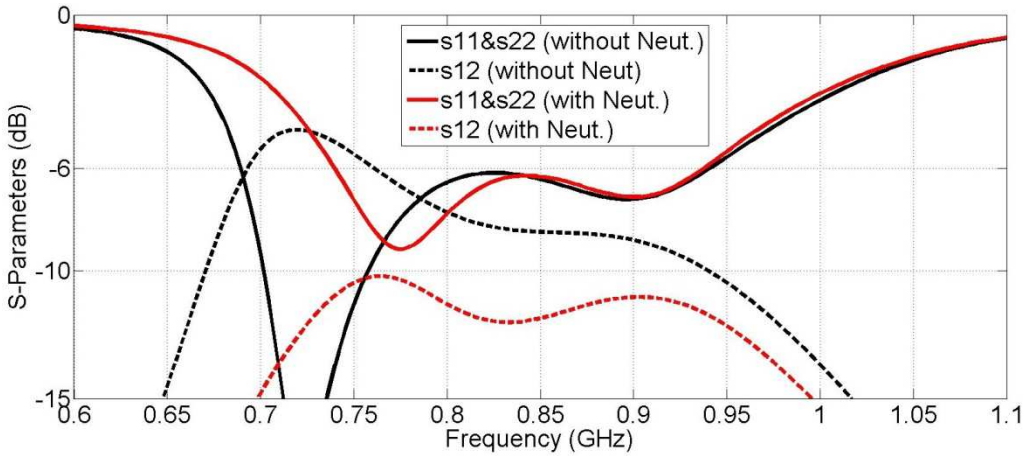

Figure 99 Effect of the Neutralization Line on Simulated S-Parameters

The simulated 3D radiation patterns for the whole antenna system (at 800MHz) can be observed in Figure 100, where the pattern for CE-1 is plotted when the other port is matched and vice versa. The rotated dipole type patterns, symmetrical along the longitudinal axis, for the two CEs verify the particular excitation of the ground plane. It produces pattern diversity which is of particular interest for low ECC.

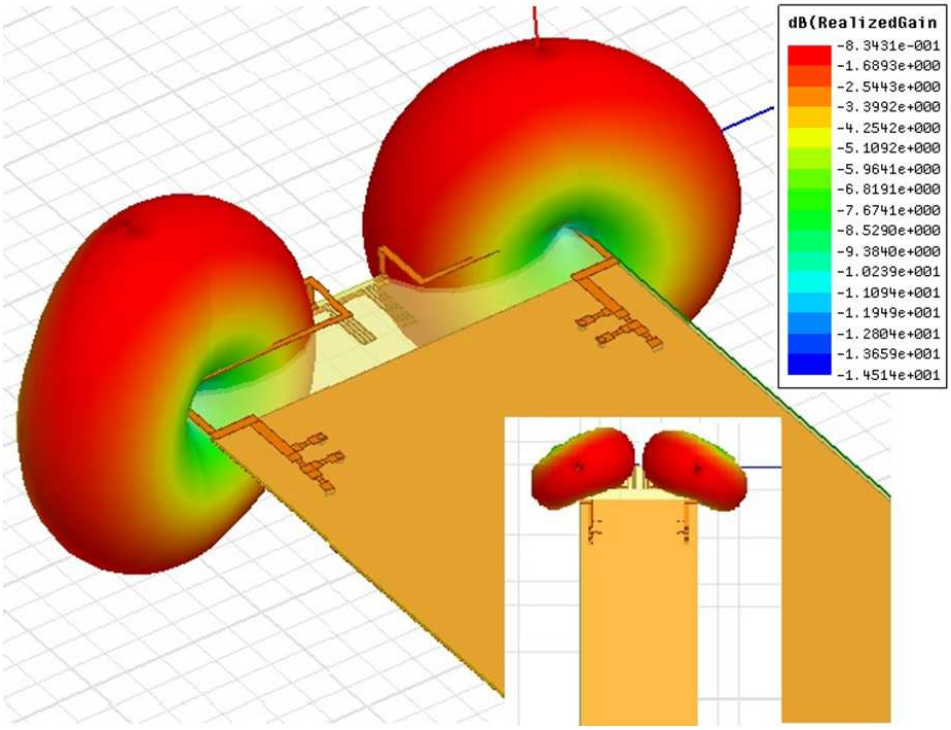

Figure 100 3D Radiation Pattern of Dual CE Antenna

2.2. MEASUREMENT RESULTS OF THE LTE MIMO ANTENNA

The proposed antenna has been manufactured on FR4 substrate (Figure 101). The S-parameter measurements have been performed, whose results are presented in Figure 102. A fair agreement can be observed between simulation and measurements. The frequency region between 740-950MHz can be covered with a reflection coefficient below -6dB and the isolation between the two ports is always higher than 11dB in the measurements. From the best knowledge of the authors, this isolation level was not achieved over such a broad band for LTE mobile phones.

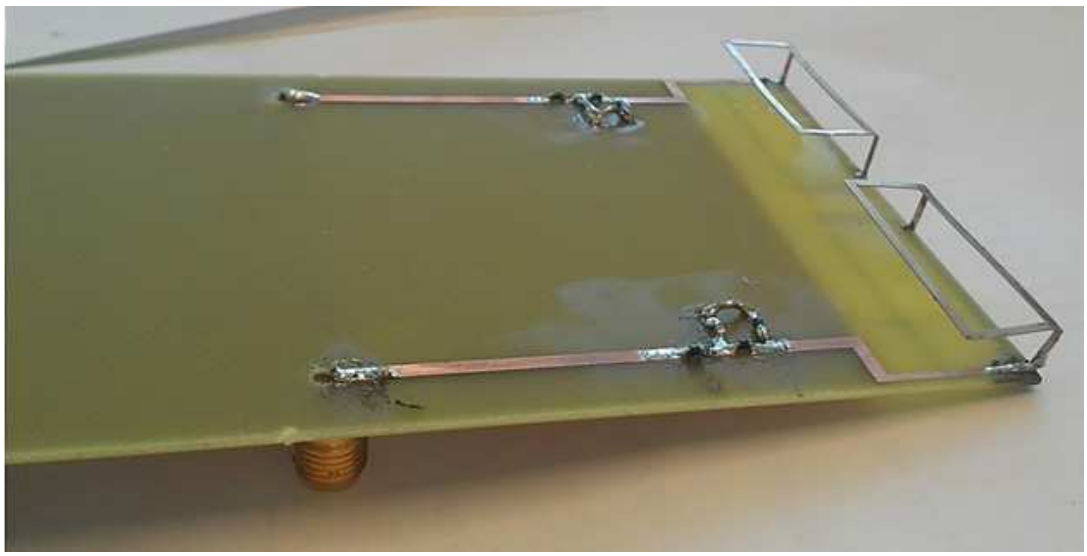

Figure 101 Manufactured MIMO Antenna Prototype

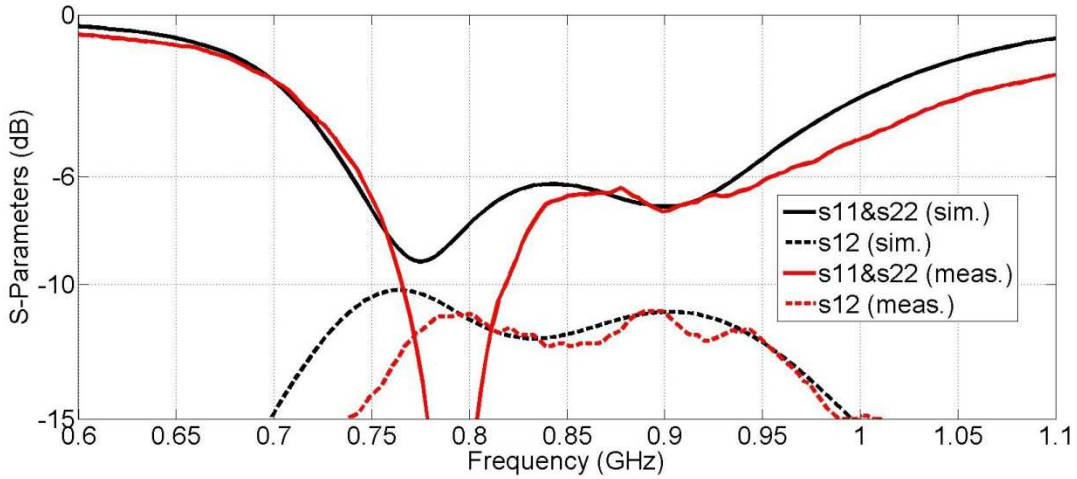

Figure 102 Simulated and Measured S-Parameters of the MIMO Antenna

The total efficiency of the MIMO antenna system was measured in a Satimo Starlab station, where the unmeasured antenna port is terminated with a matched load. The two CEs give similar performance in terms of efficiency so the result of only one CE is presented in Figure 103. The antenna has a measured total efficiency between -6dB and -4dB in the coverage band.

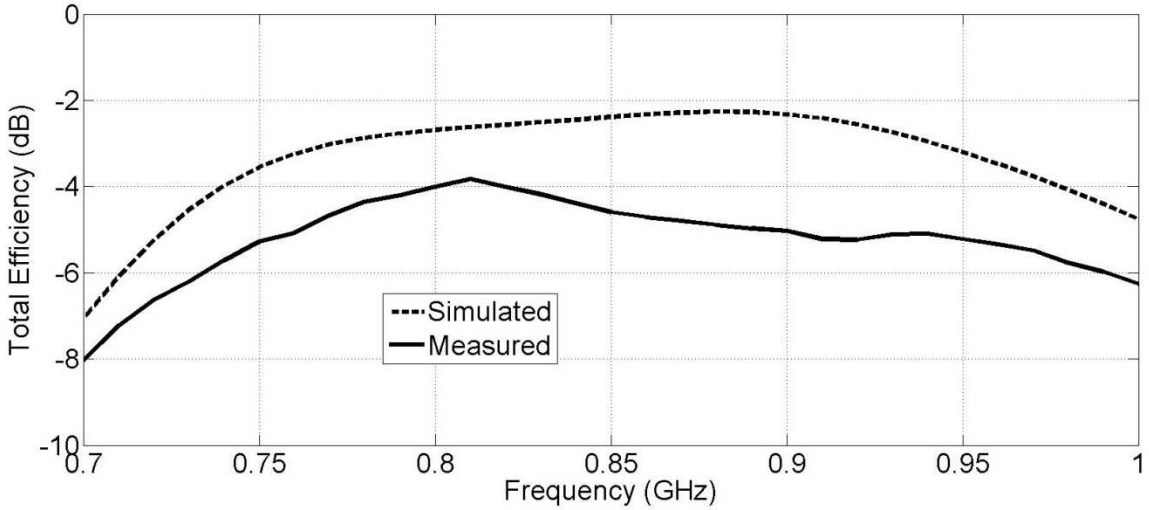

Figure 103 Simulated and Measured Total Efficiency of the MIMO Antenna

As widely known, there are two formulas used for the calculation of the envelope correlation coefficient of MIMO antenna systems. The first one presented in equation-1 uses the S-parameters of the two antennas whereas the second one (equation-2) uses the 3D complex radiation pattern. Although much simpler to calculate, Equation-1 is not suitable in this study since it may give misleading results due to the lossy antennas. For this reason, equation-2 (for an isotropic propagation environment) was used to calculate the ECC.

$$\rho_e = \frac{|s_{11}^{*}.s_{12}+s_{21}^{*}.s_{22}|^2}{(1-|s_{11}|^2-|s_{21}|^2)(1-|s_{22}|^2-|s_{12}|^2)} \qquad \text{Equation-1}$$

$$\rho_e = \frac{\left|\iint_{4\pi} F_1(\theta,\phi)^*.F_2(\theta,\phi)d\Omega\right|^2}{\left(\iint_{4\pi}|F_1(\theta,\phi)|^2 d\Omega\right).\left(\iint_{4\pi}|F_2(\theta,\phi)|^2 d\Omega\right)}$$ Equation-2

The comparison of the simulated and measured ECC using the radiation patterns is given in Figure 104. The agreement between simulation and measurement (complex radiation patterns have been recorded with the SATIMO station) seems very good. The measured ECC turned out to be below 0.5 (a generally accepted value for mobile terminals) between 765MHz and 950MHz which contains most of the coverage band. The MIMO antenna system is suitable for MIMO applications in mobile terminals, keeping in mind that other metrics like diversity gain and mean effective gain should also be measured.

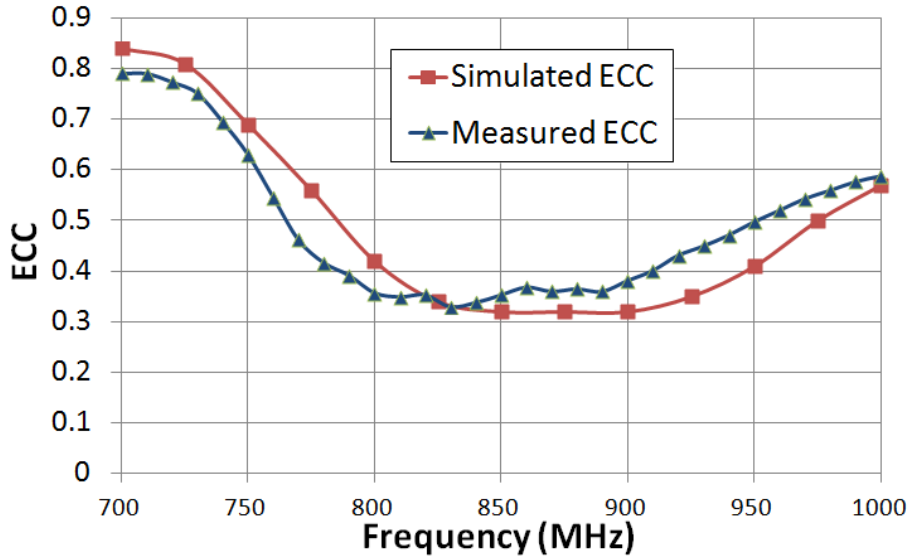

Figure 104 Simulated and Measured ECC of the MIMO Antenna

3. CONCLUSION

A novel approach using CEs for 700-960MHz and 1.7-2.7GHz coverage in mobile terminals was presented in this chapter. The approach consists of making the plain CE hollow by removing the metal plate inside and leaving a metal strip of around 1mm. In this way, a space efficient layout is obtained with weaker E-fields inside the hollow region. This space is then used for inserting a HB antenna separately fed with a high isolation between the feeds. A comparison between plain CE and hollow CE was first presented showing the negligible difference in terms of bandwidth potential performance.

The approach was then evaluated with a CE of 3mm height to cover the 700-960MHz frequency band. A monopole antenna was inserted inside this hollow CE on the substrate and it was shown that the whole target band can be covered with this dual feed structure. Another antenna was proposed in section 1.3, using again a dual-feed topology but this time the CE was also printed directly on the substrate.

Finally, in section 2, the CE idea was applied to obtain MIMO performance in the LB, using two CEs situated on the two corners of the PCB. With this layout, specific currents of the ground plane were excited for both CEs, enabling a level of default isolation. To further improve the isolation, the

neutralization line technique was applied to the CEs. The S-parameter and ECC measurements were performed and presented for the MIMO antenna.

It was shown in this chapter that it is possible to obtain the coverage of 4G communication standards in a mobile terminal with coupling element antennas. The disadvantage of the prototypes presented here can be the 3D structure without any supporting materials. This might lead to some manufacturing errors in different prototypes of the same antenna, due to tolerances. For this reason, antenna structures with a different manufacturing technology will be addressed in the next chapter, which will be capable of supporting 3D shapes for antennas.

REFERENCES FOR THIS CHAPTER

[1] A. Cihangir, F. Sonnerat, F. Ferrero, C. Luxey, R. Pilard, F. Gianesello, G. Jacquemod, “Design of Traditional and a Novel Space-Efficient Antenna-Coupling Elements for Lower LTE/GSM Mobile Phones,” Loughborough Antennas and Propagation Conference 2012 (LAPC 2012), Loughborough, UK, November 2012.

[2] A. Cihangir, F. Ferrero, C. Luxey, G. Jacquemod, “A space-efficient coupling element antenna for WWAN applications,” International Workshop on Antenna Technology (IWAT2013), Karlsruhe, Germany, March 2013.

[3] R.A. Bhatti, S. Yi, S. Park, “Compact Antenna Array With Port Decoupling for LTE-Standardized Mobile Phones,” IEEE Antennas and Wireless Propagation Letters, vol.8, pp. 1430-1433, 2009.

[4] G. Park, M. Kim, T. Yang, J. Byun, A.S. Kim, “The compact quad-band mobile handset antenna for the LTE700 MIMO application,” Antennas and Propagation Society International Symposium, APSURSI '09, June 2009

[5] R. Kuonanoja, “Low correlation handset antenna configuration for LTE MIMO applications,” Antennas and Propagation Society International Symposium (APSURSI), 2010.

[6] S. Zhang, K, Zhao, Z. Ying, S. He, “Diagonal Antenna-Chassis Mode for Wideband LTE MIMO Antenna Arrays in Mobile Handsets”, International Workshop on Antenna Technology (IWAT2013), Karlsruhe, Germany, March 2013.

[7] A. Diallo, C. Luxey, Ph. Le Thuc, R. Staraj, G. Kossiavas, “Enhanced two-antenna structures for UMTS diversity terminals,” IET Microwaves, Antennas and Propagation, vol. 2, no. 1, pp. 93-101, February 2008.

CHAPTER IV
SINGLE FEED ANTENNAS ON LDS TECHNOLOGY

This chapter presents two antenna designs which are realized on plastic material using the Laser Direct Structuring (LDS) technology. Both of these antennas utilize the parasitic strip approach (presented in Chapter II) for bandwidth enhancement. The first antenna to be presented covers the low-LTE and UMTS frequency bands of 700-960MHz and 1.7-2.2GHz, while the second antenna can cover the same bands also including the WLAN2400 and LTE2500 bands (i.e. 700-960MHz and 1.7-2.7GHz in total).

A novel point here is the realization of the antennas using Laser Direct Structuring (LDS) technology which offers more freedom in terms of antenna layout and also enables the utilisation of the available space more efficiently. As also described in [1], this process uses a thermoplastic material which has already been doped with a metal-plastic additive(Figure 105-a). A laser beam then tracks the surface of the material, according to the shape of the traces intended on it(Figure 105-b). In this way, a microscopically rough surface is created, forming the nuclei for the metallization step(Figure 105-c). Finally, the metal traces are formed by putting the laser activated material in the electroless copper baths(Figure 105-d). Using this technology, a high degree of freedom is obtained in terms of the metallization shape.

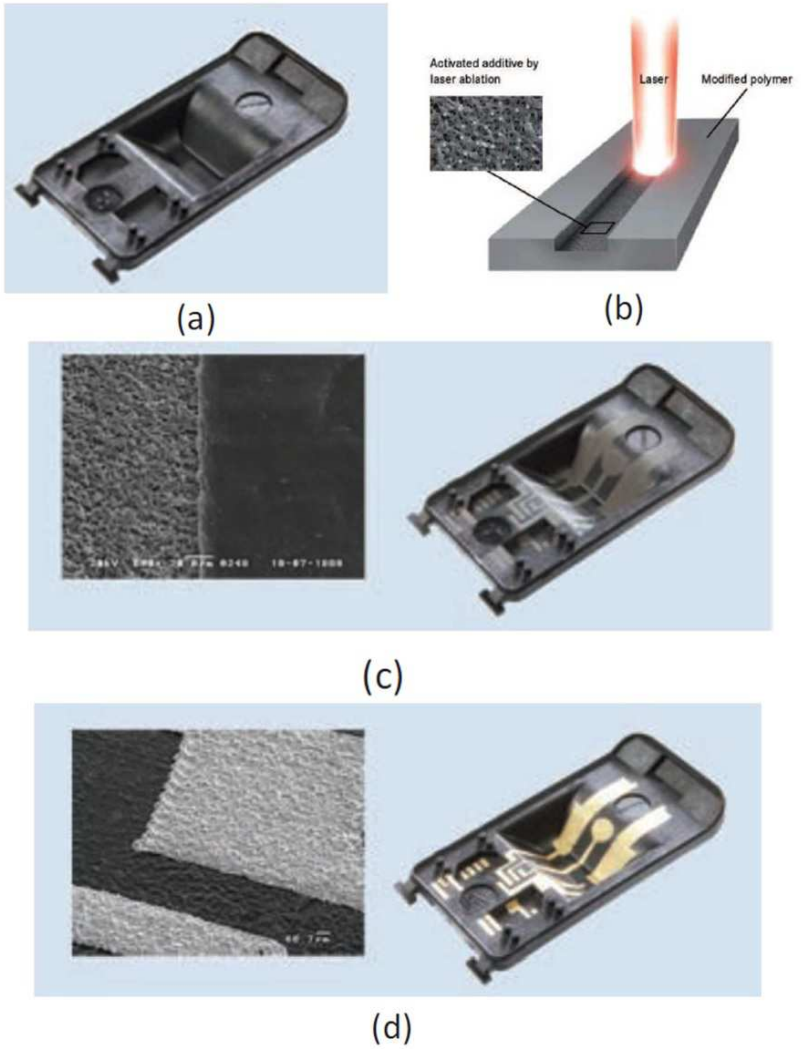

Figure 105 LDS Manufacturing Process

As also mentioned in the Introduction part, many antennas using parasitic elements for LTE/4G frequency bands have been proposed[2-5]. The common property of these antennas is their

relatively complex geometry, which might make the antenna performance sensitive to manufacturing tolerances. Here, the main target is to simplify the geometry of the antenna as much as possible by introducing a matching network having few number (targeted as less than 4) of SMD components.

1. LOW-LTE AND UMTS ANTENNA

1.1. ANTENNA MODEL

The antenna model can be observed in Figure 106. For the plastic piece, DP-T-7140 material [6] was chosen since it is appropriate for reflow soldering, considering the possible usage of lumped components on the plastic piece. This plastic piece is shown in grey colour in Figure 106 and it has a relative permittivity of 4.1 and a loss tangent of 0.0138, given by the manufacturer for 1MHz. The dimensions of the plastic mold are 57mm X 18mm with a height of 5mm. The plastic mold rests on a PCB of FR4 substrate with the dimensions 114mm X 59mm X 0.8mm. There is a ground plane of 75mm X 50mm under the PCB. The main reason of choosing 75mm for the length of the ground plane is to simulate a worst case scenario, where the antenna relies only on the 3.5 inch touch screen of a smart phone, as the ground plane. This is a generic scenario for today's smart phones so the antennas designed are able to be integrated in any smart phone. One point to consider is the additional components (which will have ground connection) in the vicinity of the touch screen so the total ground plane length might be subject to an increase. This increase in the ground plane length will shift its resonance frequency down, enabling easier coverage of the LB. For example, increasing the length of the ground plane from 75mm to 100mm will shift the fundamental wavemode frequency from 1.45GHz to 1.18GHz.

The connection between the metallizations on the plastic mold and the traces on the PCB are achieved by using two pogo pins having 3mm height, under the plastic mold. The antenna basically consists of a driven strip (shown in orange), which capacitively excites a parasitic strip (shown in red) connected to ground on one end. The design methodology when optimizing the final form of the antenna was to tune the length of the parasitic strip, in combination with the driven strip, until obtaining sufficient bandwidth potential for dual-band operation. A meander was introduced to the parasitic element for this reason in the final antenna form. Concerning the input impedance of the antenna, a matching network consisting of four lumped components was decided to be used at the antenna feed.

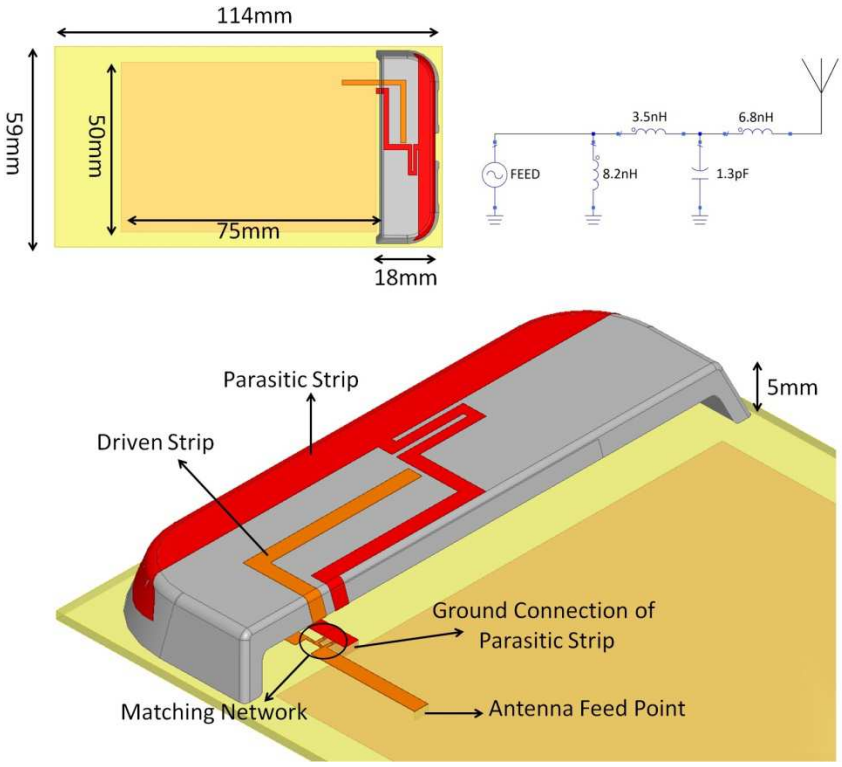

Figure 106 UMTS Antenna Model

To show the effect of the parasitic element on the input impedance of the antenna, simulations were performed in the case of "driven strip only" and "whole structure without MN". These simulation results can be observed in Figure 107, where the LB impedance is plotted between 700-960MHz and HB response plotted between 1.7-2.2GHz. It can be seen from the figure that introducing the parasitic strip creates a resonance in the LB, increasing the real part of the input impedance considerably. This behaviour enables an increase in the bandwidth potential of the antenna especially in the LB (Figure 108).

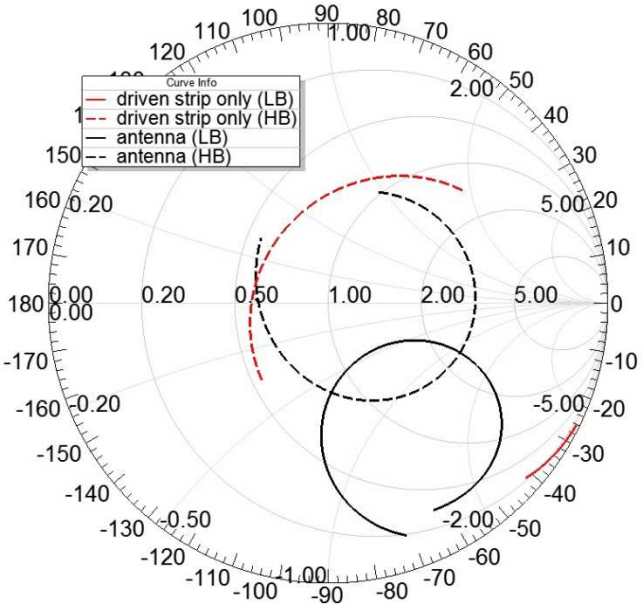

Figure 107 Simulated Input Impedance of the UMTS Antenna, with/without Parasitic Strip

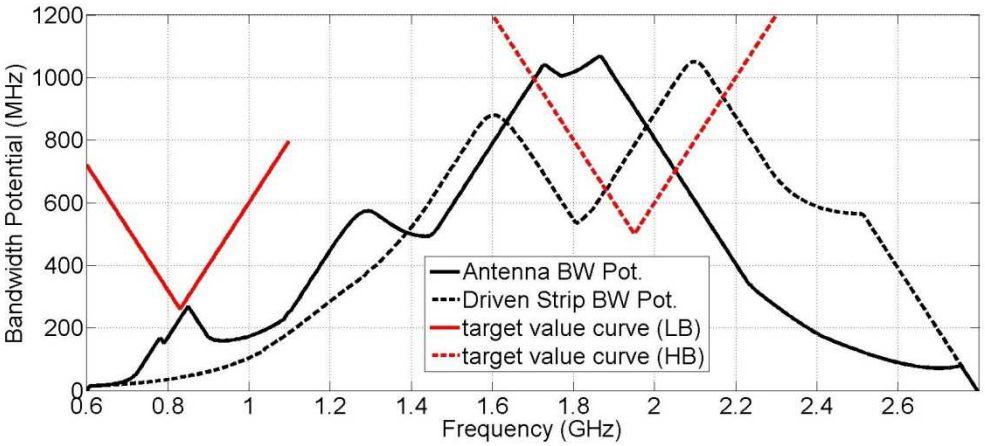

Figure 108 Bandwidth Potential of the UMTS Antenna, with/without Parasitic Strip

The effect of the parasitic element can be also seen looking at the surface current distribution in Figure 109. At 750MHz, a strong excitation of the parasitic element is observed, while its excitation is weaker at 900MHz. It can also be seen that, at both frequencies, the currents on the ground plane are excited almost at the same strength, which enables the exploitation of the low-Q property of the thick ground plane.

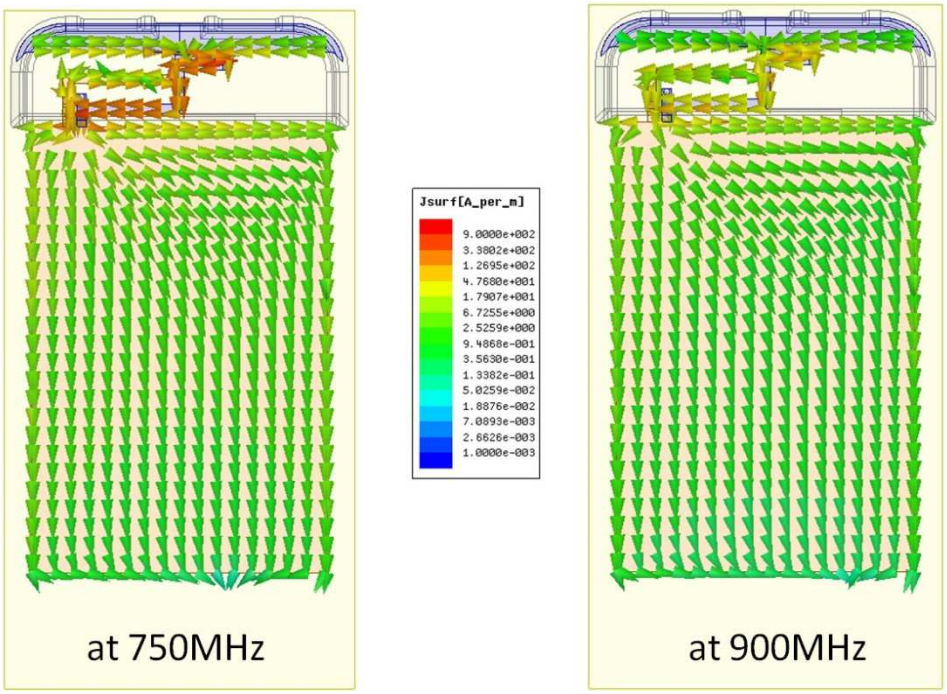

Figure 109 Current Distributions on the UMTS Antenna and Ground Plane

The simulated antenna impedance with and without MN can be observed on smith chart in Figure 110. The corresponding reflection coefficient can also be observed in Figure 111. The antenna can cover the target bands of 700-960MHz and 1.7-2.2GHz, although a small overshoot in reflection coefficient is observed around 780MHz rising up to -5dB (in simulations).

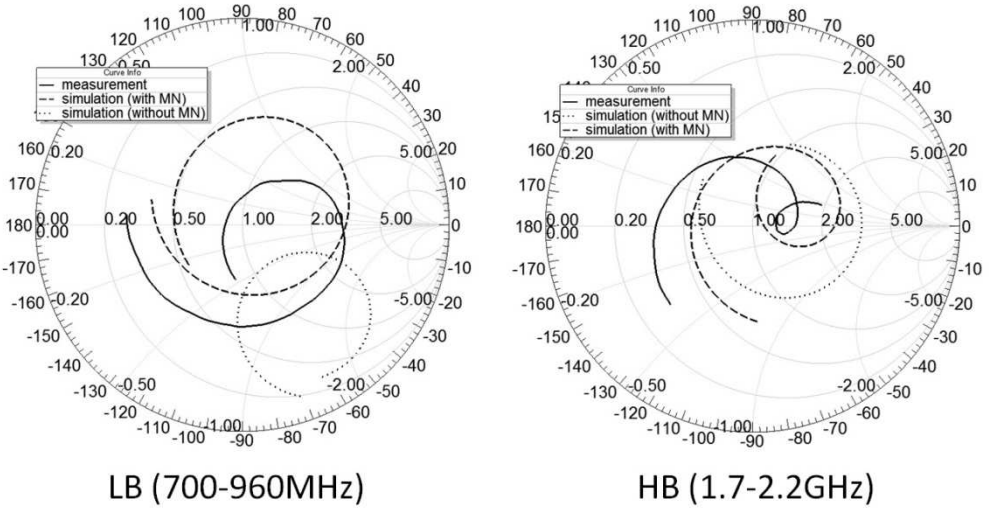

Figure 110 Simulated and Measured Input Impedance for UMTS Antenna, with/without MN

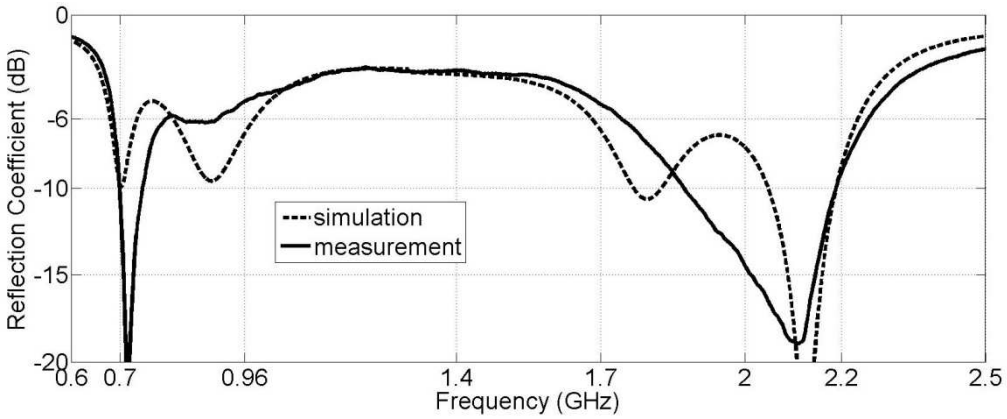

Figure 111 Simulated and Measured Reflection Coefficient for the UMTS Antenna

1.2. MEASUREMENT RESULTS

The manufactured antenna (using LDS technology) can be seen in Figure 112. For the antenna feed, an SMA connector was placed on the PCB as shown in left in Figure 112. To validate the simulation results, s-parameter measurements were performed with the manufactured prototype and are presented in Figure 110 and Figure 111. A fair agreement can be observed between simulated and measured reflection coefficients. The antenna has a measured reflection coefficient below -6dB in the LB and HB with small overshoots around 950MHz and 1.7GHz.

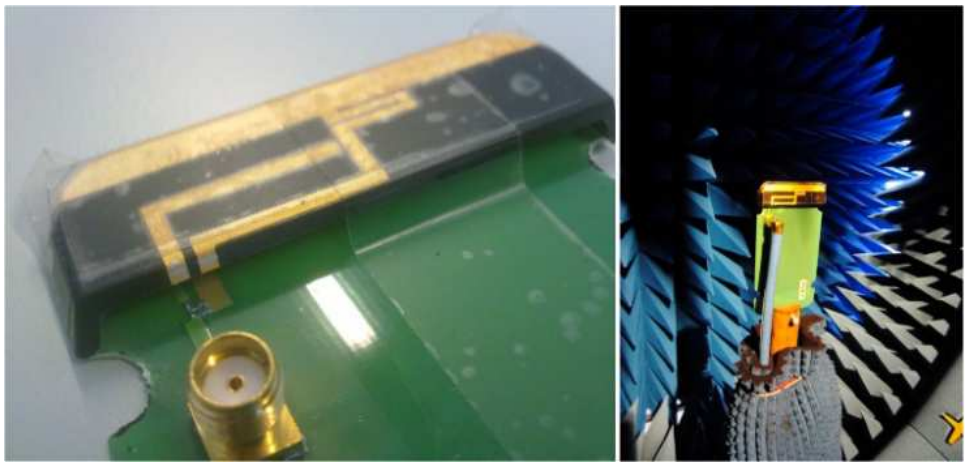

Figure 112 Manufactured UMTS Antenna Prototype and Efficiency Measurement Environment

The total efficiency measurements were also performed in a Satimo Starlab station. Two configurations were measured with this prototype, consisting of short (75mm) and long (90mm) ground plane dimensions. For the long ground plane configuration, the ground plane was extended to 90mm from 75mm by using copper tapes under the PCB. The comparison of the measured reflection coefficient for short and long GND plane configurations is seen Figure 113. Extending the ground plane to 90mm helps for slightly better coverage in the LB (around 950MHz) since most of the radiation is coming from the ground plane around this frequency and the chassis resonance is coming more towards the band of interest by increasing the length (1.28GHz instead of 1.46GHz). The effect is not significant in the HB for this antenna & MN combination.

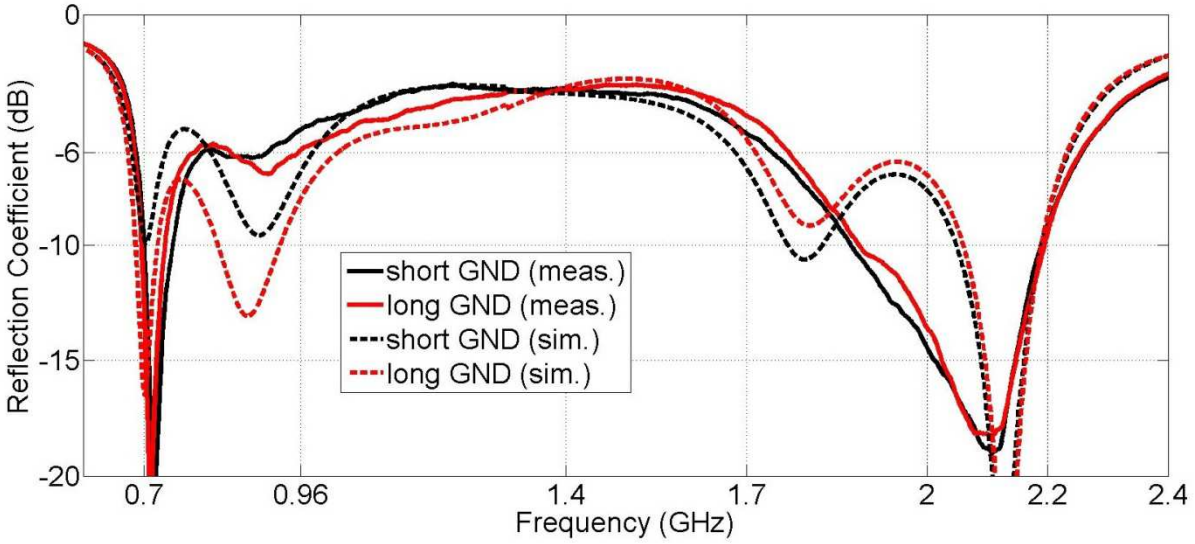

Figure 113 Measured/Simulated Reflection Coefficient of UMTS Antenna with Short/Long Ground Plane

The measured total efficiency for the two configurations can be observed in Figure 114. With the 75mm ground plane, the measured total efficiency is between -7.5dB and -3dB in the LB and between -4dB and -2dB in the HB. Increasing the ground plane length to 90mm has a considerable effect on the total efficiency in the LB, increasing the efficiency by approximately 1.5dB on average. The efficiency in the LB is now between -4dB and -2dB. The efficiency in the HB is not affected by the change, since a major part of the radiation comes from the antenna itself at this frequency range.

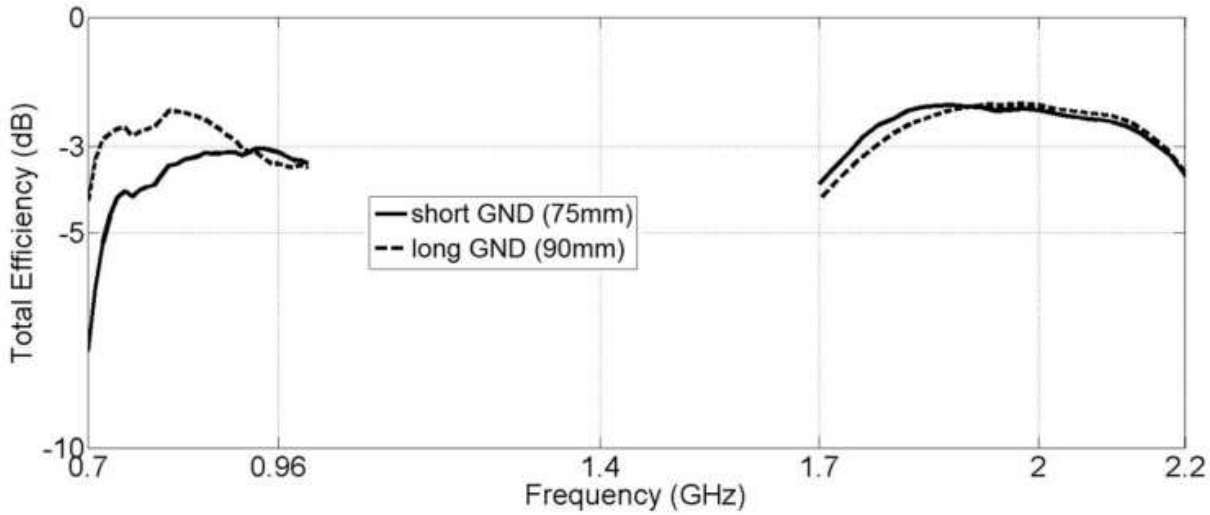

Figure 114 Measured Total Efficiency of UMTS Antenna with Short/Long Ground Plane

2. LTE ANTENNA

2.1. ANTENNA MODEL

A quite similar antenna was designed using the same dimensions for the plastic piece, the ground and the FR4 substrate. The orientation of the driven strip was changed, facing the open end to the corner of the ground plane, to exploit better the low-Q property of the ground plane especially in the HB. The parasitic strip is again excited by this driven strip via capacitive coupling, creating a resonance in the LB, increasing the bandwidth potential. Considering the bandwidth potential of the antenna, a matching network consisting of only two SMD components (a shunt inductor and a series capacitor) was evaluated at the antenna feed but due to the series resonance frequency (SRF) issue, the shunt inductor was split into two inductors, increasing the number of SMD components to three. Pogo-pins were again used under the plastic mold, for the connection of the antenna elements and PCB traces.

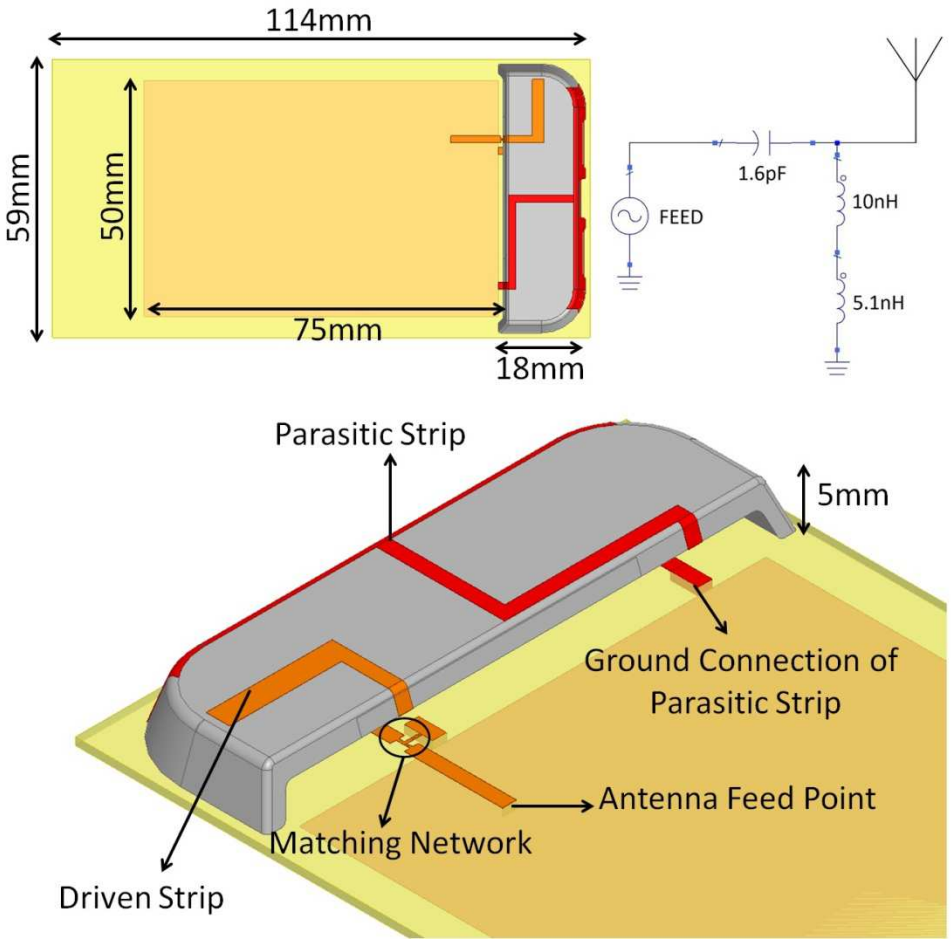

Figure 115 LTE Antenna Model

The simulations were performed for the antenna with and without the parasitic strip (driven strip only). They are presented in smith chart in Figure 116, without any MN at the feed. The introduction of the parasitic element creates a resonance in the LB, increasing the real part of the input impedance. This enables higher bandwidth potential especially in the LB (Figure 117). For the HB response, an additional resonance can also be observed after the introduction of the parasitic element, which occurs approximately around 2GHz (loop in the smith chart).

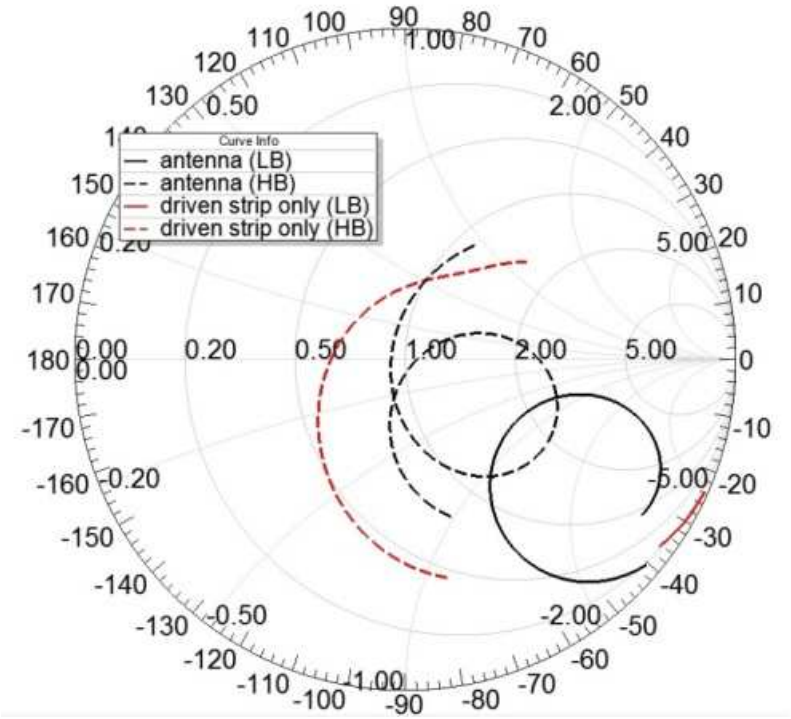

Figure 116 Simulated Input Impedance of the LTE Antenna, with/without Parasitic Strip

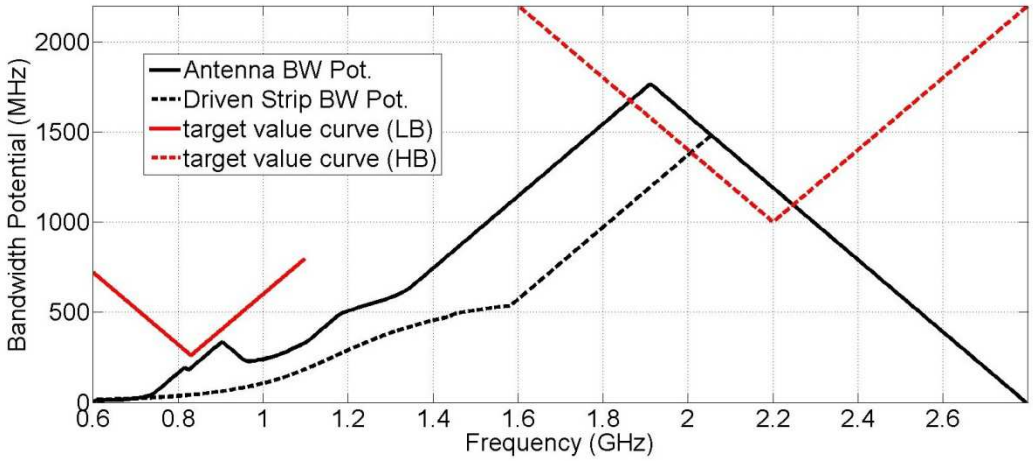

Figure 117 Bandwidth Potential of the LTE Antenna, with/without Parasitic Strip

In order to explain better the role of the parasitic strip in the HB, the input impedance of the antenna structure without MN is given again in Figure 118, with current distributions over the antenna and the ground plane at two different frequency points. There is a loop in the smith chart at 2GHz and when the corresponding surface current is observed, a strong excitation of the parasitic element can be seen. At another frequency point (2.5GHz), the excitation of the parasitic element is weak whereas the driven strip is strongly excited. This suggests that the role of the parasitic element is not confined only within the LB, it also enables higher bandwidth in the HB by creating additional resonance.

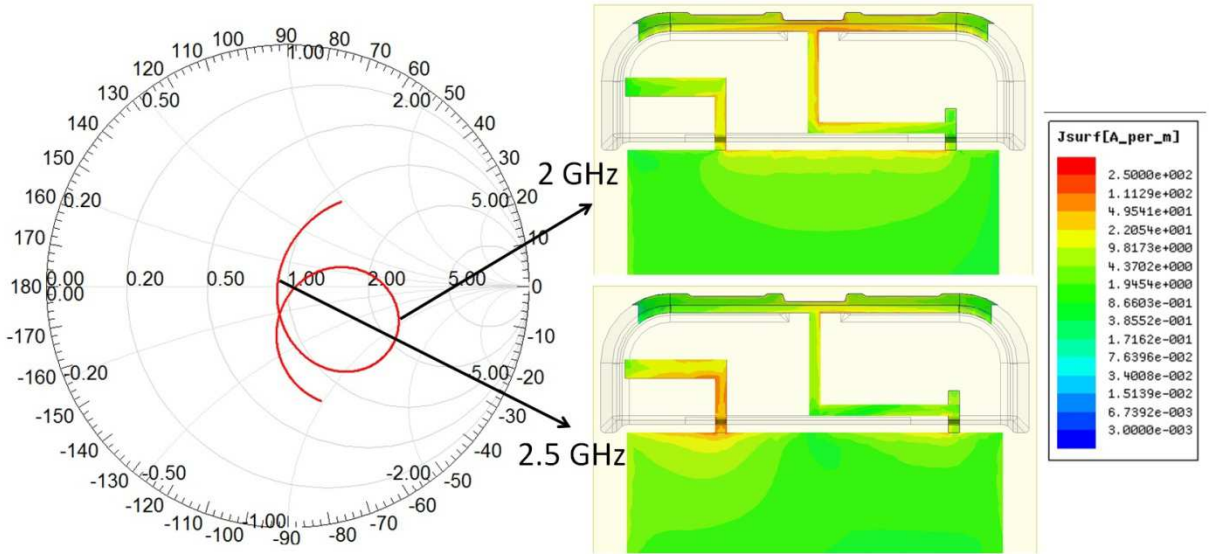

Figure 118 Surface Current Distribution of the LTE Antenna

The simulated input impedance and reflection coefficient of the antenna (with and without MN) are presented in Figure 119 and Figure 120. The antenna can cover the whole target band except some overshoots around 950MHz, 1.7GHz and 2.2GHz.

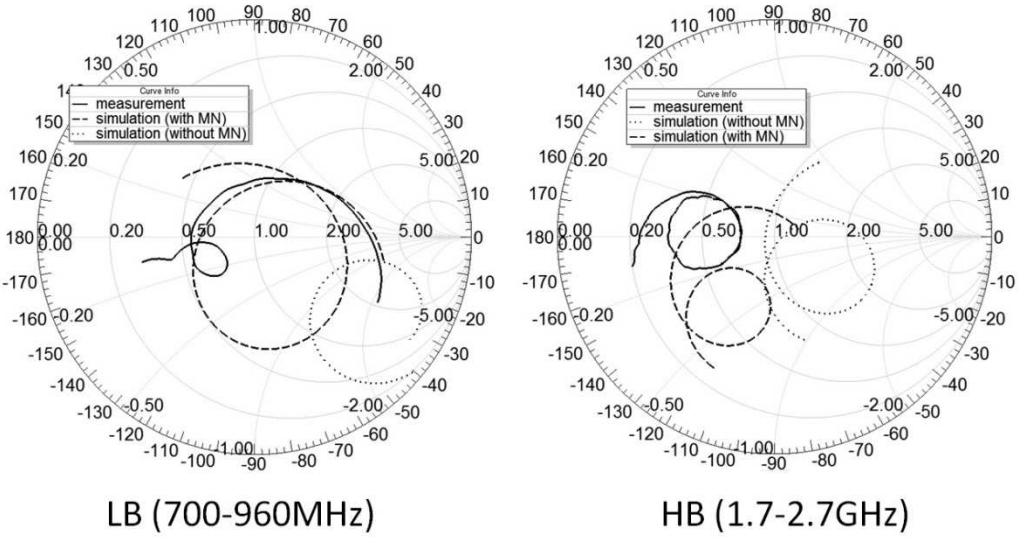

Figure 119 Simulated and Measured Input Impedance for LTE Antenna, with/without MN

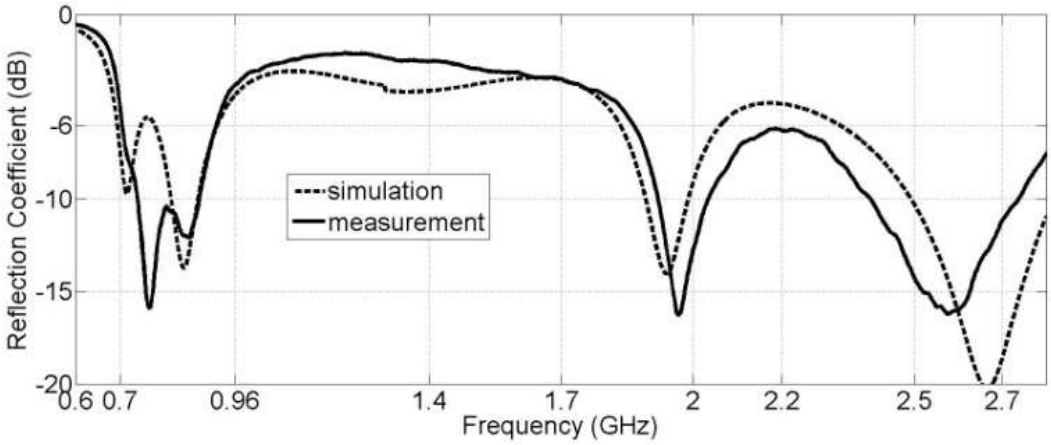

Figure 120 Simulated and Measured Reflection Coefficient of the LTE Antenna

2.2. MEASUREMENT RESULTS

The manufactured antenna prototype can be seen in Figure 121. The antenna is fed through an SMA connector placed on the PCB. The comparison of the measured and simulated reflection coefficient can be seen in Figure 119 and Figure 120. A fair agreement is observed between simulation and measurement results. The agreement is less obvious for LB in smith chart, which may be coming from the misalignment of the plastic piece on the PCB. In the HB, the difference in the input impedance is only a phase difference, coming from the possible differences on the feed line between simulation and measurement.

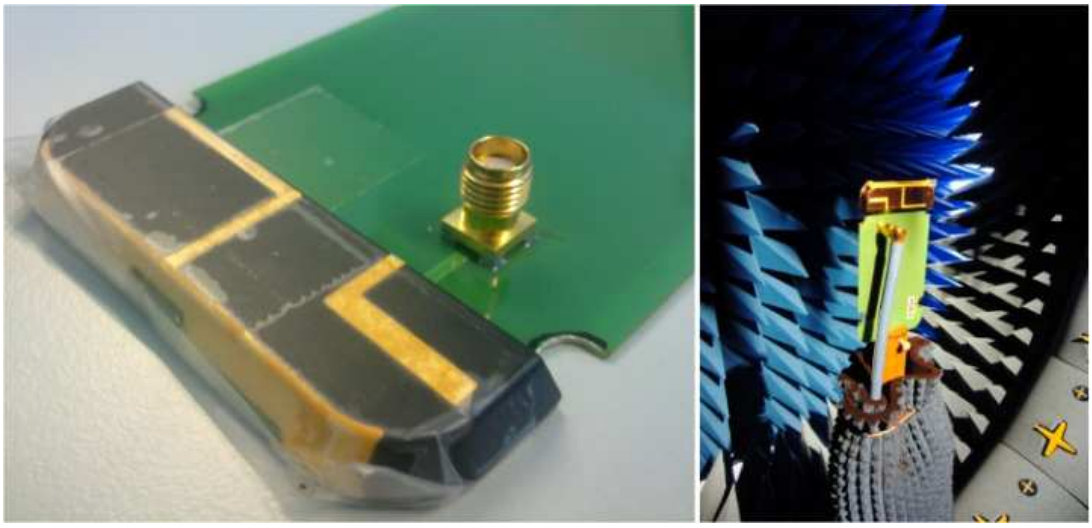

Figure 121 Manufactured LTE Antenna Prototype and Efficiency Measurement Environment

The s-parameter measurements for this antenna were performed also with the longer ground plane (90mm) configuration, whose results are presented in Figure 122. In Figure 123, an efficiency between approximately -7dB and -3dB is seen in the LB with short GND plane. However the efficiency drops further to -10dB for a narrow bandwidth, around 700MHz. When the ground plane length is increased to 90mm, an improvement is observed as expected, efficiency being between -5dB and -2.4dB. The measured efficiency is below -5dB between 700-800MHz for short ground plane and between 700-730MHz for long ground plane. The HB efficiency is not affected by the change in the length of the ground plane and is between -5dB and -1.8dB for both cases.

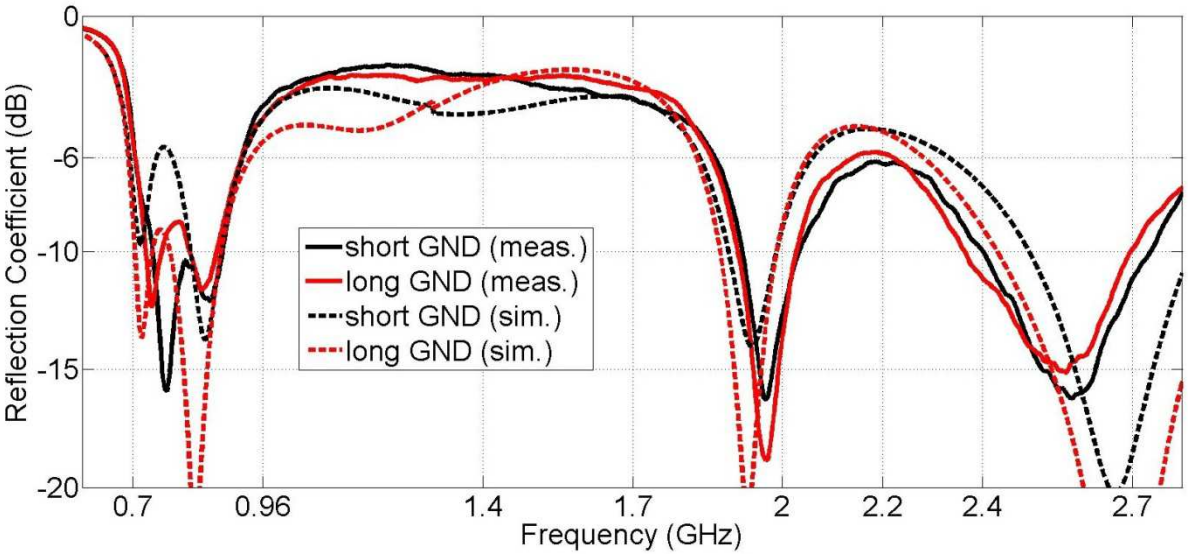

Figure 122 Measured/Simulated Reflection Coefficient of LTE Antenna with Short/Long Ground Plane

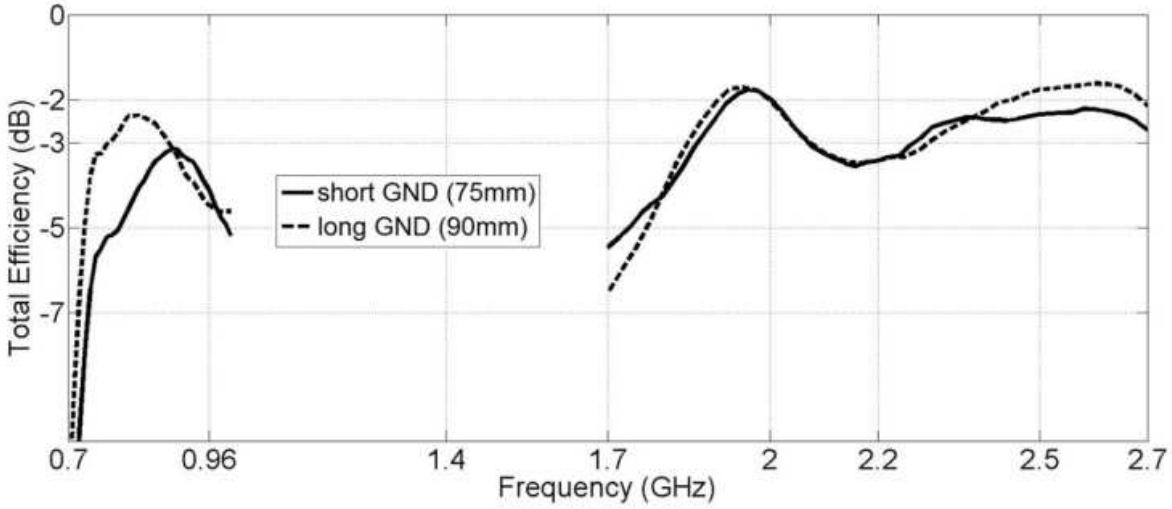

Figure 123 Measured Total Efficiency of LTE Antenna with Short/Long Ground Plane

To investigate the reason of the very low radiation efficiency at 700MHz, surface currents were plotted at 700MHz, 750MHz and 900MHz (Figure 124). The parasitic element is strongly excited at 700MHz and the current circulates following the path of: antenna feed-driven strip-parasitic strip-ground plane-back to the antenna feed. For this reason, the currents on the ground plane (especially on long edges of the PCB) are weak, when compared to the more uniform excitation (in the longitudinal direction) of the ground plane at 750MHz and 900MHz. Since most of the radiation comes from the first chassis wavemode at the lower frequencies, the low radiation efficiency can be explained by the currents circulating between the driven strip and parasitic strip and not forming the first wavemode.

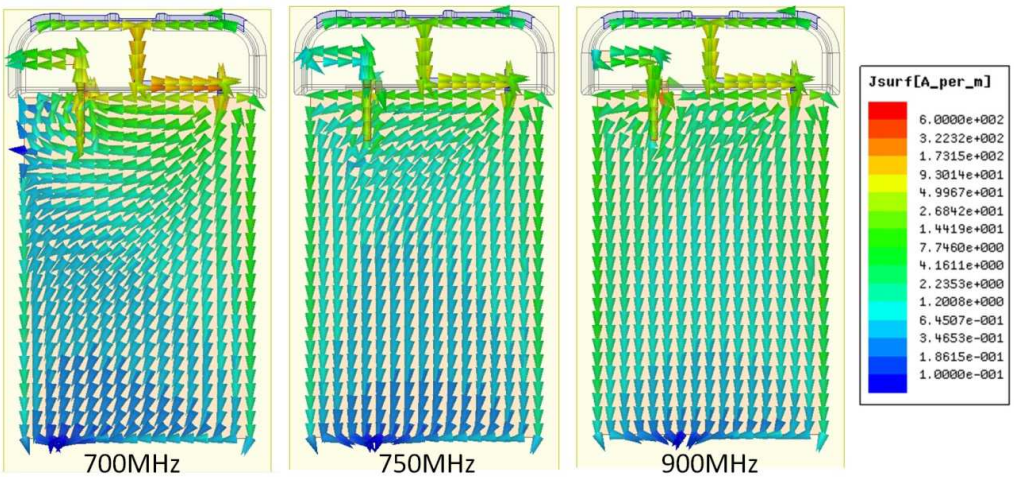

Figure 124 Surface Current Distribution of the LTE Antenna in the LB

3. INVESTIGATION OF THE USER EFFECT

The effect of the user's hand and head on the efficiency and matching of the antenna was investigated through measurements using the two antenna prototypes which were designed for free space. It is worthwhile to note that the antennas were not designed on purpose to be resistant to detuning and the main aim of the study was to form a basis for future studies.

As widely known, the user's hand and head affects the antenna performance in two ways. The first effect is the change in the reflection coefficient due to dielectric loading. The second effect is the reduced total efficiency, due to the lossy characteristics of different body tissues in the near field of the radiating elements and this last effect is difficult to avoid as a lot of power will be lost in those lossy tissues.

To investigate both these effects, s-parameter and total efficiency measurements were performed, using CTIA hand and head phantoms (Figure 125 on left taken from [7]). In order to perform a more realistic measurement, a dielectric casing made of ABS P430 material was used (white structure in Figure 125 on right). The relative permittivity of the ABS material is 2.4 and the loss tangent is 0.0053.

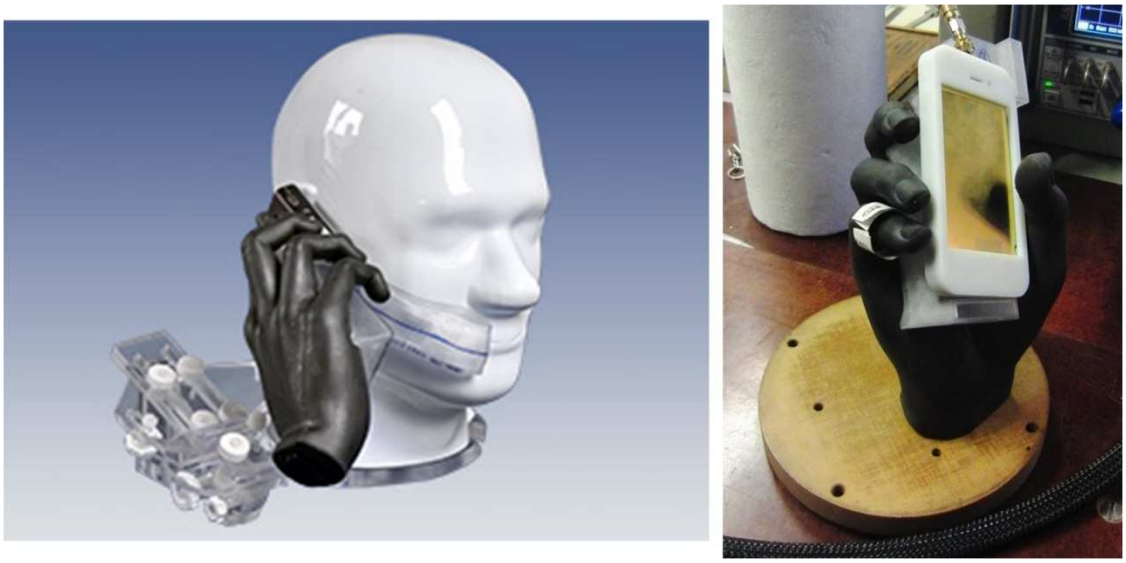

Figure 125 CTIA Hand and Head Phantoms and Dielectric Casing

Figure 126 Efficiency Measurement Setup Taking into Account the User's Head and Hand

The s-parameter measurements of the UMTS antenna in four different cases are presented in Figure 127. These four cases are defined as:

- Free Space
- Casing: The antenna placed inside the dielectric casing
- Hand: The antenna placed in the CTIA hand with the casing
- Head + Hand : The antenna with casing, placed between the CTIA hand and head phantom

It is necessary to note that the antenna was placed on the bottom of the PCB (facing the palm) in the measurements with hand, to stand for the real use case in today's mobile phones.

It is a well known fact that introducing the user's hand to an antenna will shift its operating frequency down, due to dielectric loading. This behaviour can be seen Figure 127 for the UMTS antenna. With the introduction of the hand and head into the s-parameter measurements, a shift in the frequency of minimum $|s_{11}|$ can be seen towards the lower frequencies. The detuning in the matching of the antenna is more dominant in the LB. The measured total efficiency for the four cases (free space, with casing, with casing and hand, with casing and hand and head) can be seen in Figure 128. It is observed that introducing the casing into the antenna had a positive effect on the efficiency through dielectric loading. The resonance created by the parasitic strip around 700MHz (which has lower efficiency than other frequencies since the currents are concentrated mainly on the parasitic strip so that chassis wavemode is excited weakly) is shifted down, which increases the radiation efficiency (and thus total efficiency) in the band of interest. When the hand phantom is taken into account, there is a decrease in the total efficiency of approximately 5dB in the LB, decreasing the efficiency to the levels below -8dB, due to both detuning effects and loss mechanisms. The same behaviour can also be seen in the HB, where the efficiency drops to the levels around -5dB due to losses in the hand. When the head is also taken into account with the hand, the antenna detuning gets more severe (in the LB) and further decrease is observed in the measured efficiency. The efficiency level is between -17dB and -14dB in the LB and between -13dB and -10dB in the HB.

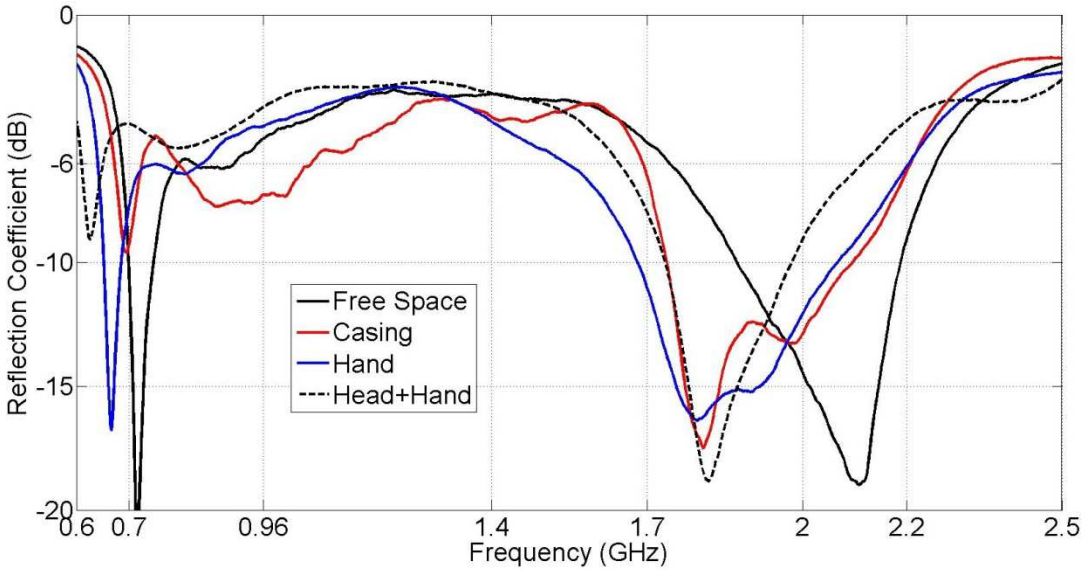

Figure 127 S-Parameter Measurements of the UMTS Antenna with User Effect

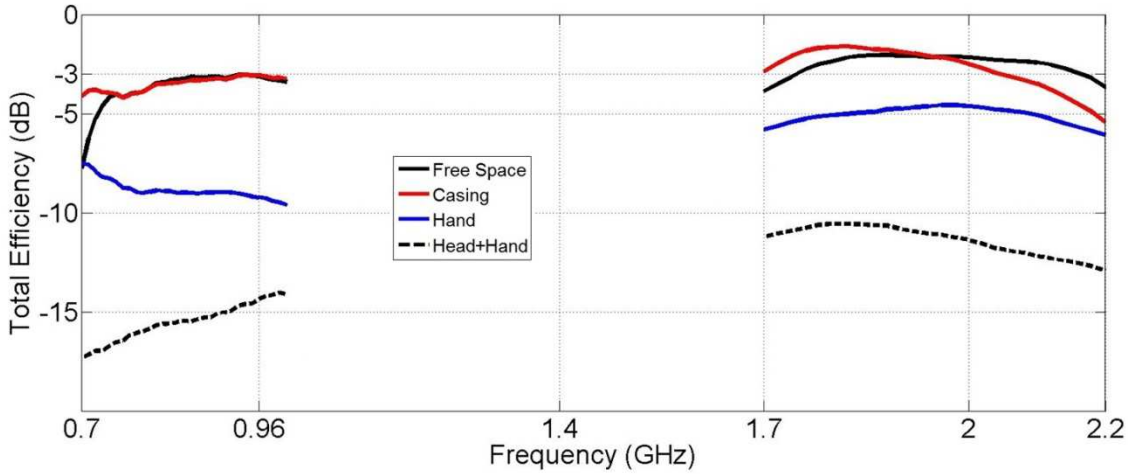

Figure 128 Total Efficiency Measurement of the UMTS Antenna with User Effect

The same comments are applicable also to the measurement results of the LTE antenna. The s-parameter and total efficiency measurement results for this antenna can be seen in Figure 129 and Figure 130 respectively. About the detuning, the antenna stays more or less tuned in the LB in "casing" and "hand" configuration except some narrow overshoots. The mismatch is severe when the head is introduced. The effect is less in the HB and the antenna is matched despite the user effect, although some overshoot is seen with the casing. For the efficiency, when the hand is taken into account, it drops to the levels between -10dB and -7.5dB in the LB and between -10dB and -3.5dB in the HB. When the head is also introduced, efficiency levels between -19dB and -17dB in the LB and between -13dB and -9dB in the HB are observed.

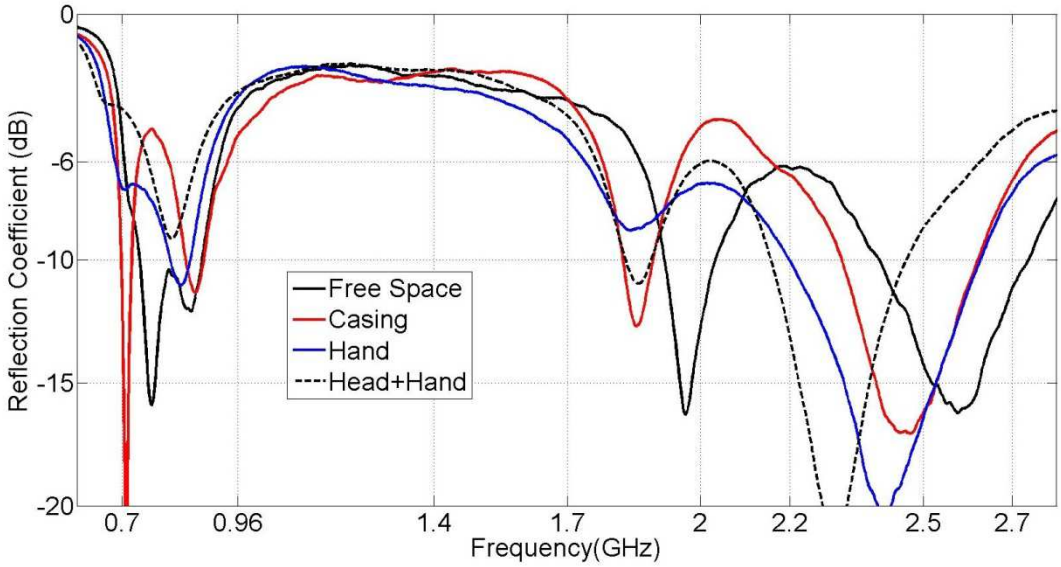

Figure 129 S-Parameter Measurement of the LTE Antenna with User Effect

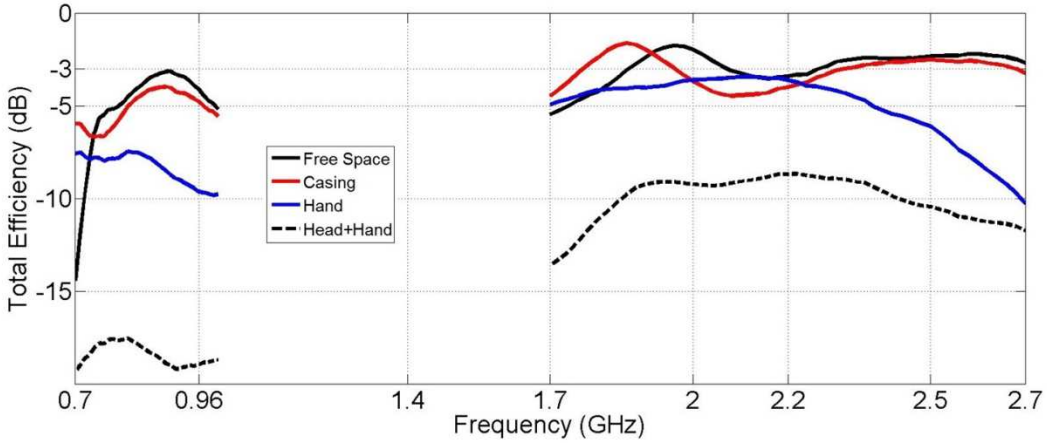

Figure 130 Total Efficiency Measurement of the LTE Antenna with User Effect

4. CONCLUSION

In this chapter, two different antenna designs were presented targeting the 4G communication frequency bands. Both antennas proposed are single feed antennas realized on plastic material using Laser Direct Structuring (LDS) technology. The major design challenge is the relatively short ground plane of 75mm, to rely only on the 3.5" touchscreen of a smart phone as the ground plane.

The first antenna consists of a driven strip, which capacitively excites a parasitic strip connected to the ground plane. With this topology, a high bandwidth potential can be achieved in the LB (700-960MHz) where the antenna is electrically small. With a four element MN introduced to the antenna feed, the low LTE (700-960MHz) and UMTS (1.7-2.2GHz) frequency range can be covered with a single feed design with a reflection coefficient below -6dB. The simulation results have been verified through measurements and total efficiency results for the antenna have been presented.

A similar topology was used for a second design where the driven strip capacitively excites a parasitic element but the orientation of the driven strip was changed. In this way, the additional coverage of the WLAN and high-LTE bands was also made possible.

Finally, an investigation about the effect of the user's hand and head was done using the two antennas. Measurements were performed with a dielectric casing, CTIA hand and head phantom to see the effect on both the s-parameters and total efficiency. Table 5 summarizes the measured total efficiency values in the presence of user hand and head. for the two prototypes. There is also a number of studies, investigating the effect of the user on antennas for mobile terminals like in [8-11]. For example in [4], a CE antenna with a shielding structure was proposed for GSM/UMTS bands. The shielding structure was used to reduce the interaction between the user and the antenna. In the "antenna on top" configuration, the measured efficiency was -10dB at 900MHz and -7.5dB in HB with hand and head. It is worthwhile to state that antenna on top configuration (when the antenna faces only the index finger) is more advantageous than "antenna on bottom" configuration used in this study since the detuning is less effective and absorption losses are less. In [9], a CE with multiband MN was used to cover low LTE/GSM/UMTS bands, with special attention to mitigate detuning in the design phase. The main target was to minimize the detuning especially in the LB when the antenna is placed on top of the PCB. The measurements were performed with the hand only in both on top and on bottom placements. An efficiency drop of approximately 7dB was seen in efficiency measurements with hand when compared to free space. In [10], a dual feed antenna structure was proposed on Rogers 4003 substrate. The LB coverage (700-960MHz) was achieved thanks to a CE and the HB coverage (1.7-2.7GHz) was done using a portion of the CE by offset feeding. This antenna was also designed on purpose to be resistant to detuning when the antenna is on top of the PCB. The measured efficiency drop (compared to free space) with the hand (when antenna is on bottom) was -6.5dB in LB and -7dB in HB. Finally in [11], the user effect was investigated on a narrowband PIFA antenna covering GSM900/DCS1800 frequency bands. An efficiency drop of 11dB at 900MHz and 8.5dB at 1800MHz was measured with hand and head when the antenna is placed on bottom of the PCB.

When the data in Table 5 are compared with corresponding results from these studies, it can be concluded that the efficiency levels obtained by the two antennas presented here are competitive in terms of total efficiency. It should also be noted that no specific effort was spent considering the user effect in the design phase, and a ground plane of only 75mm was used in this study. It was previously shown that an additional increase of 0.5dB can be obtained making the ground plane length 90mm.

Table 5 Summary of the Measured Efficiency Taking into Account the User Effects

		UMTS Antenna	LTE Antenna
With Hand	Eff. in LB	Between -7dB & -9dB	Between -8dB & -10dB
	Eff. Drop from FS (LB)	4dB	3dB
	Eff. in HB	Between -4dB & -6dB	Between -10dB & -3dB
	Eff. Drop from FS (HB)	3dB	2dB
With Hand+Head	Eff. in LB	Between -17dB & -14dB	Between -19dB & -17dB
	Eff. Drop from FS (LB)	11dB	14dB
	Eff. in HB	Between -10dB & -13dB	Between -13dB & -9dB
	Eff. Drop from FS (HB)	9dB	7dB

5. PERSPECTIVES

It was mentioned previously that the results obtained from user effect study will be used for future studies on this subject. As also mentioned in Conclusion part, there has been a number of studies to design mobile terminal antennas resistant to detuning (mismatching) when the antenna is located on the top of the PCB. This configuration is less problematic when compared to "antenna on bottom" configuration, since the antenna only faces the index finger (instead of the whole palm) which results in less severe detuning compared to bottom location. It is also worthwhile to note that the antenna is generally located at the bottom of today's smart phones. For these reasons, it would be better to focus the future studies on an antenna resistant to detuning due to user's hand and head, when the antenna is placed on the bottom of the PCB.

In addition to the antennas presented in this chapter, some more measurements were also performed on the hollow CE antennas (presented in chapter III) with the CTIA hand. The main target was first to obtain the general behaviour of the impedance change of an optimally-overcoupled antenna(placed on the bottom of PCB) in presence of the user's hand. The measured input impedances of the two different hollow CE antennas are given in Figure 131 for free space (FS) and with hand configurations.

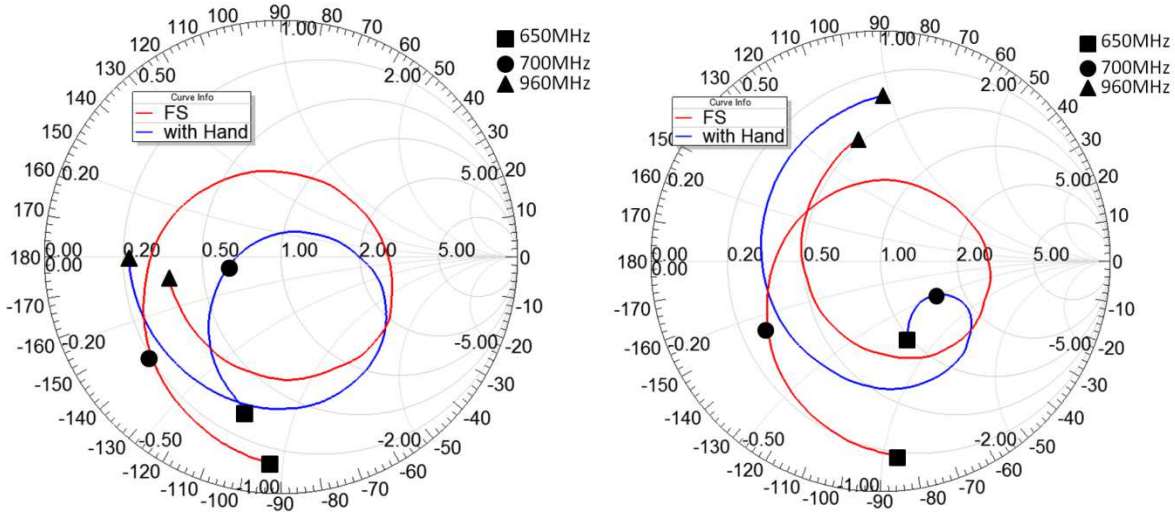

Figure 131 Measured Input Impedance of Hollow CE Antennas in FS and with Hand

Evaluating these results about the input impedance in a geometrical way in smith chart, it can be told that the impedance loop in FS condition is subject to shrinking when the user's hand is introduced. Due to the dielectric loading, the lower frequency point of the loop is pulled through the middle, where the higher frequency points are pushed out of the loop (Figure 132).

This can be verified by turning back to the results in Figure 131. For the antenna on left, the 700MHz point (shown with a circle) is initially quite outside of the starting region of the loop (in FS). When the hand is introduced, this point goes inside the loop and as a consequence the starting frequency of the loop falls to frequencies like 650MHz. The 960MHz point (shown with a triangle) which is close to the end point of the loop in FS, is pushed out of it when the hand in introduced. A similar behaviour can also be seen for the results in the smith chart on right.

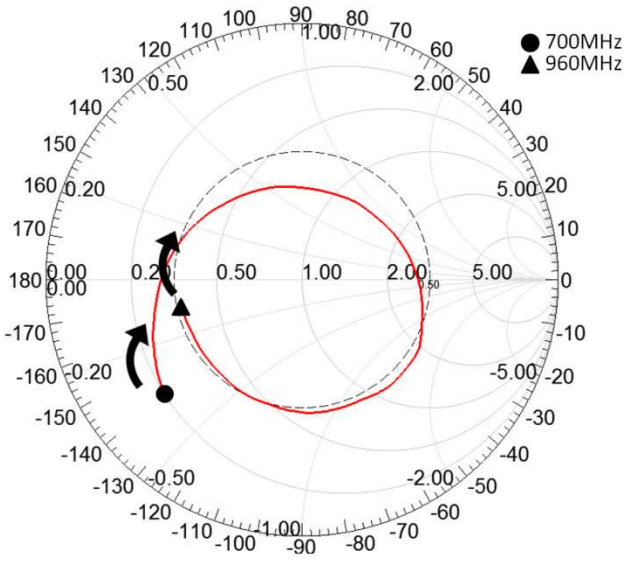

Figure 132 Geometrical Analysis of the Impedance Change with User's Hand

Using this background, initial studies were done to design an antenna resistant to detuning due to hand. The model of this initial design can be observed in Figure 133. The antenna is a dual-feed structure where the first feed is responsible for covering the LB (700-960MHz) and second feed for HB coverage (1.7-2.7GHz). The LB antenna consists of a short driven strip which capacitively excites a parasitic strip connected to ground plane through an inductor. A series inductor is used at the LB feed for impedance matching. The HB antenna is a separately fed monopole, with a two element MN at the feed. The antenna is totally printed on an FR4 substrate having dimensions of 130X60X0.8mm^3. A ground clearance region of 10mm is reserved for the antenna, making the ground plane 120mm long. The simulations of this antenna was performed in a commercial full wave electromagnetic solver, EMPIRE XCcel [12], in free space, with hand and with hand+head conditions(Figure 134).

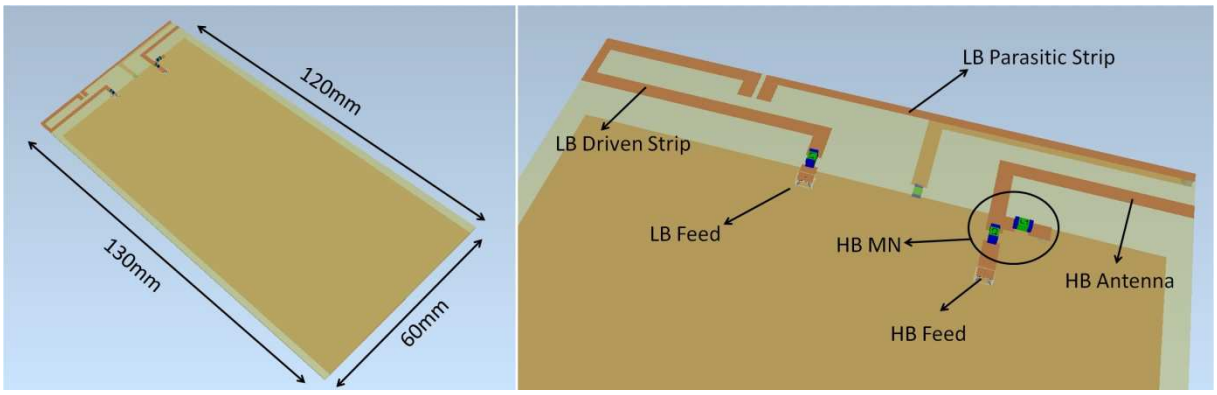

Figure 133 Simulation Model of the Antenna Resistant to Detuning

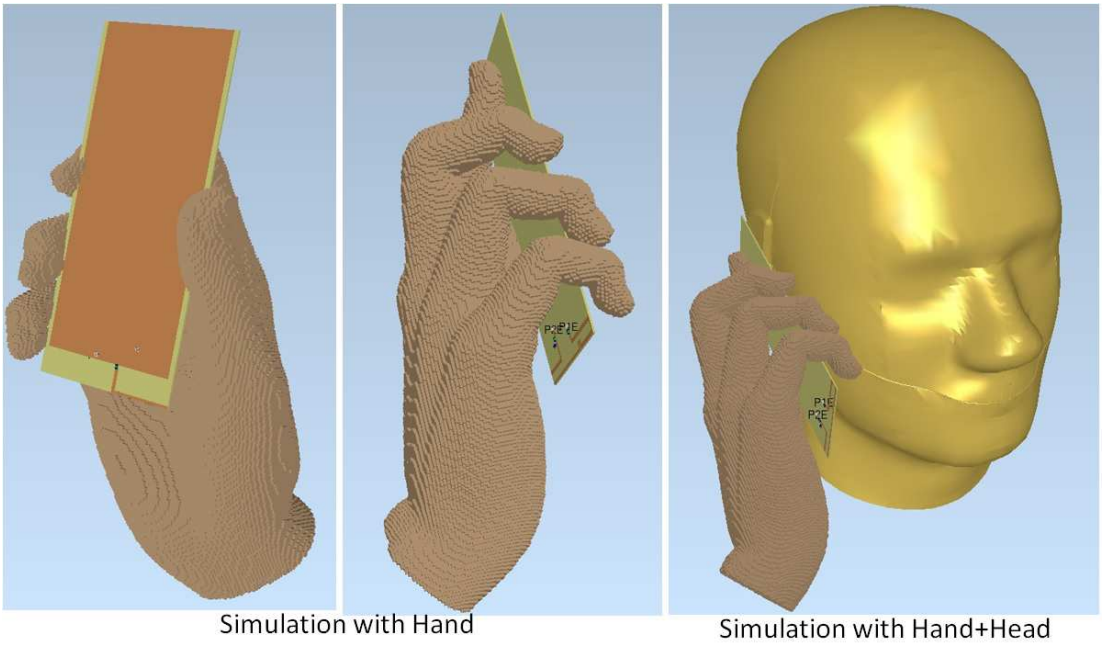

Figure 134 Simulation Models of the Antenna Considering the User

The simulated S-Parameters of the antenna in FS and "with Hand" conditions are given in Figure 135 and Figure 136. The antenna can cover the target bands with a reflection coefficient below -6dB in both FS and "with hand" conditions. In the LB, the matching bandwidth is reduced from 390MHz to 350MHz when the hand is introduced but this bandwidth is still enough to cover the LB.

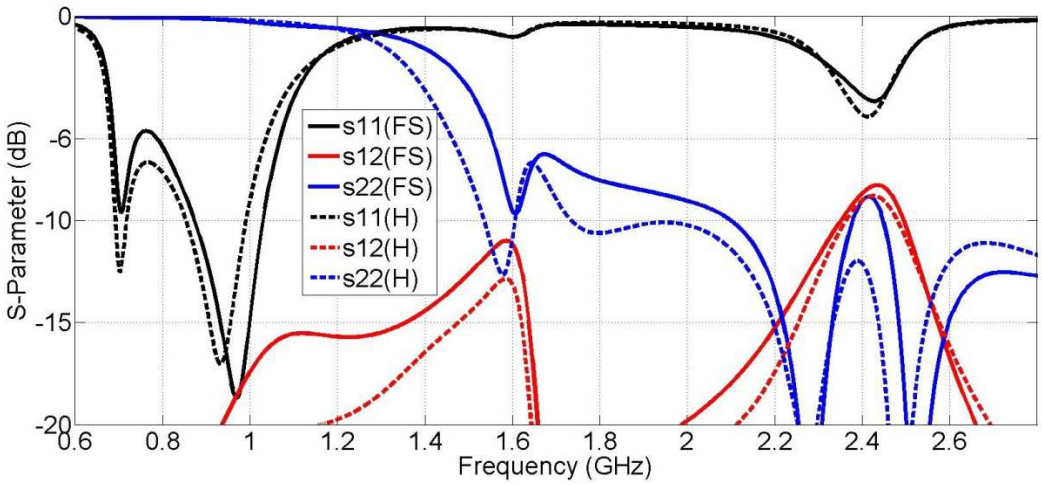

Figure 135 Simulated S-Parameters of the Antenna in FS and with Hand

The effect of the hand on the input impedance in LB occurs as foreseen. The loop in the smith chart shrinks and the high edge frequencies of the impedance are pushed out of the loop. Special attention was paid for situating the 960MHz point, such that it will not get out of the VSWR=3 circle so it will still be matched even with the hand. When the head is also taken into account in simulations, the antenna continues being matched in 700-960MHz with a reflection coefficient below -6dB(Figure 137).

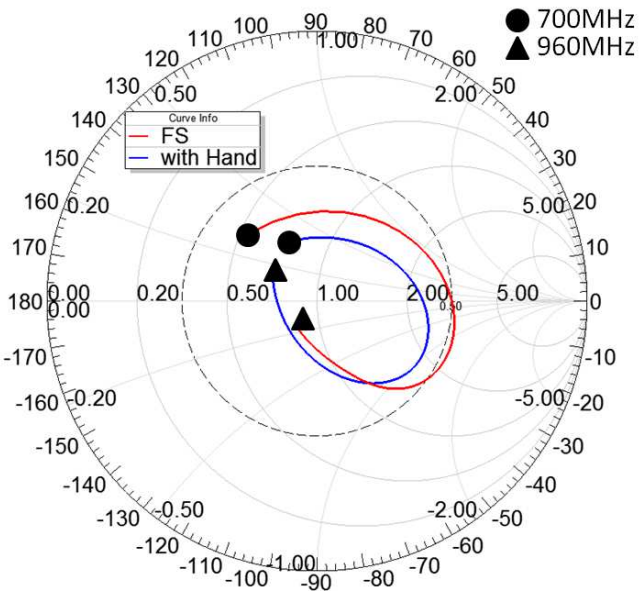

Figure 136 Simulated Input Impedance of the Antenna in FS and with Hand (Smith Chart)

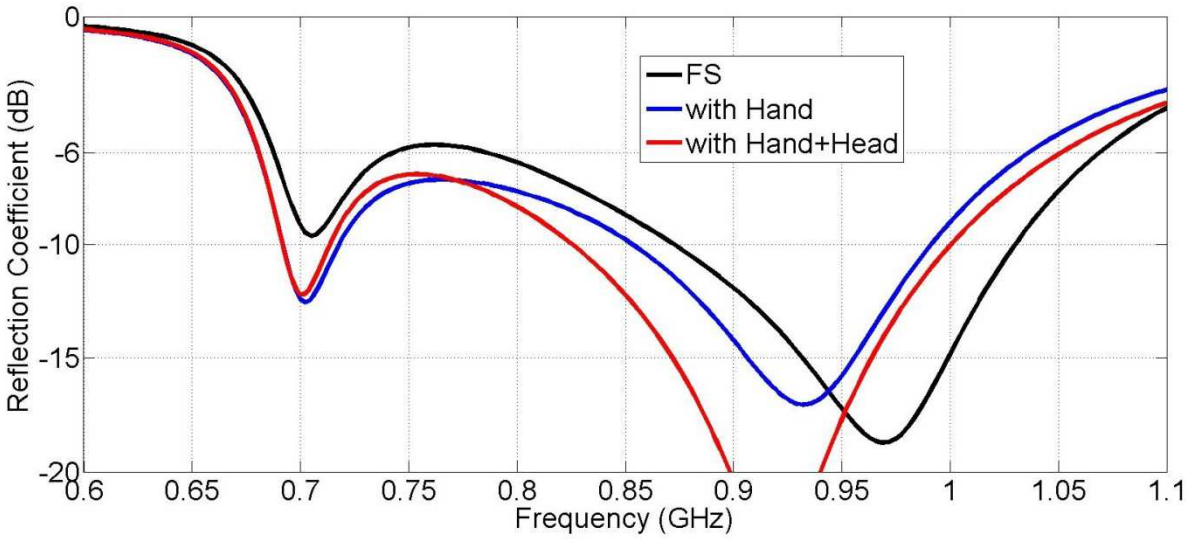

Figure 137 Simulated S-Parameters of the Antenna in LB

The proposed antenna has been manufactured. Figure 138 and Figure 139 presents a comparison of the simulated and measured S-Parameters of the antenna in FS. A good compliance can be seen between the simulations and measurements, except an overshoot in the LB, between 750-830MHz rising up to -4.5dB. However it can be told from the LB input impedance in Figure 139 that this overshoot is not something about the bandwidth potential, it can easily be overcome by tuning the component values in the LB MN.

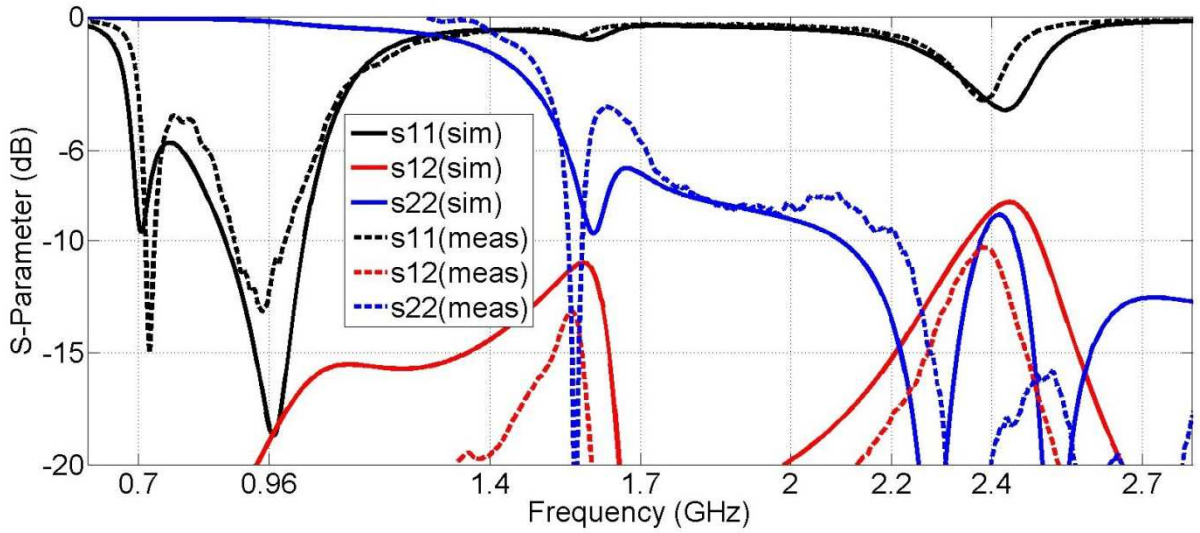

Figure 138 Simulated and Measured S-Parameters of the Antenna in FS

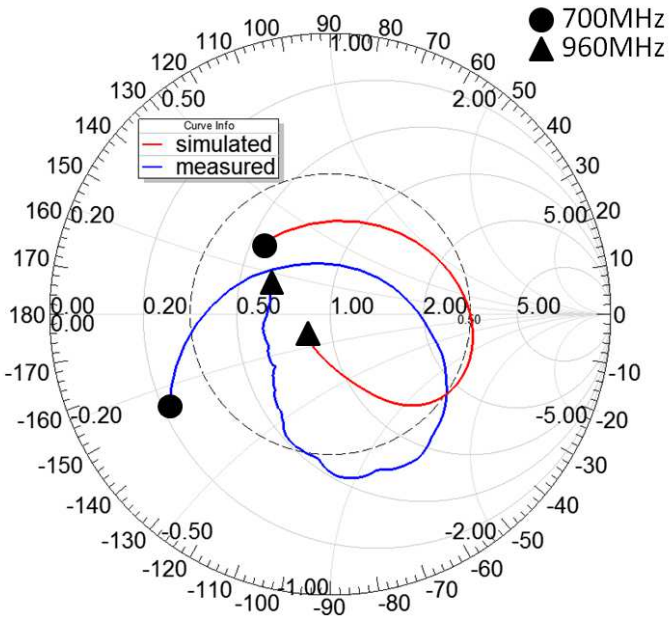

Figure 139 Simulated and Measured Input Impedance (LB Only) of the Antenna in FS (Smith Chart)

S-Parameter measurements were also performed for this manufactured prototype, using a real human hand in talking grip position when the antenna is on bottom of the PCB. The measured S-Parameters can be seen Figure 140 in dB format and also in Figure 141 for the Lb in smith chart. The antenna keeps its reflection coefficient below -6dB between 700-960MHz with LB antenna and between 1.7-2.7GHz with HB antenna, in the presence of a real user hand.

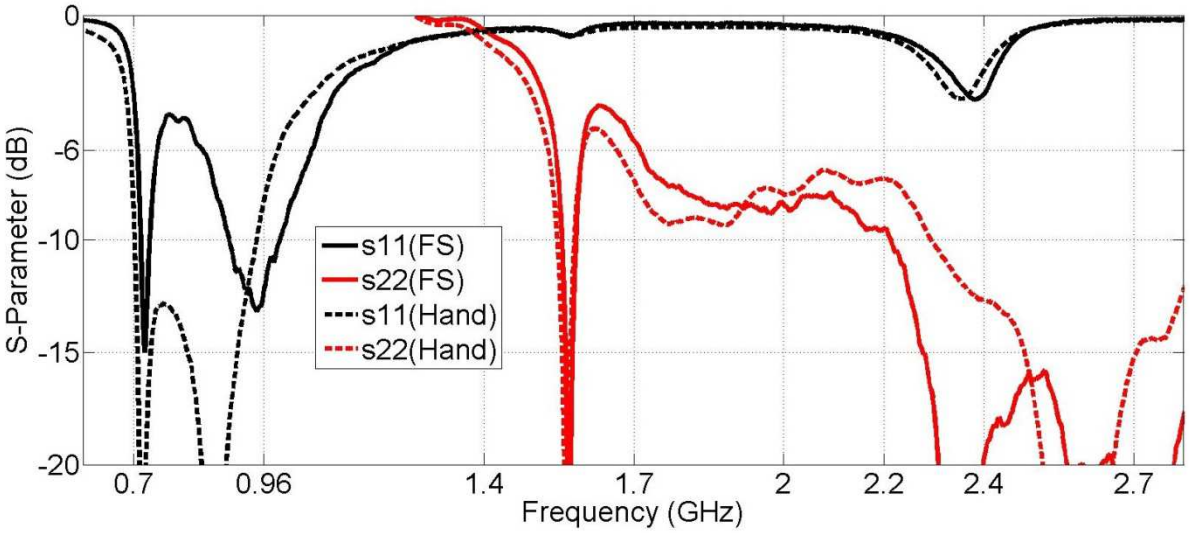

Figure 140 Measured S-Parameters of the Antenna in FS and with Hand

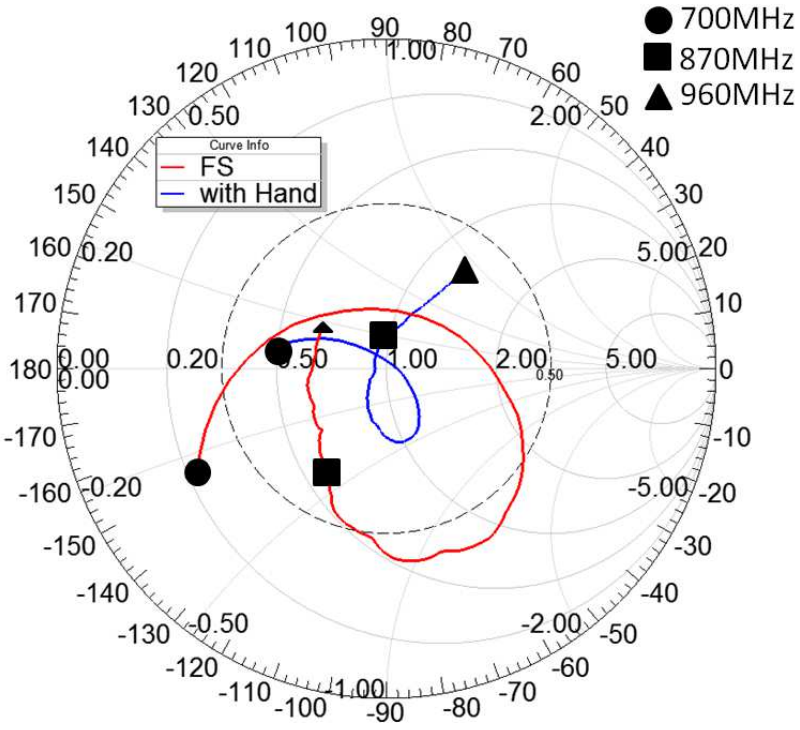

Figure 141 Measured Input Impedance of the Antenna (in LB) in FS and with Hand (Smith Chart)

For future studies, it is targeted to take this antenna as a basis and improve the design for better performance in the LB in FS condition. The S-Parameter and efficiency measurements are also next steps for validation of the concept.

REFERENCES FOR THIS CHAPTER

[1] "Laser Direct Structuring Technology (LPKF-LDS) for Moulded Interconnect Devices," Available at: http://www.lpkf.com/_mediafiles/1797-lpkf-lds-process.pdf

[2] S-C. Chen, K-L. Wong, "Wideband monopole antenna coupled with a chip-inductor-loaded shorted strip for LTE/WWAN mobile handset," Microwave and Optical Technology Letters, vol. 53, no. 6, pp. 1293–1298, June 2011.

[3] S-C. Chen, K-L. Wong, "Small-size 11-band LTE/WWAN/WLAN internal mobile phone antenna," Microwave and Optical Technology Letters, vol. 52, no. 11, pp. 2603–2608, November 2010.

[4] F-H. Chu, K-L. Wong, "On-board small-size printed LTE/WWAN mobile handset antenna closely integrated with system ground plane," Microwave and Optical Technology Letters, vol. 53, no. 6, pp. 1336–1343, June 2011.

[5] K-L. Wong, W-Y. Chen, C-Y. Wu, W-Y. Li, "Small-size internal eight-band LTE/WWAN mobile phone antenna with internal distributed LC matching circuit," Microwave and Optical Technology Letters, vol. 52, no. 10, pp. 2244–2250, October 2010.

[6] Lanxess, "POCAN DP T 7140 LDS 000000," Datasheet, 2011

[7] IndexSAR Company Website, Available: http://www.indexsar.com/ctia-sam-phantom.html

[8] J. Ilvonen, R. Valkonen, J. Holopainen, O. Kivekas, P. Vainikainen, "Reducing the interaction between user and mobile terminal antenna based on antenna shielding," 6th European Conference on Antennas and Propagation (EUCAP), 26-30 March 2012

[9] R. Valkonen, J. Ilvonen, P. Vainikainen, "Naturally non-selective handset antennas with good robustness against impedance mistuning," 6th European Conference on Antennas and Propagation (EUCAP), 26-30 March 2012

[10] R. Valkonen, A. Lehtovuori, C. Icheln, "Dual-feed, single-CCE antenna facilitating inter-band carrier aggregation in LTE-A handsets," 7th European Conference on Antennas and Propagation (EuCAP), 8-12 April 2013

[11] M. Pelosi, O. Franek, G. F. Pedersen, M. Knudsen, "User's Impact on PIFA Antennas in Mobile Phones," IEEE 69th Vehicular Technology Conference, 2009. VTC Spring, 26-29 April 2009

[12] EMPIRE XCcel, Information Available at: http://www.empire.de/

CHAPTER V
EYEWEAR ANTENNAS

This section presents some eyewear antenna concept that can cover 700-960MHz and 1.7-2.7GHz, to be used on wirelessly connected eyewear devices. Since the antennas for eyewear devices operating in 4G cellular communication standard is a new subject, firstly a feasibility study is done for the bandwidth potential of the antenna in different placement alternatives. In all the study, coupling element (CE) antennas totally printed on FR4 substrates are used. To obtain a good compliance with the major use cases, the human head is always taken into account in simulations. Afterwards, three antenna designs are proposed, with a proper dielectric casing and frame. The SAR simulations are also performed and the effect of the user hand is also investigated.

1. USE CASE AND GENERAL INFORMATION ON EYEWEAR DEVICES

Wearable devices incorporating wireless connection with the peripherals has gained a significant popularity in the last years. Some examples of such devices can be considered as the wireless keyboard and mouse, cameras, USB keys, etc. In the recent years, wearable accessories like watches, rings and glasses have also gained importance as communicating devices. One of the most popular of these devices is the eyewears (or glasses), that currently has Wi-Fi 802.11b/g or Bluetooth connection with a peripheral mobile phone or a hotspot. There are currently many ongoing projects by different companies, who target the release of these "smart eyewear" devices in 2014 like [1-5]. Some examples of these devices are presented in Figure 142. Another example of such a device [1] can be seen in Figure 143. This device has a mechanical structure that can be integrated with any glass frame especially if it is optical or solar. The battery is placed behind the user's ear, together with the Wi-Fi/Bluetooth antenna. On the side of the head, a board is found which incorporates the electronics like the touchscreen and video/audio processors. The connection of the transceiver and the antenna is done using an RF cable passing through the plastic frame of the glasses. A camera is placed in the region corresponding to the front of the head. The display issue is solved by using a prism lens in front of the eye, in a way with no disturbances to the actual sight of the eye. A photo showing the positioning of the electronics in the eyewear device is given in Figure 144.

Figure 142 Different Eyewear Devices under Development

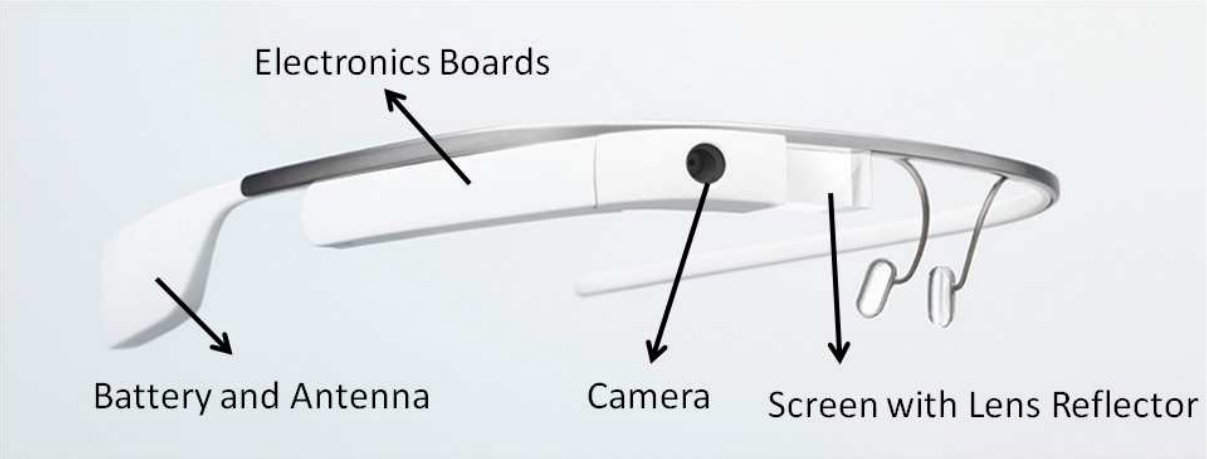

Figure 143 A Generic Eyewear Device Example

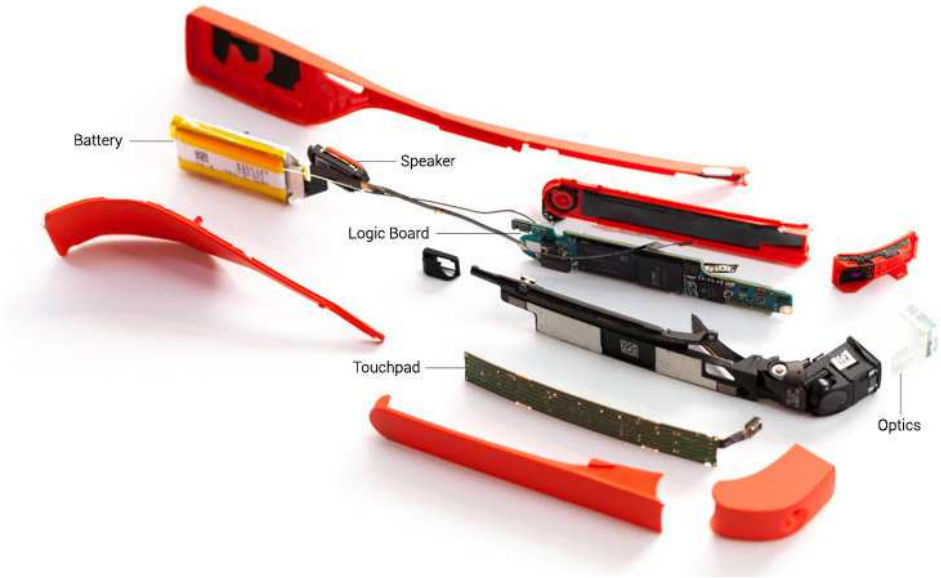

Figure 144 Teardown of the Google Glass

For now, the device can accept calls or use navigation systems by connecting to a mobile phone using Bluetooth. It also allows internet navigation if connected to a hot-spot. The antenna for this connection is placed behind the ear similar to headsets for mobile phones. This placement is practical for now, since the antennas of the same type with similar functionality were investigated extensively in the past in Bluetooth headsets[6-7]. The antenna design problem is relatively easy to solve since the space for the antenna is comparable to the wavelength at this frequency. Also since the power levels for Bluetooth are very small (generally 2.5mW), the SAR is out of concern and no regulation exists[8-9] However it is widely foreseen that these devices may replace mobile phones in the upcoming years. So, there is clearly a need for 4G cellular antennas for these eyewear devices, with satisfactory performance and compliance with the SAR requirements in the head of the user.

2. FEASIBILITY STUDY FOR EYEWEAR ANTENNAS

As an application example of coupling element (CE) antennas on eyewear devices, a feasibility study was first performed (simulations) taking into account a homogeneous user head. In the

simulations, CEs which are totally printed on the 0.8mm thick FR4 substrate were used in three different antenna locations (spotted to be available) and the bandwidth potentials and SAR values in these three locations were compared, using the commercial software EMPIRE XCcel [10]. Figure 145 shows the general model used in the simulations. The PCB that will support the antenna is modeled as FR4 substrate of 0.8mm thickness and with the dimensions given in Figure 146 (chosen as realistic dimensions versus a human head). A 90° bend is added to the PCB to stand for the region that extends in front of the eye. The CE is printed on the inner side of the PCB and the ground plane is on the outer side of the substrate.

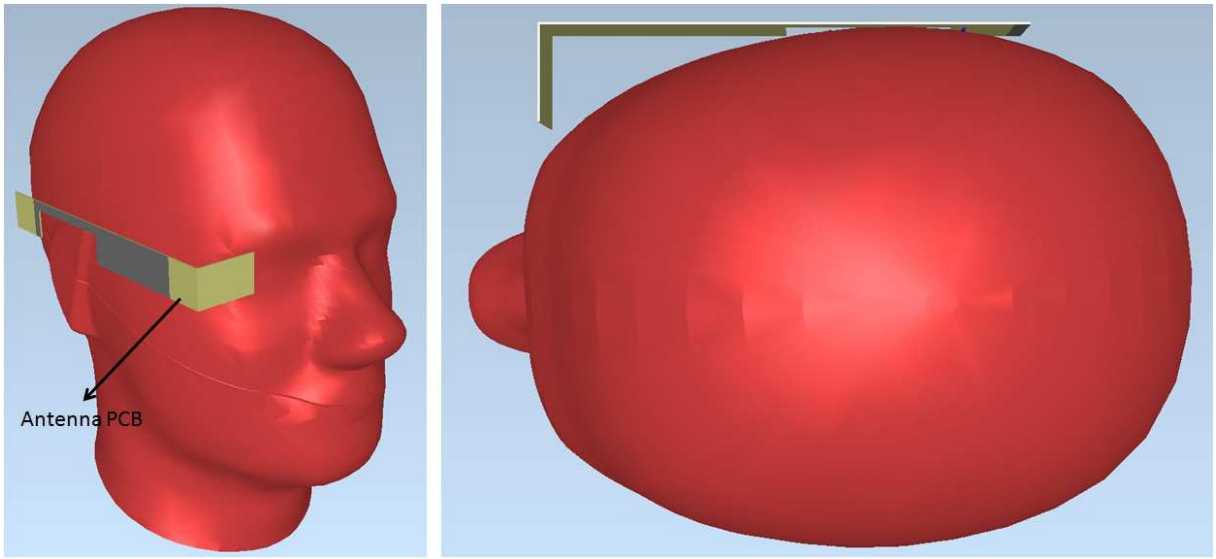

Figure 145 Simulation Setup for the Feasibility Study (3D view and top view)

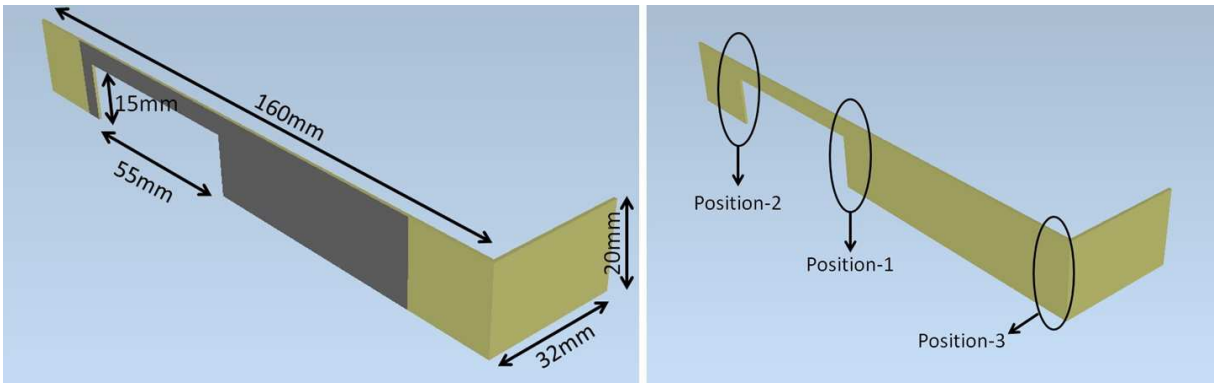

Figure 146 PCB Dimensions and Evaluated Antenna Positions

Three different antenna positions were evaluated in terms of bandwidth potential. These locations are: behind the ear, in front of the ear and close to the eye, as shown in Figure 146.

2.1. INVESTIGATION OF BANDWIDTH POTENTIAL IN POSITION-1

The simulated bandwidth potential of a basic printed CE (in the presence of the user head) in position 1 (in front of the ear) is presented in Figure 147. The bandwidth potential is computed using the Optenni Lab software using a two element MN at each frequency point as described in more detail in previous chapters, so it is an obtainable realistic value compared to theoretical values. To

cover the 4G frequency spectrum, a bandwidth potential of approximately 260MHz at 830MHz and a potential of 1GHz at 2.2GHz is necessary. It is worthwhile to note that these bandwidth potential values are the necessary values for single band coverage, with a two element MN. However since a dual-band coverage is necessary here, it was targeted to get "more than enough" bandwidth potential in the HB at the same time with enough potential in the LB. If Figure 147 is observed, it can be noted that the bandwidth potential may not be sufficient to achieve dual-band coverage (700-960MHz and 1.7-2.7GHz) with a simple MN, since the potentials in the LB and HB do not seem to be high enough. For this reason, this CE in position-1 was evaluated covering only the 1.7-2.7GHz with the introduction of a 2 element MN for SAR simulations. The simulated reflection coefficient with the MN can be seen in Figure 148.

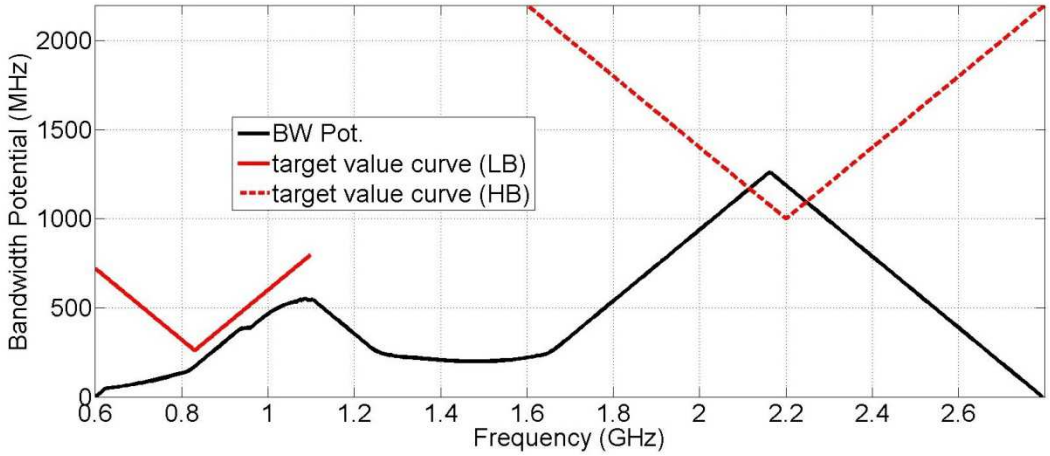

Figure 147 Bandwidth Potential for Position-1

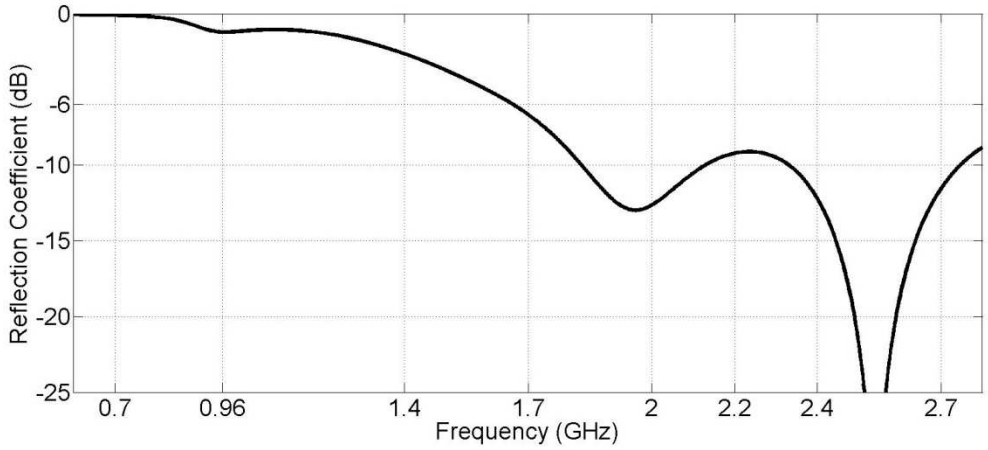

Figure 148 Reflection Coefficient for Position-1

The antenna has a radiation efficiency varying between -7.2dB and -4.4dB in 1700-2700MHz frequency range. It can be noticed that the efficiency of the eyewear antenna is considerably higher than the efficiency of mobile terminal antennas (in chapter IV) in hand+head condition, which was on average -10dB in HB. The main reason is the unnecessity of the user hand in the eyewear usage scenario, which enables getting rid of the losses due to detuning and absorption in the hand. The 3D gain pattern of the antenna at 2200MHz is presented in Figure 149. The radiation is concentrated through the direction away from the head. The gain is lower in the direction of the head due to absorption as expected. When the PCB is held in horizontal direction, the horizontal polarization is

dominant than vertical at 2200MHz with a small difference (0.7dB) between the gains of cross polarizations.

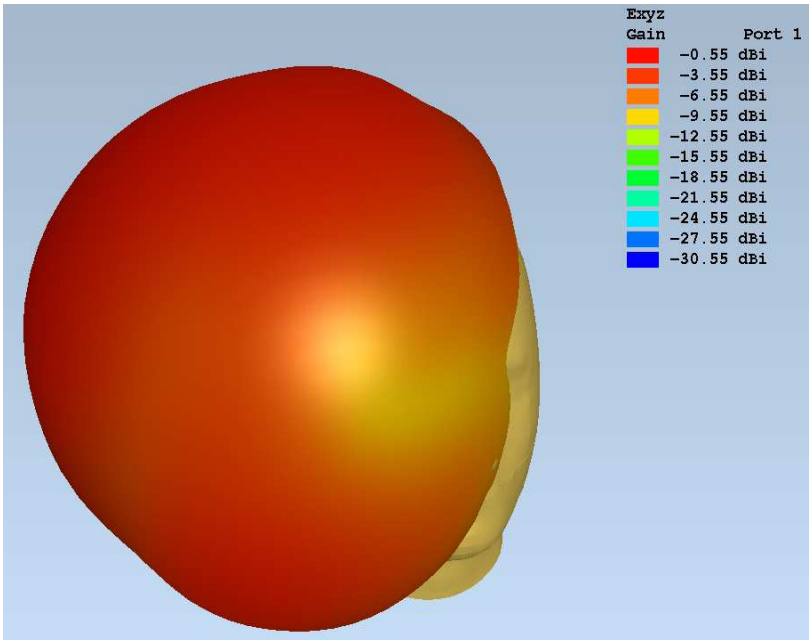

Figure 149 3D Gain Pattern for Position 1 (2200MHz)

2.2. INVESTIGATION OF BANDWIDTH POTENTIAL IN POSITION-2

The bandwidth potential for the CE printed on the substrate in position-2 (behind the ear) is presented in Figure 150. Placing the antenna in this position significantly has the advantage of higher bandwidth potential, sufficient for simultaneous coverage of LB and HB. The main reason of this higher BW potential especially in the LB is the stronger excitation of the ground plane in this position, when compared to previous one. A MN of two elements was inserted at the feed of the antenna and the reflection coefficient in Figure 151 was obtained for SAR simulations.

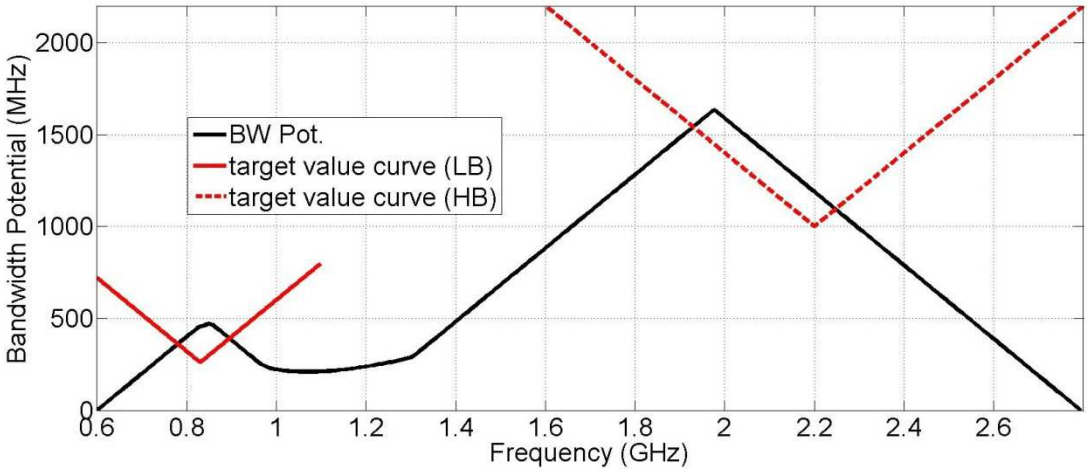

Figure 150 Bandwidth Potential for Position-2

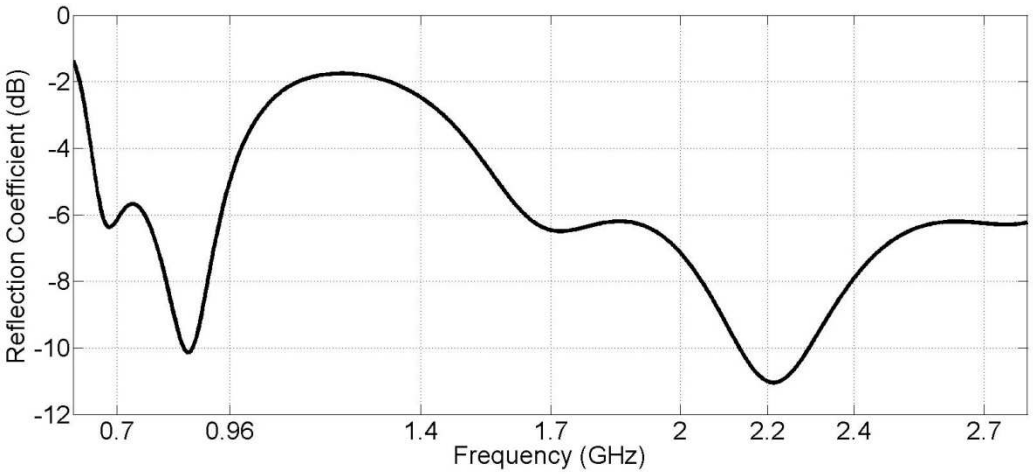

Figure 151 Reflection Coefficient for Position-2

The simulated radiation efficiency is between -11dB and -9.7dB in LB and approximately -7dB in the HB. As explained before, the radiation efficiencies are considerably higher than the general efficiencies of mobile terminal antennas (-14dB in LB and -10dB in HB for antennas in Chapter IV). The 3D patterns can be observed in Figure 152 for two different frequencies, showing the radiation away from the head. The cross polarization level is about 9dB in LB and 5dB in HB where the horizontal polarization is dominant.

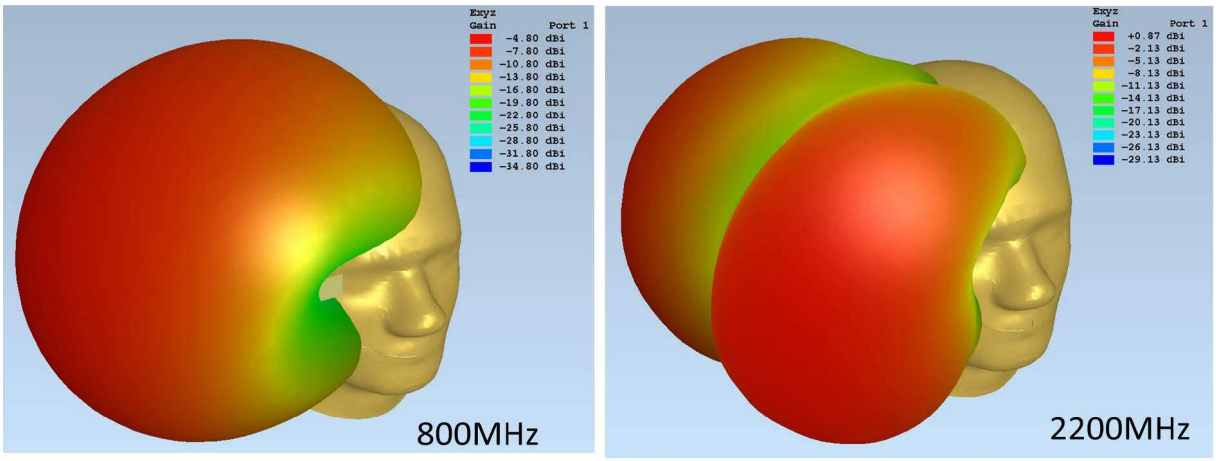

Figure 152 3D Gain Pattern for Position 2

2.3. INVESTIGATION OF BANDWIDTH POTENTIAL IN POSITION-3

The simulated bandwidth potential and the reflection coefficient of the antenna (with a three element MN) in position-3 (close to the eye) are given in Figure 153 and Figure 154 respectively.

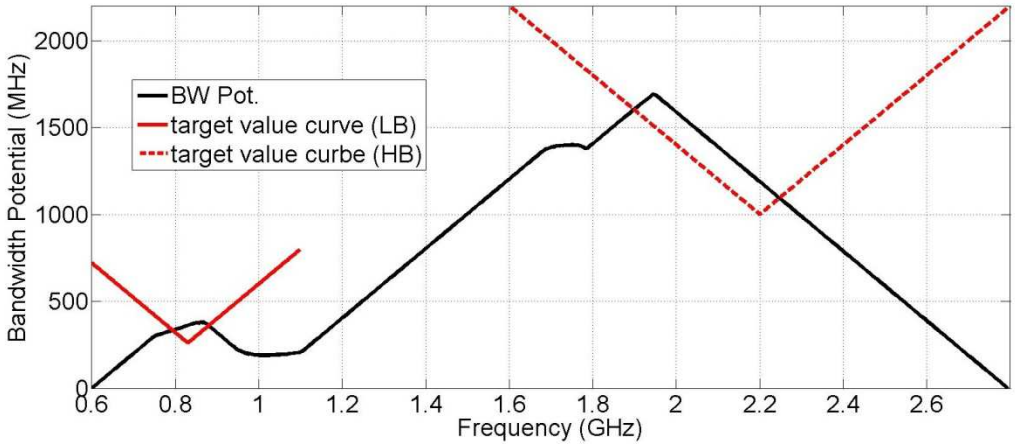

Figure 153 Bandwidth Potential for Position-3

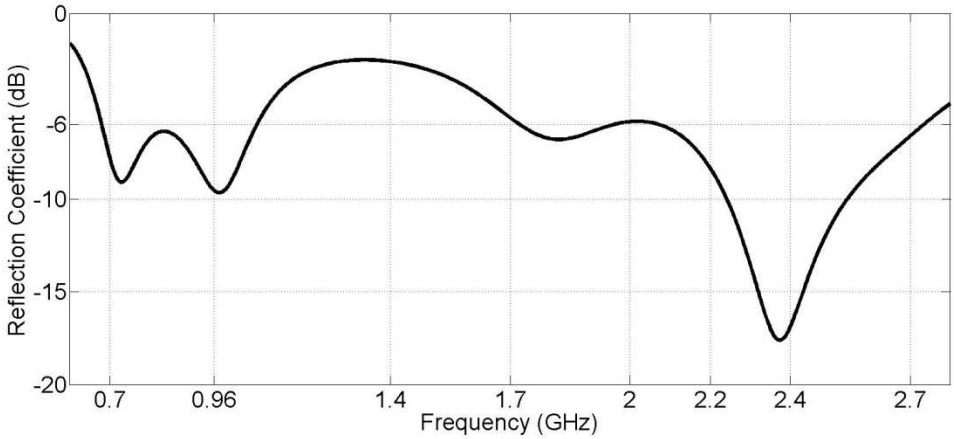

Figure 154 Reflection Coefficient for Position-3

The radiation efficiency is simulated to be between -9dB and -8dB in the LB and between -4.8dB and -3.8dB in the HB. The efficiency values seen in this position are quite higher than previous positions since the CE is located further away from the head when compared to others. The 3D patterns are presented in Figure 155. The horizontal polarization is generally dominant with a cross polarization of 6dB in LB and 4dB in HB.

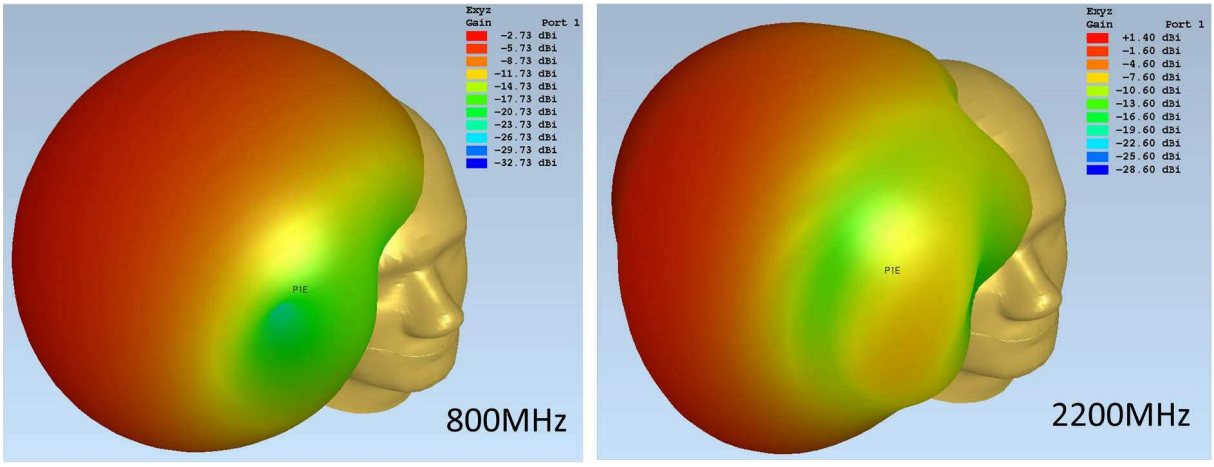

Figure 155 3D Gain Pattern for Position 3

2.4. COMPARISON OF SAR PERFORMANCES IN THREE LOCATIONS

Using the three CEs with associated MNs in the three different locations, a comparison about the SAR was performed. The simulation results are summarized in Table 6. The SAR results are presented both for the 1g SAR standard [11] (maximum limit 1.6W/kg, accepted in U.S) and 10g SAR standard [12] (maximum limit 2W/kg, accepted in Europe). The results are given also as normalized to 0.25W incident power (maximum of 2W in 1/8 second) and 0.25W antenna input after (at an incident power level to obtain 0.25W after mismatch). The SAR values that are below the allowed limit are shown in bold in the table. It can be seen that the SAR values are higher than the SAR values found from the measurements of a typical mobile phone, due to the proximity of the antenna feed to the head, the lack of a shielding ground plane under the antenna and also the lack of a dielectric casing material between the antenna and the head. It is also worthwhile to note that the radiation efficiency values are higher than a typical mobile phone, since for a mobile terminal, the antenna is covered by the hand in one direction and by the head in the other direction, which increases the losses due to absorption and mismatching. Another result to note is the lower SAR value of the location-3 in comparison to the other two locations, since the distance of the antenna element to the tissue is larger. As a conclusion, it can be told that the simulated 1g SAR values are above the standard limit, whereas 10g SAR values are generally acceptable or close to the limit.

Table 6 SAR Comparison for Eyewear Antenna Locations

			0.25W incident power		0.25W power after mismatch	
Position	Freq (MHz)	Radiation Eff (%)	1g SAR	10g SAR	1g SAR	10g SAR
1	1900	25	7.86	3.32	8.37	3.53
1	2200	36	4.31	2.07	4.88	2.35
1	2500	42	4.36	**1.54**	4.39	**1.55**
2	835	10	4.33	2.08	4.96	2.39
2	1900	20	2.97	**1.47**	3.89	**1.92**
2	2200	21	4.18	**1.99**	4.54	2.16
2	2500	21	3.68	**1.83**	4.69	2.33
3	835	13	4.17	2.03	5.50	2.68
3	1900	38	2.47	**1.18**	3.19	**1.53**
3	2200	33	2.22	**1.04**	2.60	**1.22**
3	2500	37	1.96	**0.82**	2.11	**0.89**
Limit			1.6	2	1.6	2

It is well known that the situation with a real head is different from the case with SAM phantom, since the real human head is composed of different tissues at different locations of the head. It was demonstrated in [13-15], that different parts of the body (for example the eyes) may resonate where the fields tend to increase and do not decay with distance. For this reason, a collaboration was established with Loughborough University to investigate the SAR with a visible human (VH) phantom in simulations (Figure 156). Comparisons using simulation results with different human head models were done in [16-17]. Here, the SAR simulation results with VH phantom give similar results with the simulation results using SAM phantom, except minor differences, due to small changes in the distance of the tissues to the head. It is observed that for all antenna positions and frequencies, the maximum SAR is observed on the side of the head. However, for antenna positions 1 and 3, secondary hot spots can be seen around the eye.

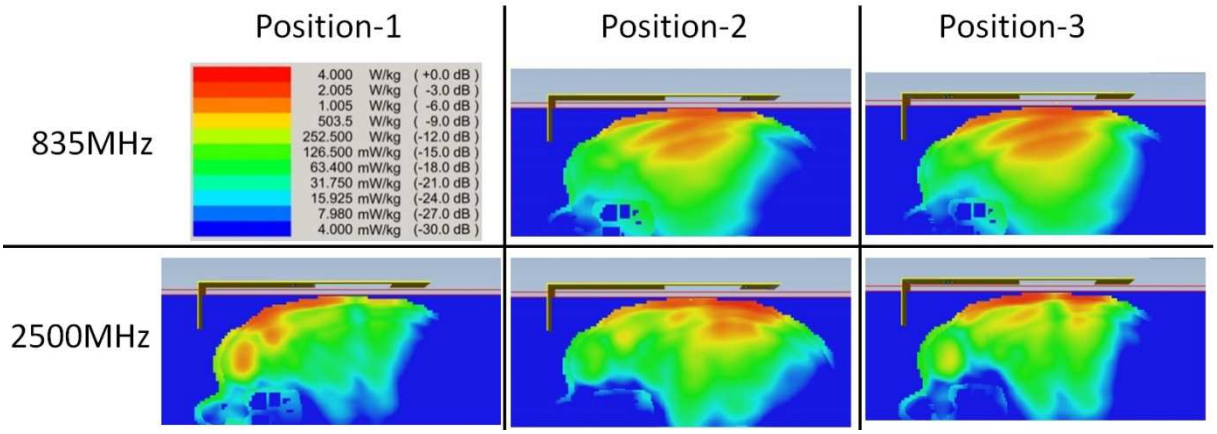

Figure 156 Simulated SAR with the Visible Human Phantom

3. EYEWEAR ANTENNA SOLUTIONS FOR 4G COVERAGE

Keeping in mind the results of the feasibility study, it was foreseen as possible to use printed CEs with corresponding matching networks, to obtain coverage of the 700-960MHz and 1.7-2.7GHz for 4G cellular communication standard. For this purpose three different CE antennas are proposed in this section. With the first antenna, the band between 700-2700MHz is continuously covered (including also the GPS operating frequency band), whereas the other two antennas can cover 700-960MHz and 1.7-2.7GHz simultaneously.

For a more realistic scenario, a dielectric casing with relative permittivity of 2.97 and a loss tangent of 0.029 was modeled and used in the simulations as seen in Figure 157. The 0.8mm thick FR4 substrate is fixed inside the casing using some slits. There is an air gap of 1mm between the PCB and inner edge of the casing (the edge close to the head) and a 3mm air gap between the PCB and outer edge of the casing. The thickness of the dielectric casing is chosen as 1mm. The excitation of the antenna is to be done using a WFL connector (Figure 158, [18]) on the outer side of the PCB, where the CE antennas are also printed. The other face of the PCB (the face towards the head) is used as the ground plane. Three holes are left on the outer face of the casing, to get the WFL cables outside of the casing, for three antenna structures fed from different points on the PCB. This way, a generic frame and casing is obtained, to be compliant with all three antenna prototypes. This model has been manufactured using 3D printing with a semi-rigid material in the facilities of Loughborough University. The manufactured prototype can be observed in Figure 159 on a SAM head phantom.

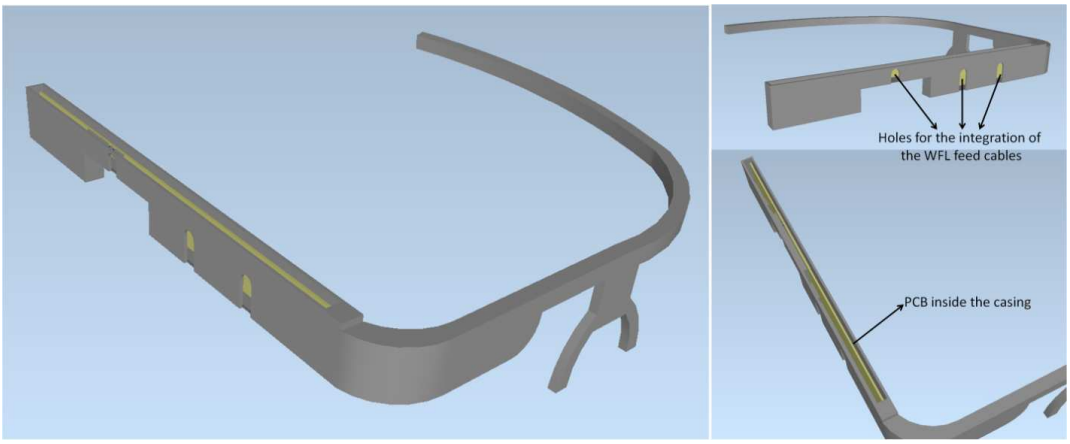

Figure 157 Eyewear Frame Model

Figure 158 WFL Connectors

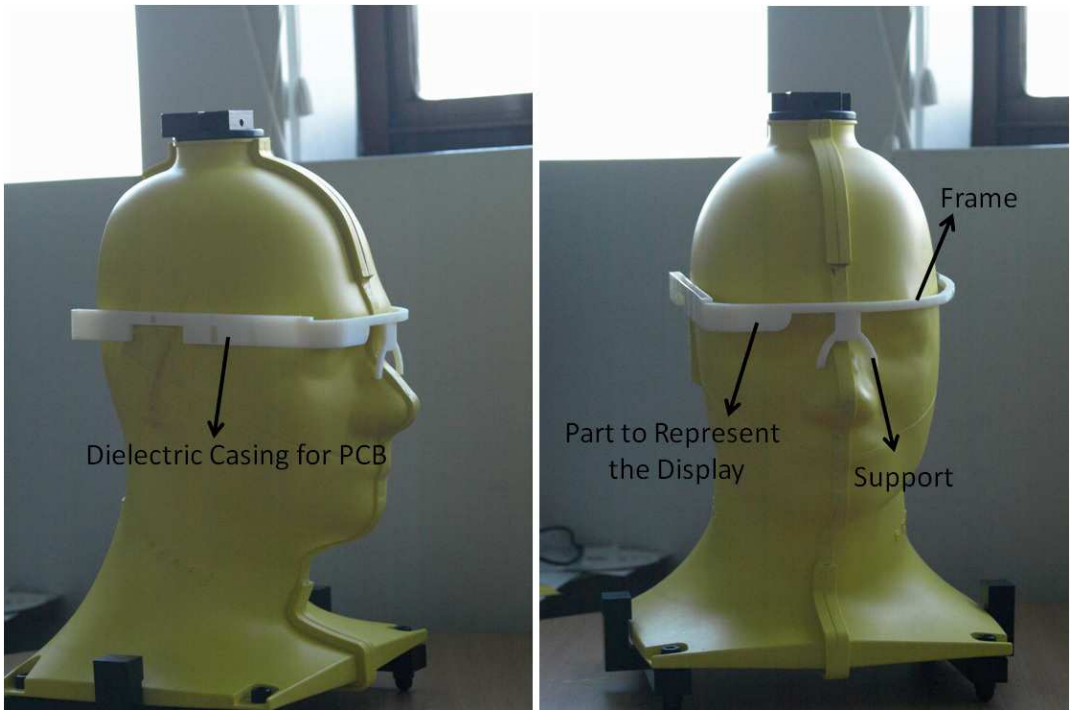

Figure 159 Manufactured Eyewear Frame

For the use cases of the eyewear antennas in real life, three scenarios were evaluated. The first scenario is the eyewear antenna and frame worn onto the head, which is foreseen as the major use case of the device. The antennas were designed and optimized for this scenario. Two other scenarios were also evaluated in the simulations, which are the free space condition and "with head+hand" condition. The free space condition can be evaluated as the use case, where the eyewear device is not worn by the user but should still be functional for the possibility of an incoming call. The other condition, "with head+hand" is the situation when the user changes the settings or the applications of the device, using the touch screen on the side with one or several fingers.

3.1. EYEWEAR ANTENNA-1

The first antenna designed is a CE, printed on the substrate, just behind the ear as seen in Figure 160. The feeding of the CE is done from the edge and a ground clearance is created at the bottom of

the CE. A matching network of 3 lumped components is introduced at the antenna feed. The simulation setups including the frame, casing, antenna, hand and the head can be observed on left of Figure 161 for the "head" configuration and on the right for the "head+hand" configuration.

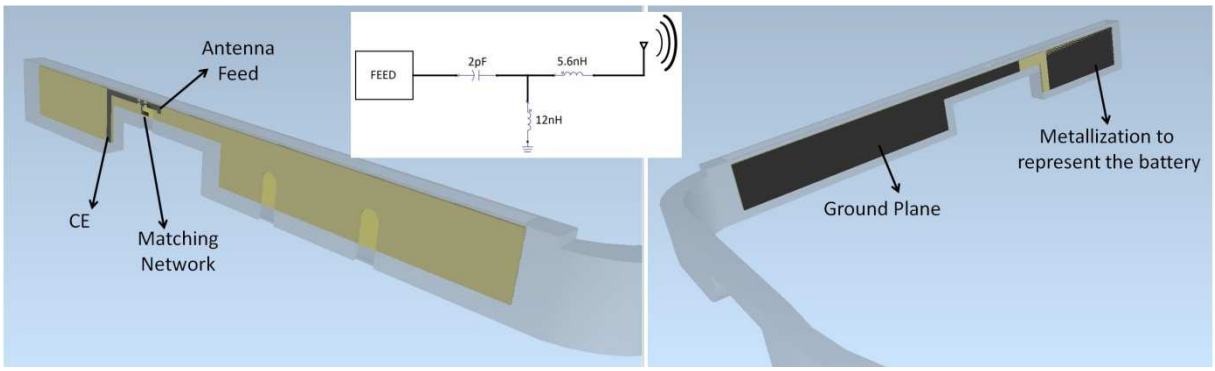

Figure 160 Eyewear-Antenna-1 Model

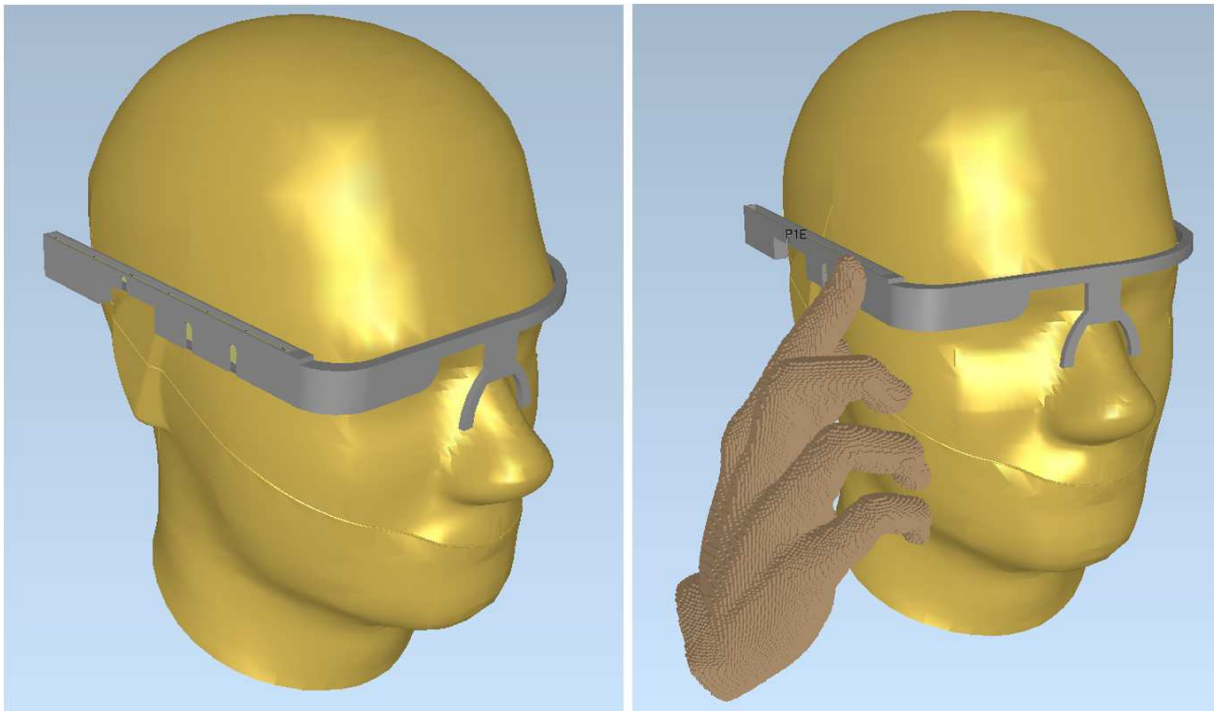

Figure 161 Positioning of the Head and Hand Phantom in Two Simulation Scenarios

The simulated input impedance, with and without the matching network can be seen in Figure 162 (in head configuration), in smith chart form plotted between 700-2700MHz. The corresponding reflection coefficient is shown in Figure 163. The antenna has a reflection coefficient below -6dB between 700-2700MHz, covering GPS operating frequency in addition to the 4G cellular communication frequency band.

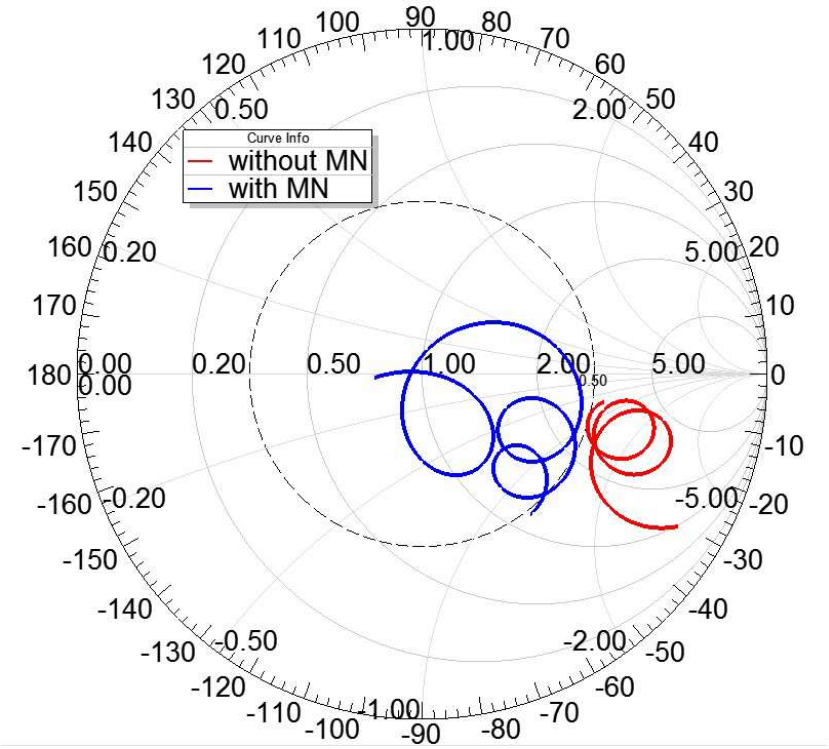

Figure 162 Simulated Impedance with Head (with and without MN) for Eyewear Antenna-1

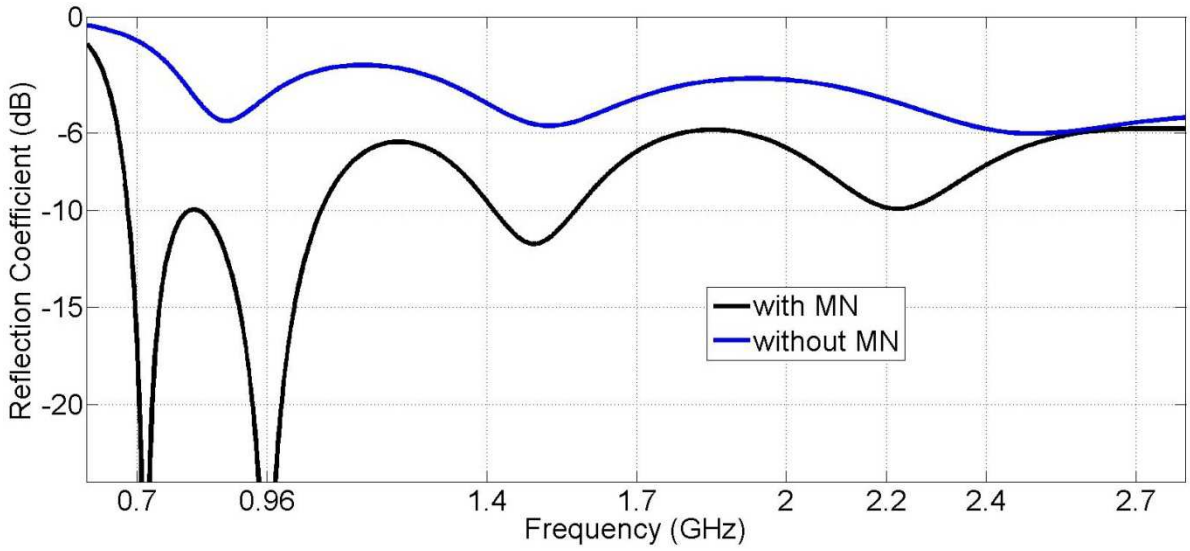

Figure 163 Simulated Reflection Coefficient (with and without MN) for Eyewear Antenna-1

Figure 164 shows the simulated 3D gain pattern of the antenna in 800Mhz and 2200MHz. The radiation is concentrated away from the head as expected due to the absorption by the head. Table 7 summarizes the simulated SAR values for three different frequencies both for 1g and 10g standards, normalized for 0.25W input power. As seen, the SAR values are high when compared to the limit in the standards (1.6W/kg for 1 gram of tissue and 2W/kg for 10 gram). The main reason is the proximity of the radiating element to the tissue in the eyewear device when compared to a typical mobile terminal, considering the antennas are generally placed on the bottom of the terminal. The SAR values can be lowered to some extent by arranging the output power from the transmitter or by increasing the distance of the antenna to the head, which will results in a thicker eyewear frame.

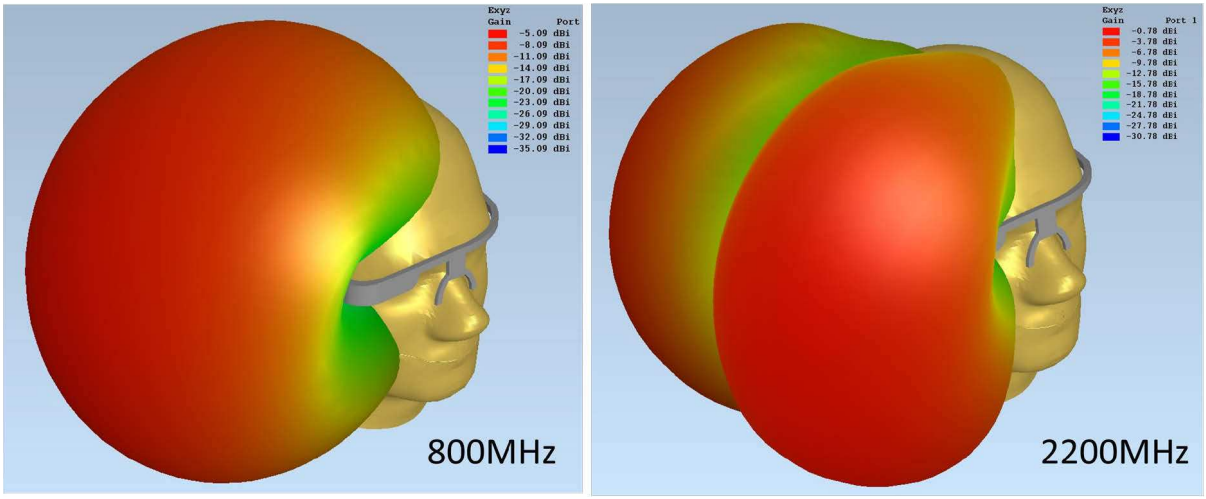

Figure 164 Simulated 3D Gain Pattern of Antenna-1

Table 7 Simulated SAR for Eyewear Antenna-1

	1g SAR	10g SAR
900MHz	5.17	2.99
2100MHz	11.28	4.90
2400MHz	8.75	3.28

The antenna was simulated also in the three use cases, mentioned before. The reflection coefficient "with head", "free space" and "with head+hand" can be observed in Figure 165. The effect of the finger close to the antenna casing do not show a significant impact on the antenna impedance and do not cause detuning, since the CE is further away from the finger. In free space, the reflection coefficient is still below -6dB in the LB, but it goes above -6dB (rising up to -3.5dB) between 1.85-2.35GHz in the HB.

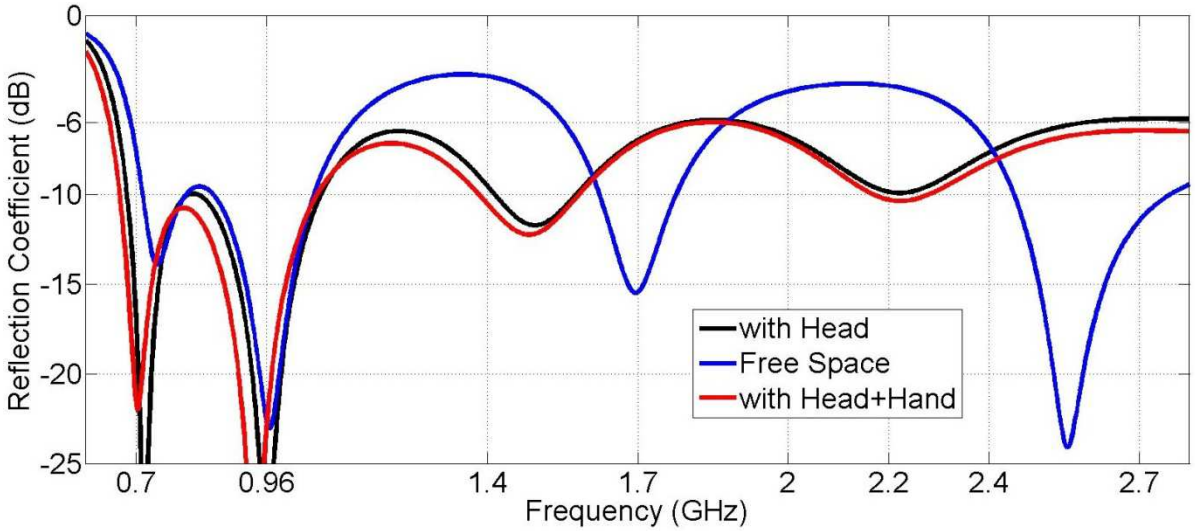

Figure 165 Simulated Reflection Coefficient for Eyewear Antenna-1 in Different Scenarios

The simulated radiation efficiency is between -13dB and -9.5dB in the LB and between -8.5dB and -6.5dB in the HB (Figure 166) in head condition. As also mentioned before, the efficiency values are considerably higher than a typical mobile terminal antenna, namely -14dB in LB and -10dB in HB for the antennas in chapter IV. The introduction of the hand do not cause significant change in the LB, but decreases the radiation efficiency by 0.5-2dB in the HB.

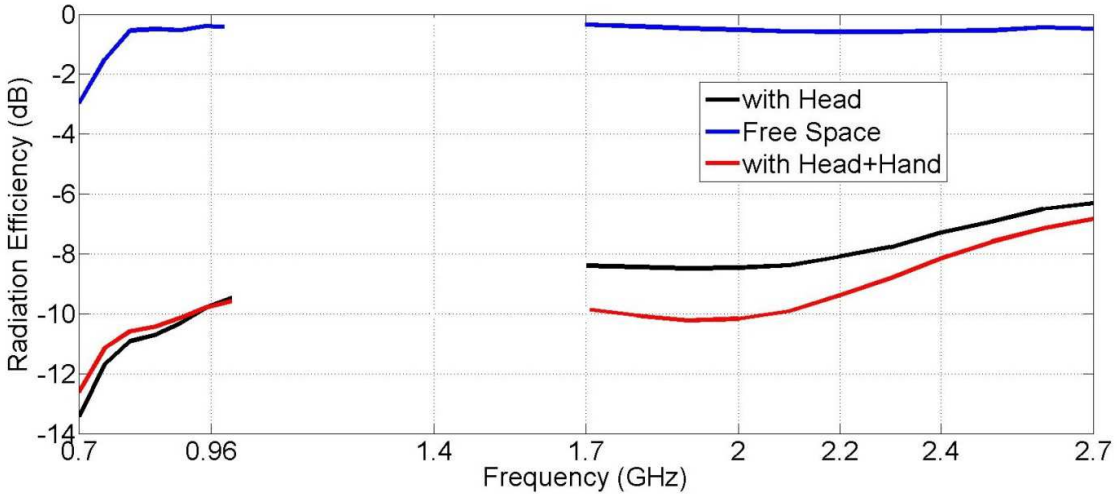

Figure 166 Simulated Radiation Efficiency for Eyewear Antenna-1 in Different Scenarios

3.2. EYEWEAR ANTENNA-2

For the second eyewear antenna design, the CE has been moved to the other edge of the PCB, close to the eye (Figure 167). There is again a MN of three lumped components at the antenna feed. The effect of the MN on the antenna input impedance can be evaluated in Figure 168, where the curves are plotted between 700-960MHz for the LB (smith chart on the left) and 1.7-2.7GHz for the HB (smith chart on right).

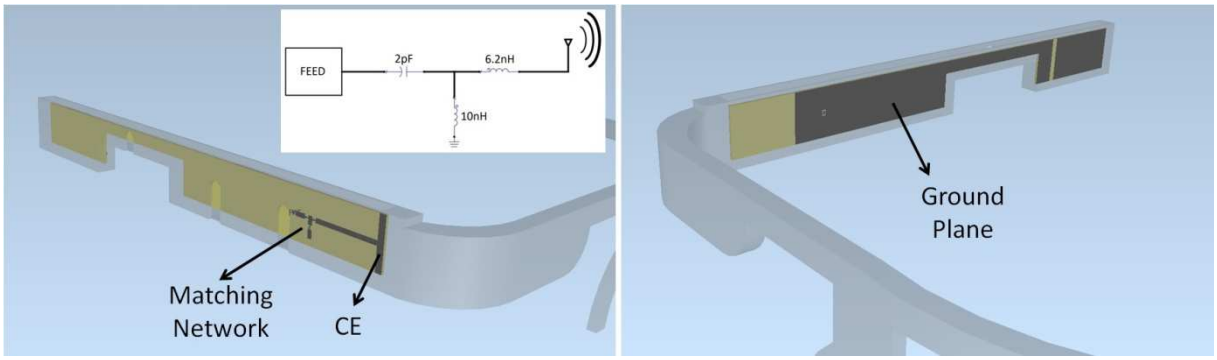

Figure 167 Eyewear-Antenna-2 Model

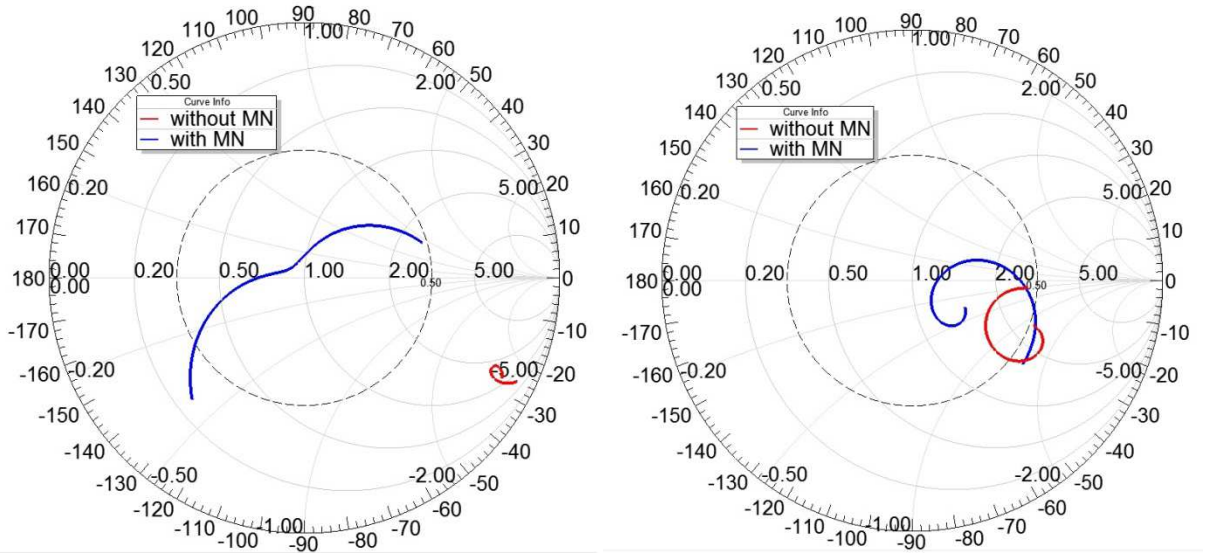

Figure 168 Simulated Impedance with Head (with and without MN) for Eyewear Antenna-2 (LB on left, HB on right)

The antenna has a reflection coefficient below -6dB between 710-960MHz in the LB and between 1.35-2.4GHz in the HB. There is slight overshoot of up to -5dB between 2.4-2.7GHz of the target band.

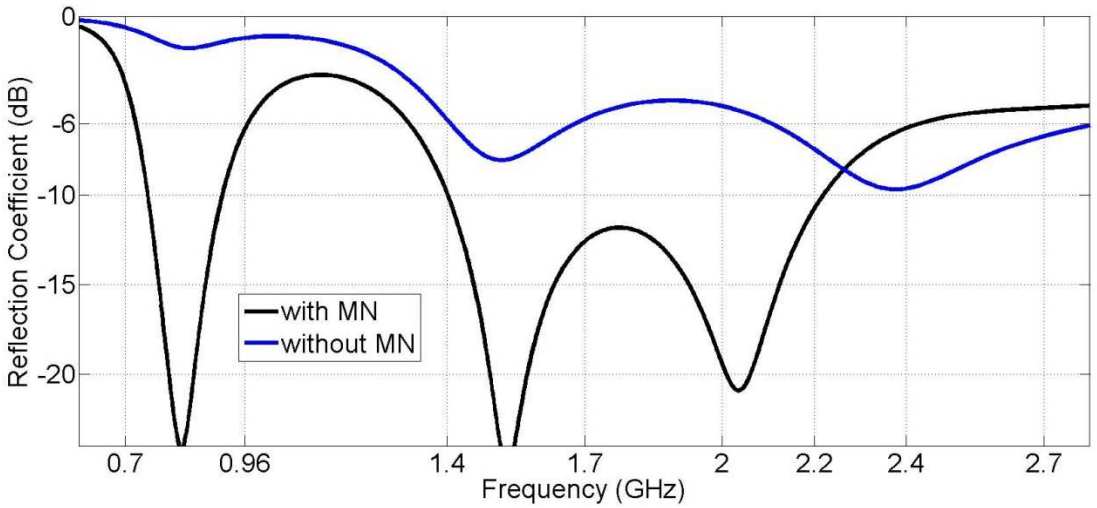

Figure 169 Simulated Reflection Coefficient (with and without MN) for Eyewear Antenna-2

Figure 170 presents the 3D gain pattern in two different frequency points. The simulated SAR values again yield high values (Table 8) as in the previous prototype, being higher than the maximum limit for 0.25W input power.

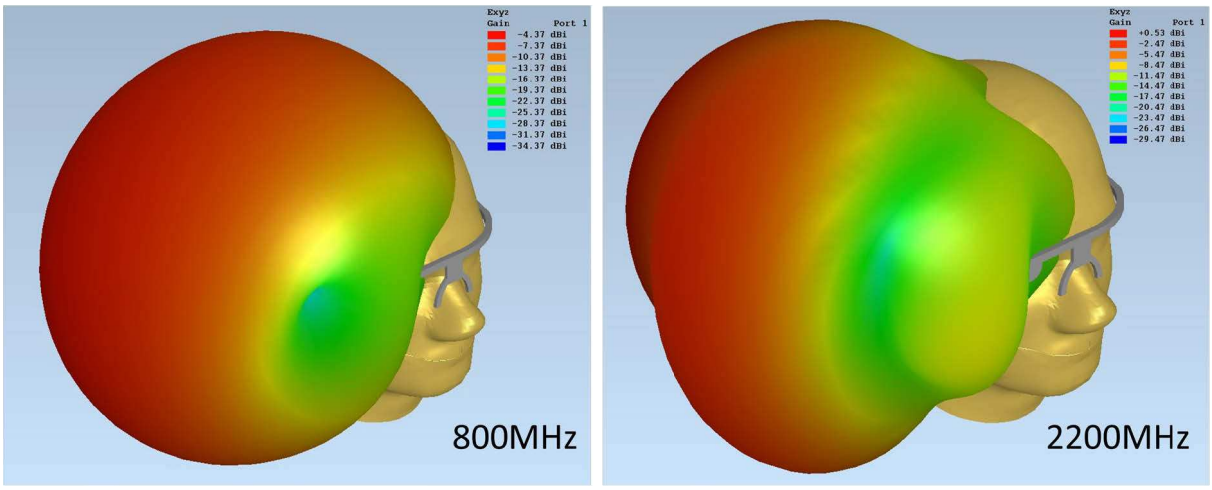

Figure 170 Simulated 3D Gain Pattern of Antenna-2

Table 8 Simulated SAR for Eyewear Antenna-2

	1g SAR	10g SAR
900MHz	4.13	2.39
2100MHz	9.80	4.62
2400MHz	7.25	3.13

When the reflection coefficient for different scenarios is observed in Figure 171, it can again be seen that the detuning is not effective due to the finger. However it is seen that the finger effect is more noticeable compared to previous antenna since the finger is closer to the radiating element. In free space, the LB performance is preserved but an overshoot up to -3.5dB is seen in HB above 2.4GHz.

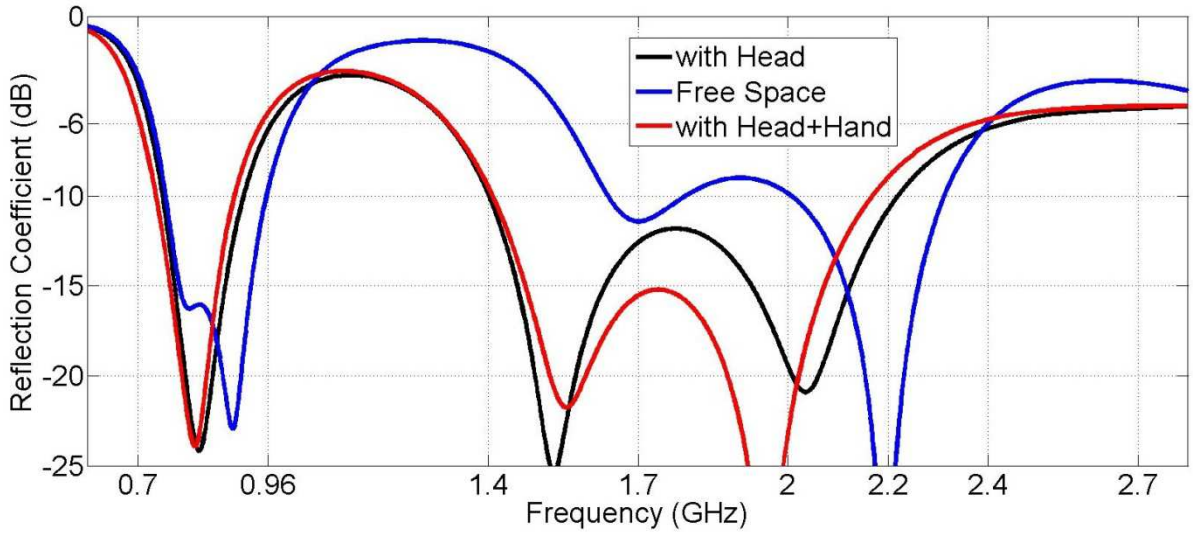

Figure 171 Simulated Reflection Coefficient for Eyewear Antenna-2 in Different Scenarios

The simulated radiation efficiency is between -11dB and -10dB in the LB and between -6.5dB and -5dB in the HB (Figure 172) for "with head" scenario. The effect on radiation efficiency is minimal

with the introduction of the hand in the LB, however a decrease of approximately 2dB is seen in the HB.

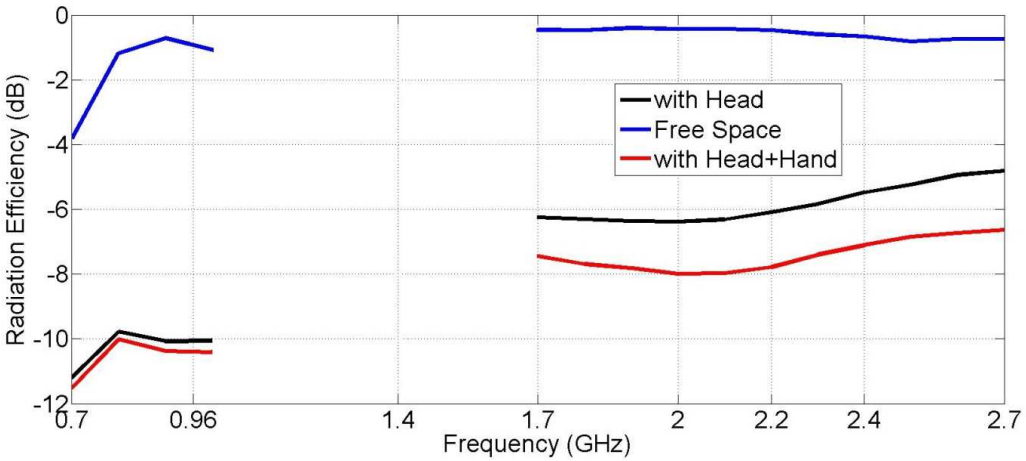

Figure 172 Simulated Radiation Efficiency for Eyewear Antenna-2 in Different Scenarios

3.3. EYEWEAR ANTENNA-3

For the third antenna design, the CE is located in the middle of the PCB section in front of the ear (Figure 173), with a MN of three lumped elements at the feed. The impedance of the antenna with and without MN is presented in Figure 174.

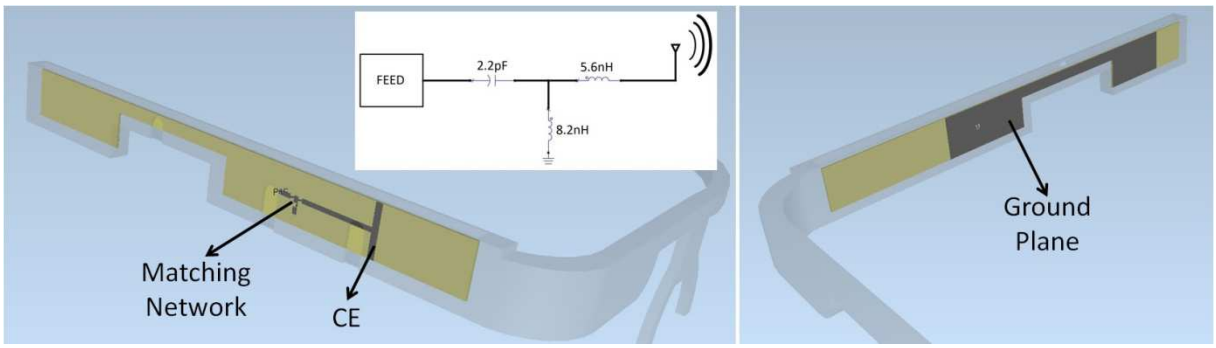

Figure 173 Eyewear-Antenna-3 Model

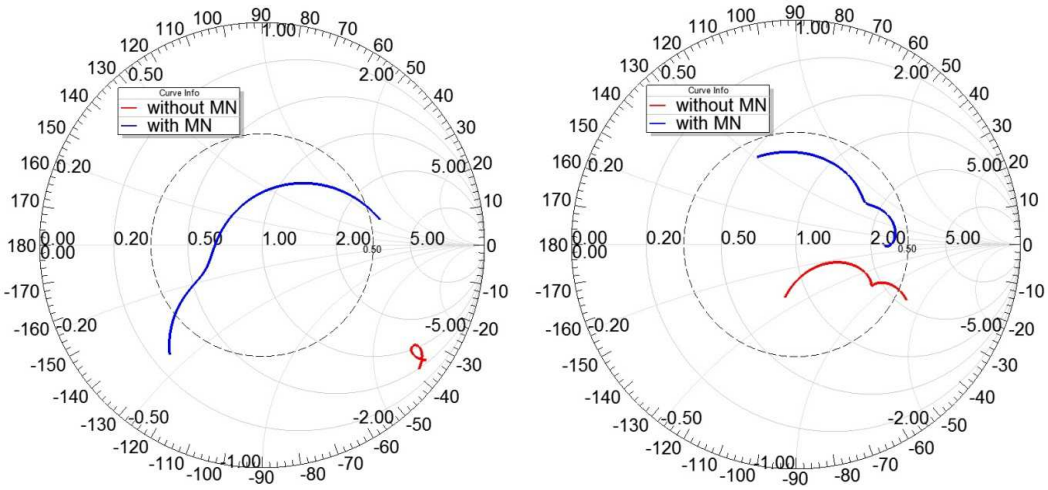

Figure 174 Simulated Impedance with Head (with and without MN) for Eyewear Antenna-3 (LB on left, HB on right)

The third antenna proposed, has a reflection below -6dB between 710-950MHz and 1.55-2.7GHz (Figure 175).

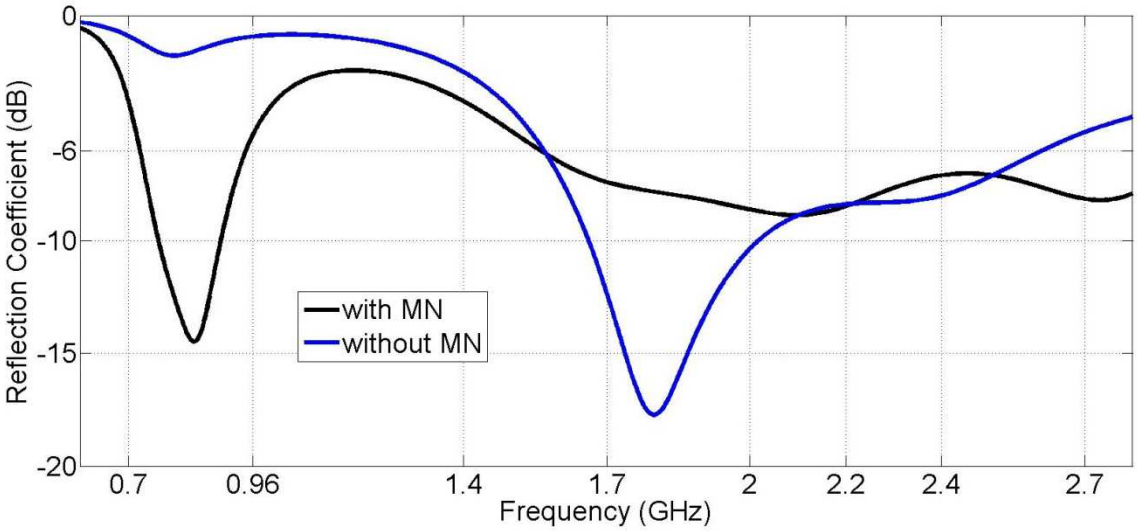

Figure 175 Simulated Reflection Coefficient (with and without MN) for Eyewear Antenna-3

Figure 176 shows the simulated 3D pattern of the antenna. The results of the SAR simulations for three frequency points are given in Table 9.

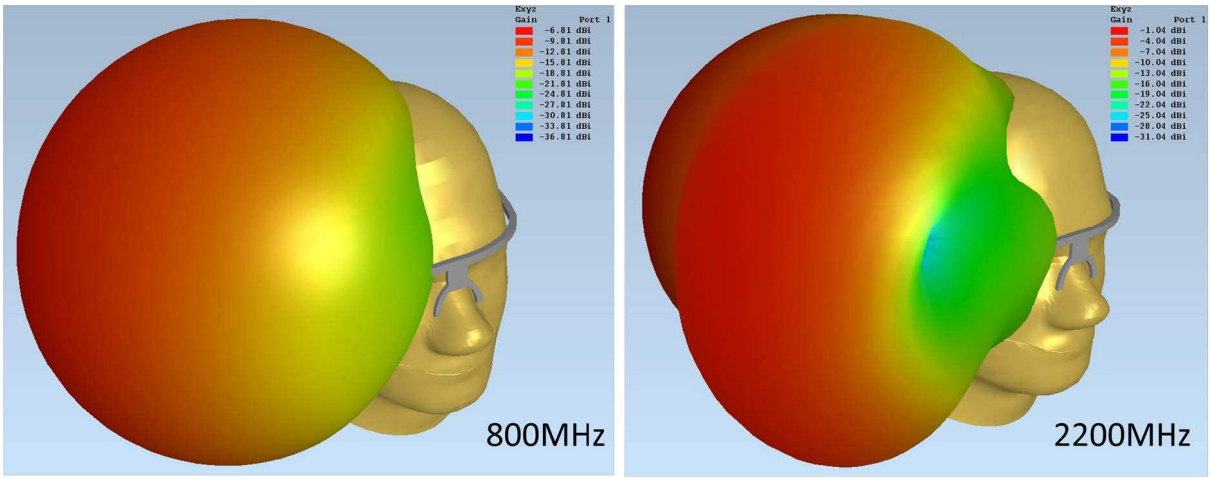

Figure 176 Simulated 3D Gain Pattern of Antenna-3

Table 9 Simulated SAR for Eyewear Antenna-3

	1g SAR	10g SAR
900MHz	4.67	2.55
2100MHz	8.77	4.18
2400MHz	7.76	3.51

As in previous designs, the hand does not cause any detuning on the antenna reflection coefficient(Figure 177). However, in free space condition, the HB coverage is effect significantly, having a reflection coefficient below -6dB only between 2-2.55GHz.

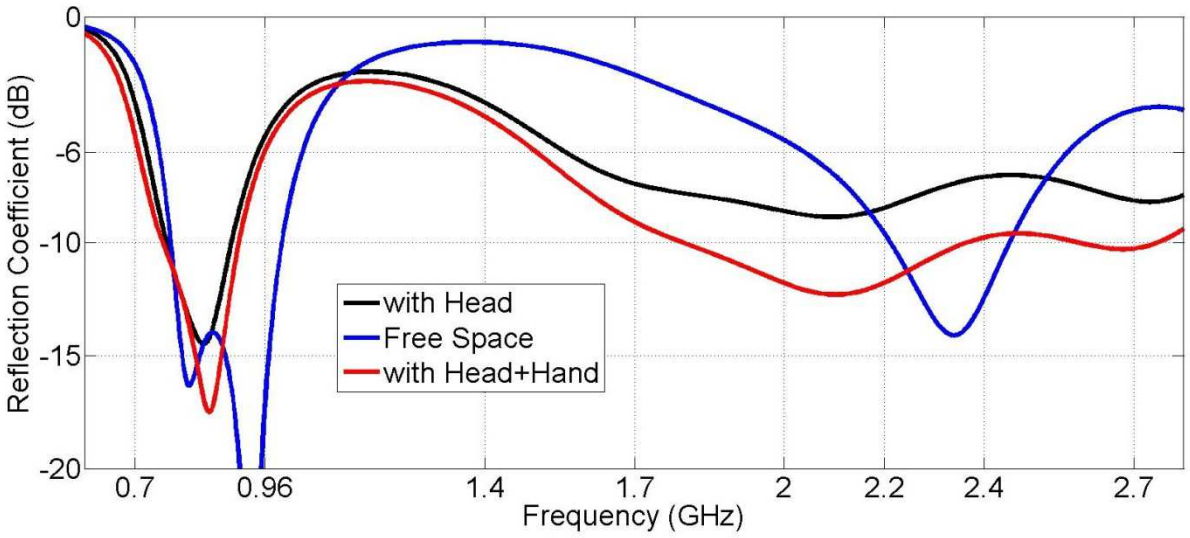

Figure 177 Simulated Reflection Coefficient for Eyewear Antenna-3 in Different Scenarios

The simulated radiation efficiency is between -14dB and -12.5dB in the LB and between -8dB and -6.5dB in the HB (Figure 178) with the head. The hand causes an efficiency drop of up to 1.5dB in the HB.

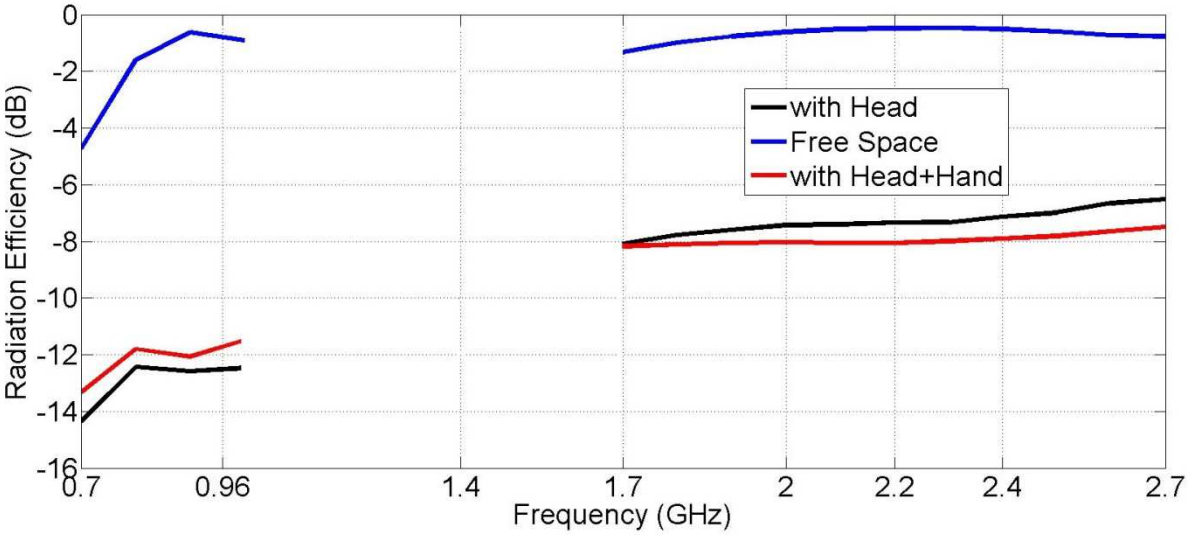

Figure 178 Simulated Radiation Efficiency for Eyewear Antenna-3 in Different Scenarios

4. CONCLUSION

In this chapter, an application example of CEs was presented, differently from mobile terminal antennas. The CEs were used to obtain coverage in the 4G cellular communication bands, in an eyewear structure, which are gaining popularity in the market as wirelessly connected wearable devices. Firstly, a feasibility study was performed using three different locations (behind the ear, in front of the ear and close to the eye) for the CEs, comparing the bandwidth potential and the expected SAR value. It was shown through the simulation results that placing the antenna just in front of the ear was giving the worst bandwidth potential. The potential was higher in "close to the eye" location and the highest behind the ear. It should be noted that these results are subject to

change due to modifications on the system ground plane. For the SAR, the minimum value was observed with "close to the eye" location since the radiating structure is further from the head when compared to the other two locations.

Taking into account the feasibility study, three antennas were designed, with a dielectric casing & frame. The first antenna, which is placed behind the ear, had the highest operating bandwidth with a continuous coverage from 700MHz up to 2.7GHz with a three element MN at the feed. The other two designs cover the 700-960MHz and 1.7-2.7GHz. The simulated radiation efficiencies are generally on the level of -12dB for the LB and -7dB for the HB. However, there is a significant increase in the radiation efficiency when the CE is placed close to the eye, since the head is further from the antenna, reducing the losses. For evaluating the real use case of the device, simulations were performed also with the user hand and in free space condition. It was shown through simulations that the hand does not cause a significant detuning, however poorer reflection coefficient behavior may be seen in free space, as expected.

5. PERSPECTIVES

The first target concerning the eyewear antennas is the fabrication of the antennas and the corresponding PCBs with MNs. Using the PCBs with the already manufactured dielectric frames, the measurements for the S-Parameters and total efficiency will be realized considering free space, with head and with hand+head conditions, as well as SAR measurements.

For the future steps, a MIMO scenario will be considered. The first idea about obtaining MIMO operation is to place one antenna on the right side of the head and the other to the left side. In this way, a good isolation level was observed in the initial simulations since the head acts as an absorbing element between the antennas, increasing the isolation. Considering the general characteristics of the radiation pattern (radiating away from the head), a low ECC value is also foreseen with this topology.

Another possible investigation will be based on the effects of the metallic frames instead of dielectric frames. The effect of metallic frames on the SAR of mobile terminals has been previously investigated in [19-23], showing the possibility of significant effects. For this reason, simulation and measurements will be repeated with metallic frames to compare the general antenna characteristics (with dielectric frame) as well as SAR levels.

REFERRENCES FOR THIS CHAPTER

[1] "Google Glass," Available at:http://www.google.com/glass/start/

[2] "M100 Smart Glass," Available at:http://www.vuzix.com/UKSITE/consumer/products_m100.html

[3] "RECON Jet," Available at: http://www.reconinstruments.com/products/jet/

[4] "Olympus MEG4.0," Available at: http://www.olympus.co.jp/jp/news/2012b/nr120705meg40j.jsp

[5] "Optinvent ORA," Available at: http://optinvent.com/see-through-glasses-ORA

[6] H. Jidhage, A. Stjernman, "Hooked loop antenna concept for bluetooth headset applications," IEEE Antennas and Propagation Conference 2004 (AP-S 2004), July 2004, pp. 3521-3524.

[7] J-H. Chou, S-W. Su, "Matching a bluetooth headset antenna on a small system ground by using a conductive wire," Microwave and Optical Technology Letters, vol. 51, no. 12, December 2009, pp. 2802- 2805.

[8] K-L. Wong, M-R. Hsu, W-Y. Li, S-W. Su, A. Chen, "Study of the bluetooth headset antenna with the user's head," Microwave and Optical Technology Letters, vol. 49, no. 1, January 2007, pp. 19-23.

[9] J. Anguera, A. Andújar, C. Picher, L. González, C. Puente, S. Kahng, "Behavior of several antenna topologies near the human head at the 2.4-2.5 GHz band," Microwave and Optical Technology Letters, vol. 54, no. 8, August 2012, pp. 1911- 1916.

[10] EMPIRE XCcel, Information available at: http://www.empire.de/

[11] IEC, "Human Exposure to Radio Frequency Fields From Hand-Held and Body- Mounted Wireless Communication Devices—Human Models, Instrumentation, and Procedures—Part 1: Procedure to Determine the Specific Absorption Rate (SAR) for Hand-Held Devices Used in Close Proximity to the Ear (Frequency Range of 300 MHz to 3 GHz)," IEC 62209-1:2005, 2005.

[12] IEEE, "IEEE recommended practice for determining the peak spatial-average specific absorption rate (SAR) in the human head from wireless devices: Measurement techniques," IEEE Std 1528, 2003.

[13] W. G. Whittow and R. M. Edwards, "A study of changes to specific absorption rates in the human eye close to perfectly conducting spectacles within the radio frequency range 1.5 to 3.0GHz," IEEE Trans. Antennas and Propag., vol. 52, no. 12, pp. 3207–3212, 2004.

[14] V. Singh, A. Qusba, A. Roy, R. A. Castro, K. Mcclure, R. Dai, R. J. Greenberg, J. D. Weiland, M. S. Humayun, and G. Lazzi, "Specific Absorption Rate and Current Densities in the Human Eye and Head Induced by the Telemetry Link of an Epiretinal Prosthesis," IEEE Trans. on Antennas and Propagation, vol. 57, no. 10, pp. 3110–3118, 2009.

[15] W.G. Whittow, C.J. Panagamuwa, R.M. Edwards and J.C. Vardaxoglou, "On the effects of straight metallic jewellery on the specific absorption rates resulting from face-illuminating radio communication devices at popular cellular frequencies," Phys. Med. Biol., Vol. 53, pp. 1167-1182, 2008.

[16] B. Beard, et al., "Comparisons of Computed Mobile Phone Induced SAR in the SAM Phantom to That in Anatomically Correct Models of the Human Head," IEEE Trans. Electromagnetic Compatibility, vol. 48, no. 2, pp. 397–407, 2006.

[17]M. Siegbahn et al., “An International Interlaboratory Comparison of Mobile Phone SAR Calculation With CAD-Based Models,” IEEE Transactions on Antennas and Prop., vol. 52, no. 4, pp. 804–811, 2010.

[18]Hirose Electric Group, Available at: http://www.hirose.com/

[19]G. Bellanca, G. Caniato, A. Giovannelli, P. Olivo, S. Trillo, “Effect of field enhnancement due to the coupling between a cellular phone and metallic eyeglasses,” Microwave and Optical Technology Letters, vol. 48, no. 1, January 2006, pp. 63- 65.

[20]C.J. Panagamuwa, W.G. Whittow, R.M. Edwards, J.C. Vardaxoglou, “A Study of the Effects of Metallic Pins on SAR using a Specific Anthropomorphic Mannequin (SAM) Head Phantom,” The Second European Conference on Antennas and Propagation(EUCAP), 2007. 11-16 Nov. 2007

[21]C.J. Panagamuwa, W.G. Whittow, R.M. Edwards, J. Ma, J.C. Vardaxoglou, “Effects of metallic spectacles on SAR when using communications enabled PDAs in front of the face,” Loughborough Antennas and Propagation Conference(LAPC), 2008. pp.361,364, 17-18 March 2008

[22]O. Ojerinde, O. C.J. Panagamuwa, W.G. Whittow, R.M. Edwards, “SAR variations in the face due to semi-rimmed spectacles and polarized sources at GSM900 and GSM1800,” 3rd European Conference on Antennas and Propagation(EUCAP), 2009. pp.2962,2966, 23-27 March 2009

[23]M. H. Mat, M. F. B. A. Malek, W. G. Whittow, S. H. Ronald, M. S. Zulkefli, N. Saudin, and L. Mohamed, “The influence of human head model wearing metal-frame spectacles to the changes of SAR and antenna gain: simulation of frontal face exposure,” Progress In Electromagnetics Research, Vol. 137, 453-473, 2013.

CONCLUSION

Several different antenna designs have been proposed in this thesis, for mobile terminals operating in the 4G frequency bands, i.e 700-960MHz and 1.7-2.7GHz. A variety of strategies have been evaluated like single/multi-feed and also passive/active antennas. Antenna alternatives for different mobile communication devices (like electronic eyewear) operating in 4G standards have also been mentioned.

Tunable components have been evaluated in circuits placed at the feed of mobile terminal antennas to achieve frequency band reconfigurability in Chapter II. MEMS switches and BST tunable capacitors were used as the tunable components, which are under development in the scope of the Artemos project by partners. Two antennas exploiting the MEMS switches were proposed and the main aim was to obtain a band switching behavior, to select either LB (700-960MHz) or HB (1.7-2.7GHz) operation. Two such antenna designs were proposed, where one of the design uses two SPDT MEMS switches to select between one of the two MN branches and the other uses only one switch to select one of the two driven strips. Due to components' reliability difficulties, S-Parameter measurements could be performed for only one of these prototypes. For the measurement of the other prototype, passive antennas were manufactured and band-switching performance was verified this way. The target bands could be covered comfortably with a reflection coefficient below -6dB (observed as generally below -7dB or -8dB) in the measurements. The passive prototypes were also used for the total efficiency measurements, which are on average 50% in the LB and 65% in the HB. It should be noted that these values will for sure be subject to a slight decrease taking into account the insertion losses of the MEMS switches. Another antenna design was also proposed using a BST capacitor to tune the input impedance of the antenna in the 700-960MHz frequency range. The coverage of the HB was achieved with a separately fed antenna composing a dual-feed system. The measurement results of this antenna is planned to be done as soon as the integration of the BST capacitor to the antenna PCB is done.

The main advantage of the antennas with tunable components is the relatively lower reflection coefficient obtained especially in the LB (around -8dB), when compared to other passive prototypes. This would result in higher total efficiency than passive prototypes however considering also the insertion losses of the tunable elements and also the effect of the bias lines, a similar level in terms of total efficiency can be foreseen. On the other hand, the main drawback was the reliability of the tunable elements. The main reason is the continuing design & optimization phase for these components by their manufacturers (in Artemos project). More reliability and repeatability is foreseen after the finalization of the optimization phase of the components. Another disadvantage when compared to passive prototypes is the additional losses due to internal resistances of the tunable elements, which will in return cause decrease in the total efficiency. There is also the disadvantage about the carrier aggregation for LTE-A standards. For example for the band-switching topologies (with MEMS switches), it is not possible to use inter-band carrier aggregation since either the LB or HB is matched at a time.

In Chapter II, a study about the circuit model representation of a driven strip with a grounded parasitic strip was also carried out. The accordance of the circuit model was verified through electromagnetic simulations. Another issue addressed in this chapter was the radiation efficiency drop, that occurs in the HB for the antennas using parasitic strips. Solution techniques have been proposed using some modified topologies.

A summary of the tunable antennas mentioned in Chapter II can be seen in Table 10. The green shaded results in the table indicate measurement results with passive prototypes, blue shaded results indicate active measurements and yellow fields indicate simulations.

Table 10 Summary of the Performance of Tunable Antennas

	S11(dB) in LB		S11(dB) in HB		Eff(dB) in LB		Eff(dB) in HB		PCB Length	GND Length	Height
	Max	Min	Max	Min	Min	Max	Min	Max			
MEMS-1	-7	-16.2	-3.8	-30	- 3.7	-1.5	-3.5	-1.1	120mm	107mm	-
MEMS-2	-5.7	-17	-11.3	-33.7	-4.9	-1.7	-2.5	-1.1	115mm	100mm	-
BST	-3.2	-27.3	-4.9	-32	-	-	-	-	120mm	105mm	-

Dual-feed antenna structures using coupling elements were proposed in Chapter III, again covering the 4G standard frequencies. In these designs, the plain CE which was used extensively in the literature for mobile terminal antennas was modified, making it hollow. The coverage of the LB was achieved using these hollow CEs, with appropriate matching networks. Separately-fed monopole type antennas were used for the HB coverage, obtaining high isolation levels thanks to both antenna placement and band-stop characteristics of the matching networks. Measured total efficiency levels of 40-50% and 50% (on average) were obtained in the LB and HB respectively, which are over the 50% level generally expected in free space for mobile terminal antennas. These antennas had the advantage of being appropriate for both intra-band and inter-band carrier aggregation. A further advantage of the dual-feed topology is the opportunity to get rid of a diplexer in the RF front-end for inter-band carrier aggregation, which is definitely needed in a single feed antenna. An application example of the hollow CEs was further proposed in the same chapter, by placing two CEs on the corners of the PCB, to achieve MIMO operation in the LB (between 740-960MHz). The isolation between the two elements in lower LTE band was enhanced using a neutralization line between the antennas.

In Chapter IV, single-feed antenna designs manufactured using LDS technology were presented. Both antennas consist of a driven strip which capacitively excites a grounded parasitic strip for bandwidth enhancement. One of these antennas covers the low LTE/GSM/UMTS bands, whereas the other covers all the 4G bands. The main challenge for these antennas was the short ground plane (75mm, considered because of the 3.5 inch touchscreens common in most of modern smartphones), which makes it difficult to cover down to 700MHz. The total efficiencies of the antennas with 75mm ground plane were on average 35% in LB and 50% in HB. When the ground plane length was increased to 90mm, the LB efficiency was increased by approximately 10%, without any significant change in the HB. The effect of the user's hand and head was investigated on these antennas through measurements, to form a basis for future studies. The first results of this study were also presented at the end of the chapter, proposing an antenna topology resistant to detuning due to the hand of the user (in simulations only).

A comparison of passive antenna prototypes from Chapter III and Chapter IV is presented in Table 11, in terms of dimensions, reflection coefficient and efficiency. All the values presented in the table are measured results.

Table 11 Summary of the Performance of Passive Antennas

	S11(dB) in LB		S11(dB) in HB		Eff(dB) in LB		Eff(dB) in HB		PCB Length	GND Length	Height
	Max	Min	Max	Min	Min	Max	Min	Max			
HollowCE	-4.7	-9.1	-2.8	-27.5	-6	-1.9	-4.3	-1	114mm	100mm	3mm
PrintedCE	-3.1	-9	-3.8	-15	-5.1	-1.5	-4.3	-1.2	114mm	100mm	-
UMTS LDS	-5	-22	-5.2	-19	-7.7	-3	-3.9	-2	114mm	75mm	5mm
LTE LDS	-3.8	-15.9	-3.5	-16.3	-14	-3.1	-5.5	-1.7	114mm	75mm	5mm

Finally in Chapter V, antennas using coupling elements were proposed for 4G operation in an eyewear antenna. First, a feasibility study was presented by evaluating three different positions for the CE on the PCB of the electronic eyewear device, considering the bandwidth potential and SAR. Afterwards, three antennas were proposed with appropriate matching networks. The behavior of these three antennas was evaluated in different use cases like free-space, with the head and with head and hand (to stand for the user changing applications or settings by putting his finger on the touchpad).

To sum up, it can be told that the desired performances in terms of reflection coefficient (below -6dB) and total efficiency (higher than 50% in free space) have been achieved with the novel antenna designs in this thesis. A final note can be made be on the utilization of active tunable elements, comparing the tunable/passive antenna designs in this thesis. As presented, the passive antennas can reach the target performance without any tunable components in free space condition. This way, the additional losses, complexity (like biasing circuit) and reliability concerns from the tunable elements can be avoided. However, the utilization of the tunable components can be very useful for minimizing the effect of the user and increasing the total efficiency of the antenna for instance in a tunable matching unit at the antenna feed .

FUTURE PERSPECTIVES

A possible improvement for the antennas presented in this thesis can be to minimize the effect of the user on the reflection coefficient and by this way increase the total efficiency taking into account the user's hand, head or both. The user effect (hand and head) have been investigated for the single-feed antennas in Chapter IV (antennas on LDS) and it was seen through measurements that the antennas (placed on the bottom of PCB) get detuned (towards lower frequencies) when the hand of the user is taken into account.

A different antenna design technique was recently proposed in [1-3], considering in the design phase the matching performance of the antenna in the presence of the user. This technique relies on combining the antenna design with circuit design concepts to cover 700-960MHz, 1.7-2.2GHz and 3.3-3.8GHz frequency bands [1]. The novelty of the design is to transfer the complexity of the antenna design to the complexity of the circuit before the antenna (at the antenna feed). The main aim is to get a very wideband antenna so the detuning effect due to the user (which unavoidably exists) is minimized by this way. In these designs, multiple simple IFA type radiators are used. The first and second order resonances of these radiators are selected and combined together to get a wideband response using diplexers and power divider/combiners resulting in a single-feed topology. These circuitries are composed of lumped SMD inductors/capacitors with up to 27 lumped elements.

This approach proves to be very robust to detuning due to user effects in cases like right/left hand and with head (in right/left hand configurations). When this methodology is compared with the results of the antennas in Chapter IV of this thesis, it is evident that the total efficiency is considerably lower (on average) in this methodology for free space condition (between 5-40% in LB and 15-55% in HB). This relatively low efficiency may cause a problem for the mobile phone manufacturers during the manufacturing tests in free space condition. Although robust to detuning, the measured efficiency with the user hand in [1] (5% in LB, 10% in HB on average) is also lower by approximately 3dB when compared to the antennas in this thesis. The results are approximately the same for the measurement with the head. However, one good advantage of this approach is that the designs can be integrated to any mobile phones by changing the values of the components in the circuitry.

Keeping this in mind, the main focus for the future studies on the user effects of the antennas in this thesis should be to minimize the detuning. For this purpose, some rule of thumbs were deduced in Chapter IV, from the measurements with hand/head to foresee the possible changes in the input impedance with user effects. Using this background, the first results from a dual-feed antenna design was presented with both simulations and measurements.

Another study was also started to design a wideband antenna as to cover 700MHz-2700MHz continuously, both to minimize the detuning due to user effects and also to enable the coverage of possible other standards (like GPS). The main target is to obtain a very high bandwidth potential around 1700MHz (which is the center frequency in this case) and thus obtain a very wideband antenna. For this purpose, the first simulation results of the antenna given in Figure 179 can be seen in Figure 180. The antenna consists of a driven strip printed under the plastic piece (same as the plastic pieces in antennas manufactured with LDS technology), which capacitively excites a loop antenna connected to the system ground plane at both ends. To increase the electrical length of the loop, two lumped inductors (each 25nH) are modeled in series with the loop, located at the

grounding points. A two element matching network consisting of a shunt capacitor (0.6pF) and series inductor (5.6nH) is used at the feed.

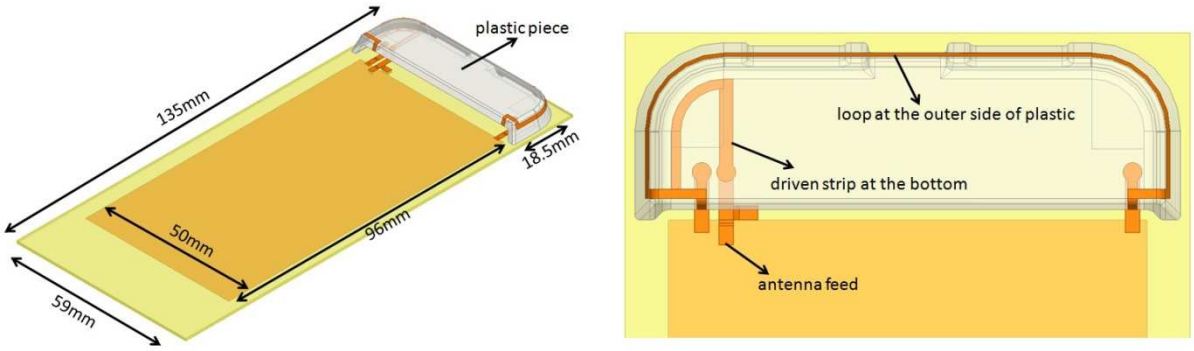

Figure 179 Parasitic Loop Antenna Model

As seen in Figure 180, the antenna can cover the interval of 700-2700MHz continuously with a reflection coefficient below -6dB. The simulated radiation efficiency of the antenna is given in Figure 181. A relatively low radiation efficiency is seen around 700MHz (30%) whose main reason is the high loss resistance values of the 25nH inductors modeled in simulations. It is foreseen that the efficiency can be increased by using lower value inductors (hence lower losses), by increasing the physical length of the loop by meandering.

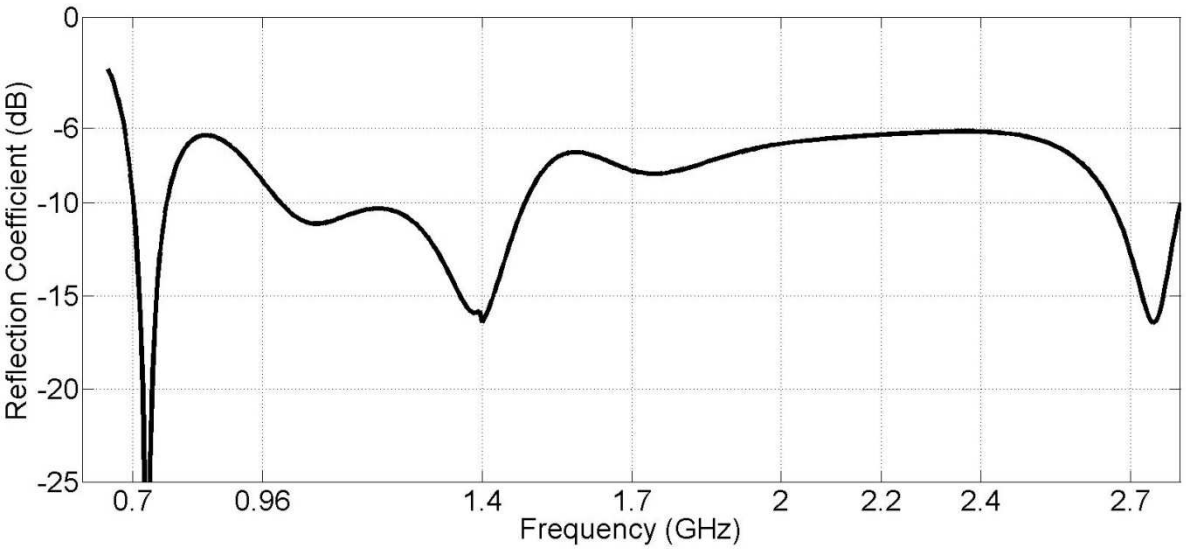

Figure 180 Simulated Reflection Coefficient of the Parasitic Loop Antenna

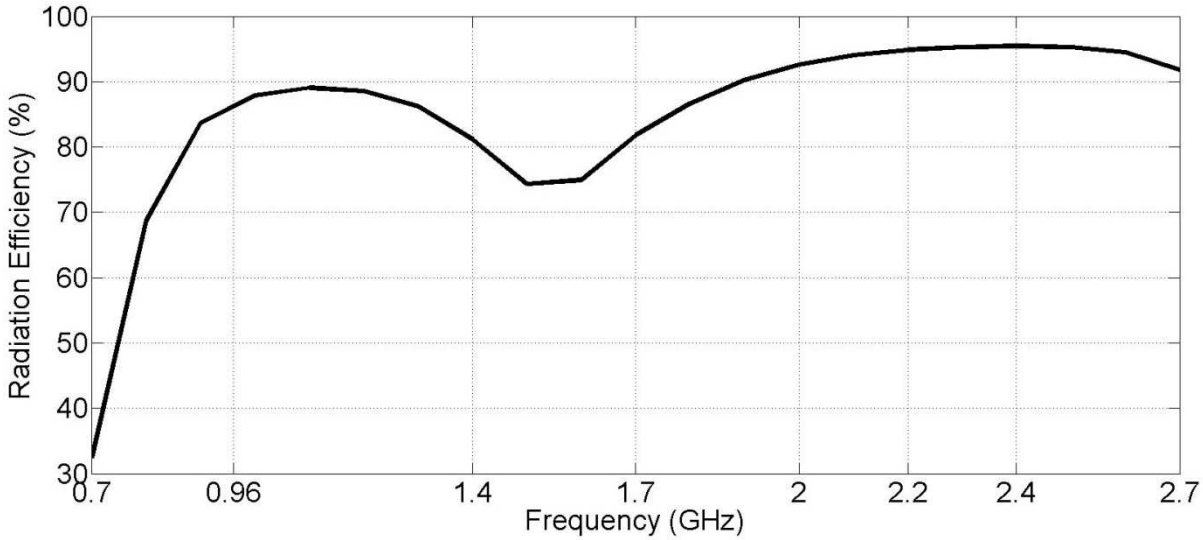

Figure 181 Simulated Radiation Efficiency of the Parasitic Loop Antenna

REFERRENCES FOR THIS CHAPTER

[1] F. Sonnerat, “Développement d’antennes innovantes pour les terminaux mobiles 4G tenant compte de l’interaction avec l’utilisateur : solutions circuits et antennes envisageables,” Ph.D. dissertation, Dept. MO., Télécom Bretagne-Université Européenne de Bretagne, 3 October 2013.

[2] F. Sonnerat, R. Pilard, F. Gianesello, F. Le Pennec, C. Person, D. Gloria, “Innovative LDS antenna for 4G applications,” 7th European Conference on Antennas and Propagation (EuCAP), pp.2773,2776, 8-12 April 2013.

[3] F. Sonnerat, R. Pilard, F. Gianesello, F. Le Pennec, C. Person, D. Gloria, P. Brachat, C. Luxey “Innovative 4G Mobile Phone LDS Antenna Module Using Plastronics Integration Scheme,” AP-S 2013 (Antenna and Propagation Symposium), Orlando, USA, 7-13 July 2013.

LIST OF FIGURES

LIST OF TABLES

PUBLICATIONS

JOURNAL PAPERS

1. **A. Cihangir**, F. Sonnerat, F. Ferrero, R. Pilard, F. Gianesello, D. Gloria, P. Brachat, G. Jacquemod, C. Luxey, "Neutralisation technique applied to two coupling element antennas to cover low LTE and GSM communication standards," Electronics Letters , vol.49, no.13, pp.781,782, June 20 2013

2. **A. Cihangir**, W. Whittow, C. Panagamuwa, F. Ferrero, G. Jacquemod, F. Gianesello, C. Luxey, "Feasibility study of 4G cellular antennas for eyewear communicating devices," Antennas and Wireless Propagation Letters [ACCEPTED FOR PUBLICATION]

3. **A. Cihangir**, F. Ferrero, G. Jacquemod, P. Brachat, C. Luxey, "Neutralized Coupling Elements for MIMO Operation in 4G Mobile Terminals," Antennas and Wireless Propagation Letters [ACCEPTED FOR PUBLICATION]

INTERNATIONAL CONFERENCE PAPERS

1. **A. Cihangir**, F. Ferrero, C. Luxey, G. Jacquemod, "A novel multi-band antenna design with matching network for use in mobile terminals," 6th European Conference on Antennas and Propagation (EUCAP), 2012, pp. 1667-1671

2. **A Cihangir**, F. Sonnerat, F. Ferrero, C. Luxey, R. Pilard, F. Gianesello, G. Jacquemod, "Design of traditional and a novel space-efficient antenna-coupling elements for lower LTE/GSM mobile phones," Loughborough Antennas and Propagation Conference (LAPC 2012)

3. F. Sonnerat, R. Pilard, F. Gianesello, D. Gloria, F. Le Pennec, C. Person, **A. Cihangir**, F. Ferrero, C. Luxey, P. Brachat, "Wideband LDS antenna using two radiating elements," Loughborough Antennas and Propagation Conference (LAPC 2012)

4. **A. Cihangir**, F. Ferrero, C. Luxey, G. Jacquemod, F. Sonnerat, R. Pilard, F. Gianesello, D. Gloria, P. Brachat, "Combination of Two Neutralized Coupling Element Antennas for Low LTE and GSM Mobile Phones," IEEE AP-S/USNC-URSI Symposium, 2013

5. **A Cihangir**, F Ferrero, C Luxey, G Jacquemod, "A space-efficient coupling element antenna for WWAN applications," 2013 International Workshop on Antenna Technology (iWAT), pp.55-58

6. **A Cihangir**, F Ferrero, C Luxey, G Jacquemod, P Brachat, "A bandwidth-enhanced antenna in LDS technology for LTE700 and GSM850/900 standards," 7th European Conference on Antennas and Propagation (EuCAP), 2013, pp. 2786-2789

7. **A. Cihangir**, F. Ferrero, C. Luxey, G. Jacquemod, E. Larique, R. Robin, P. Brachat, " Tunable Antennas Using MEMS Switches for LTE Mobile Terminals," Loughborough Antennas and Propagation Conference (LAPC 2013)

8. **A. Cihangir**, F. Ferrero, C. Luxey, G. Jacquemod, A. Reinhardt, L. Dussopt, N. Lorphelin, N. Obeid, P. Brachat, "Investigation of Tunable Matching Circuits for Multiband 4G Handsets," 8th European Conference on Antennas and Propagation (EuCAP), 2014 [ACCEPTED]

9. **A. Cihangir**, F. Ferrero, C. Luxey, G. Jacquemod, A. Reinhardt, L. Dussopt, N. Lorphelin, C. Pavageau, P. Brachat, "Utilization of Tunable Components for 4G Frequency Reconfigurable Mobile Terminal Antenna," 2014 International Workshop on Antenna Technology (iWAT) [ACCEPTED]

NATIONAL CONFERENCE PAPERS

1. **A. Cihangir**, F. Ferrero, C. Luxey, G. Jacquemod, P. Brachat, "Conception d'un nouvel élément antennaire de couplage pour terminaux mobiles LTE/UMTS/GSM," Journées Nationales Microondes (JNM), 2013

2. **A. Cihangir**, F. SONNERAT, F. Ferrero, R. Pilard, F. Gianesello, D. Gloria, C. Luxey, G. Jacquemod, P. Brachat, "Antenne en technologie LDS pour terminaux mobiles LTE700 et GSM850/900," Journées Nationales Microondes (JNM), 2013

AWARDS

3rd place in "IET Best Student Paper" contest in LAPC2013

ABSTRACT

With the introduction of the fourth generation (4G) of cellular mobile communications, there has been an increase in the frequency bands that a generic mobile phone should be able to operate. This requirement poses some challenges in the design of the transceiver modules of the device as well as the RF front-end and the antenna.

From the antenna design point of view, the newly added frequency bands especially LTE bands 12-13-17 which goes down to 700MHz creates the main design challenge: covering 700-960MHz (30% bandwidth) in the low-band, considering also backward compatibility with the former technologies like GSM850/900. Since the space reserved for the antenna is electrically small in this frequency range, special design techniques are necessary to obtain the required bandwidth for a generic mobile terminal antenna.

It should also be taken into account in the design phase, that the antenna needs to be appropriate for operation in the data-rate enhancement techniques like MIMO (multiple input multiple output) and carrier aggregation in LTE-Advanced. Furthermore, considering the real use cases of the mobile terminal, the effect of the user (hand, head and both) on the antenna performance should also be investigated.

In this thesis, several antenna designs for 4G coverage in mobile terminals are proposed. Different antenna topologies are evaluated consisting of tunable/passive antennas as well as single/multi-feed structures.

RÉSUMÉ

Avec l'introduction des standards de communication de quatrième génération (4G) dans la téléphonie mobile, les bandes de fréquence dans lesquelles un téléphone mobile générique doit fonctionner ont naturellement augmenté. Ces évolutions ont induit de nouveaux challenges techniques notamment en ce qui concerne la conception des modules d'émission-réception, du frontal RF mais surtout des antennes.

Les bandes de fréquences nouvellement ajoutées, en particulier les bandes LTE 12/13/17 qui descendent jusqu'à 700 MHz, constituent le défi antennaire majeur: couvrir la bande basse des 700-960MHz (30%) notamment en incluant la bande GSM850/900 compte tenu de la rétrocompatibilité avec les standards 3G. Etant donné que l'espace réservé pour l'antenne dans un terminal portatif est électriquement petit (dans cette gamme de fréquences basses), des techniques de conception spécifiques doivent être mises en œuvre pour pouvoir couvrir toute la bande de fréquence basse.

Dans la phase de conception, il doit également être pris en compte le fait que l'antenne ou les antennes puissent incorporer des techniques d'amélioration de débit de données telles que le MIMO (Multiple Input Multiple Output) et l'agrégation de porteuse (Carrier Aggregation) pour le LTE-Advanced. De plus, si l'on considère des cas d'utilisation réalistes, les effets de l'utilisateur (main, tête) sur les performances globales du terminal doivent aussi être examinés.

Dans cette thèse, plusieurs concepts d'antennes 4G pour les futurs terminaux mobiles sont proposés. Différentes topologies antennaires sont évaluées notamment des antennes reconfigurables / passives ainsi que des structures à alimentation simples et multiples.